

Effect of Cross-linking and Chain Defects on the Crystallization of
Poly(ethylene glycol)

Dissertation

zur Erlangung des Doktorgrades der Naturwissenschaften
(Dr. rer. nat.)

der

Naturwissenschaftlichen Fakultät II
Chemie, Physik und Mathematik

der Martin-Luther-Universität
Halle-Wittenberg

vorgelegt von

Herrn MSc. Muhammad Haris Samiullah
geb. am 05.11.1984 in Karachi, Pakistan

Gutachter:

1. Prof. Dr. Jörg Kreßler

2. Prof. Dr. Jörg C. Tiller

Verteidigung: 21.02.2018

Table of Contents

1. General Introduction	7
1.1. Polymer Networks and Gels.....	7
1.2. Types of Polymer Networks	9
1.2.1 Chemical Networks	10
1.2.1.1 Thermosetting Resins.....	10
1.2.1.2 Vulcanization	11
1.2.2 Physical Networks.....	12
1.2.2.1 Microcrystallite Formation	12
1.2.2.2 Microphase Separation	13
1.2.2.3 Supramolecular Interactions	13
1.3. Theories of Gelation	15
1.3.1 Statistical Theories of Gelation	16
1.3.1.1 Carother's Theory of Gelation	16
1.3.1.2 Flory-Stockmayer Theory of Gelation	17
1.4. Crystallization of Poly(Ethylene Glycol).....	21
1.5. The Odd-Even Effect	25
1.6. Motivation and Objectives	27
2. Experimental Section	30
2.1. Materials	30
2.2. Instrumentation	31
2.2.1 Attenuated Total Reflection-Infrared Spectroscopy (ATR-IR).....	31
2.2.2 Nuclear Magnetic Resonance Spectroscopy (NMR)	31
2.2.3 Differential Scanning Calorimetry (DSC)	33
2.2.4 Temperature Dependent Small Angle X-ray Scattering (SAXS)	33
2.2.5 Temperature Dependent Wide Angle X-ray Scattering (WAXS).....	35
2.2.6 Matrix Assisted Laser Desorption/Ionization–Time of Flight (MALDI-ToF) Spectrometry	36
2.2.7 Polarized Optical Microscopy (POM).....	36
2.2.8 Inductively Coupled Plasma Mass Spectrometry (ICP-MS).....	36
2.3. Syntheses	37
2.3.1 Synthesis of PEG Networks	37
2.3.1.1 Synthesis of PEG-Alkyne	37
2.3.1.2 Synthesis of PEG(S)-Azide.....	39
2.3.1.3 Network Formation <i>via</i> Cu(I)-Catalyzed Azide-Alkyne Cycloaddition <i>Click</i> Reaction.....	40
2.3.2 Synthesis of PEG ₁₁ -TR-PEG ₁₁	41

2.3.2.1 Synthesis of PEG ₁₁ -Azide	42
2.3.2.2 Synthesis of PEG ₁₁ -Alkyne	44
2.3.2.3 Synthesis of PEG ₁₁ -TR-PEG ₁₁ <i>via</i> Cu(I)-Catalyzed Azide-Alkyne Cycloaddition <i>Click</i> Reaction	45
2.3.3 Synthesis of PEG ₁₁ -TR-(CH ₂) _n -TR-PEG ₁₁	47
2.3.3.1 Synthesis of PEG ₁₁ -TR-(CH ₂) _n -TR-PEG ₁₁ , <i>n</i> = 2-6	47
2.3.3.2 One-pot syntheses of PEG ₁₁ -TR-(CH ₂) _n -TR-PEG ₁₁ with <i>n</i> = 7-8	50
2.3.3.3 Synthesis of Dimethyl-bis(triazole) Spacers Me-TR-(CH ₂) _n -TR-Me (<i>n</i> = 4-6)	53
3. Result and Discussion	54
3.1. Well-Defined Poly(ethylene glycol) Networks via Cu(I)-Catalyzed Azide-Alkyne Cycloaddition Reaction	54
3.1.1 Network Structure and Defects	57
3.1.2 Thermal Properties	60
3.1.3 Isothermal Crystallization Kinetics	63
3.1.4 Non-isothermal Crystallization Kinetics	73
3.1.5 Swelling Measurements	78
3.1.6 Temperature Dependent Wide Angle X-ray Scattering (WAXS)	82
3.1.7 Temperature Dependent Small Angle X-ray Scattering (SAXS)	87
3.2. Crystallization and Structural Studies of Linear Poly(ethylene glycol) Chains with a Well-Defined Point Defect in the Middle of the Polymer Chain	91
3.2.1 Crystallization of PEG ₁₁ -TR-PEG ₁₁	91
3.2.2 Structural Changes of PEG ₁₁ -TR-PEG ₁₁	93
3.3. Solid-State Phase Transitions and Odd-Even Effect in Poly(ethylene glycol) Crystals Induced by Chain Defects of Variable Lengths	97
3.3.1 Phase Transitions in PEG ₁₁ -TR-(CH ₂) _n -TR-PEG ₁₁ with <i>n</i> = 2,3,5	100
3.3.2 Phase Transitions in PEG ₁₁ -TR-(CH ₂) _n -TR-PEG ₁₁ with <i>n</i> = 6,7,8	106
3.3.3 Phase Transitions in PEG ₁₁ -TR-(CH ₂) ₄ -TR-PEG ₁₁	111
3.3.4 The Odd-Even Effect	115
4. Conclusions	118
5. References	121
6. Appendix	131
7. List of Publications	157

List of Abbreviations

^{13}C NMR	Carbon(13) Nuclear Magnetic Resonance Spectroscopy
^1H NMR	Hydrogen (Proton) Nuclear Magnetic Resonance Spectroscopy
ATR-IR	Attenuated Total Reflection- Infrared Spectroscopy
CDCl_3	Chloroform (Deuterated)
CuAAC	Cu(I)-Catalyzed Azide-Alkyne Cycloaddition Reaction
CP ^{13}C MAS NMR	Cross-Polarization Magic Angle Spinning Carbon(13) Nuclear Magnetic Resonance
SEM	Scanning Electron Microscopy
DCM	Dichloromethane
DMF	Dimethylformamide
DMSO	Dimethyl Sulfoxide
$\text{DMSO-}d_6$	Dimethyl Sulfoxide (Deuterated)
DQ NMR	Double-Quantum Nuclear Magnetic Resonance Spectroscopy
DSC	Differential Scanning Calorimetry
EC crystal	Extended chain crystal
FC crystal	Folded chain crystal
FTIR	Fourier Transform Infrared Spectroscopy
FWHM	Full Width At Half Maximum
ICP-MS	Inductively Coupled Plasma Mass Spectrometry
IF	Integer folded crystal
IUPAC	International Union of Pure and Applied Chemistry
LCP	Liquid Crystalline Polymers
MALDI-TOF	Matrix Assisted Laser Desorption/Ionization-Time Of Flight
MQ NMR	Multi-Quantum Nuclear Magnetic Resonance Spectroscopy
$\text{Me-TR-(CH}_2)_n\text{-TR-Me}$	Dimethyl-bis(Triazole) units ($n = 4,5,6$)
NIF	Noninteger folded crystals
NFT	Numerical Fractionation Technique
NMR	Nuclear Magnetic Resonance Spectroscopy
PEG	Poly(ethylene glycol)

PEG(400)	Poly(ethylene glycol) chain having molar mass of 400 g/mol
PEG(400)-Alkyne	Alkyne modified poly(ethylene glycol) chain having molar mass of 400 g/mol
PEG(S)	Three-arm "star-shaped" poly(ethylene glycol)
PEG(S)-Alkyne	Alkyne modified three-arm "star-shaped" poly(ethylene glycol)
PEG(S)-Azide	Azide modified three-arm "star-shaped" poly(ethylene glycol)
PEG(S-1000)	Poly(ethylene glycol) network comprised of linear PEG chains (1000 g/mol) and three-arm "star-shaped" PEG unit.
PEG ₁₁	Poly(ethylene glycol) chain having 11 repeating units
PEG ₂₂	Poly(ethylene glycol) chain having 22 repeating units
PEG ₁₁ -TR-(CH ₂) _n -TR-PEG ₁₁	Two PEG ₁₁ chains coupled together by two triazole ring in the middle of the chain, separated from each other by <i>n</i> number of methylene units
PEG ₁₁ -TR-PEG ₁₁	Two PEG ₁₁ chains along with one triazole ring in the middle PEG ₁₁ -TR-(CH ₂) _n -TR-PEG ₁₁
PEG-TR'	High-temperature phase of PEG ₁₁ -TR-(CH ₂) _n -TR-PEG ₁₁ after the incorporation of one triazole unit in its crystal
PEG-TR''	High-temperature phase of PEG ₁₁ -TR-(CH ₂) _n -TR-PEG ₁₁ after the incorporation of two triazole unit in its crystal
POM	Polarized Optical Microscopy
PVA	Poly(vinyl alcohol)
QENS	Quasielastic Neutron Scattering
SAXS	Small Angle X-ray Scattering
SBS	Polystyrene- <i>b</i> -polybutadiene- <i>b</i> -polystyrene
SP ¹³ C MAS NMR	Single Pulse Magic Angle Spinning Carbon(13) Nuclear Magnetic Resonance
THF	Tetrahydrofuran
TR	1, 4-disubstituted 1,2,3-triazole
WAXS	Wide Angle X-ray Scattering

1. General Introduction

1.1. Polymer Networks and Gels

Cross-linked polymers are a class of materials with a broad range of technical and biological applications. Their diverse application spectrum spans from their usage in tire industry¹ to be an important class of materials for making scaffolds for tissue engineering^{2,3}. Although for last several decades, these materials are subject to extensive experimental and theoretical investigations, still there are some challenges present to deal with. By definition, a polymer network is a three-dimensional structure formed by the cross-linking of polymer chains, either by chemical or physical bonding. Among large spectrum of their characteristics, two of the most important are their large deformation elasticity and improved resistance to solvent attack. As for later, in contrast to uncross-linked polymer chains, polymer networks do not dissolve in solvents but rather get swollen by holding a large number of solvents molecules within their structure. These diluted or swollen networks are also termed as gels.

Swelling of cross-linked polymer networks in the presence of a solvent is a phenomenon of great theoretical and practical importance. Its applications range from membrane separation technology and various biomedical usages to numerous physiological processes. When the dry polymer network gets in contact with suitable solvent molecules (which can be either small molar mass solvent molecules, oligomers or polymer chains^[4,5]), the network's chains try to disperse or mix with the solvent molecules causing an increase in the system's entropy. However, stretching of network chains due to the swelling or volume expansion of the network counterbalance this phenomenon. A good solvent/polymer interaction and low cross-link density favor the swelling process in the absence of other factors are e.g. pH-value of the solvent, temperature, presence of ionizable groups, etc. At any given time, the degree of swelling or the swelling ratio can be calculated as follows

$$Q = \frac{m_s - m_d}{m_d} \quad (1.1)$$

where Q is the swelling ratio, m_s is the mass of swollen network and m_d represents the mass of dry network.

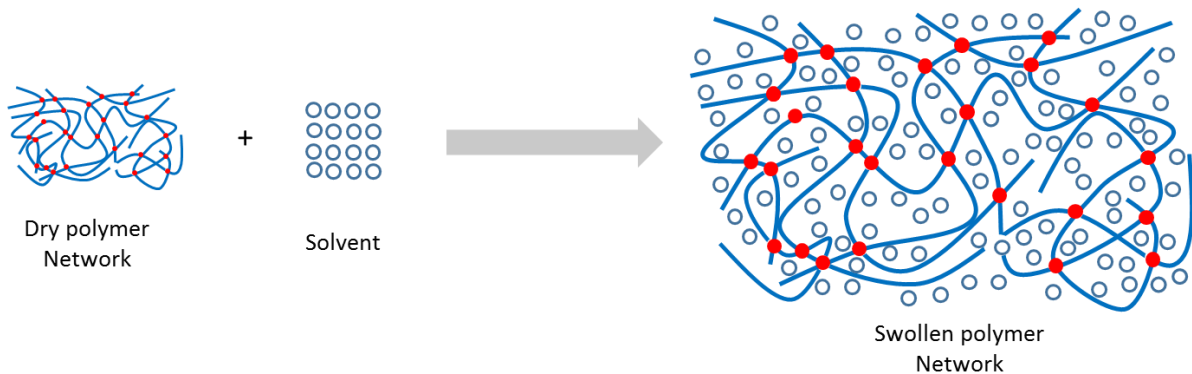


Figure 1.1: Schematic representation of swelling of a polymer network.

Typically, the cross-linking density is determined by the swelling of networks in a good solvent. The Flory-Rehner theory⁶ is one of the widely used theories related to the swelling of polymer networks and commonly used for the determination of their cross-linking density. This theory is based on the following three assumptions⁷

- i. The change of the Gibbs free energy of the system upon swelling is the sum of the change in the Gibbs free energy of mixing of polymer and solvent and the elastic deformation of polymer strands

$$\Delta G = \Delta G_{mix} + \Delta G_{el} \quad (1.2)$$

- ii. The mixing term can describe by the mean field Flory-Huggins theory
- iii. The affine deformation model will be considered to describe the elastic deformation phenomenon. A general expression of the Flory-Rehner theory is

$$-[\ln(1 - v_2) + v_2 + \chi_1 v_2^2] = V_1 n_c \left(v_2^{\frac{1}{3}} - \frac{v_2}{2} \right) \quad (1.3)$$

where, v_2 is the volume fraction of polymer in the swollen state, V_1 is the molar volume of the solvent, n_c is the number of network chain segments between two crosslinks, and χ_1 is the Flory-Huggins solvent-polymer interaction parameter. Although, Eq. 1.3 is a basic form of the Flory-Rehner theory, however, several modified versions of this equation have also been developed to suit different experimental conditions.⁸

1.2. Types of Polymer Networks

There are different kinds of polymer networks or gels, depending upon the type of subunits they consist of and types of bonding they have. For example, the subunits are either small multifunctional molecules bonded together to form an extensive three-dimensional network (e.g. epoxy resins), or long polymer chains connected by relatively small cross-linker units (e.g. vulcanized rubber). Typically, polymer networks are categorized into two classes depending upon the nature of bonds that connect the basic subunits. The first type is chemical networks where the bonds, linking the subunits, are covalent whereas the second category is physical networks, where cross-linking occurs

mainly due to non-covalent interaction. A brief description of both of these kinds of networks is as follows.

1.2.1 Chemical Networks

To form chemical networks, multifunctional subunits are connected *via* covalent bonds to form a three-dimensional cross-linked structure. These types of networks are permanent, and their chemical structure does not get affected by heating or by any solvent. For chemical networks formation, the functionality of the monomer units is critical. According to IUPAC, the functionality of a monomer can be defined as the number of covalent bonds a monomeric unit can form with other reactants.⁹ For instance, adipic acid and 1,3-propanediol are examples of difunctional monomers, glycerol is considered as a trifunctional monomer while pentaerythritol is a good example of tetrafunctional monomers.⁹ Hence, for this type of chemical networks which are made up from one type of subunits, the requirement of the minimum degree of functionality is more than two^{9,10}, i.e. $f > 2$. However, in the case of chemical networks made from two or more than two kind of subunits, at least one of the subunit must have the functionality more than two while the other subunits must be at least bifunctional molecules. Some of the typical examples of chemical networks are discussed below.

1.2.1.1 Thermosetting Resins

Epoxy resins are an excellent example for such kind of chemical networks. It is a two-component system where the first component is a low molar mass bifunctional polymer with two epoxide functional groups, while the second component is a multifunctional cross-linker also known as the hardener. When the polymer chain and the cross-linker unit are mixed in an appropriate proportion, a three-dimensional end-linked network is formed with enhanced final mechanical properties¹¹.

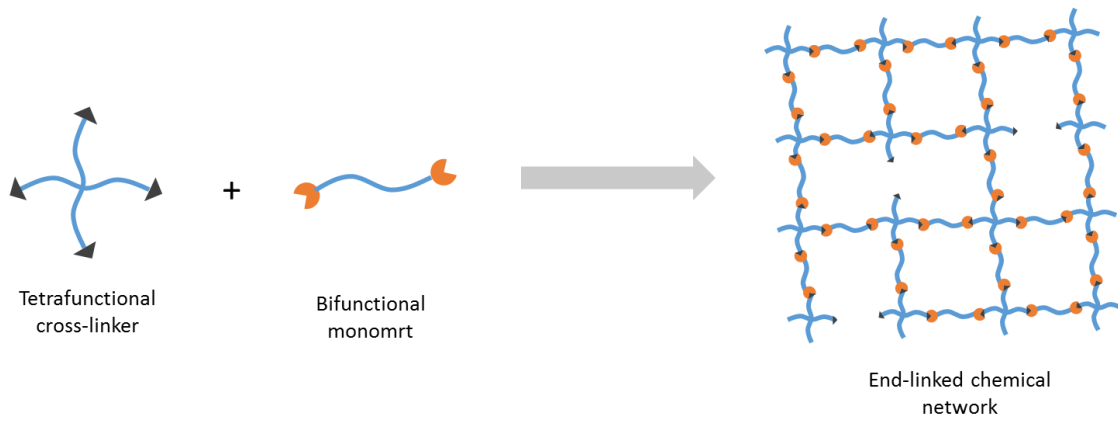


Figure 1.2: Formation of chemical polymer network via end-linking polymerization

1.2.1.2 Vulcanization

One basic method, on which the whole rubber industry relies upon, is the vulcanization of rubber¹². In this type of chemical networks, long polymer chains with multiple functional groups present in their backbone are connect together by a relatively small multifunctional molecule. These functional groups in the polymer chains are either unsaturated double bonds or any other pendant functional group present in the repeating unit of the polymer chain. For example, natural rubber or polyisoprene contains double bonds in its backbone which are capable of reacting with one, two or up to eight sulfur atoms to form mono-, di- or polysulfide links¹³, also known as sulfur bridges. Figure 1.3 demonstrates the basic idea of this kind of network formation process.

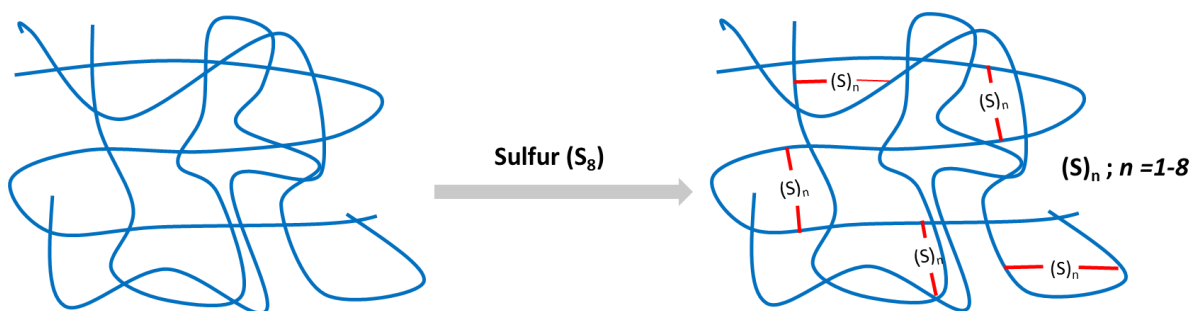


Figure 1.3: Formation of chemical polymer network using sulfur as a cross-linking unit.

1.2.2 Physical Networks

In physical polymer networks, the cross-linking occurs due to physical interactions between the subunit molecules rather than the formation of any chemical linkage. These type of networks are usually temporary networks i.e. their physical state is stable under certain conditions and were easily disintegrated to their primary subunits when the conditions are not favorable. The temperature is one of the most critical parameters for all of these types of networks. That is why they were often referred to as thermoreversible networks.^{14,15} Some of the mechanisms by which these thermoreversible networks can be formed are discussed below.

1.2.2.1 Microcrystallite Formation

Above certain critical concentrations, some semi-crystalline polymers are capable of forming microcrystalline regions even in their dissolved state (see Figure 1.4). These microcrystallites act as the physical cross-links in the system and provide a suitable mechanical strength to the whole system. One of the best common examples of this type of polymer network is the making of edible jelly, where gelatin (a hydrolyzed form of collagen) forms a large number of small crystallites in the solution which provide structural stability to the whole system. Poly(vinyl alcohol) (PVA) cryogels^{16,17,18} also belong to this class of physical networks. They are made by the repeated freezing and thawing of PVA-water solution. This procedure produces the microcrystalline domains of PVA in the PVA-water system which act as physical crosslinks for PVA cryogels.

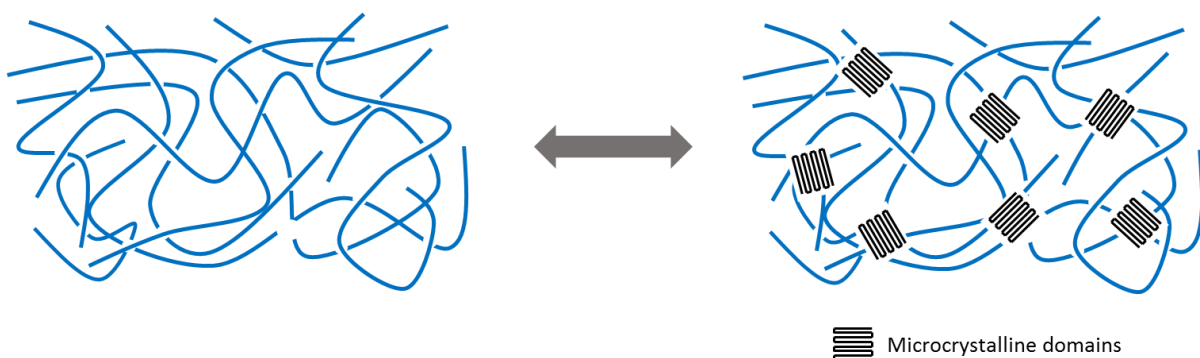


Figure 1.4: Formation of physical polymer network via microcrystallite formation.

1.2.2.2 Microphase Separation

In this particular type of polymer networks, a block copolymer made from two or more types of chemically different and immiscible polymers rearranges itself at lower temperatures to produce a microphase-separated structure. Figure 1.5 shows an example of microphase separation of polystyrene-*b*-polybutadiene-*b*-polystyrene (SBS) triblock copolymer. As the terminal polystyrene blocks are immiscible with polybutadiene chains and have a higher stiffness at room temperature ($T_g = 100\text{ }^\circ\text{C}$), they tend to form rigid microdomains within the polybutadiene copolymer matrix. These rigid microdomains act as physical cross-links for the system, resulting in an increase in the overall elastic behavior of the material. However, heating the SBS triblock copolymer above the glass transition temperature of polystyrene softens the terminal polystyrene blocks and make the whole block copolymer matrix to flow viscoelastically. These materials are also known as thermoplastic elastomers.

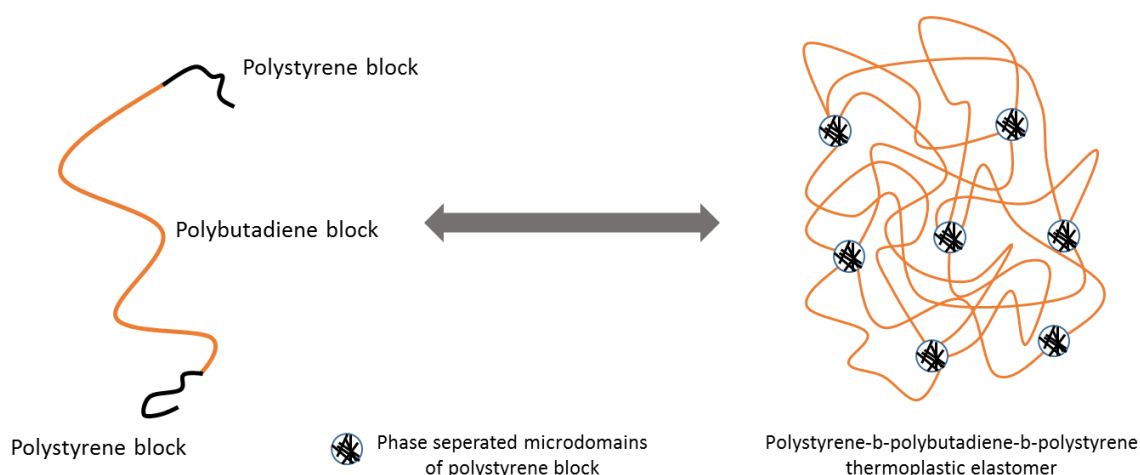


Figure 1.5: Formation of physical polymer network via microphase-separated domain formation.

1.2.2.3 Supramolecular Interactions

In this type of polymer networks, macromolecular chains are cross-linked because of the non-covalent or transient links such as hydrogen bonding¹⁹, hydrophobic interactions²⁰, transition metal complexation²¹, ionic attractions²², π - π stacking²³, etc. Supramolecular

polymer networks possess the characteristics of both chemical and physical networks, and under favorable conditions, they are capable of forming strong structural materials. However, they can also easily dissociate under other conditions such as variation in temperature, pH value, the polarity of the solvent, redox interactions, competitive ligation, etc. Here it will be worth mentioning that the terms supramolecular polymer gels and supramolecular polymer networks²⁴ represent two different materials. Supramolecular polymer gels consist of low molar mass molecules which self-assemble into the three-dimensional structure through the above-mentioned non-covalent types interactions. In contrast, supramolecular polymer networks already possess the long covalently bonded polymeric chains but also contain functionalized pendent groups which are capable of coupling together non-covalently, to form a network structure (see Figure 1.6 (a) and (b)).

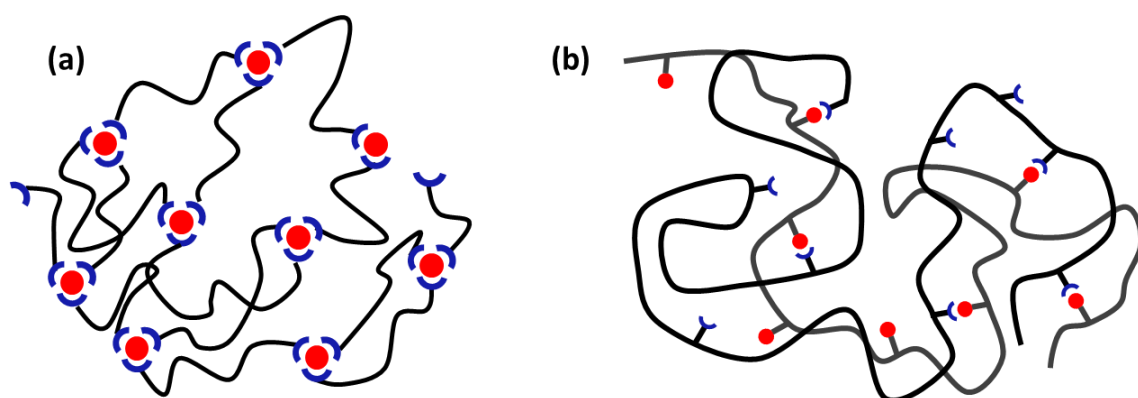


Figure 1.6: (a) Supramolecular polymer gels from lower molar mass subunits, (b) Supramolecular polymer networks formed from long polymer chains functionalized with mutually attractive motifs.

Non-covalent interactions greatly differ in their strength, as shown in Figure 1.7²⁵. Depending upon the type of non-covalent interactions used for the final cross-linking step, the supramolecular polymeric materials can be designed to have different final mechanical properties.

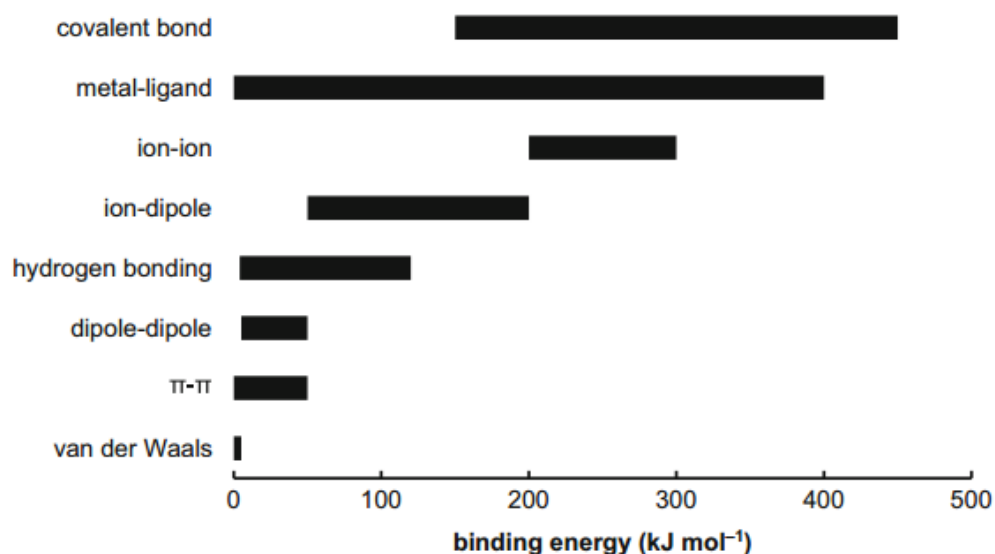


Figure 1.7: The most common types of noncovalent interactions along with their binding energies.²⁵

1.3. Theories of Gelation

When the small molecular subunits form a network, the whole reaction mixture becomes immobilized. That stage in the network-forming polymerization reaction is known as gel point, and the phenomenon is called gelation. For the understanding of a gelation process and to predict the gel point of the system, several theories and methods have been proposed and can be broadly divided into two types i.e. statistical methods and kinetic methods. Kinetic methods like Numerical Fractionation Technique²⁶ (NFT) or Percolation theory²⁷ can be used to calculate and forecast the gelation process, however, they are found to be relatively more complicated and require lengthy and time-consuming computer simulations to produce any useful results. Although it will be the statistical methods which are discussed in more detail later in this section, it is important to mention here that all theories possess their advantages and disadvantages. The selection of any particular method depends on the type of system to be analyzed, the amount of information available about the system, the level of detail required, and the availability of computer resources.

1.3.1 Statistical Theories of Gelation

Among the most common statistical methods, dealing with network formation or gelation mechanisms are:

1.3.1.1 Carother's Theory of Gelation

Wallace Carother introduced a series of mathematic relationships²⁸ for the step-growth polymerization reaction in order to find out the average degree of polymerization \overline{X}_n at any given monomer conversion p (i.e. extent of reaction).²⁸ These relations are also known as Carother's equations and depending upon the functionality of monomer units and stoichiometric ratio of monomers in the reaction system, there has been several versions of these equations. For instance, the simplest case would be where two bifunctional monomers are present in a system in equimolar amount. In order to find out the average degree of polymerization \overline{X}_n at any given value of extent of reaction p , Eq. 1.4 will be used

$$\overline{X}_n = \frac{1}{1 - p} \quad (1.4)$$

This simplest case discusses the formation of only a linear polymer via the step-growth polymerization, where the higher degree of polymerization \overline{X}_n can be predicted only at very higher monomer conversion.

Furthermore, monomers with the functionality greater than two ($f > 2$) introduce branching in the polymer chains and the average degree of polymerization \overline{X}_n depends on the average functionality f_{av} per monomer unit in the system. However, when the stoichiometrically equimolar amount of functional groups are present in the reaction system, then at a certain value of extent of reaction p , the average degree of polymerization \overline{X}_n becomes infinity. This stage of reaction is called the *gel point* and that extent of reaction value where gelation happens is called *critical extent of reaction* p_c . A modified Carother's equation²⁹ provides a relationship between the average functionality f_{av} of monomers and the extent of reaction at the gel point p_c , provided

that the functional groups are present in stoichiometrically equivalent amount in the polymerization system. A general expression for the extent of reaction p will be

$$p = \frac{2}{f_{av}} - \frac{2}{\overline{X}_n f_{av}} \quad (1.5)$$

At the gel point, the value of \overline{X}_n becomes infinite and the expression for the critical extent of reaction p_c at the gel point is given by

$$p_c = \frac{2}{f_{av}} \quad (1.6)$$

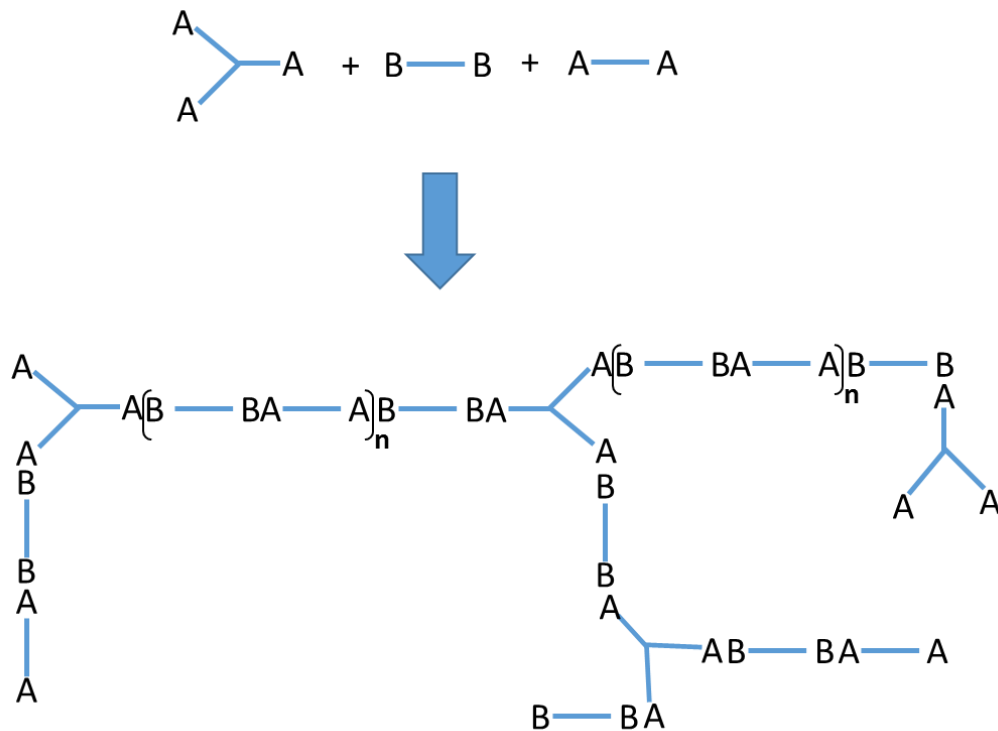
Eq. 1.6 is a simple equation to predict the gel point of the system, however, one of the limitations of this theory is that it only predicts the critical extent of reaction p_c values for those systems where the functional groups are present in stoichiometrically equivalent amount. Any imbalance in the monomer concentration will result in incorrect and unrealistic values for the whole system.

1.3.1.2 Flory-Stockmayer Theory of Gelation

In order to derive an expression for predicting the extent of reaction at the gel point p_c , a statistical approach was used by Flory^{30,31} and Stockmayer³² in the early 1940s and it is one of the most popular and widely used theories for the gelation processes. They calculated the extent of reaction of a system when the weight-average degree of polymerization \overline{X}_w of the growing branched molecule approaches an infinite value. However, The Flory-Stockmayer theory is based on the following two assumptions:

- i. The reactivity of all functional groups will be similar and independent of molecular size.
- ii. There will be no intramolecular reactions between functional groups on the same molecule.

In order to derive a mathematical expression let's assume a polycondensation reaction among monomers A—A with B—B along with A_f , where f represents the functionality of monomer and for this system $f = 3$. A schematic representation of this reaction system is shown in Scheme 1.1.



Scheme 1.1: Schematic representation of branched polymer formed by the reaction of A—A with B—B along with trifunctional branching unit A_3 .

Here, A_f represents a multifunctional *branch unit* while the segments between the two branch units are called the *chain segments* and n can have any value from zero to infinity. A new term, *branching coefficient* α , was introduced and is defined as a probability that a given functional group of a branch unit at the end of a polymer chain segment leads to another branch unit. The criterion for the gelation process in any system which contains a branch unit of functionality f is that at least one of the $(f - 1)$ chain segments should be connected to another branch unit. Hence the probability of this to happen is simply $1/(f - 1)$ and it is known as critical branching coefficient, α_c .

$$\alpha_c = \frac{1}{(f - 1)} \quad (1.7)$$

The f in Eq. 1.7 represents the functionality of the branch units, however, in the case of more than one type of multifunctional branch unit present in the system, an average f value of all the multifunctional branch units will be used.

The probability α can be related to the extent of reaction p , by determining the probability of finding a chain segment, in the network structure. For this purpose, let p_A and p_B represent the extents of the reaction of A and B functional groups and ρ denotes the ratio of all A groups that are part of branch units (both reacted and unreacted) to the total number of all A groups in the mixture. Consequently, the probability for a group B reacted with a branch unit can be represented by $p_B\rho$ and the probability that it has reacted with a non-branched A—A unit will, therefore, be $p_B(1 - \rho)$.

Hence, the probability of obtaining a chain segment for the above system will be $p_A [p_B (1 - \rho) p_A]^n p_B\rho$ and by taking summation over all values of n will yield

$$\alpha = \frac{p_A p_B \rho}{1 - p_A p_B (1 - \rho)} \quad (1.8)$$

To simplify it further, either p_A or p_B can be replaced by the term r , where r represents the ratio of A groups to all B groups.

$$r = \frac{p_A}{p_B} \quad (1.9)$$

Then Eq. 1.8 can be reconstructed as

$$\alpha = \frac{r p_A^2 \rho}{1 - r p_A^2 (1 - \rho)} = \frac{r p_B^2 \rho}{1 - r p_B^2 (1 - \rho)} \quad (1.10)$$

By combining the Eq. 1.10 and Eq. 1.8, one comes to a useful expression for the extent of reaction, (for A functional groups) at the gel point

$$p_c = \frac{1}{\sqrt{[r [1 + \rho(f - 2)]]}} \quad (1.11)$$

Eq. 1.11 shows the critical extent of reaction only for the system mentioned above. However, for a more general expression which can be used for other cases e.g. systems with more than one type of multifunctional branch units, etc. the following expression for the critical extent of reaction at the gel point was used.

$$p_c = \frac{1}{\sqrt{[r [(f_{w,A} - 1)(f_{w,B} - 1)]]}} \quad (1.12)$$

where $f_{w,A}$ and $f_{w,B}$ are weight-average functionalities of A and B functional groups, respectively.

Although the expression for the critical conversion at the gel point derived by the Flory-Stockmayer model is relatively straightforward to use, experimental results were often different from the predicted values. Mostly, values of the critical extent of reaction of real-time experiments were higher than the predicted value and this was mainly due to the two underlying assumption, this theory is based on. Intramolecular reactions between the two functional groups of the same growing molecule cannot be avoided completely rather than reduced by adjusting certain parameters. These reactions were not only responsible for the delay of the gelation process, but they also produce elastically inactive loops which do not contribute to the overall network formation process rather than extending the chain segments between two cross-links. Furthermore, the second assumption of equal reactivity of all functional groups also becomes less and less valid with the progress of reaction because as the reaction proceeds, the functional groups present on the surface of growing molecules are more probable to react with other unreacted functional groups as compared to those who are trapped within the cross-linked structure of the network.

Some other but relatively less important theories are

- the cascade theory of Gordon^{33,34}

- the Miller-Macosko recursive method³⁵
- the stochastic graphs theories of Bruneau³⁶

Although, there are also some other theories which can be found in the literature^{37,38} the first two theories are the simplest and frequently used for the analysis of the gelation process.

1.4. Crystallization of Poly(Ethylene Glycol)

Being a water-soluble, biocompatible and semicrystalline polymer, poly(ethylene glycol) is an important synthetic polymer with a range of applications in various sectors. It is synthesized *via* the anionic polymerization of ethylene oxide (EO) and depending on the final molar mass of the polymer, it is either called as poly(ethylene oxide)(PEO; $M_n \geq 20,000$ g/mol) or poly(ethylene glycol) (PEG; $M_n \leq 20,000$ g/mol).³⁹ PEG has been investigated comprehensively in the past in order to gain a better understanding of its crystallization process. As early as the beginning of the twentieth century, different molecular structure models, such as meanderform model,⁴⁰ 9_5 ,^{41,42} 9_3 ,⁴³ and 7_5 ^{44,45} helix models was proposed for a crystalline PEG chain. However, it was the 7_2 helix model, proposed initially by Tadokoro *et al.* ^{46–48} which gained a widespread acceptance as a most appropriate model for a crystalline PEG chain. Though, shortly after them, different other research groups^{49,50} also come up with the same 7_2 helix model, independently.

According to the initially proposed molecular structure model (Figure 1.8 (a)), a PEG chain in its crystalline state has a helical structure with the helical symmetry isomorphous to the point group D_7 . In the 7_2 helix of PEG chain, seven monomeric units turn two times per fiber period (pitch) with the succession of *trans*, *trans*, and *gauche* conformations.⁴⁷ However, the detailed crystal structure reported later for PEG chains confirms the 7_2 helical structure of PEG chains but with considerably distorted helical symmetry (Figure 1.8 (b)).⁴⁸ The monoclinic unit cell of PEG contains four helical PEG chains, with the cell parameter values as $a = 8.05$ Å, $b = 13.04$ Å, $c = 19.48$ Å, and $\beta = 125.4^\circ$ along with the space group $P2_1/a-C_{2h}$.^{5.48} Furthermore, a planar zigzag conformation (Figure 1.8 (c)) is also reported⁵¹ for PEG chain, but only when it is

subjected to two-fold stretching. This *all-trans* conformation of PEG chain is only stable under stretched conditions and changes rapidly to the 7_2 helix conformation once the stress was removed. PEG also exists in various other crystal modifications by forming crystalline complexes e.g. with HgCl_2 ,⁵² and urea⁵³ etc.

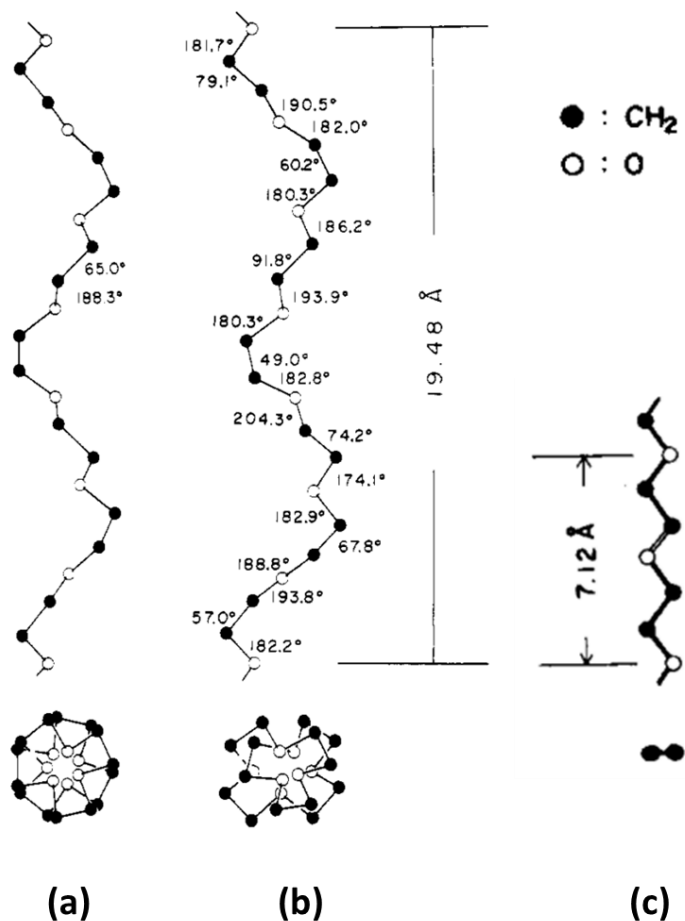


Figure 1.8: (a) Molecular structure model of PEG with the helical symmetry isomorphous to the point group D_7 ⁴⁷ (b) crystal structure model of PEG with distorted helical symmetry⁴⁸ (c) Zig-zag crystal modification of PEG chain when subjected to twofold stretching.⁵¹

Analogous to the crystallization of other linear polymers, the formation of extended chain (EC) crystals of PEG are more thermodynamically favorable than folded-chain (FC) crystals, which are usually formed due to kinetic reasons. It was found that poly(ethylene glycol) chains with molar masses $M_n \leq 3000$ g/mol^{54,55} crystallizes only in extended chain fashion, whereas, n -times folded chain structures are formed for higher molar mass PEGs

($M_n \geq 3000$ g/mol).^{56–59} The fold number n has usually an integer value (integer folded *IF* crystals) and it depends on the molar mass, crystallization temperature and crystallization time of the polymer.^{57,58} During the heating or annealing process, these metastable folded-chain crystals thicken to thermodynamically more stable forms i.e. either extended-chain or smaller fold number crystals, in a stepwise manner (also known as *lamella thickening*). Moreover, noninteger folded (NIF) PEG crystals have also been observed during the initial stages of crystallization.⁶⁰ However, because of being thermodynamically less stable, they were transformed into integer folded *IF* crystals during the later stages of crystallization.⁶¹ When the fold length of *NIF* crystal exist between *IF* ($n = i$) and *IF* ($n = i + 1$) crystals, the transformation from *NIF* to *IF* may proceeds by both isothermal lamella thickening and thinning processes, depending upon the thermodynamic driving force and molecular diffusional motion along the chain axis.⁶¹ However, this transformation of *NIF* to *IF* crystals is increasingly hampered by the increase in the molar mass of the chain and for very long chain lengths, these *NIF* crystals might permanently exist.⁵⁶ PEG crystals with different fold numbers in the same sample^{58,62–64} are also been observed.

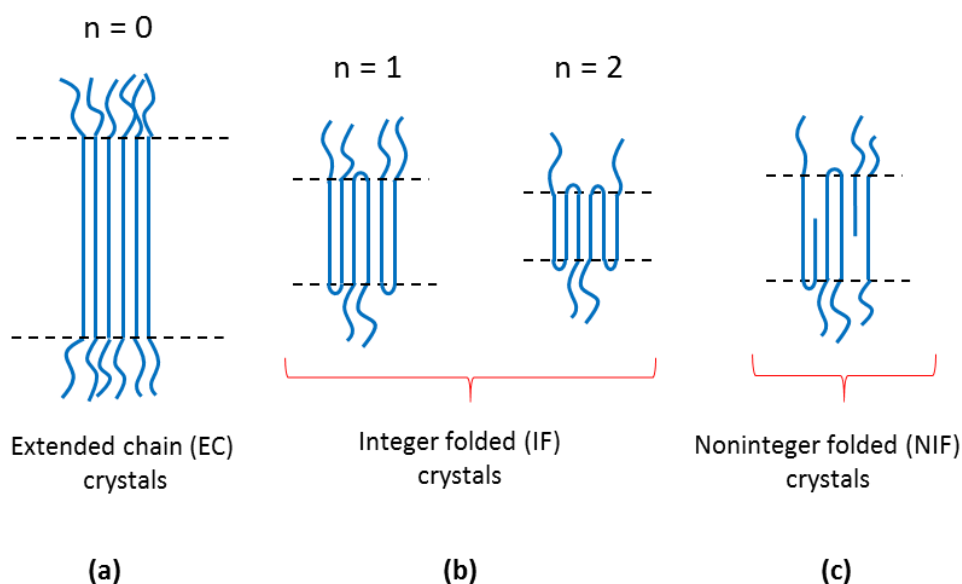


Figure 1.9: Schematic representation of (a) extended chain (EC) with fold number $n = 0$, (b) once and twice integer folded (IF) crystals, $n = 1,2$ and (c) noninteger folded (NIF) chain crystals

Macroscopic properties of polymers are usually influenced by their microscopic chain structures.⁶⁵⁻⁶⁷ Although in smaller amounts, but the presence of chain defects in a polymer backbone effect their crystallization, thermal, and mechanical characteristics. These defects are either intentionally introduced to tailor the final properties of the polymer or can be a result of an effort to create any particular chain architectures i.e. network or branched structures. These defects can either be randomly distributed, i.e. copolymerization of different monomers^{68,69} or can be well-defined and specifically located on a polymer backbone.

Chain ends, comonomer units, coupling moieties, and stereo- and regio-defects etc. can all be considered a point defect in a polymer chain and depending upon their type and size, they can either be incorporated into or excluded from the polymer crystal during crystallization.⁷⁰⁻⁷⁶ Polyethylene (PE) has been extensively studied for both kinds of defects. For instance, randomly distributed defects due to the copolymerization of ethylene and propylene monomer,⁶⁹ or various type of well-defined point defects⁷⁷⁻⁸⁰ on the polyethylene chain. However, some of the pioneering work on studying the effect of chain defects on the crystallization behavior of PEG chain was performed by Cheng *et al.*⁸¹⁻⁸⁴ They investigated the crystallization behavior of PEG chains coupled by different isomers of benzene dicarbonyl dichloride units, resulting in phenylene ester point defects in middle of PEG chain. They found out that, these phenylene ester point defects were excluded out from the PEG crystal during the crystallization process and place themselves on the lamella basal surface. Influence of 1,4-disubstituted 1,2,3-triazole (*TR*) unit on various properties of poly(ethylene glycol) has already been reported.⁸⁵⁻⁸⁷ However, the effect of *TR* unit on the crystallization behavior of PEG is seldom studied.⁸⁸ It seems important that more effort should have been made to study its effect on PEG crystallization as this *TR* unit is produced during the Cu(I) catalyzed Azide-Alkyne Cycloaddition (CuAAC) *click* reactions, which are an important class of coupling reactions often used to produce different PEG architectures.⁸⁹⁻⁹¹

1.5. The Odd-Even Effect

Non-monotonic changes in the material's structure and properties due to either even or an odd number of their basic structural units is a phenomenon repeatedly observed in various fields of natural sciences. The structural unit can be e.g. a CH₂ group, one metal atom or a repeating unit of the polymer. The effect of this phenomenon can be either observed at the macroscale, like changes in the melting points of *n*-alkanes⁹² or at microscale e.g. the difference in properties of nanoclusters made from an odd or even number of atoms.^{93,94} This effect was also noticed in the larger abundance and stability of isotopes of chemical elements with an even number of nucleons compared to their neighbors in the periodic table of elements with respective odd numbers. This Oddo-Harkins rule is valid for all chemical elements with the exception of the lightest elements, which are the basis for nucleosynthesis.^{95,96}

In 1877, A. Bayer was first to observe the melting point alternation effect in homologous series of fatty acids and alkane α,ω -dicarboxylic acids.⁹⁷ He observed that members with the even number of methylene units show higher melting points as compared to their odd numbered neighbor. However, as the CH₂ units increase, this relative difference starts to diminish, gradually.

Although, a comprehensive crystallographic work had already been published in 1928 by Caspari,⁹⁸ it was Boese's group that carried out a thorough investigations on the crystallographic structure of *n*-alkanes,⁹⁹ α,ω -alkanedithiols¹⁰⁰ α,ω -alkanediols¹⁰¹, and α,ω -alkanediamines,¹⁰¹ via single-crystal X-ray diffraction analysis and determined its relationship with their final melting temperature. They came up with a simple geometric demonstration of different crystal packing for odd and even members of a homologous series and suggested that the lower melting temperature of the members with the odd number of methylene units is due to their loose crystal packing and lower crystal density as compared to their neighbors in the series. In addition to the melting temperatures T_m , other properties, such as enthalpy and entropy of melting,¹⁰²⁻¹⁰⁶ solubilities,^{107,108} sublimation energies,¹⁰³ densities,¹⁰⁴ and mechanical properties,^{109,110} have also been reported to exhibit a zig-zag change with respect to the number of methylene groups in the α -mono- and α,ω -disubstituted *n*-alkanes. Moreover, liquid crystals,¹¹¹⁻¹¹⁴ organic

self-assembled monolayers,^{115–117} micellizations of surfactants^{118,119}, etc. are a few of the many areas where the odd-even effect is frequently observed.

This zig-zag behavior of physical properties has also been observed for polymers and among them, the liquid crystalline polymers¹²⁰ (LCP) are probably the most reported materials which demonstrate this odd-even effect. For instance, odd or even number of methylene units present in the flexible part of polyester-based polymeric liquid crystals^{120,121} induce an alternating behavior in the final melting and clearing temperatures of these LCPs. In another example, solid-state ¹³C NMR studies by Mizuno *et al.* on their polyester-based LCPs, having varying lengths of flexible spacer units, also show an odd-even fluctuation in the activation energy of the local polymer chain's motion, in its nematic phase.¹²² Moreover, this effect was also observed in the electronic properties of polymeric semiconductors where, for instance, a non-monotonic dependence of the charge-carrier mobility has been reported for thiophene-based polymeric semiconductors¹²³ caused by the number of methyl groups in their side chains.

In addition to the methylene groups, the odd or even number of monomer units also represents an odd-even effect on the final properties of same polymers. For instance, the degree of polymerization of aminoethylene repeating units in the side chains of the polyaspartamide backbone results a unique odd–even effect on its gene transfection profiles and endosomal escape properties¹²⁴ while in the case of self-assembled nanowires based on oligopeptide-substituted perylene bisimides, a “two-fold” odd–even effect¹²⁵ in their circular dichroism spectra was observed due to the number of both L-alanine units and methylene spacer units in their backbone. A zig-zag effect on melting temperature and refractive index of cyclic oligoesters due to the degree of oligomerization¹²⁶ or an alteration in the permeability characteristics of polyelectrolyte multilayer membranes,¹²⁷ are some of the few examples which show that the odd-even effect can be visible in polymeric systems, due to its number of repeating units as well. The validity for the occurrence of an odd-even effect in polymer systems is even observed *via* Monte Carlo simulations,¹²⁸ where the junctions with an odd or even number of functional groups in a polymer network, influences the shear modulus and

network's topological properties (i.e. the number of primary and secondary loops) in a zig-zag manner.

Although an odd-even effect is usually expected for the thermodynamical properties of materials in their crystalline state, however, recently this effect was also observed in the dynamical properties of materials even in their liquid phase. For instance, Yang *et al.* recently reported glass-forming diammonium citrate ionic liquids which show a unique alternating pattern of their glass transition temperature,¹²⁹ diffusion coefficient and rotational relaxation time¹⁰⁹ due to the odd or even number of methylene groups in their precursor units. They also performed quasi-elastic neutron scattering (QENS) measurements on liquid *n*-alkanes and observed an odd–even effect for their translational diffusional properties in the liquid states.¹³⁰ They showed that the even numbered *n*-alkanes exhibit up to 30 times faster dynamics near their respective melting point as compared to their neighboring odd member.

1.6. Motivation and Objectives

Crystallization of polymer chains can be described as a phase transition from their disordered (melt or solution) state to an ordered crystalline structure. However, when synthetic polymers crystallize, they do it only partially and acquire a morphology made up of both amorphous and crystalline domains. Several factors and parameters affect the relative volume of these two domains (degree of crystallinity) e.g. chains rigidity, the degree of branching, chains length, crystallization temperature, the rate of cooling, etc. In addition to these factors, alterations like the introduction of cross-linking in a linear polymer system or the placement of random/well-defined defect(s) along the polymer backbone, are also capable of changing the final crystal morphology of the polymer. In this work, the effect of both of these modifications will be investigated on poly(ethylene glycol) *via* different spectroscopic, scattering, optical and calorimetric techniques.

Cross-linked poly(ethylene glycol) (PEG) networks have long been used and developed for applications ranging from drug delivery systems¹³¹ and tissue engineering scaffolds¹³² to polymeric electrolytes¹³³ and biosensor applications.¹³⁴ Over the years, various

methods have been developed for creating PEG networks^{135–142} however, the end-linking of functional precursors provides the best opportunity to have control over the internal structure of networks. Cu(I) catalyzed azide-alkyne cycloaddition (CuAAC) *click* reactions^{143,144} are found to be a better choice as a coupling reaction due to their insensitivity toward various functional groups, fast reaction rates, and high yields compared to the other methods. Although there have been already some efforts for synthesizing polymer networks via *click* chemistry,^{90,145–147} however, it will worth an effort to reconstruct these structures to have a better understanding of these materials. Hence, the goal for the first part of this work is to design and synthesize poly(ethylene glycol) based networks by using CuAAC *click* reactions. Two types of PEG networks are synthesized i.e. *type A* networks formed by reacting together two different types of three-arm star PEG oligomers while *type B* networks are synthesized by coupling three-arm star and linear PEG oligomers having the molar masses of 300, 400, 1000, 2000 and 6000 g/mole. Throughout this text, three-arm star PEGs are denoted as PEG(S) and its modified species as PEG(S)-Azide or PEG(S)-Alkyne. All the linear PEG oligomers are denoted by their molar masses, e.g., PEG(400), etc., and its derivatives as e.g. PEG(400)-Alkyne. The PEG networks were represented by their respective precursors: e.g., a *type A* network of two three-arm star PEG(S) was named as PEG(S-S) while *type B* networks made from PEG(S) and a linear PEG(400) are indicated as PEG(S-400). To analyze the crystallization behavior of PEG networks, differential scanning calorimetry (DSC) and temperature dependent small angle and wide angle X-ray measurements (SAXS, WAXS) are conducted. Swelling measurements are also performed for PEG network while to investigate the network defects, multi-quantum (MQ) NMR experiments are also performed.

In the second part, the aim of the study will be to gain a fundamental understanding of the influence of different types and sizes of defects on the crystal structure of poly(ethylene glycol). Previously, Cheng *et al.* investigated the effect of a point defect of the PEG chain by introducing terephthalate, phthalate or isophthalate units to the middle of the polymer chain.^{81,82,148} However, the effect of a 1,2,3-triazole unit in this role has never been investigated before and it will be worth an effort to investigate its influence on polymer crystal morphology, as Cu(I) catalyzed azide-alkyne cycloaddition *click*

reaction has often been used for modifying the polymer architectures.^{89–91} For this purpose two different types of defects are introduced in a poly(ethylene glycol) chain. At first, a single 1,4-disubstituted 1,2,3 triazole ring *TR* is introduced as a well-defined point defect in the middle of poly(ethylene glycol) chain by coupling two monomethyl poly(ethylene glycol) chains with 11 repeating units *PEG*₁₁, via the CuAAC *click* reaction. Later in the text, this polymer will be abbreviated as PEG₁₁-TR-PEG₁₁. In the second case, two *PEG*₁₁ chains are coupled with a series of α , ω -diyne units via the CuAAC *click* reaction, in order to have two 1,4-disubstituted 1,2,3 triazole rings *TR*, separated from each other by a different number of methylene units, in the middle of a PEG chain. The formed polymer chains will be denoted as PEG₁₁-TR-(CH₂)_{*n*}-TR-PEG₁₁, where *n* = 2-8. Their thermal behavior is investigated with differential scanning calorimetry (DSC) measurements, while temperature dependent wide angle and small angle X-ray scattering (WAXS, SAXS) studies are also conducted to investigate their crystallization behavior and nanostructure formation. Finally, solid state cross-polarization (CP) and single-pulse (SP) ¹³C NMR spectroscopy and polarized light microscopy are also carried out to further investigate their morphological behavior.

2. Experimental Section

2.1. Materials

For the synthesis of poly(ethylene glycol) networks, hydroxy-terminated three-arm PEG (1000 g/mol) was purchased from Sigma-Aldrich with each arm having a degree of polymerization of 6 to 7 repeating unit. Linear hydroxyl-terminated PEGs of the molar mass of 300, 400, 1000, 2000 and 6000 g/mol were purchased from Fluka. For the precursor's synthesis, propargyl bromide, sodium hydride, methanesulfonyl chloride, triethylamine, and sodium azide were purchased from Sigma-Aldrich and used as received. For the *click* reaction, $\text{CuSO}_4 \cdot 5\text{H}_2\text{O}$ and sodium ascorbate were purchased from Alpha Aeser. THF purchased from VWR International was dried over calcium hydride and freshly distilled before use.

For the syntheses of $\text{PEG}_{11}\text{-TR-(CH}_2)_n\text{-TR-PEG}_{11}$ and $\text{PEG}_{11}\text{-TR-PEG}_{11}$ linear oligomers, poly(ethylene glycol) monomethyl ether (500 g/mol) PEG_{11} , where the subscript represents the degree of polymerization, was purchased from Sigma-Aldrich and was used after drying by azeotropic distillation with toluene. 1,6-heptadiyne (97%), 1,7-octadiyne (98%), 1,8-nonadiyne (98%), 1,7-dibromoheptane (97%), 1,8-dibromooctane (98%), lithium acetylide-ethylenediamine complex (90%), iodomethane (≥ 99),

triethylamine (99%), methanesulfonyl chloride (mesyl chloride) ($\geq 99.7\%$) sodium azide ($\geq 99\%$), bromotris(triphenylphosphine) copper(I) (98%), *tert*-butanol (99.5%), anhydrous DMF, DMSO and deuterated DMSO- d_6 were all purchased from Sigma Aldrich and used as received. Moreover, 1,5-hexadiyne (50% in pentane Alfa Aesar), 1,9-decadiyne ($\geq 98\%$, TCI Chemicals) and dichloromethane (VWR International) were also used without any further treatment. THF (VWR International) was dried over calcium hydride and freshly distilled before use. $CDCl_3$ and DMSO- d_6 was purchased from Armar AG.

2.2. Instrumentation

2.2.1 Attenuated Total Reflection-Infrared Spectroscopy (ATR-IR)

ATR-IR measurements were performed on a Bruker Tensor VERTEX 70 equipped with a golden gate diamond ATR cell. For the analysis OPUS 6.5 software was used. All measurements were carried out at room temperature and within the range of 400 to 4000 cm^{-1} . After cleaning the crystal (diamond) area and measuring the background spectrum, both types of either solid or liquid sample were placed on top of the crystal surface. Although a minuscule amount of sample material is required for this kind of measurement, the amount should be sufficient to cover the whole crystal area. To improve the contact with the surface, a pressure arm is placed over the sample to press the sample against the crystal surface. 16-32 scans were performed to obtain the final spectra depending upon the quality of results obtained.

2.2.2 Nuclear Magnetic Resonance Spectroscopy (NMR)

Solution NMR spectra were recorded on a Varian Gemini 2000 operating at 400 MHz for 1H NMR and 200 MHz for ^{13}C NMR spectroscopy. $CDCl_3$ and DMSO- d_6 were used for NMR

analysis while the measurements were performed at 27 °C. For PEG networks, ^{13}C -MAS single-pulse experiments were run on a BRUKER AVANCE 400 with a standard 4 mm VT-MAS probe. Typical MAS rates were about 8 kHz, and low-power decoupling was applied to remove the J-coupling. For ^1H multi-quantum (MQ) measurements, the low-field NMR experiments were performed on a Bruker minispec mq20 with a magnetic field of $B_0 = 0.47\text{ T}$ and 90° and 180° pulse lengths of 1.6–2.4 and 3.2–5.2 μs , respectively. The samples were swollen to equilibrium in D_2O as the swelling increases the molecular mobility of the network chains, which ensures a sufficiently slow transverse relaxation of the ^1H NMR signal. The temperature was held at 27 °C by a standard BVT3000 temperature controller. Buildup curves of the longitudinal T_1 relaxation were measured by a saturation recovery experiment with a variable relaxation delay. The pulse sequence for the MQ NMR experiment was described in detail in the literature.¹⁴⁹ The relaxation delay between the scans was chosen to be 1 s, which is several times larger than the T_1 of the network ($T_1 \approx 0.3\text{ s}$) but shorter than those of the residual water protons of the D_2O . Depending on the polymer concentration, the number of scans for each point in the MQ NMR experiment was varied between 512 and 2048 scans.

In the case of $\text{PEG}_{11}\text{-TR-PEG}_{11}$ and $\text{PEG}_{11}\text{-TR-(CH}_2)_n\text{-TR-PEG}_{11}$, BRUKER AVANCE 400 with a standard 4 mm VT-MAS probe was used to perform ^{13}C MAS single-pulse (SP) and cross-polarization (CP) experiments. ^1H decoupling (TPPM) was applied to remove dipolar broadening with typical MAS rates were 11 kHz for $\text{PEG}_{11}\text{-TR-PEG}_{11}$ and 10 kHz for $\text{PEG}_{11}\text{-TR-(CH}_2)_n\text{-TR-PEG}_{11}$ samples. The sample temperature was controlled by a standard BRUKER VT-controller and calibrated with methanol.¹⁵⁰ For $\text{PEG}_{11}\text{-TR-PEG}_{11}$ analysis, the spectra were recorded after rapid cooling of the samples from $T = 30\text{ }^\circ\text{C}$ to $T = -15\text{ }^\circ\text{C}$ where it was kept for at least 30 min for crystallization. Typically, 512 scans were accumulated, resulting in a time frame for every experiment of approximately 1 h at a given temperature. However, for $\text{PEG}_{11}\text{-TR-(CH}_2)_n\text{-TR-PEG}_{11}$ oligomers, the spectra were recorded after cooling of the samples from $T = 30\text{ }^\circ\text{C}$ to $T = -20\text{ }^\circ\text{C}$ during the second heating cycle in steps of $\Delta T = 5\text{ }^\circ\text{C}$. The measurement time per step was approximately 4 h, collecting 1024 scans.

2.2.3 Differential Scanning Calorimetry (DSC)

Differential scanning calorimetry (DSC) measurements were performed under nitrogen flow using a Mettler Toledo DSC 822e module. About 8-12 mg of sample was filled in aluminum pans for all measurements.

In the case of PEG networks, samples were first heated to $T = 125\text{ }^{\circ}\text{C}$ in order to remove the previous thermal history, and after holding this temperature for 5 min, they were cooled to $T = -20\text{ }^{\circ}\text{C}$ with the rate of $10\text{ }^{\circ}\text{C}/\text{min}$. The samples were heated again to $80\text{ }^{\circ}\text{C}$ at $10\text{ }^{\circ}\text{C}/\text{min}$, to record their melting endotherm. These measurements were performed for both, PEG networks and linear PEG samples. For the isothermal crystallization measurements of PEG networks, after heating the samples above their melting point, they were cooled to a pre-decided crystallization temperature T_c , with the fastest cooling rate possible (between 30 and $50\text{ }^{\circ}\text{C}/\text{min}$). Samples were held at T_c until the crystallization process finished and later heated at the rate of $10\text{ }^{\circ}\text{C}/\text{min}$ to record their melting endotherm for that particular T_c . For the non-isothermal crystallization measurements of the PEG networks, the samples were first heated to $T = 125\text{ }^{\circ}\text{C}$ in order to remove any thermal history while they were cooled then to $-40\text{ }^{\circ}\text{C}$ with different cooling rates, i.e. $2.5\text{ }^{\circ}\text{C}/\text{min}$, $5\text{ }^{\circ}\text{C}/\text{min}$, $10\text{ }^{\circ}\text{C}/\text{min}$ and $20\text{ }^{\circ}\text{C}/\text{min}$. After holding the final temperature for about 5 min, samples were reheated with the same heating rate, to record their melting behavior.

PEG₁₁-TR-PEG₁₁ and PEG₁₁-TR-(CH₂)_{*n*}-TR-PEG₁₁ oligomers were first heated to $T = 125\text{ }^{\circ}\text{C}$ in order to remove their thermal history while after holding them at this temperature for 5 min they were cooled to $T = -40\text{ }^{\circ}\text{C}$ with the cooling rate of $1\text{ }^{\circ}\text{C}/\text{min}$. The samples were reheated to $60\text{ }^{\circ}\text{C}$, to record the final melting endotherm.

2.2.4 Temperature Dependent Small Angle X-ray Scattering (SAXS)

Temperature dependent small angle X-ray scattering (SAXS) measurements were performed using Cu K α radiation from a Rigaku Rotaflex rotating anode equipped with a

pinhole collimator and a Bruker Hi-Star 2D detector. The q -scale was calibrated using silver behenate. Measured SAXS intensities were corrected for background scattering using the one-dimensional scattering function.¹⁵¹

$$I_{q^2} = \frac{a}{w} \cdot \sum_n \left(\frac{e^{-\frac{(q-n \cdot q^*)^2}{2 \cdot w^2}} \cdot \sin^2(n_s \cdot \pi \cdot cr)}{n^2} \right) \cdot e^{-q^2 \cdot u^2} \cdot q^2 \quad (2.1)$$

where q is the scattering vector, I is the Intensity, a and w are the respective amplitude and width of the first order peak, q^* is the scattering vector of the first maximum, n_s the order of the peak, and $e^{-q^2 \cdot u^2}$ is the exponential Debye-Waller factor. For PEG networks, samples were placed in the Linkam hot stage attached to the SAXS equipment. Samples were first heated above their melting temperatures to remove any thermal history and then cooled to $T = -10$ °C with the rate of 10 °C/min. Samples were then reheated and measurements were performed in step of $\Delta T = 10$ °C for 1800 s (30 min) except for PEG(S-1000) where $\Delta T = 5$ °C due to the lower melting point.

For PEG₁₁-TR-PEG₁₁ and PEG₁₁-TR-(CH₂) _{n} -TR-PEG₁₁, the samples were first heated above their melting temperatures to remove any thermal history and also to facilitate the transfer of sample into the capillary tube. Glass capillaries with a diameter of 1 mm were filled with the molten polymers and were sealed with a flame. Then, they were placed in the Linkam hot stage attached with the SAXS setup. Liquid nitrogen was used to cool the samples below room temperature and the calibration was carried out with silver behenate. PEG₁₁-TR-PEG₁₁ was cooled to $T = 0$ °C and the traces were taken in steps of $\Delta T = 8$ °C during heating. However, PEG₁₁-TR-(CH₂) _{n} -TR-PEG₁₁ samples were cooled to $T = -20$ °C and the temperature dependent SAXS measurements were performed in steps of $\Delta T = 5$ °C during heating. Different scattering durations (1200 s to 3600 s) were used for different samples and at different temperatures in order to get a good scattering profile (signal to noise ratio).

2.2.5 Temperature Dependent Wide Angle X-ray Scattering (WAXS)

Temperature dependent wide angle X-ray scattering (WAXS) measurements were performed in Bragg-Brentano geometry using a PANalytical Empyrean Diffractometer, equipped with a position sensitive detector (PIXcel-3D). The samples were placed on silicon zero-background substrate in a TTK 450 temperature chamber from Anton Paar. The measurements were done under dry nitrogen with nickel-filtered Cu K α radiation ($\lambda = 1.5418 \text{ \AA}$). The spectra were recorded in a scan range of $6^\circ < 2\theta < 60^\circ$ with a step size of $\Delta 2\theta = 0.053^\circ$ and a counting time per step of 93 s. In the case of PEG networks, the sample was first heated to 80°C and then cooled to -20°C with the rate of $5^\circ\text{C}/\text{min}$. WAXS diffractograms were recorded during heating the samples at every $\Delta T = 10^\circ\text{C}$ step.

For PEG₁₁-TR-(CH₂)_{*n*}-TR-PEG₁₁, the samples were first heated to $T = 80^\circ$, followed by cooling to $T = -40^\circ\text{C}$ at $5^\circ\text{C}/\text{min}$. The WAXS diffractograms were recorded in steps of $\Delta T = 2^\circ\text{C}$ from $T = -10^\circ\text{C}$ till the complete melting of the samples. In the case of PEG₁₁-TR-PEG₁₁, the sample was cooled to $T = -4^\circ\text{C}$ and held there for 20 min and then reheated in steps of $\Delta T = 4^\circ\text{C}$ until the final melting. The spectra were recorded in a scan range of $6^\circ \leq 2\theta \leq 60^\circ$ with a step size of $\Delta 2\theta = 0.053^\circ$ and a counting time per step of 44 s.

To record the 2D-diffraction oriented pattern of PEG₁₁-TR-(CH₂)₂-TR-PEG₁₁, a diffractometer with a 2D detector (Vantec 500, Bruker, AXS, Madison, WI, USA) along with pinhole collimated (Ni-filtered) Cu K α radiation was used. The calibration was carried out using silver behenate. The exposure time was 180 min, and the sample to detector distance was 9.85 cm. Glass capillaries ($\varnothing 1 \text{ mm}$, Hilgenberg, GmbH, Malsfeld, Germany) were used to fill the sample. Orientation in PEG₁₁-TR-(CH₂)₂-TR-PEG₁₁ sample was introduced by cooling the sample within the capillary to $T \approx 5\text{-}10^\circ\text{C}$ and then an air jet moves the sample about 1 cm away from its original position in the capillary. Later, the sample was quenched using liquid nitrogen to preserve the induced orientation in the PEG₁₁-TR-(CH₂)₂-TR-PEG₁₁ sample and stored at -20°C .

2.2.6 Matrix Assisted Laser Desorption/Ionization–Time of Flight (MALDI-ToF) Spectrometry

Bruker Autoflex III system was used to perform MALDI-ToF measurements of PEG₁₁-TR-(CH₂)_n-TR-PEG₁₁ ($n = 3, 4$ and 6). The ratio of the matrix to the polymer to salt in CHCl₃ was fixed to 100:10:1. 1,8,9-anthracenetriol (dithranol) and lithium trifluoroacetate (LiTFA) were used as matrix and salt, respectively. In the case of PEG₁₁-TR-PEG₁₁, measurements were carried out with the ratio of the THF solutions of the matrix to polymer to salt as 100:10:1 (matrix: $c = 20$ mg/mL; polymer: $c = 20$ mg/mL; salt: $c = 10$ mg/mL). 1,8,9-anthracenetriol (dithranol) and sodium trifluoroacetate (NaTFA) was used as a matrix and salt, respectively.

2.2.7 Polarized Optical Microscopy (POM)

Polarized optical microscopy (POM) measurements were performed with an Axioplan 2 imaging microscope from Zeiss equipped with a LINKAM THMS 600 hot stage. The images were taken using an AxioCam MRc camera from Zeiss. The measurements were done under a constant stream of dry nitrogen to avoid any moisture. PEG₁₁-TR-(CH₂)₄-TR-PEG₁₁ was first heated to and held at $T = 80$ °C for 5 min and then cooled down to $T = 5$ °C with a rate of 5 °C/min. After the completion of the crystallization process, the sample was heated to 18 °C and then cooled back to 5 °C. Finally, the sample was reheated until its complete melting.

2.2.8 Inductively Coupled Plasma Mass Spectrometry (ICP-MS)

Inductively coupled plasma mass spectrometry (ICP-MS) was performed on both PEG₁₁-TR-PEG₁₁ and PEG networks samples, using an ESI-sampler SC-2 (Elemental Scientific, Inc.) and an X-Series II ICP-MS instrument (Thermo Fisher Scientific) operating with a collision cell. First, the samples were mineralized with nitric acid (67%, trace metal grade, Normatom/PROLABO) at $T = 70$ °C for 2 h and later diluted with water to an acid concentration of 2 %. The calibration was carried out with ICP multi-element standard solution XVI (Merck) also containing 2 % nitric acid. Three measurements were

performed with flow rates of 5 mL/min of He/H₂ (93%/7%), an Ar carrier flow rate of 0.76 L/min and an Ar make-up flow rate of 15 L/min.

2.3. Syntheses

The syntheses section is subdivided into three parts where initially the synthesis of poly(ethylene glycol) networks will be discussed while in the second section, the synthesis of PEG₁₁-TR-PEG₁₁ will be described. Lastly, the synthesis procedure of PEG₁₁-TR-(CH₂)_n-TR-PEG₁₁ ($n = 2-8$) will be discussed in detail.

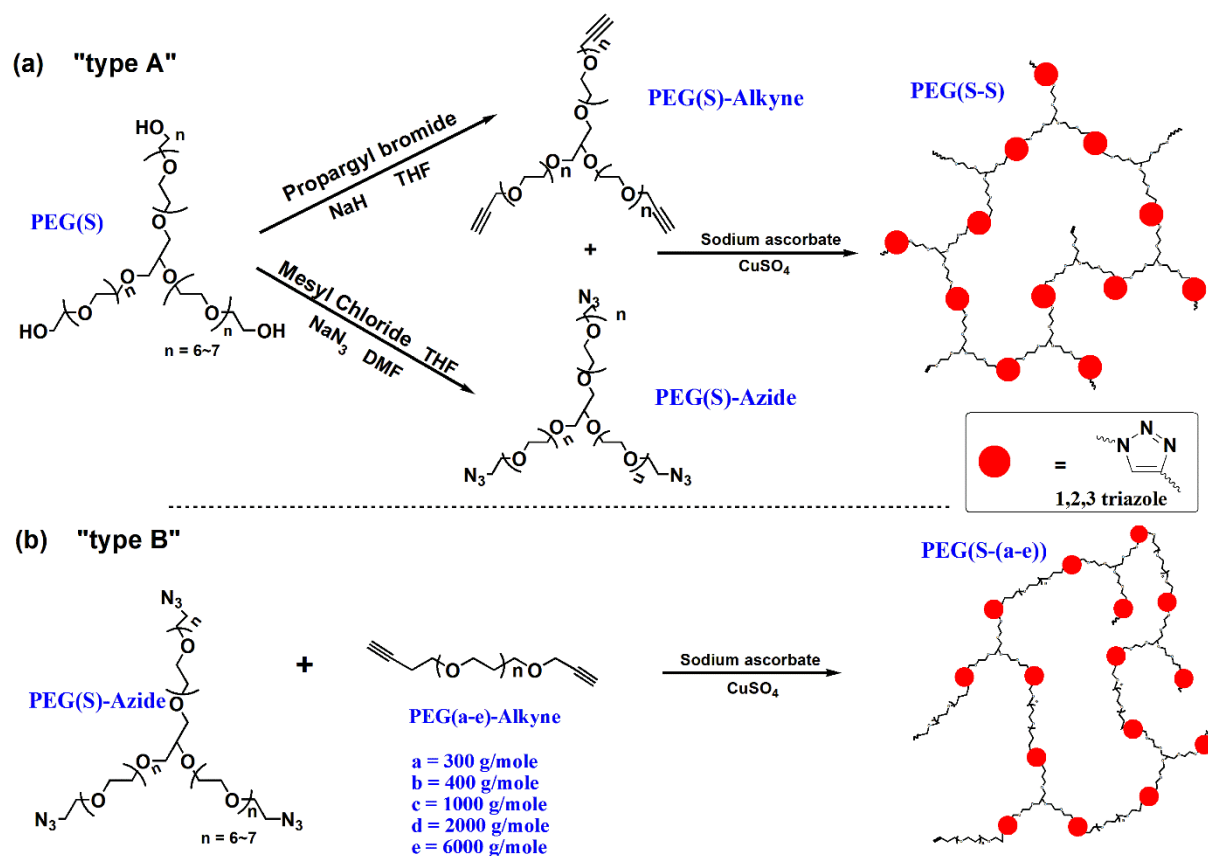
2.3.1 Synthesis of PEG Networks

Two types of PEG networks were synthesized, i.e. *type A* networks were formed by reacting two types of three-arm star PEG oligomers together. *Type B* networks were synthesized by coupling the three-arm star PEG chains with linear PEG oligomers, having the molar masses of 300, 400, 1000, 2000 and 6000 g/mol. A comprehensive schematic overview of PEG network formation is shown in Scheme 2.1

2.3.1.1 Synthesis of PEG-Alkyne

The formation of PEG-Alkyne of different molar masses was achieved by following the methods already reported in the literature.^{141,153} In a typical case of PEG(400), 2.4 g of sodium hydride (available as 60 % dispersion in mineral oil) was dissolved in 50 mL anhydrous THF in a 250 mL flask. Then at 0 °C, a mixture of 10 g (25 mmol) of PEG(400) in 150 mL dry THF was added dropwise to the sodium hydride/THF mixture. Hydrogen gas will be released during the reaction; hence proper ventilation must be ensured. The system was stirred for about 30 min at 0 °C and afterwards, 8.92 g of propargyl bromide:toluene (80:20 v/v) solution (72 mmol), diluted with 50 mL THF, was added drop-wise to the reaction mixture. The reaction was allowed to proceed at 0 °C for another 2 h and then overnight at room temperature. Sodium bromide, produced during the reaction, was precipitated and filtered out after the reaction. The solvent was removed under vacuum, and the crude mixture was passed through a silica column. Initially, an ethyl acetate and dichloromethane mixture (10:1 v/v) was used while later a

dichloromethane and methanol mixture (10:1 v/v) was used to collect the product. Figure 2.1 shows the ^1H NMR spectrum of PEG(400)-Alkyne. ^1H NMR spectra of PEG(300)-Alkyne, PEG(1000)-Alkyne, PEG(2000)-Alkyne, PEG(6000)-Alkyne and PEG(S)-Alkyne are shown in the Appendix (Figure A1-A5)



Scheme 2.1: Scheme of an overall synthesis route for the formation of both (a) *type A* and (b) *type B* PEG networks.¹⁵²

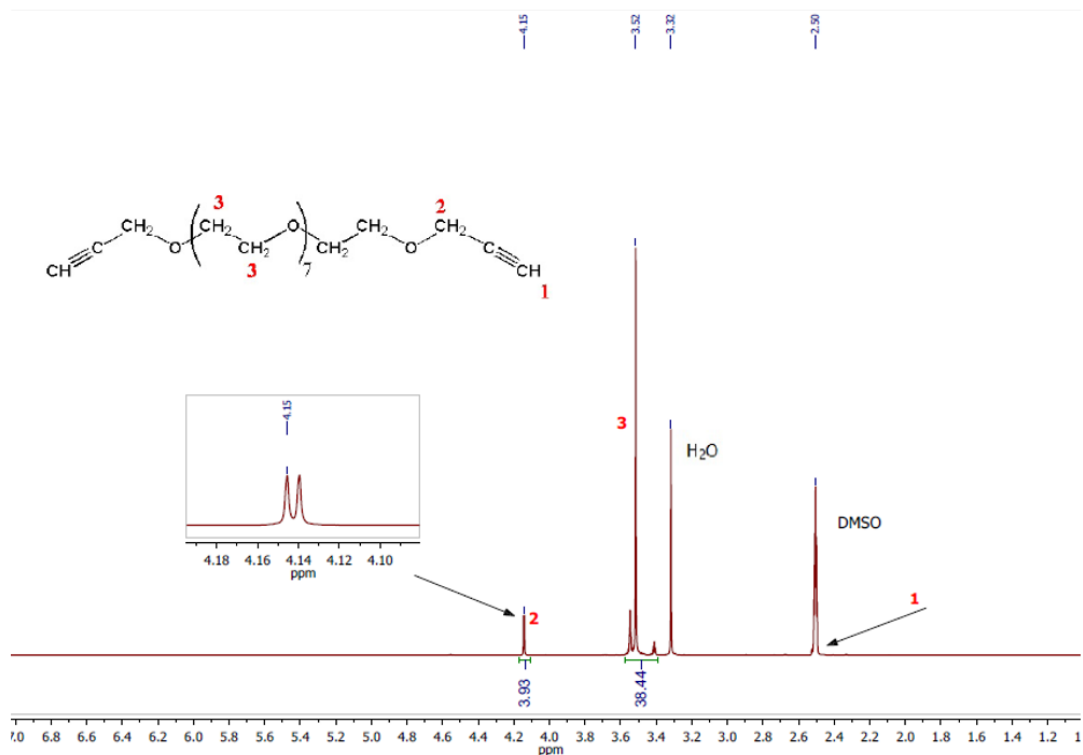


Figure 2.1: ^1H NMR spectrum of PEG(400)-Alkyne in $\text{DMSO-}d_6$ (400 MHz, 27 °C).¹⁵²

2.3.1.2 Synthesis of PEG(S)-Azide

The azide functionalized star-shaped PEG precursor was synthesized by reacting three-arm poly(ethylene glycol) (PEG(S)) (1000 g/mol) with methanesulfonyl chloride (mesyl chloride) and sodium azide^{154,155}. As a typical procedure, 10 g of PEG(S) (10 mmol) was dissolved in 150 mL anhydrous THF together with 3.634 g (36 mmol) of triethylamine, in a 500 mL flask. At 0 °C, 4.124 g (36 mmol) mesyl chloride diluted with 50 mL THF was added dropwise to the reaction mixture. The reaction was allowed to proceed at room temperature overnight. After the reaction, precipitates were filtered, and THF was removed via the rotary evaporator. Mesyl-PEG was obtained by extraction with DCM and water. The organic phase of DCM was dried using sodium sulfate and after solvent evaporation, white PEG(S)-mesyl was obtained. In the second step, 1.95 g (30 mmol) of sodium azide was added to the mixture of 5 g of PEG(S)-mesyl in 100 mL anhydrous DMF, and the reaction was allowed to run for 36 h at 70 °C. Three-arm PEG(S)-Azide was

obtained after filtering out the precipitates and drying the solvent. Figure 2.2 shows the ^1H NMR spectrum of PEG(S)-Azide.

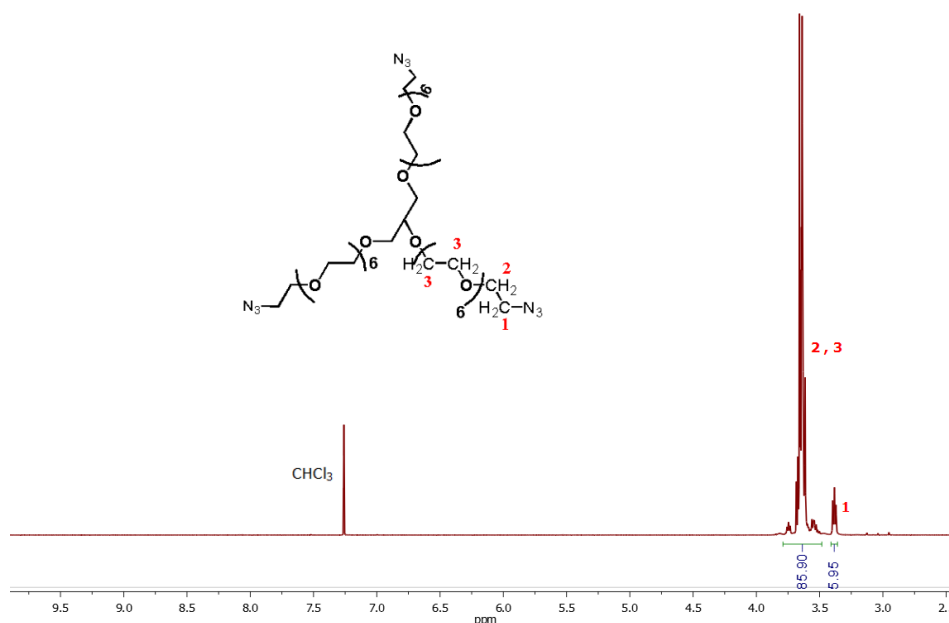


Figure 2.2: ^1H NMR spectrum of PEG(S)-Azide in CDCl_3 (400 MHz, 27 °C).¹⁵²

2.3.1.3 Network Formation *via* Cu(I)-Catalyzed Azide-Alkyne Cycloaddition *Click* Reaction.

PEG networks were formed by coupling azide and alkyne functional group modified PEG precursors in equimolar amount *via* the CuAAC *click* reaction. The CuSO_4 and sodium ascorbate system¹⁵⁶ in an aqueous environment was used for all PEG networks. In a typical case of PEG(S-400), 1 g (1 mmol) of PEG(S)-Azide along with 0.6 g (1.5 mmol) of PEG(400)-Alkyne and 30 mg of $\text{CuSO}_4 \cdot 5\text{H}_2\text{O}$ (10 mmol % of azide functional groups used) was dissolved in 11 mL of deionized water and stirred for a few minutes in a vial in order to make the reaction mixture homogeneous. As the gelation time and final properties depend on the initial polymer concentration, all the PEG networks were formed with the initial polymer concentration of 15 % (w/v) in water. After that, 50 mg of sodium ascorbate (20 mmol % of azide functional groups used) dissolved in small amounts of water was added to the vial. Within a few minutes, the reaction mixture becomes a cross-

linked gel which was washed with water and ammonia solution for the next 4 to 5 days to remove the residual copper ions. In order to find out the copper contents in the final PEG networks, ICP-MS measurements were performed. It was found that all the PEG networks contain less than 2.2 mg/kg of copper ions in their system, which is even less than half of the amount, present in commercially pure PEG material (i.e. Cu \approx 5 mg/kg¹⁵⁷). As the formed network is not soluble in any solvent, solid state ¹³C MAS NMR spectroscopy of dry PEG(S-400) was performed to confirm the formation of expected structure. Figure 2.3 shows the solid state ¹³C MAS NMR spectra of PEG(S-400) network.

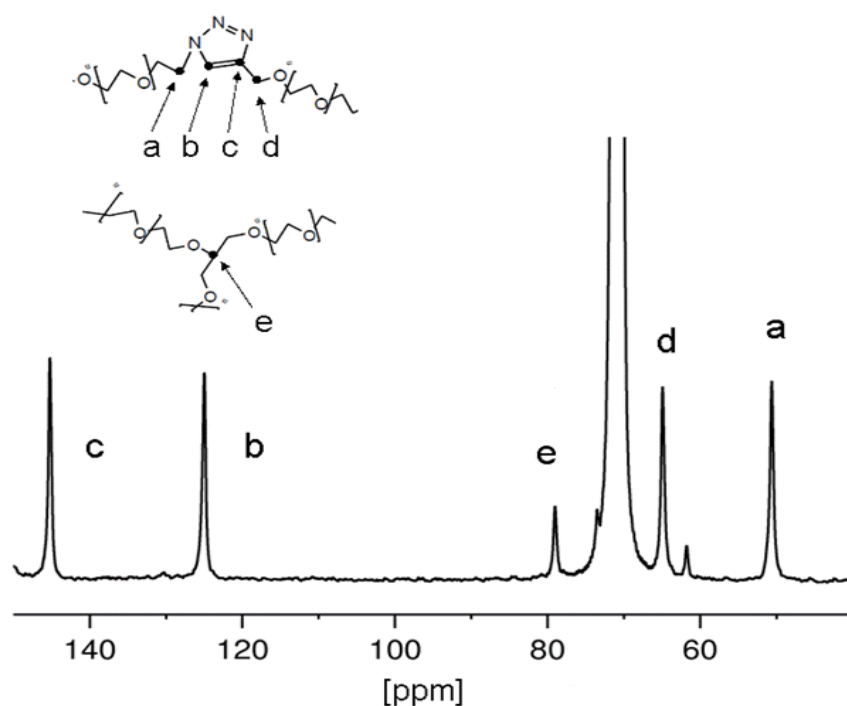
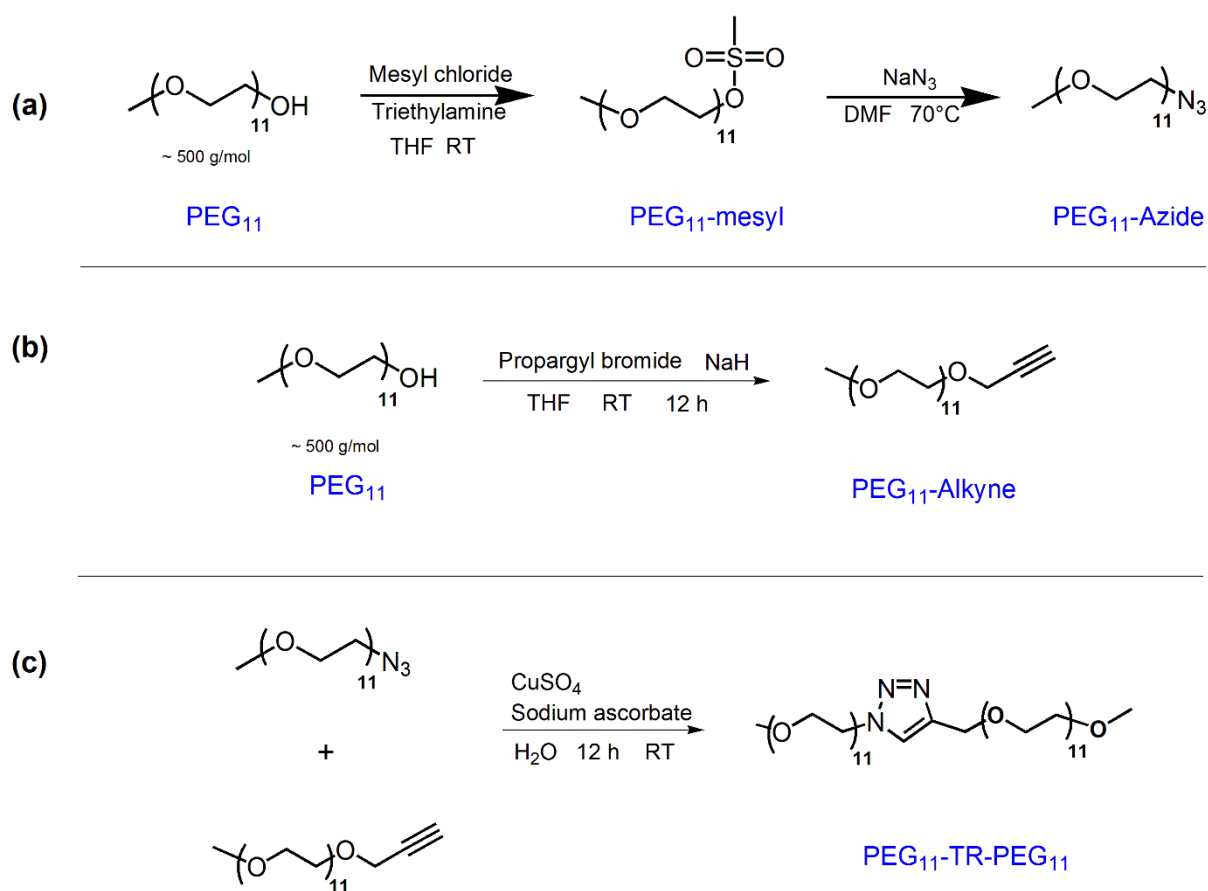


Figure 2.3: ¹³C MAS NMR spectrum of PEG(S-400) network at 27 °C.¹⁵²

2.3.2 Synthesis of PEG₁₁-TR-PEG₁₁

Two monomethyl poly(ethylene glycol) chains with 11 repeating units, PEG₁₁, were coupled together using CuAAC reaction in order to have a 1,4-disubstituted 1,2,3-triazole unit *TR*, in the middle of the chain. The synthesis detail of the precursor modification and the final coupling reaction is shown in Scheme 2.2 and discussed below.



Scheme 2.2: Schematic representation of synthesis route for (a) PEG₁₁-Azide, (b) PEG₁₁-Alkyne and (c) PEG₁₁-TR-PEG₁₁

2.3.2.1 Synthesis of PEG₁₁-Azide

PEG₁₁ was terminally functionalized with the azide moiety by treatment with mesyl chloride and sodium azide according to the protocol published elsewhere.¹⁵² In a typical procedure, 10 g (20 mmol) of PEG₁₁ was dissolved in 100 mL anhydrous THF in a 250 mL two-neck round bottom flask, followed by the addition of 2.42 g (24 mmol) triethylamine. The contents of the flask were cooled down to approximately 0 °C by placing the flask in an ice bath. Subsequently, 2.75 g (24 mmol) of methane sulfonyl chloride, diluted with 20 mL THF, was added dropwise to the reaction mixture using a dropping funnel and the reaction was allowed to proceed overnight at room temperature. The reaction mixture was filtered to remove the white precipitate of triethylamine hydrochloride and the THF was removed on a rotary evaporator. The crude product was purified by extraction with

dichloromethane and brine while later, sodium sulfate was added to the organic phase to remove traces of water. Finally, the purified PEG₁₁-mesyl (yield 80%) was obtained as a colorless liquid after drying in a rotary evaporator. The product was further dried in a vacuum oven at 60°C, overnight.

In the second step, 5 g PEG₁₁-mesyl (10 mmol) and 1.3 g (20 mmol) sodium azide were added in 75 mL anhydrous DMF in a round bottom flask equipped with a magnetic stirrer bar and the reaction was carried out for 36 h at 70°C. The precipitates of sodium methanesulfonate salt were filtered off and the solvent was removed under vacuum to recover PEG₁₁-Azide (yield 85%). The reaction route is outlined in Scheme 2.2a. The ¹H NMR spectrum of PEG₁₁-Azide is shown Figure 2.4 while a comparison of ¹³C NMR spectra of PEG₁₁ and PEG₁₁-Azide is shown in Figure 2.5, in order indicate a complete conversion of PEG₁₁ to PEG₁₁-Azide.

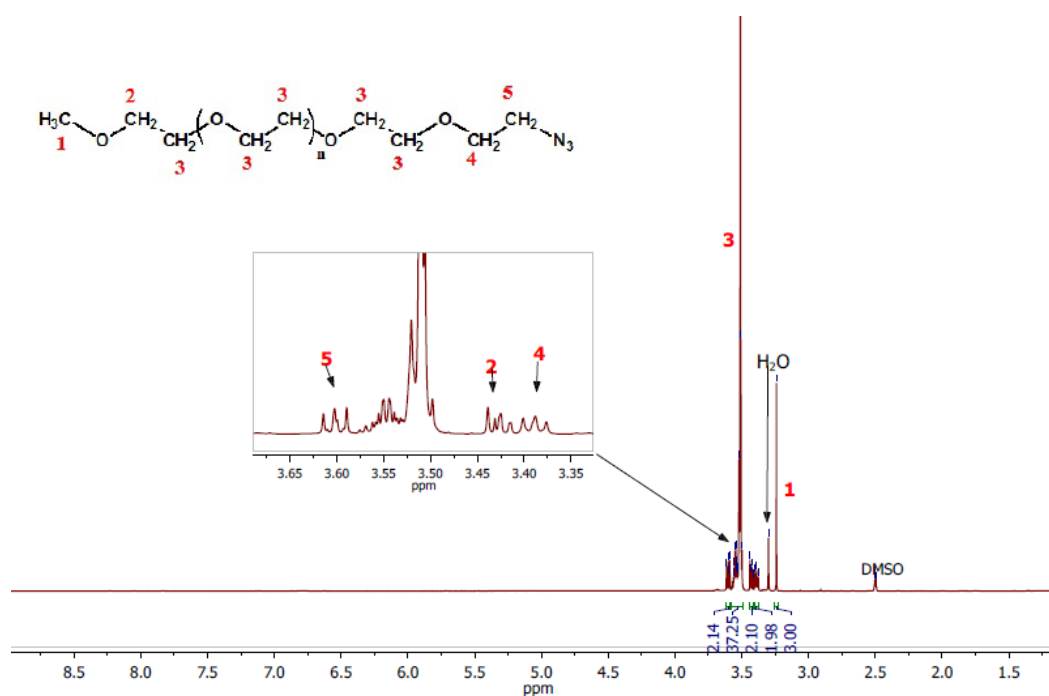


Figure 2.4: ¹H NMR spectrum of PEG₁₁-Azide in DMSO-*d*₆ (400 MHz, 27 °C).

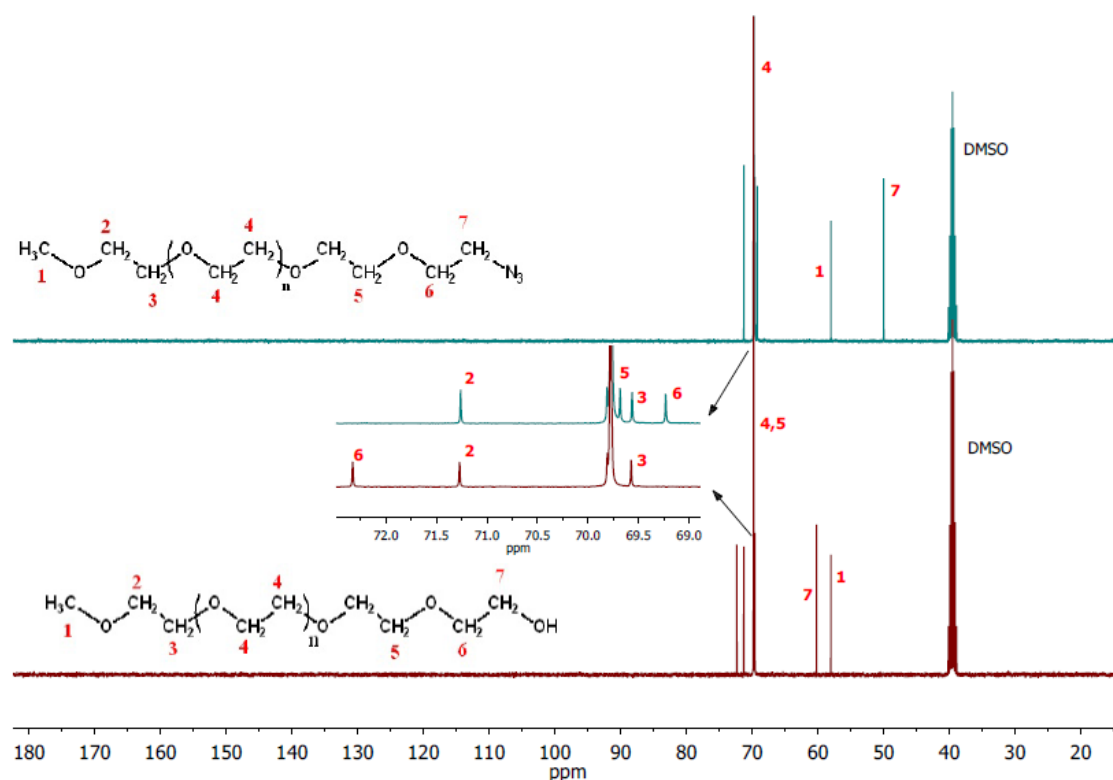


Figure 2.5: ¹³C NMR spectra of PEG₁₁-Azide (top) and PEG₁₁ (bottom) in DMSO-*d*₆ (100 MHz, 27 °C).

2.3.2.2 Synthesis of PEG₁₁-Alkyne

In a typical procedure¹⁴¹(Scheme 2.2b), PEG₁₁ (5.00 g; 10 mmol) was dissolved in anhydrous tetrahydrofuran (50 mL) and was introduced dropwise into a solution of sodium hydride/mineral oil (0.6 g; 15 mmol of NaH) and tetrahydrofuran (50 mL) under nitrogen flow. After 30 min of stirring, propargyl bromide solution (80 wt.% in toluene 2.23 g (15 mmol of propargyl bromide)) was added slowly, and the reaction mixture was stirred for 12 h. After the reaction was finished, few drops of water were added to quench any unreacted sodium hydride contaminants while later, the white precipitate of sodium bromide was filtered out from the reaction mixture. The solvent was removed under vacuum and the crude mixture was passed through a silica column. Initially, an ethyl acetate:dichloromethane mixture (10:1 v/v) was used, while finally, a

dichloromethane:methanol (10:1 v/v) mixture was applied. Yield: 86 %. ^1H NMR spectrum of PEG₁₁-Alkyne is shown Figure 2.6

2.3.2.3 Synthesis of PEG₁₁-TR-PEG₁₁ *via* Cu(I)-Catalyzed Azide-Alkyne Cycloaddition *Click* Reaction

For synthesis of PEG₁₁-TR-PEG₁₁ (Scheme 2.2c), PEG₁₁-Azide (1.05 g; 1.00 mmol), PEG₁₁-Alkyne (1.07 g; 1.00 mmol) and copper(II) sulfate pentahydrate (75.00 mg; 0.30 mmol) were dissolved in deionized water (5 mL) and stirred for 5 min in order to make the reaction mixture homogeneous. After that, sodium ascorbate (120.00 mg, 0.60 mmol), dissolved in water (1 mL), was added. The reaction mixture was stirred for 12 h. After the reaction, the crude mixture was extracted using dichloromethane (50 mL) and concentrated under vacuum. Unreacted precursors and copper catalyst were removed using a silica column. Initially, a mixture of acetone and ethyl acetate (8:2 v/v) was used as eluent while a mixture of acetone and methanol (10:1 v/v) was used to extract the product. The product was dried in a vacuum of a freeze-drier (Yield: 70%). The copper catalyst was completely removed from the final product, after the chromatographic purification, as no traces of copper were detected in the ICP-MS measurements. The ^1H NMR spectrum of PEG₁₁-TR-PEG₁₁ is shown in Figure 2.7 while the ^{13}C NMR spectrum of PEG₁₁-TR-PEG₁₁ and the FT-IR spectrum are shown in the Appendix (Figure A6 and Figure A19, respectively).

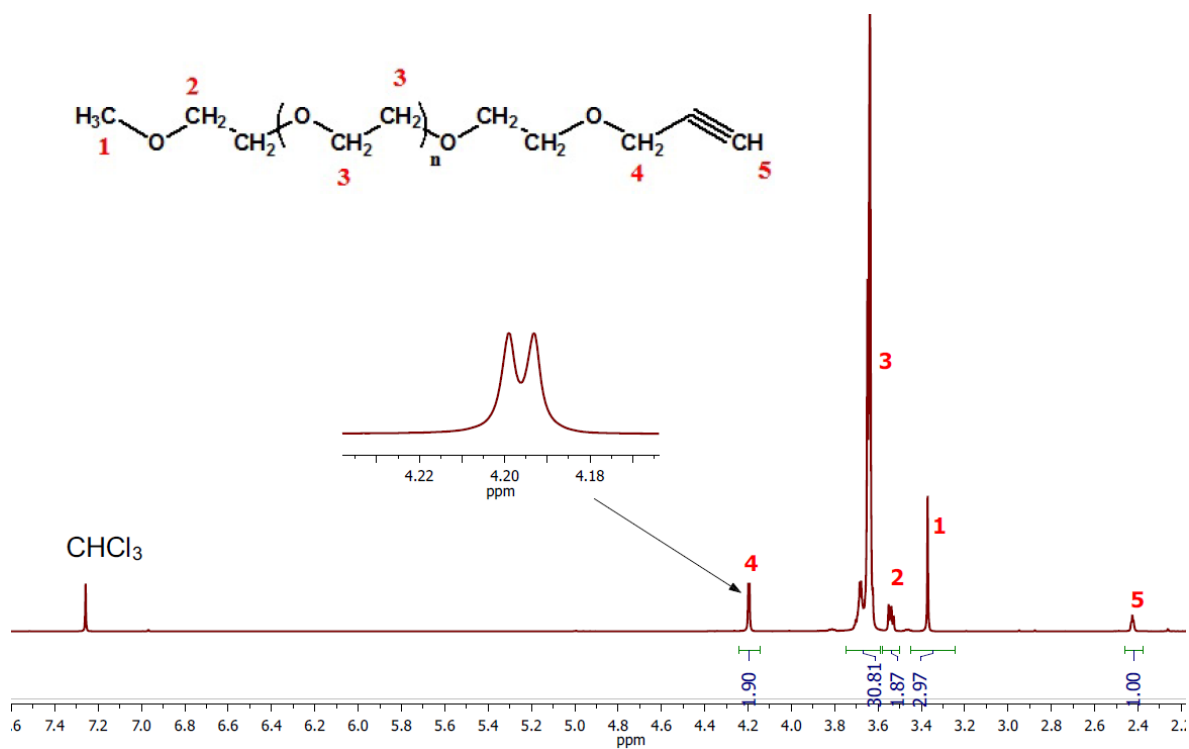


Figure 2.6: ¹H NMR spectrum of PEG₁₁-Alkyne in CDCl₃ (400 MHz, 27 °C).

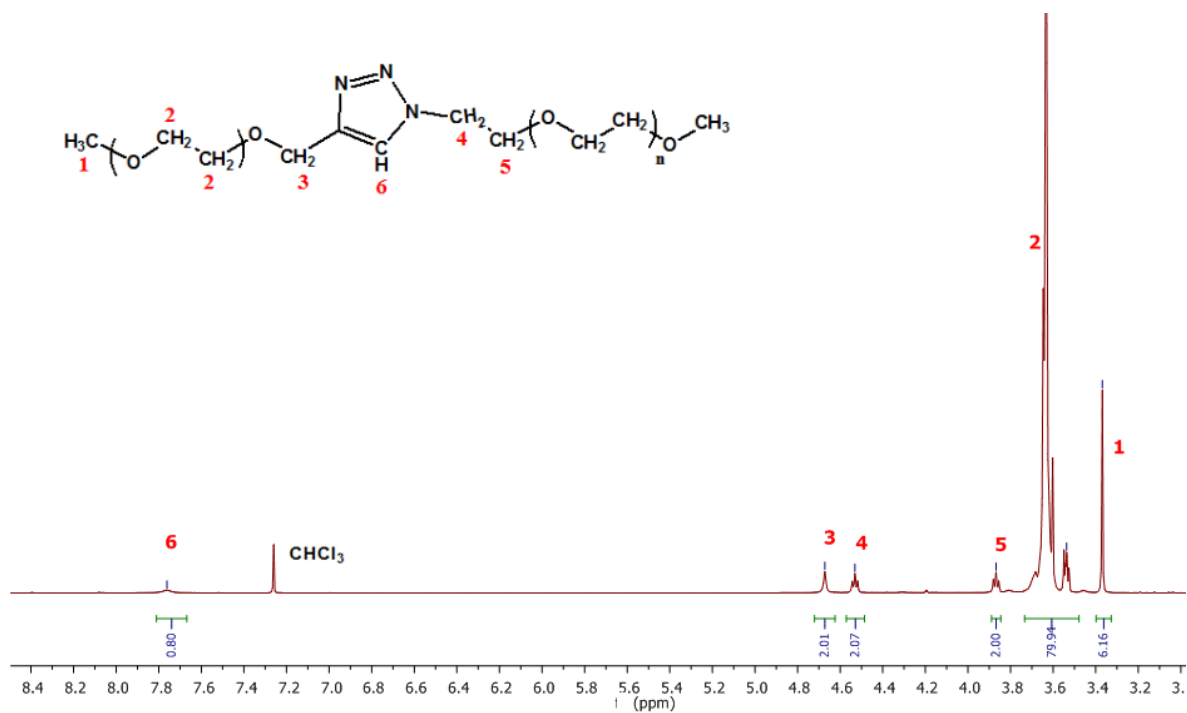


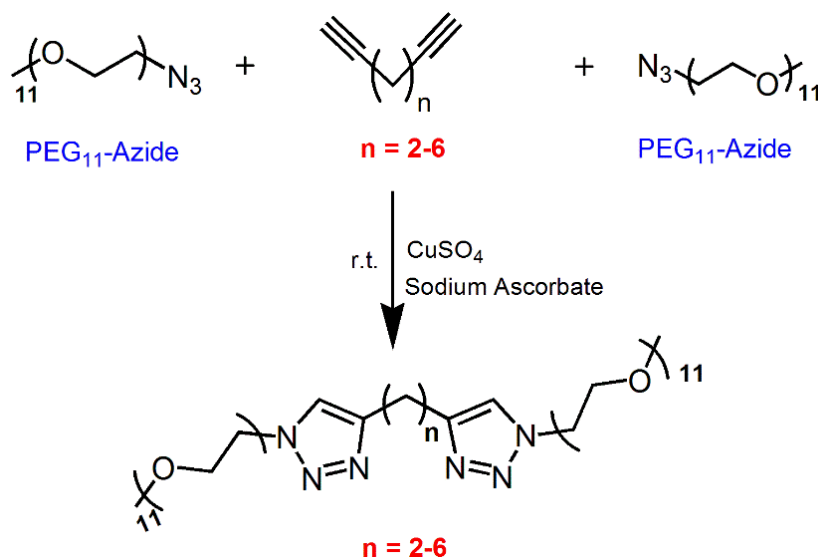
Figure 2.7: ¹H NMR spectrum of PEG₁₁-TR-PEG₁₁ in CDCl₃ (400 MHz, 27 °C).⁸⁸

2.3.3 Synthesis of PEG₁₁-TR-(CH₂)_n-TR-PEG₁₁

For the synthesis of linear PEG₁₁-TR-(CH₂)_n-TR-PEG₁₁ ($n = 2-8$), two PEG₁₁ chains were attached on either side of a homologous series of α , ω -diyne units via CuAAC reaction. As a result of the *click* reaction, two 1,4-disubstituted 1,2,3 triazole rings TR were formed between the two PEG₁₁ chains, separated only by a different number of methylene units. Thus, the final product will be abbreviated as PEG₁₁-TR-(CH₂)_n-TR-PEG₁₁, where $n = 2-8$. At first, synthesis of PEG₁₁-TR-(CH₂)_n-TR-PEG₁₁ for $n = 2-6$ will be discussed where commercially available α,ω -diyne units were used. However, in a later section, the one-pot procedure will be presented, where α , ω -diyne units were synthesized in the same pot before the formation of PEG₁₁-TR-(CH₂)_n-TR-PEG₁₁, $n = 7, 8$. Details regarding the synthesis procedure of PEG₁₁-Azide have been described in Section 2.3.2.1.

2.3.3.1 Synthesis of PEG₁₁-TR-(CH₂)_n-TR-PEG₁₁, $n = 2-6$

PEG₁₁-TR-(CH₂)_n-TR-PEG₁₁, with $n = 2-6$ were synthesized by reacting PEG₁₁-Azide with 1,5-hexadiyne, 1,6-heptadiyne, 1,7-octadiyne, 1,8-nonadiyne, and 1,9-decadiyne, respectively, using CuAAC *click* reaction (Scheme 2.3). As a typical example, the synthesis of PEG₁₁-TR-(CH₂)₄-TR-PEG₁₁ is described as follows: 1.1 g (2.2 mmol) PEG₁₁-Azide and 0.07 g (0.28 mmol) CuSO₄·5H₂O were dissolved in 10 mL 50 % v/v water/tert-BuOH mixture. After the solution becomes homogenous, 0.1 g (1 mmol) of 1,7-octadiyne was introduced. **Caution:** Care has to be taken during this step as all the dialkynes are toxic and very volatile in nature with an unpleasant odor. Finally, sodium ascorbate (0.2 g, 1 mmol) was added, and the reaction mixture was allowed to stir overnight at room temperature.



Scheme 2.3: Synthesis scheme of PEG₁₁-TR-(CH₂)_n-TR-PEG₁₁, where $n = 2-6$

For purification, the reaction mixture was first diluted with brine and then extracted with dichloromethane. The organic phase was dried using sodium sulfate and the crude product was concentrated by solvent evaporation. Next, column chromatography with silica as a stationary phase was used. Due to the very marginal difference in polarity and a molecular weight between PEG₁₁-azide and the final product, a relatively large SiO₂ : product ratio was required (50:1 w/w). Acetone and ethyl acetate (70:30 v/v) mixture was used as a mobile phase to elute the product from the silica column (yield \approx 40%). Figure 2.8 shows the ¹H NMR spectrum of PEG₁₁-TR-(CH₂)₄-TR-PEG₁₁ while a comparison of ¹³C NMR spectra of PEG₁₁-TR-(CH₂)₄-TR-PEG₁₁ and PEG₁₁-Azide is shown in Figure 2.9. It can be seen that the PEG₁₁-TR-(CH₂)₄-TR-PEG₁₁ sample is considerably clean and free from PEG₁₁-Azide. (¹H NMR and ¹³C NMR spectra of PEG₁₁-TR-(CH₂)_n-TR-PEG₁₁ $n = 2,3,5,6$ are given in Appendix from Figure A7 to Figure A14 while MALDI-TOF spectra for $n = 3,4,6$ are shown in Figure A38, Appendix).

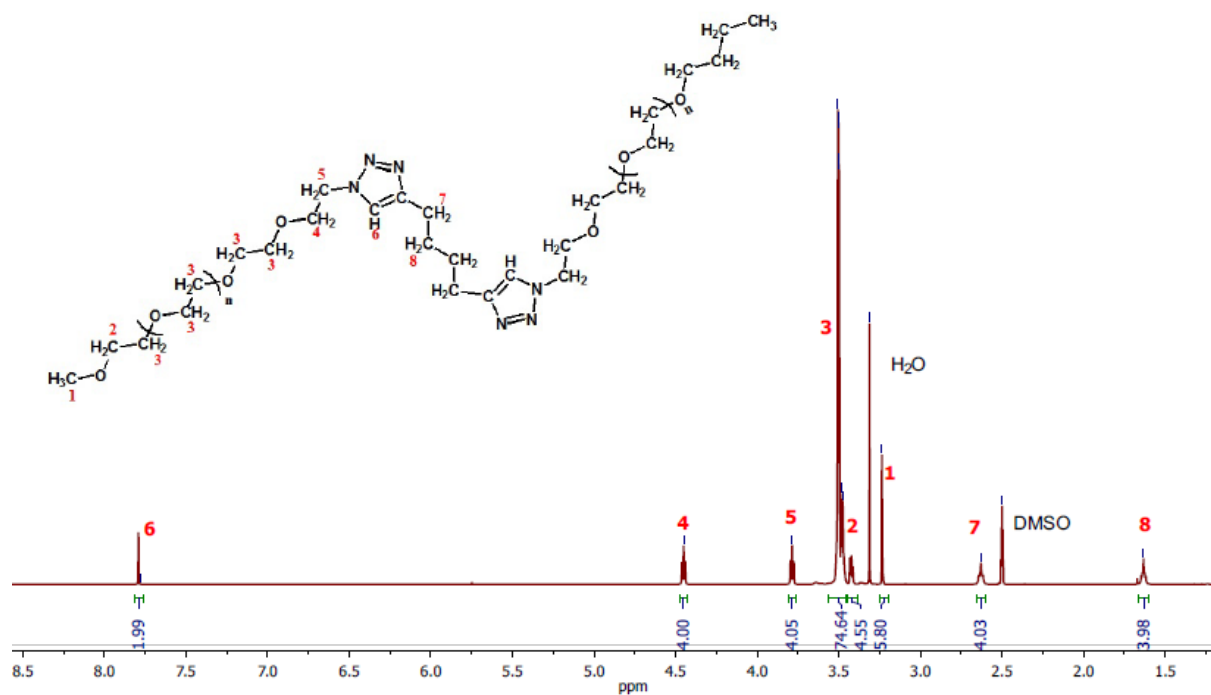


Figure 2.8: ^1H NMR spectrum of $\text{PEG}_{11}\text{-TR}(\text{CH}_2)_4\text{-TR-PEG}_{11}$ in $\text{DMSO-}d_6$ (500 MHz, 27 °C).

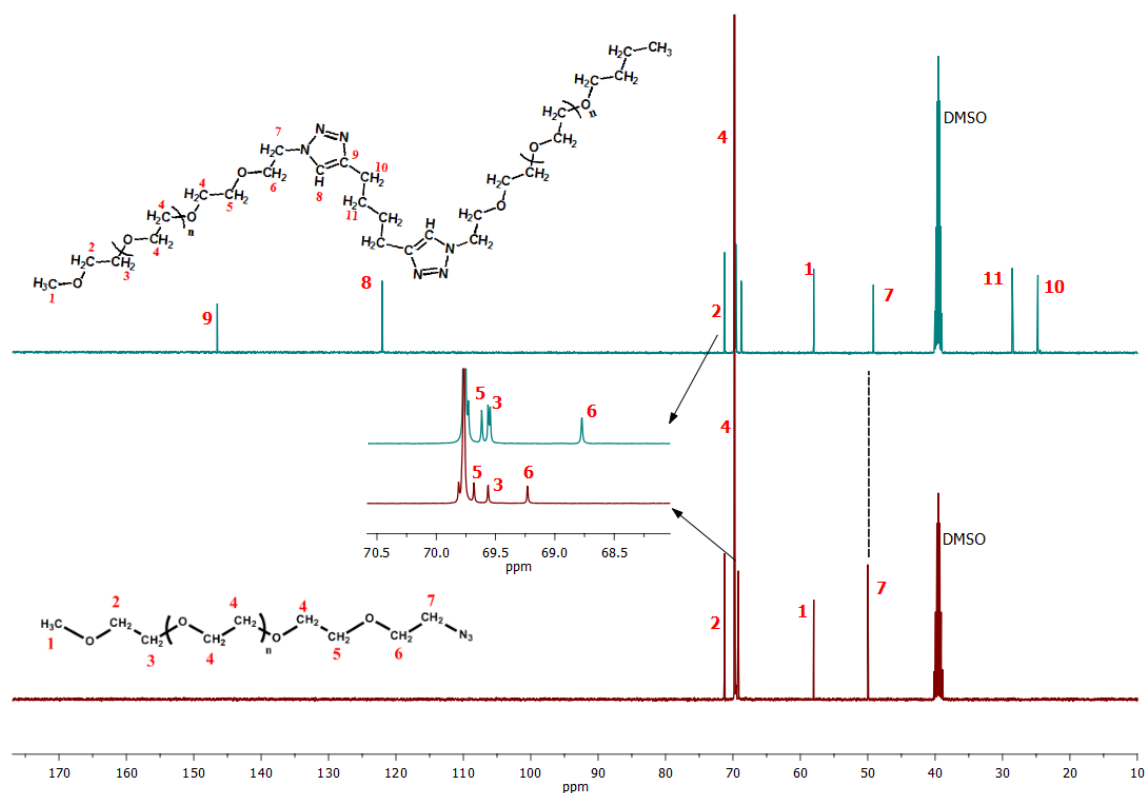
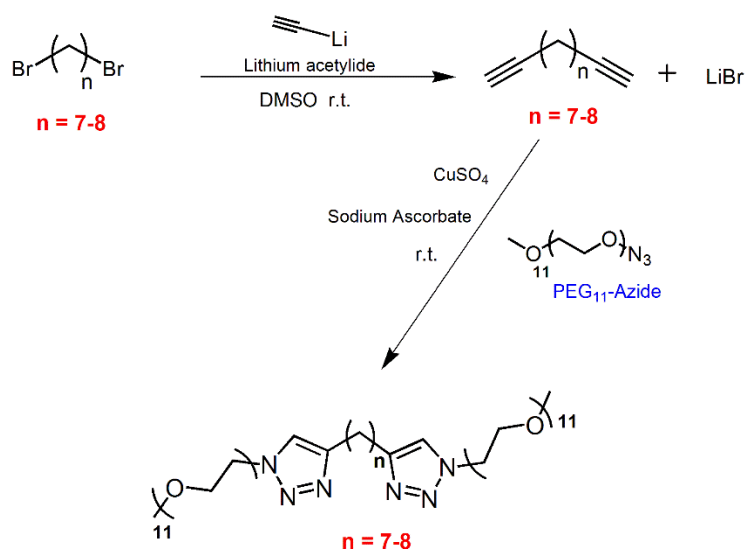


Figure 2.9: ^{13}C NMR spectra of $\text{PEG}_{11}\text{-TR}(\text{CH}_2)_4\text{-TR-PEG}_{11}$ (top) and $\text{PEG}_{11}\text{-Azide}$ (bottom) in $\text{DMSO-}d_6$ (125 MHz, 27 °C).

2.3.3.2 One-pot syntheses of PEG₁₁-TR-(CH₂)_n-TR-PEG₁₁ with $n = 7-8$

The reaction scheme of PEG₁₁-TR-(CH₂)_n-TR-PEG₁₁, $n = 7-8$, is outlined in Scheme 2.4. 1,7-dibromoheptane and 1,8-dibromooctane were transformed into the respective dialkynes by treating with lithium acetylide ethylenediamine complex in anhydrous DMSO¹⁵⁸, followed by CuAAC type *click* reaction with PEG₁₁-Azide to produce PEG₁₁-TR-(CH₂)_n-TR-PEG₁₁ with $n = 7-8$. As an example, the syntheses of PEG₁₁-TR-(CH₂)₇-TR-PEG₁₁ was carried out as 0.276 g (3 mmol) lithium acetylide ethylenediamine complex was weighed in a 20 mL vial and closed by the septum. Argon is used to purge the vial as lithium has a tendency to react with nitrogen to form lithium nitride. 4 mL DMSO was introduced via syringe, and the reaction mixture was stirred at 0 °C for a while. Then, 1,7-dibromoheptane (256 mg, 1 mmol) was added dropwise, and the reaction was carried out overnight at room temperature with continuous stirring. In the next step, small amounts of water were introduced slowly to convert any unreacted lithium acetylide in the system. **Caution:** This step is exothermic and should be done under a fume hood with proper ventilation. Subsequently, the reaction mixture was diluted with 5 mL water, followed by the addition of CuSO₄·5H₂O (0.1 g) and PEG₁₁-Azide (1.1 g, 2.2 mmol). The stirring continued until the solution became homogenous. Finally, sodium ascorbate (0.2 g) was added to start the reaction that continued overnight at room temperature. For purification, in the first step, the reaction mixture was diluted with brine and extracted with dichloromethane. The organic phase was dried over sodium sulfate and concentrated using rotary evaporator.



Scheme 2.4: One-pot synthesis of PEG₁₁-TR-(CH₂)_n-TR-PEG₁₁, with $n = 7-8$.

Before proceeding with column chromatography, residual DMSO traces should be removed from the crude mixture as it can disturb the behavior of the product's mobility in the silica column. Usually, drying is carried out under high vacuum for this purpose, however, in our case, bubbling the mixture with a slow but continuous stream of nitrogen at 40 °C overnight, gave the perfect results. Finally, a purified product was recovered after column chromatography with SiO₂ as the stationary phase (50:1 w/w of SiO₂: product). Acetone and ethyl acetate mixture (70:30 (v/v)) was used as a mobile phase to elute the product (Yield ≈ 25%). ¹H NMR and ¹³C NMR spectra of PEG₁₁-TR-(CH₂)₇-TR-PEG₁₁ are shown in Figure 2.10 and Figure 2.11, respectively while the corresponding spectra of PEG₁₁-TR-(CH₂)₈-TR-PEG₁₁ are available in the Appendix (Figure A15 and Figure A16).

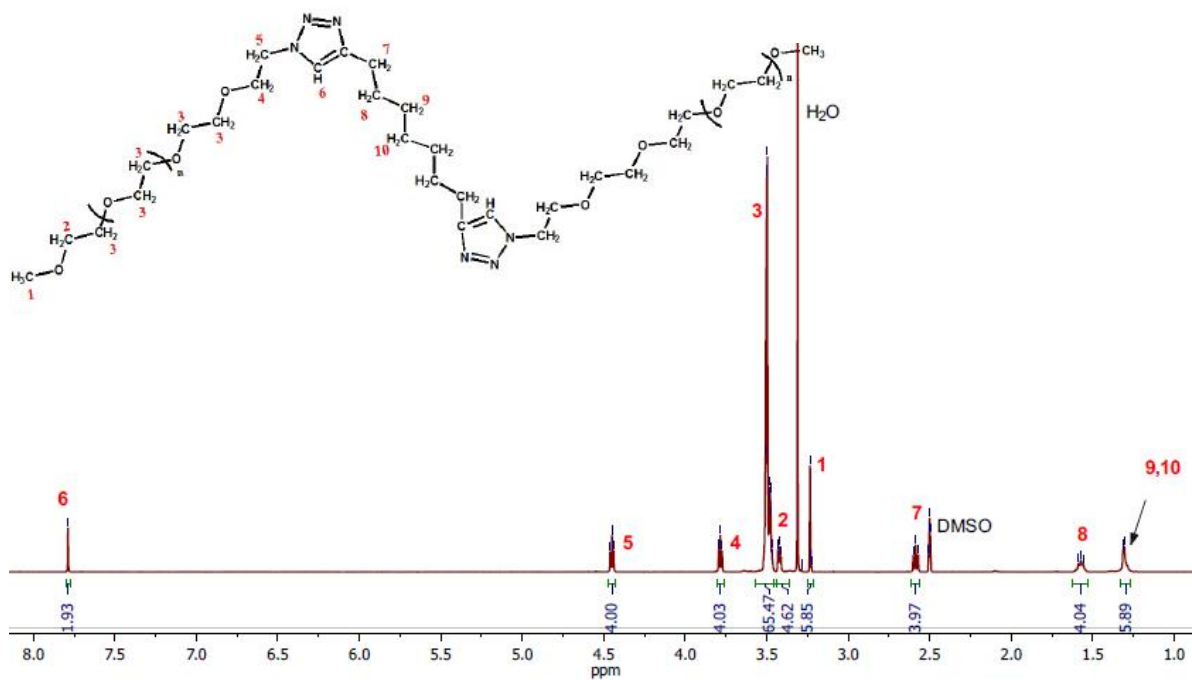


Figure 2.10: ^1H NMR spectrum of PEG₁₁-TR-(CH₂)₇-TR-PEG₁₁ in DMSO-*d*₆ (500 MHz, 27 °C)

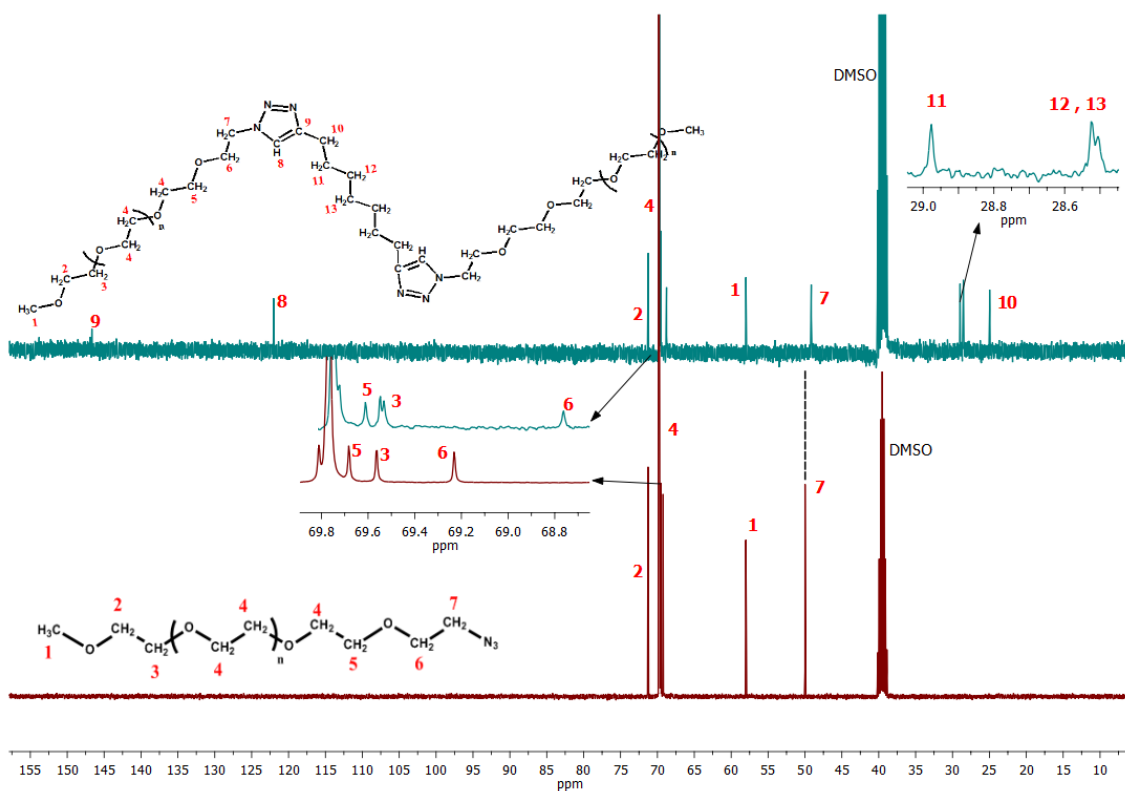
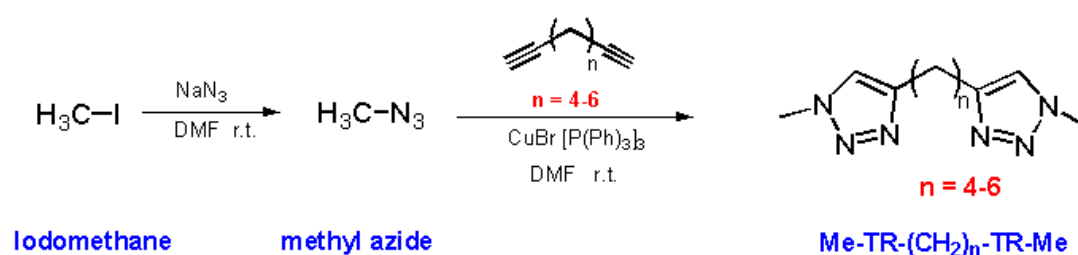


Figure 2.11: ^{13}C NMR spectra of PEG₁₁-TR-(CH₂)₇-TR-PEG₁₁ (top) and PEG₁₁-Azide (bottom) in DMSO-*d*₆ (100 MHz, 27 °C).

2.3.3.3 Synthesis of Dimethyl-bis(triazole) Spacers Me-TR-(CH₂)_n-TR-Me (*n* = 4-6)

Varying length of bis(triazole) spacers Me-TR-(CH₂)_n-TR-Me, (*n* = 4-6), were synthesized by producing in situ methyl azide¹⁵⁹ followed by its CuAAC *click* reaction with the respective α,ω -diyne units (Scheme 2.5). **Caution:** In any case, attempts to isolate methyl azide should be avoided as it is highly susceptible to explode upon any sudden shock when concentrated.



Scheme 2.5: Synthetic route for Me-TR-(CH₂)_n-TR-Me (*n* = 4-6) from iodomethane and different dialkyne units.

In a typical example of synthesizing Me-TR-(CH₂)₄-TR-Me, 1.3g (9.1 mmol) of iodomethane was dissolved in 10 mL DMF along with 0.76 g (12 mmol) of sodium azide in a 50 mL flask and was allowed to stir overnight. In the next step, 0.48 g of 1,7 octadiyne was given to the system along with 0.42 g (0.4 mmol) of bromotris(triphenylphosphine)copper(I) as a catalyst and the reaction mixture was allowed to run overnight at room temperature. After the reaction was completed, the catalyst was filtered off, and the crude product was diluted with brine and extracted with dichloromethane. The organic phase was separated and dried over sodium sulfate and concentrated under vacuum (yield = 60%). ¹H NMR spectra for Me-TR-(CH₂)_n-TR-Me (*n* = 4-6) are shown in Appendix (Figure A17).

3. Result and Discussion

3.1. Well-Defined Poly(ethylene glycol) Networks via Cu(I)-Catalyzed Azide-Alkyne Cycloaddition Reaction

Both *type A* and *type B* PEG networks were successfully synthesized using CuAAC *click* chemistry via the previously mentioned synthetic procedure. FT-IR spectroscopy is used to investigate the network formation. Alkyne and azide moieties have their unique bands in their FT-IR spectrum, and it was expected that these peaks disappear after network formation. As a typical example, FT-IR spectra of PEG(400)-Alkyne and PEG(S)-Azide as well as the formed network, i.e. PEG(S-400) are shown in Figure 3.1. The PEG(400)-Alkyne has two characteristic bands at around 2113 cm^{-1} and 3240 cm^{-1} . The first band at 2113 cm^{-1} belongs to the stretching vibration of two carbon atoms having a triple bond while the second peak appears due to the stretching vibration between the terminal hydrogen and the carbon atom of the alkyne moiety. In the case of PEG(S)-Azide, the presence of the azide group is evident by the appearance of stretching band at around 2100 cm^{-1} . However, in the spectrum of the PEG(S-400) network, the respective peaks of azide and

alkyne moieties vanished completely, indicating a complete conversion within the detection limits of FT-IR spectroscopy (approximately 2 %).

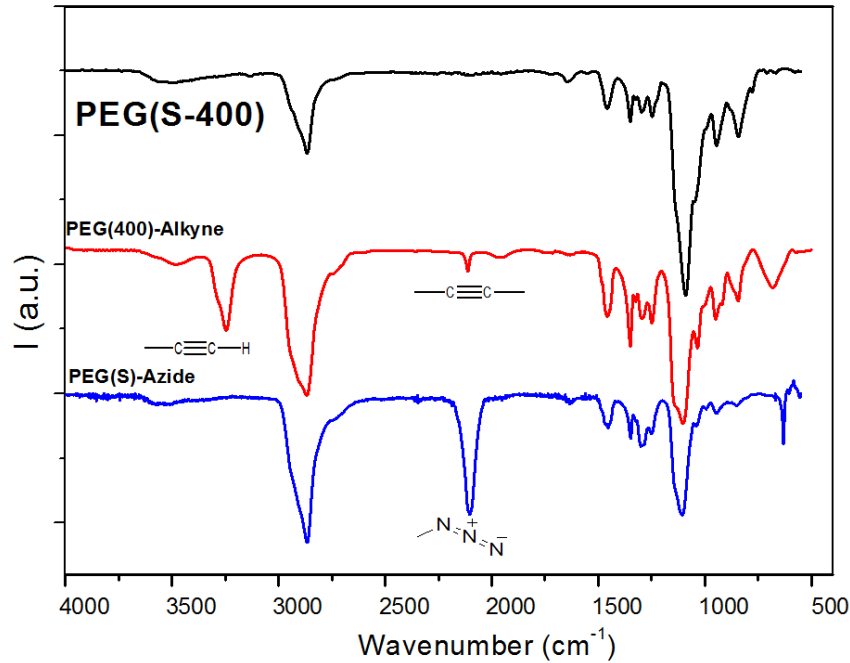


Figure 3.1: FT-IR spectra of PEG(400)-Alkyne, PEG(S)-Azide and PEG(S-400).¹⁵²

One might assume the formation of ideal PEG networks in which, according to IUPAC definitions, all chains are connected at both ends to different cross-link units.¹⁶⁰ However, in reality, defects in a network like dangling chain ends or inelastic loops cannot be avoided completely (detailed discussion below). According to the Flory-Stockmayer theory of gelation¹⁰ the critical conversion p_c at the gel point for polymer networks can be calculated by the following equation .

$$p_c = \frac{1}{\sqrt{r(f_{alkyne} - 1)(f_{azide} - 1)}} \quad (3.1)$$

Here, r is the stoichiometric ratio of alkyne to azide functional groups and as both functional groups are present in equimolar amount, the value of $r = 1$. f_{alkyne} and f_{azide} represents the functionality of respective monomers and its values are 2 and 3, respectively. Moreover, for *type A* and *type B* PEG networks, the value of critical

conversion p_c will be 0.5 and 0.71, which means that the gelation point will be reached after 50 % and 71 % conversion of the functional groups, respectively. When the gelation point is reached, it becomes difficult for the remaining functional groups to react in the same way as before due to their severely hindered mobility in the newly formed network structure. However, the Flory-Stockmayer theory of gelation is based on two assumptions, i.e. equal reactivity of all functional groups and absence of intramolecular reactions. In our system, the first assumption can be accepted but the second one is not valid. Intramolecular reactions are always present in cross-linking processes and at best, one can only reduce their amount but never avoid them completely. These intramolecular reactions do not contribute to the formation of the infinite network rather they increase the critical conversion limit of the whole system. So when the system reaches its gelation point, the overall conversion of functional groups is much higher than the limit calculated by the Flory-Stockmayer equation.

Secondly, post-gelation reactions also increase the final conversion of functional groups. For instance, intramolecular and intermolecular reactions among the chains of the same network do happen even after the gelation process, provided the chains are in close proximity to each other. Moreover, the likelihood of reactions between the unreacted monomer with the unreacted functional groups of network's chains via the diffusion processes also exist. The size of these monomers is comparatively smaller than the network's mesh size which allows them to penetrate into the network structure and react with any other unreacted functional group present deep inside the network structure. Hence, the final conversion will be higher as compared to the theoretical conversion limit, but even after that, there will be a finite possibility of unreacted functional groups. However, they are far too small in number to be detected by either FT-IR or ^{13}C MAS NMR spectroscopy. FT-IR spectra of PEG(S-S), PEG(S-300), PEG(S-1000), PEG(S-2000), PEG(S-6000) are provided in the Appendix; Figure A18.

3.1.1 Network Structure and Defects

During the gelation process the intramolecular reactions are always present together with the desired intermolecular reactions between the growing chains. As one can only reduce their amount but never eradicate them completely from the system, the formed network cannot be characterized as an *ideal network* as it introduces *defects* in the network structure during the gelation process. According to the IUPAC definition of perfect/ideal networks, all network chains are connected on both ends to different network junctions¹⁶⁰ as shown in Figure 3.2. However, in the case of non-ideal networks, defects like dangling chain ends, inelastic loops, etc. are the non-avoidable part of network systems.

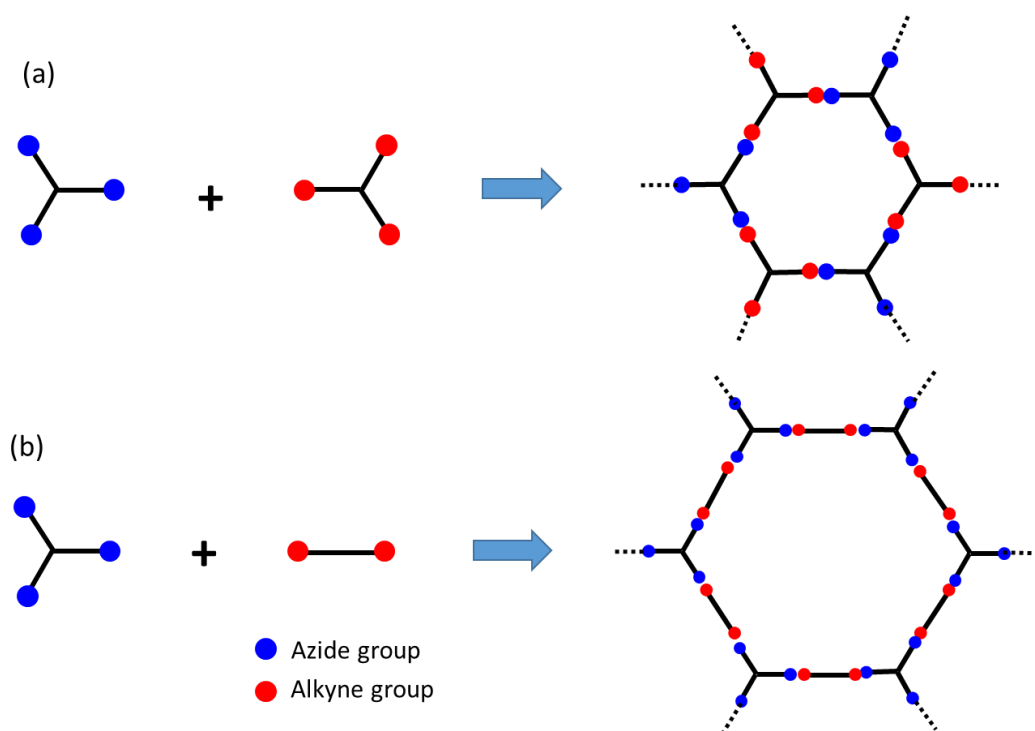


Figure 3.2: Schematic representation of cross-linking topologies of ideal networks made of (a) *type A* samples from the reaction of PEG(S)-Azide and PEG(S)-Alkyne and (b) *type B* samples from PEG(S)-Azide and linear PEG-Alkyne chains.¹⁵²

Figures 3.2(a) and 3.2(b) demonstrate the ideal network structure of *type A* and *type B* networks where all the reactive endgroups of the oligomers units are connected to different junction points, forming single links between them. However, there are possibilities of other type of links formed between the two cross-linking points. In the

type A samples, in addition to single links (Figure 3.3(a)) we can also have double links, i.e. two arms of a star oligomer are connected with two arms of another star (Figure 3.3(b)) which, ultimately, only act as an extension of network chains and result only in increasing the mesh size of the network. In *type B* samples, along with single links (Figure 3.3(c)) and double links (Figure 3.3(d)), there are dangling chain ends (Figure 3.3(e)), which are terminated in a way so that no unreacted functional group will be present, ultimately making it difficult for other spectroscopic methods to detect them.

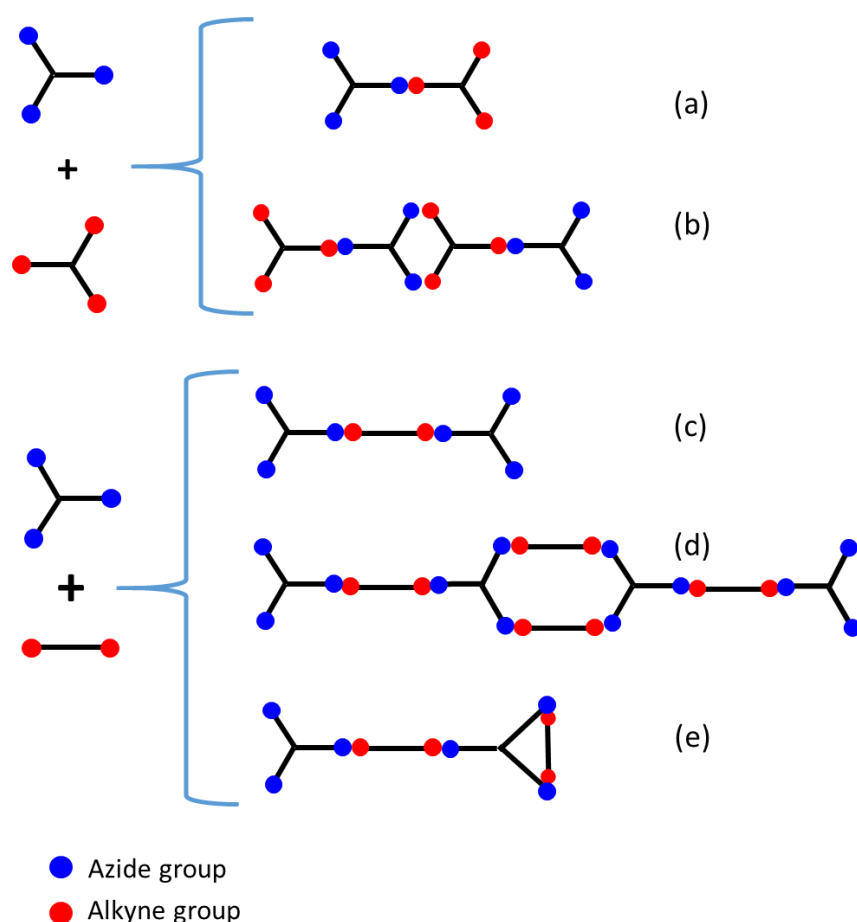


Figure 3.3: Examples of possible network chain links for *type A* and *type B* samples. (a) and (b) single links and double links for *type A* samples while (c), (d) and (e) single links, double links and dangling chain ends for *type B* samples.¹⁵²

To quantify the relative amount of these network topologies, the ^1H DQ NMR technique are used. The details of the experimental procedure are well described in the literature¹⁵² and will thus only briefly summarized here. ^1H DQ NMR is a robust and

quantitative method for the analysis of the dynamics and structural details in polymer networks. It permits the determination of residual homonuclear dipolar coupling (RDC) between the two nearby protons, e.g. protons of close CH₂ groups in the polymer backbone while providing the possibility of avoiding the effect of couplings from far away protons.

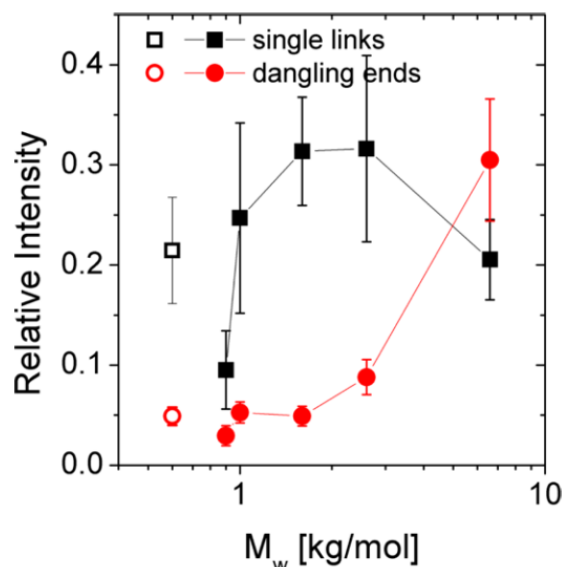


Figure 3.4: Dependence of the intensity of single links and dangling ends vs length of network chains; (full symbols) for the *type B* samples and (open symbols) for the *type A* sample.¹⁵²

Figure 3.4 provides the results of these measurements on both types of samples while Table 3.1 summarizes the values of single, double and higher-order links with the respective amount of dangling chain ends for all samples. It can be observed that our PEG networks are far away from being called an ideal network because as aside from single links, it also contains other types of higher order links which do not effectively contribute to the gelation process. The maximum amount of single links was found in PEG(S-2000) network which was approximately 34%.

Table 3.1: The Relative amount of single, double and higher-order links along the estimation of dangling chains end of both *type A* and *B* sample from ^1H DQ-NMR measurements.

	Single links	Double links	Higher-order links	Dangling chain ends
	%	%	%	%
PEG(S-S)	22.5 ± 1.6	40.2 ± 3.1	37.3 ± 1.5	4.9 ± 0.9
PEG(S-300)	9.8 ± 1.4	19.7 ± 3.5	70.5 ± 2.1	2.95 ± 0.8
PEG(S-400)	26 ± 0.9	50 ± 4.9	24 ± 4	5.3 ± 0.2
PEG(S-1000)	32.9 ± 1	52.8 ± 4.5	14.3 ± 3.5	4.9 ± 0.7
PEG(S-2000)	34 ± 4	13.6 ± 7	52.4 ± 3	8.8 ± 1.6
PEG(S-6000)	26.8 ± 2.2	22.5 ± 9.2	50.7 ± 7	30.5 ± 3.5

The results from ^1H double quantum (DQ) NMR spectroscopy measurements on both *type A* and *type B* samples show that the networks are not ideal. But this is also not surprising, as they further support the results of the swelling experiments (discussed later).

3.1.2 Thermal Properties

The DSC traces of all PEG networks are recorded from $-20\text{ }^\circ\text{C}$ to $80\text{ }^\circ\text{C}$ at $10\text{ }^\circ\text{C}/\text{min}$. Values of melting temperature T_m , enthalpy of melting ΔH_m , and degree of crystallinity X_c of all PEG networks are given in Table 3.2. To see the influence of cross-linking on the crystallization process, the same measurements are also performed for linear poly(ethylene glycol) chains as well.

DSC traces of only PEG(S-1000), PEG(S-2000) and PEG(S-6000) are shown in Figure 3.5(a) because PEG(S-S), PEG(S-300) and PEG(S-400) are completely amorphous and do not show any crystallization and melting peaks (see Appendix; Figure A20). In Figure 3.5(b), a comparison is made between PEG(S-1000) and linear PEG(1000) to visualize their melting behavior under the same measurement conditions (for similar plots of PEG(S-

2000) and PEG(S-6000), see Figure A21 (a-b) in the Appendix). All DSC measurements are normalized by the sample mass to give these comparisons a more realistic aspect.

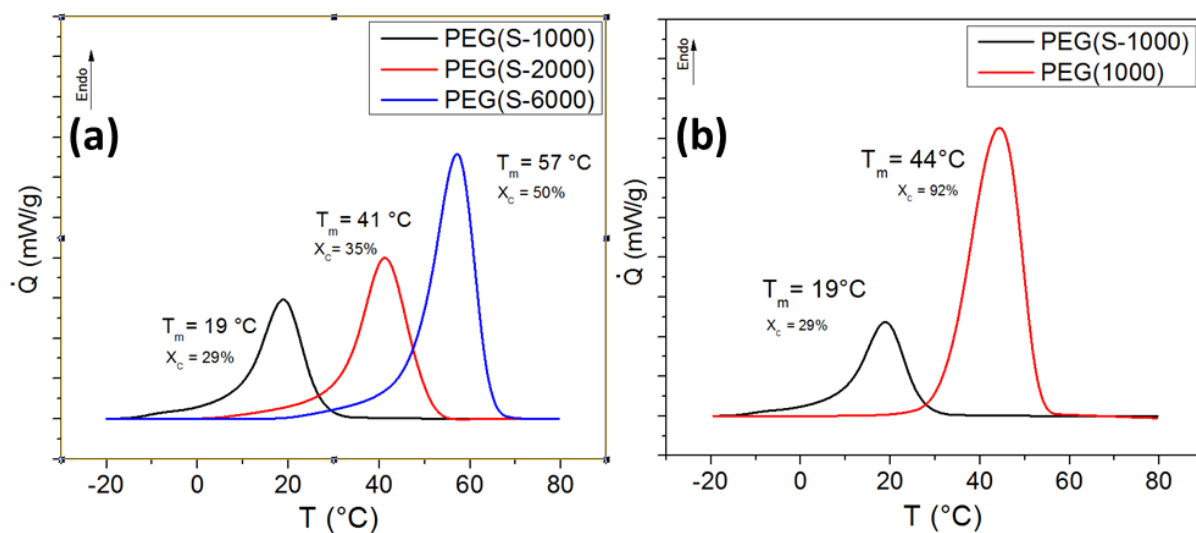


Figure 3.5: (a) DSC traces of PEG networks (PEG(S-1000), PEG(S-2000) and PEG(S-6000) along with their respective melting temperature T_m and crystallinity X_c . (b) A combined DSC plot of PEG(S-1000) and PEG(1000).

It can be observed that the melting peaks of PEG networks are relatively broad and low in intensity as compared to the linear PEG chains with comparable molar masses between the two cross-links of the PEG networks. Lower melting temperature and peak broadening signify the fact that PEG networks crystallize with relatively smaller lamella thickness and possess a wide distribution of crystal sizes. However, on the other hand, linear PEG(1000) has a relatively sharp melting peak and a higher degree of crystallinity, which indicates a narrow crystal size distribution and relatively large lamella thickness. The degree of crystallinity values are calculated by dividing the enthalpy of melting ΔH_m values of PEG network samples or linear PEG chain by the enthalpy of melting ΔH_m^0 values of 100% crystalline PEG chains

Table 3.2: Melting temperature T_m , enthalpy of melting ΔH_m and degree of crystallinity X_c of PEG networks and linear PEG chains obtained by DSC.

Sample	Melting Temperature, T_m (°C)	Enthalpy of melting ΔH_m (J/g)	Degree of crystallinity ^{a)} X_c (%)
PEG(S-S)	-	-	0
PEG(S-300)	-	-	0
PEG(S-400)	-	-	0
PEG(S-1000)	19	57.1	29
PEG(S-2000)	41	68.9	35
PEG(S-6000)	57	98.5	50
PEG(1000)	44	181.2	92
PEG(2000)	63	171.4	87
PEG(6000)	69	175.3	89

The degree of crystallinity X_c of all PEG networks is determined from the enthalpy of melting, ΔH_m

$$X_c = \frac{\Delta H_m}{\Delta H_m^o} \quad (3.2)$$

where ΔH_m^o represents the enthalpy of melting of a 100% crystalline PEG. The value of $\Delta H_m^o = 197 \text{ J/g}^{161}$ is used for these calculations. It can be observed in Table 3.2 that poly(ethylene glycol) chains of molar masses 1000, 2000 and 6000 g/mol showed a higher degree of crystallinity and melting temperature when they were linear and uncross-linked as compared to their relatively immobilized state when they become a part of a cross-linked network. The connected chain ends, and temporary and permanent entanglement are some of the major factors due to which PEG networks exhibit a lower degree of crystallinity and melting temperature. A schematic representation of PEG crystals in a network is shown later in the SAXS discussion section.

3.1.3 Isothermal Crystallization Kinetics

Isothermal crystallization kinetics of PEG networks is studied by differential scanning calorimetry (DSC). The samples were heated above their respective melting temperatures to remove any thermal history and then cooled rapidly (30-50 °C/min) to various crystallization temperatures T_c . The samples were held at T_c until the complete crystallization process finishes.

In order to demonstrate the different steps of the evaluation procedure for these isothermal crystallization measurements, Figure 3.6(a) shows a typical DSC trace of an isothermal crystallization of PEG(S-6000) at $T_c = 45^\circ\text{C}$. Initially, a time-lag, known as induction time, between the start of the experiment and the actual beginning of the crystallization process should be excluded from the calculations, which usually corresponds to the thermal stabilization of the DSC equipment.¹⁶² After adjusting the induction time, the isothermal crystallization measurement was assumed to start from the point A and the time t is set to $t = t_0$. As the time proceeds, the heat flow due to the exothermal crystallization process is observed in the DSC trace and it reaches its maximum value at point B. Afterward, the crystallization process starts to slow down and was considered complete when no further change in the heat flow was observed at C.

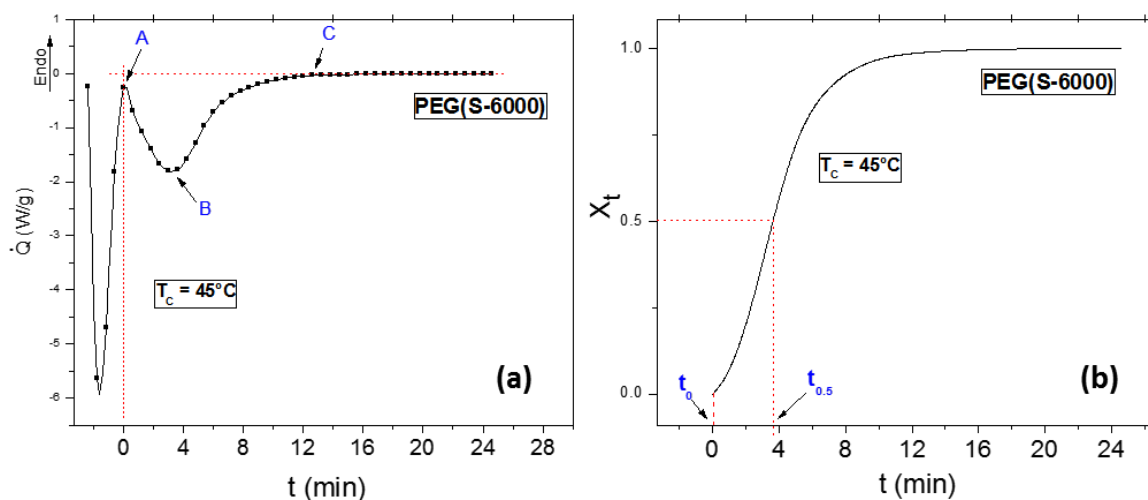


Figure 3.6: (a) DSC exothermal peak for the isothermal crystallization of PEG(S-6000) at a crystallization temperature of 45 °C. (b) Time-dependent relative degree crystallinity X_t vs the crystallization time t plot (*crystallization isotherm*) of PEG(S-6000) at a crystallization temperature of 45 °C, obtained by Eq. 3.3.

From the crystallization exotherms, the time-dependent relative degree of crystallinity X_t at time t can be calculated by the following equation¹⁶³

$$X_t = \frac{\int_0^t \left(\frac{dH_C}{dt}\right) dt}{\int_0^\infty \left(\frac{dH_C}{dt}\right) dt} = \frac{A_t}{A_\infty} \quad (3.3)$$

where A_t is the area under the DSC exothermal curves from t_0 (start of crystallization time) to time t and A_∞ is the total area under the crystallization curve i.e. from t_0 to t_∞ . The integration of the crystallization exotherm gives typical *S-shaped* plots, representing the progress of the crystallization process with time and called *crystallization isotherms* (see Figure 3.6 (b)). The plots were normalized between 0 and 1 representing the start and completion of the crystallization process, respectively. One of the important parameters deduced from these plots is the crystallization half-time $t_{0.5}$ which is defined as the time required to reach 50 % of overall crystallinity at any particular crystallization temperature T_C . Crystallization isotherms of PEG(S-1000), PEG(S-2000) and PEG(S-6000) are shown in Figure 3.7, and the respective values of $t_{0.5}$ at different T_C are listed in Table 3.3.

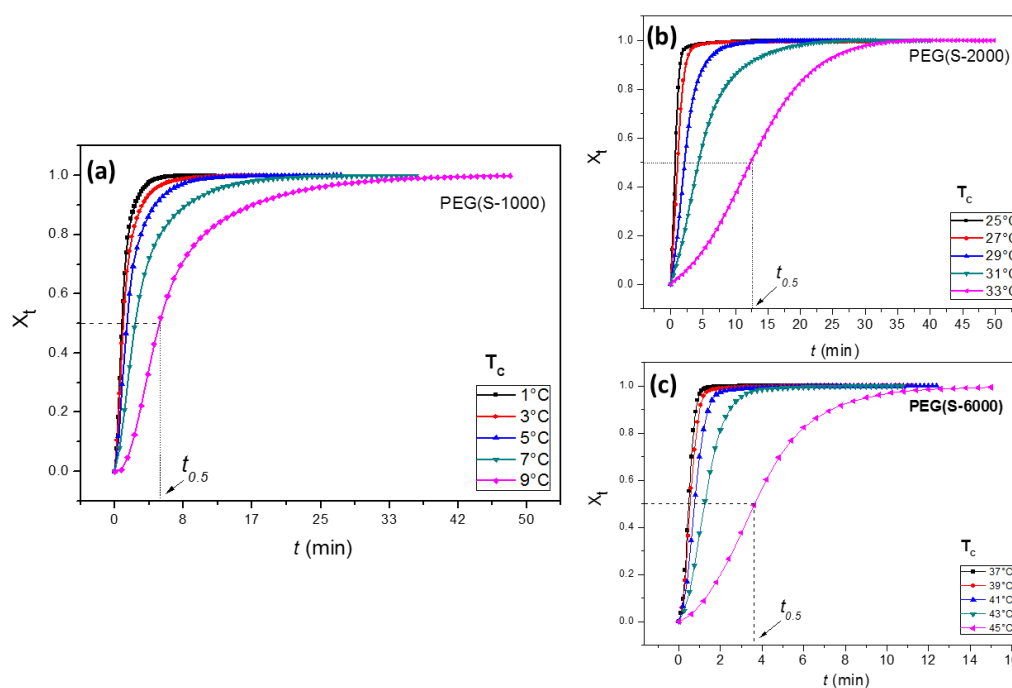


Figure 3.7: Crystallization isotherms (X_t vs t) for (a) PEG(S-1000), (b) PEG(S-2000) and (c) PEG(S-6000).

A more conventional approach to quantitatively analyze these kinetic measurements is by the well-known Avrami equation.¹⁶⁴ For an isothermal crystallization process, a time-dependent relative degree of crystallinity X_t can be represented as,

$$X_t = 1 - \exp(-kt^n) \quad (3.4)$$

Linearizing Eq. 3.4 by taking the double logarithm yields

$$\ln[-\ln(1 - X_t)] = \ln k + n \ln t \quad (3.5)$$

where n represents the Avrami exponent, t is the crystallization time, and k represents the overall crystallization rate constant which is comprised of the contributions from the nucleation and crystal growth processes. The Avrami exponent n is composed of two terms i.e. $n = n_d + n_n$, where n_d represents the dimensionality of the growing crystals and n_n represents the time dependence of the nucleation process (i.e. either sporadic or instantaneous).¹⁶² The value of n lies between 1 and 4 depending on the mutual behavior of the nucleation and crystal growth processes. As a typical example, the linearized double-logarithmic plot of PEG(S-6000) at $T_c = 45^\circ\text{C}$ is shown in Figure 3.8.

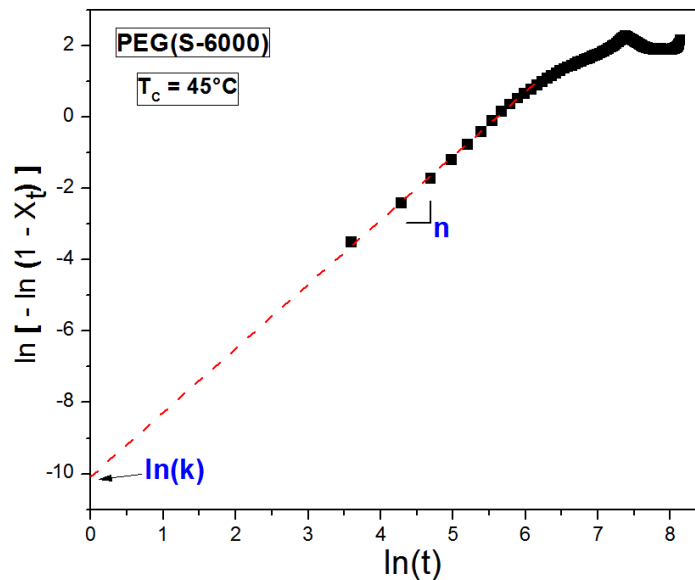


Figure 3.8: Evaluation of n and k from the Avrami plot of PEG(S-6000) at $T_c = 45^\circ\text{C}$.

For the calculation of k and n , one has to perform a linear fit to the initial linear part of the plot as the observed change in slope later in the measurement represents the onset of the secondary crystallization process.¹⁶⁵ Typically, secondary crystallization occurs

when the sample is completely comprised of spherulites and these spherulites begin to start impinging on each other. This later increase in crystallinity usually involves the crystal thickening and/or the development of entire new lamellae stacks from the amorphous regions within a spherulite.¹⁶⁶ In their investigation, Lorenzo *et al.*¹⁶² suggested that the selection of the relative degree of crystallinity range is critical for a good Avrami fitting of the data. The initial data points ($X_t < 3\%$) can be ignored due to the experimental errors while towards the end of the crystallization process, the secondary crystallization process should also be avoided to prevent any errors in the values of n and k . Their study shows that considering the relative crystallinity values from 3 to 20 % is sufficient for a good Avrami fit. Avrami plots of isothermal crystallization measurements of PEG(S-1000), PEG(S-2000) and PEG(S-6000) are shown in Figure 3.9, and corresponding values of k and n are given in Table 3.3.

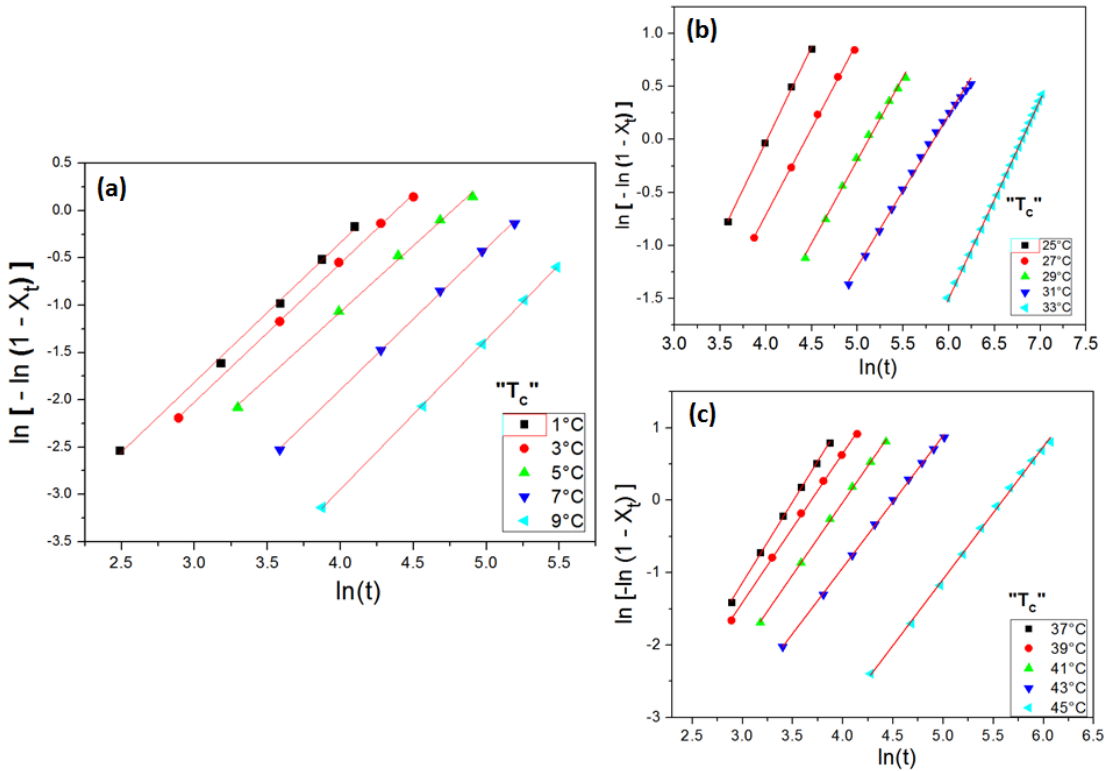


Figure 3.9: Double-logarithmic Avrami plots of the isothermal crystallization measurements of (a) PEG(S-1000), (b) PEG(S-2000) and (c) PEG(S-6000) networks.

From Table 3.3, it can be concluded that the values of the Avrami exponent n for all three types of PEG networks are similar in the range from 1.4 to 2.2. From these n values, it can be proposed that the crystallization morphology of all three PEG networks might be a mixture of one-dimensional needle-like and two-dimensional disk-like crystal structures. However, these crystalline entities are too small in order to be seen by the polarized optical microscopy. A typical behavior of Avrami rate constant k is also observed for all three PEG networks as it decreases with increasing crystallization temperature T_c , indicating a slowing down of the overall crystallization process at higher T_c .

Table 3.3: Respective values of Avrami rate constant k at each crystallization temperature T_c , Avrami exponent n , crystallization half time $t_{0.5}$ and activation energies E_A of PEG(S-1000), PEG(S-2000) and PEG(S-6000) networks.

T_c °C	k min^{-1}	n	$t_{0.5}$ min	E_A kJ/mol
PEG (S-1000)				
1	1.9E-03	1.57	0.9	-132 ± 15
3	1.6E-03	1.5	1	
5	1.3E-03	1.4	1.4	
7	3.8E-04	1.5	2.5	
9	9.3E-05	1.6	5.4	
PEG (S-2000)				
25	7.4E-04	1.8	0.8	-286 ± 33
27	7.2E-04	1.6	1.1	
29	3.2E-04	1.6	2.2	
31	2.3E-04	1.4	4.4	
33	2.8E-06	1.8	12.4	
PEG (S-6000)				
37	8.9E-04	2.2	0.5	-236 ± 32
39	5.0E-04	2.1	0.5	
41	3.2E-04	2.0	0.8	
43	2.7E-04	1.8	1.2	
45	3.5E-05	1.8	3.6	

At the two characteristic transition temperatures i.e. glass transition temperature T_g and equilibrium melting temperature T_m^o the values of the rate of crystallization of a polymer are vanishingly small and between these two temperatures, it forms a bell-shaped curve (see Figure 3.10 (a)) The specific shape of this curve is a result of the crystal growth being slowed by increasing viscosity at temperatures close to T_g , and by diminishing thermodynamic drive for the nucleation process, as the melting point is approached.

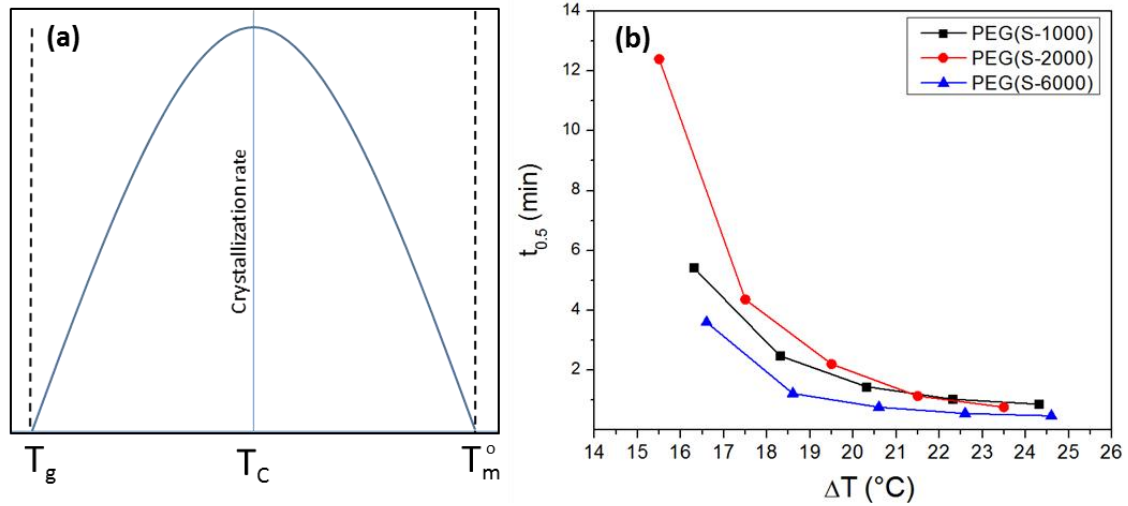


Figure 3.10: (a) Schematic representation of a bell-shaped behavior of crystallization rate between T_g and T_m^o (b) Half-time of crystallization $t_{0.5}$ vs the degree of undercooling $\Delta T = T_m^o - T_c$ of PEG(S-1000), PEG(S-2000) and PEG(S-6000) networks.

Half-time of crystallization $t_{0.5}$ is also an important parameter for the discussion of crystallization kinetics and is defined as the time taken from the beginning of the crystallization process until 50 % of its completion. It can either be obtained from the time-dependent relative degree of crystallinity X_t isotherms (see Figure 3.7) or can be calculated using the following relation¹⁶⁷

$$t_{0.5} = \left(\frac{\ln 2}{k} \right)^{\frac{1}{n}} \quad (3.6)$$

The dependence of $t_{0.5}$ on the degree of undercooling ΔT (i.e. $\Delta T = T_m^o - T_c$) of PEG(S-1000), PEG(S-2000) and PEG(S-6000) is shown in Figure 3.10 (b). As it can be seen from

Eq. 3.6 that the half-time of crystallization $t_{0.5}$ is inversely proportional to the rate of crystallization k , so for all three PEG networks, values of $t_{0.5}$ are higher for T_c near T_m^o (i.e. smaller undercooling temperatures) indicating a relatively slow crystallization process of the PEG networks. On the other hand, $t_{0.5}$ values decreases gradually with increasing undercooling temperatures, exhibiting a faster crystallization process. However, $t_{0.5}$ values also follow a similar but opposite trend with respect to T_c , and $t_{0.5}$ values of all three PEG networks are expected to increase again with the further increase in undercooling temperatures and will have their maximum value near T_g .

To further study the behavior of the Avrami rate constant k at different crystallization temperature T_c , the Arrhenius relationship (Eq. 3.7) was used to determine the isothermal crystallization activation energy E_A of PEG networks.^{168,169}

$$k^{1/n} = k_o \exp\left(-\frac{E_A}{RT_c}\right) \quad (3.7)$$

or

$$\frac{\ln k}{n} = \ln k_o - \frac{E_A}{RT_c} \quad (3.8)$$

where k_o is the temperature-independent pre-exponential factor, T_c is the isothermal crystallization temperature, and R is the universal gas constant. From the slope of $(\ln k)/n$ vs $1/T_c$ plot, the value of E_A can be obtained. Figure 3.11 shows the plots of $(\ln k)/n$ vs $1/T_c$ for PEG(S-1000), PEG(S-2000) and PEG(S-6000) networks and the Isothermal crystallization activation energies E_A are tabulated in Table 3.3.

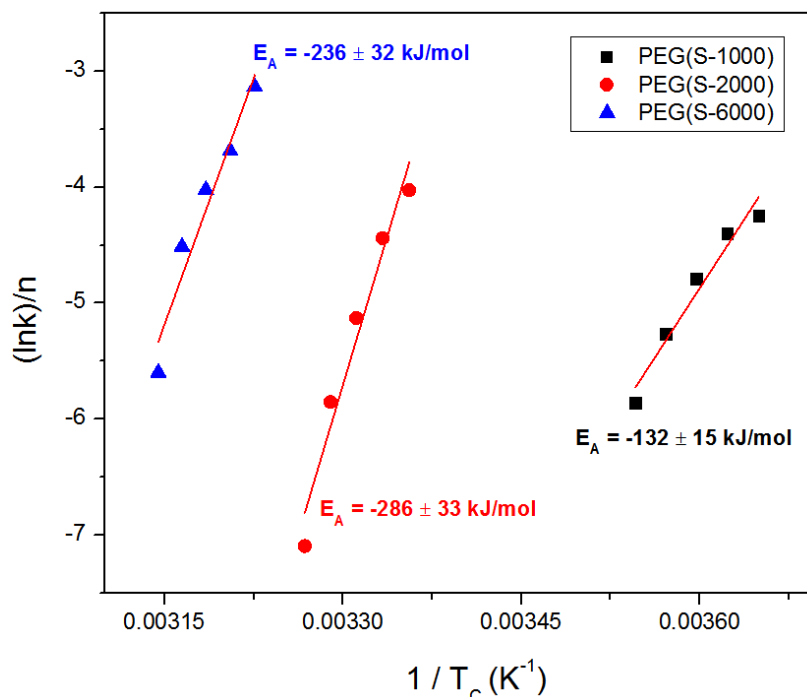


Figure 3.11: Plots of $(\ln k)/n$ vs $1/T_c$ for PEG(S-1000), PEG(S-2000) and PEG(S-6000) using linearized Arrhenius Equation (Eq. 3.8).

It is important to mention here that the sign of the activation energy is only an indication of the initial state of the system before it crystallizes. The activation energy values are negative when crystallization is initiated by cooling the system from its melt state while it will be positive when crystallization begins by heating the system from its glassy state.¹⁷⁰ It can be observed that for PEG(S-2000) and PEG(S-6000), the E_A values are relatively large i.e. -286 ± 33 kJ/mol and -236 ± 32 kJ/mol while for the PEG(S-1000) network, it is much smaller i.e. -132 ± 15 kJ/mol. One of the apparent reasons for this lower E_A value of PEG(S-1000) can be the smaller lamella thickness values of its crystallites. It has been a well-known fact that the smaller molar mass molecules (also for the lower molar mass PEG chains¹⁷¹) crystallize more easily with lower activation energy as compared to their higher molar mass (longer) counterparts. Although, PEG(S-1000) has the highest cross-link density among the other PEG networks and due to which it is least crystalline and has smallest crystallite sizes (see WAXS discussion). However, on the other hand, these smaller size crystallites can be formed rather easily with low activation energy barrier as compared to the larger crystallites of other PEG networks. Apart from the relative crystal sizes, entanglements can also be regarded as a reason for

an increase in E_A values for PEG(S-2000) and PEG(S-6000). It was reported¹⁷² earlier that the critical entanglement molar mass M_e for a PEG chain is around $M_e \approx 1600$ g/mol and as the PEG(S-2000) and PEG(S-6000) has a longer chain length between the cross-links than this M_e limit, these entanglements will also play their role in impeding the crystallization process and consequently, increasing the E_A values for these networks.

Equilibrium Melting Temperature T_m^o : The equilibrium melting temperature T_m^o of a polymer is defined as the melting temperature of an infinite stack of extended chain crystals which are large in perpendicular directions to the chain axis while the chain ends have established an equilibrium state of pairing with each other.¹⁷³ It is common for polymers that their experimentally observed melting temperatures T_m are a function of their T_c and as their crystallization process usually starts well below their T_m^o , extrapolation of experimental data is usually performed to obtain T_m^o values (Hoffman-Weeks¹⁷⁴ method). It is important to mention here that there is a persistent debate¹⁷⁵⁻¹⁷⁸ about the validity of this method to calculate the equilibrium melting temperature T_m^o of a polymer. Nevertheless, this method will be used to calculate the equilibrium melting temperature T_m^o , for the present PEG networks. Eq. 3.8 shows the Hoffman-Weeks relationship,

$$T_m = \alpha T_c + (1 - \alpha) T_m^o \quad (3.9)$$

where α is the stability parameter and its value depends upon the crystal size and its perfection. Its value lies between 0 and 1, where $\alpha = 0$ means that the crystal structure is perfect and there is no influence of crystallization temperature T_c on the melting point T_m , i.e. $T_m = T_m^o$, whereas $\alpha > 0$ shows that the polymer crystals are more imperfect and unstable.¹⁷⁹ In a typical T_m vs T_c plot, a linear extrapolation of data to the $T_m = T_c$ line yields the equilibrium melting temperature T_m^o for a semicrystalline polymer.

After isothermally crystallizing the PEG networks at different crystallization temperature T_c , samples were reheated at 10 °C/min to record the respective melting endotherm for that particular T_c . Hoffman-Weeks plots for PEG(S-1000), PEG(S-2000) and PEG(S-6000) networks are shown in Figure 3.12 while the corresponding values of T_m^o and α are

tabulated in Table 3.4. (DSC melting endotherms of PEG(S-1000), PEG(S-2000) and PEG(S-6000) for different isothermal crystallization temperatures T_c are shown in Figure A22 (a-c) in the Appendix)

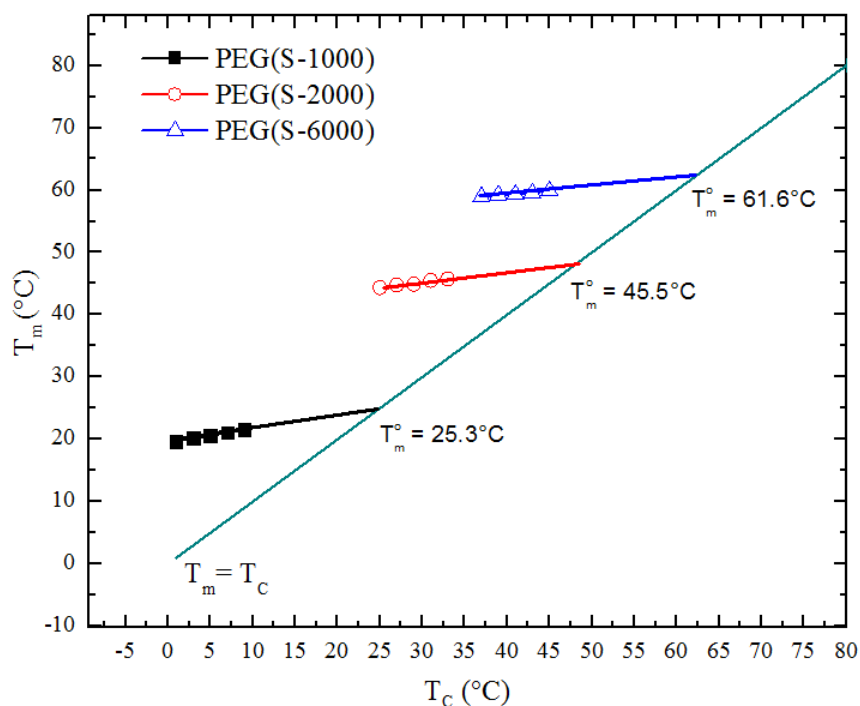


Figure.3.12: Hoffman-Weeks plots of PEG(S-1000), PEG(S-2000) and PEG(S-6000).

Table 3.4: Equilibrium melting point T_m^o , the stability parameter α and correlation coefficient of linear regression R^2 of PEG(S-1000), PEG(S-2000) and PEG(S-6000) networks.

	T_m^o (°C)	α	R^2
PEG(S-1000)	25.3	0.23	0.996
PEG(S-2000)	45.5	0.17	0.967
PEG(S-6000)	61.6	0.11	0.965

As it was mentioned earlier that smaller values of α represent a more stable and large-sized crystal structure. Therefore, the smallest value of α for PEG(S-6000) suggests that

it contains relatively larger size crystals having more stability and regularity as compared to PEG(S-2000) and PEG(S-1000). This might be due to the decrease in the cross-linking density with the increase in chain length between the two cross-links, which makes the PEG chains in the networks more mobile and flexible, allowing them to form bigger and relatively more stable crystals. These results are also in good agreement with the SAXS results (discussed later), where only for the PEG(S-6000) network, higher order diffraction peaks are observed which indicates a relatively regular and ordered crystal structure.

3.1.4 Non-isothermal Crystallization Kinetics

For non-isothermal crystallization kinetic studies, PEG(S-1000), PEG(S-2000) and PEG(S-6000) are crystallized at different cooling rates i.e. 20 °C/min, 10 °C/min, 5 °C/min and 2.5 °C/min and their respective crystallization exotherms are shown in Figure 3.13. It can be observed that crystallization peaks of all PEG networks get broader and shifted towards lower temperatures with increasing cooling rates. This decrease in the non-isothermal crystallization temperature T_p with the cooling rates is due to the fact that at higher cooling rates, the PEG chains do not react fast enough to the change in temperature and as a result, they crystallize at relatively lower temperatures.

S-shape plots of the relative degree of crystallinity X_t vs the crystallization time t for PEG(S-1000), PEG(S-2000) and PEG(S-6000) at different cooling rates are shown in Figure 3.14. It can be observed that the higher the cooling rate, the shorter will be the time required to complete the crystallization process. This is an expected behavior for the PEG networks, as at slower cooling rates, more time is needed to complete the crystallization process and vice versa.

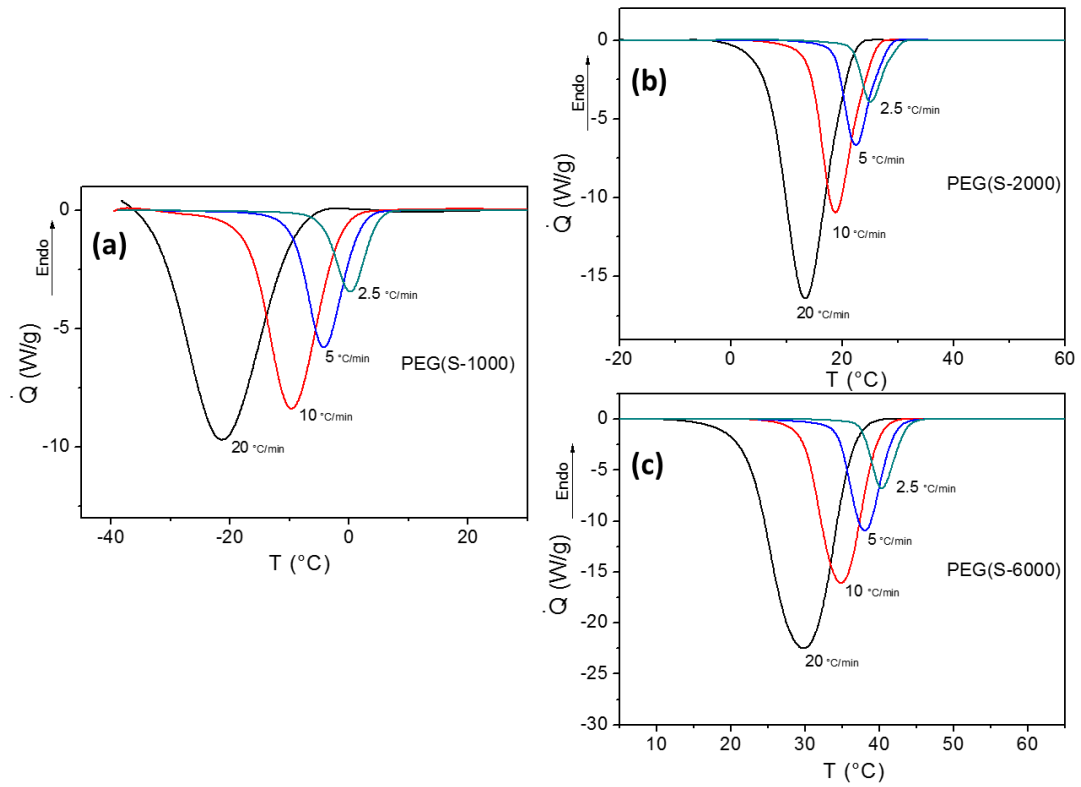


Figure 3.13: Non-isothermal crystallization exotherms of (a) PEG(S-1000), (b) PEG(S-2000) and (c) PEG(S-6000) at different cooling rates obtained by DSC measurements.

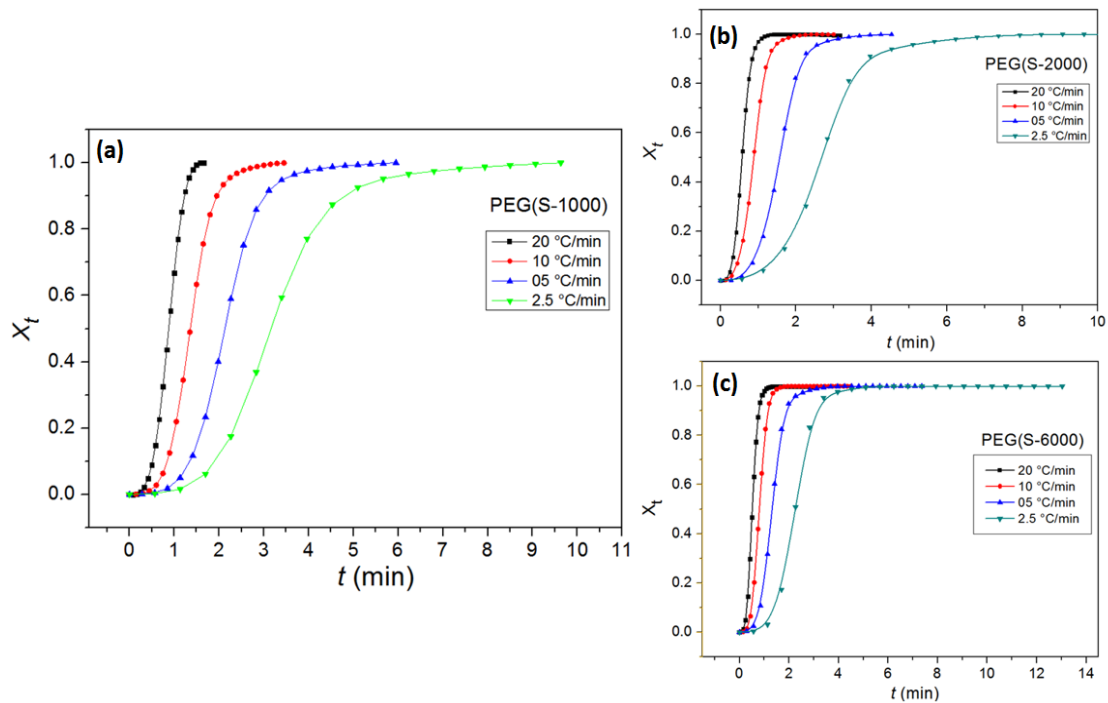


Figure 3.14: X_t vs t plots for (a) PEG(S-1000), (b) PEG(S-2000) and (c) PEG(S-6000) at different cooling rates obtained by DSC measurements.

To analyze the non-isothermal crystallization kinetics, Ozawa¹⁸⁰ modified the Avrami equation and presented a model where he assumes that the non-isothermal crystallization process contains infinitesimally small isothermal crystallization steps. He introduces the factor of cooling rate ϕ into the basic Avrami equation and defines time-dependent relative crystallinity X_t at any given temperature T as

$$X_t = 1 - \exp\left[-\frac{K(T)}{\phi^m}\right] \quad (3.10)$$

Linearization of Eq. 3.10 gives

$$\ln[-\ln(1 - X_t)] = \ln K(T) - m \ln \phi \quad (3.11)$$

where m is the Ozawa exponent and $K(T)$ is the cooling function which is influenced by the dimensionality of crystal growth and is a measure for the rate of the crystallization process. However, in various reported works^{163,181,167,182}, this model is found invalid as it is unable to produce a linear $\ln[-\ln(1-X_t)]$ vs $\ln\phi$ plots, necessary to obtain the $K(T)$ and m parameters.

In pursuit of finding a workable method, Lui *et al.*¹⁸³ combined the Avrami and Ozawa equations in order to evaluate the non-isothermal crystallization process. According to their model, in the non-isothermal crystallization process the relation between crystallization time t and temperature T can be written as

$$t = \frac{T_0 - T}{|\phi|} \quad (3.12)$$

where, T is the temperature at any given time t and T_0 is the initial temperature at which crystallization starts i.e. t_0 . As the Avrami equation relates X_t with time t while the Ozawa equation relates X_t with cooling rate ϕ , a correlation between ϕ and t could be made as follows

$$\log \phi = \log F(T) - \alpha_0 \log t \quad (3.13)$$

where $F(T)$ is the rate parameter, and it equals to

$$F(T) = \left[\frac{K(T)}{k} \right]^{1/m} \quad (3.14)$$

where, $K(T)$ is a rate constant from Ozawa equation (Eq. 3.10) and k , is the Avrami rate constant (Eq. 3.4). $F(T)$ defines the value of the cooling rate required to reach a defined degree of crystallinity at unit crystallization time, while α_0 is the ratio of Avrami exponent n and Ozawa exponent m ($\alpha_0 = n/m$). Using Eq. 3.13, the plot of $\log(\phi)$ vs $\log(t)$ for any specific degree of crystallinity value should be a straight line where values of $F(T)$ and α_0 can be calculated from its intercept and slope, respectively. Figure 3.15 shows the $\log(\phi)$ vs $\log(t)$ plots for PEG(S-1000), PEG(S-2000) and PEG(S-6000) networks for different degree of crystallinities using the combined Avrami-Ozawa approach.

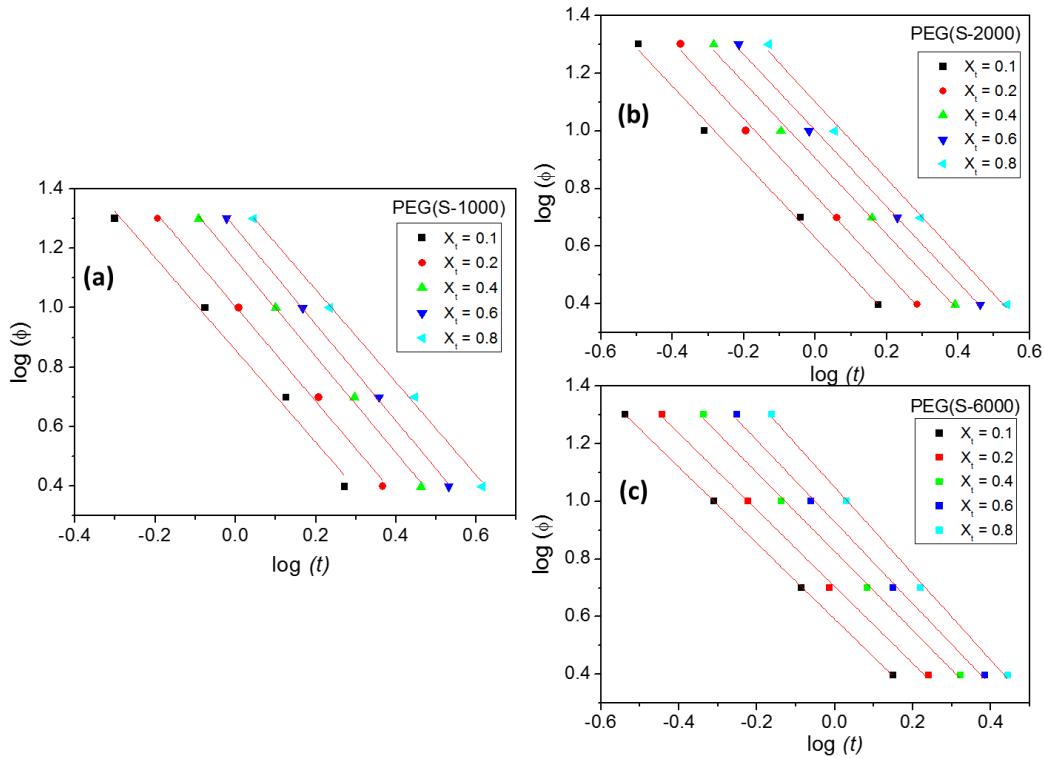


Figure 3.15: $\log(\phi)$ vs $\log(t)$ plots of (a) PEG(S-1000), (b) PEG(S-2000) and (c) PEG(S-6000).

Table 3.5: X_t , α_0 and $F(T)$ values of PEG(S-1000), PEG(S-2000) and PEG(S-6000) networks together with the regression coefficient R^2 .

X_t	PEG(S-1000)			PEG(S-2000)			PEG(S-6000)		
	α_0	$F(T)$	R^2	α_0	$F(T)$	R^2	α_0	$F(T)$	R^2
0.1	1.5	7.2	0.986	1.3	4.3	0.993	1.3	3.9	0.999
0.2	1.6	10.1	0.996	1.3	5.9	0.994	1.3	5.0	0.997
0.4	1.6	14.5	0.997	1.3	7.9	0.995	1.4	6.6	0.997
0.6	1.6	18.6	0.999	1.3	10.0	0.997	1.4	8.5	0.996
0.8	1.6	23.7	0.997	1.3	12.6	0.994	1.5	11.0	0.997

The $\log(\phi)$ vs $\log(t)$ plots show a linear behavior and from the slope and intercept values α_0 and $F(T)$ parameters are calculated and tabulated in Table 3.5. A good linearity of these plots (as observed from R^2 values) shows the appropriateness of the combined Avrami-Ozawa method for these non-isothermal crystallization measurements. It can be observed in Table 3.5 that values of $F(T)$ decreases as the molar mass between the crosslink increases, i.e. from PEG(S-1000) to PEG(S-6000). Thus, it means that less time was required for PEG(S-6000) network chains to reach any relative degree of crystallinity value X_t as compared to PEG(S-1000) network.¹⁸⁴ For instance, for $X_t = 0.2$ (20 % crystallinity), $F(T)$ value of PEG(S-1000) network was 10.1 while it decreases for PEG(S-2000) to 5.9 and reaches the minimum value of 5.0 for PEG(S-6000). This behavior can be attributed towards the varying degree of cross-linking in PEG networks as the cross-link density is highest in PEG(S-1000) network causing the PEG chains in the network to crystallize relatively slow along with the lower overall degree of crystallinity. As it was mentioned before that the parameter α_0 is the ratio of Avrami n and Ozawa m exponents and for all three PEG networks. This value remains close to unity and almost constant with respect to X_t . This implies that the kinetic model proposed by Liu *et al.*¹⁸⁵ seems to be successful in describing the non-isothermal crystallization kinetics for these PEG networks.

3.1.5 Swelling Measurements

For swelling measurements, PEG networks are vacuum dried overnight before being soaked in deionized water for the next 24 h. To track their swelling progress, samples were weighed after 1h, 2h, 4h, 8h and 24h, respectively.

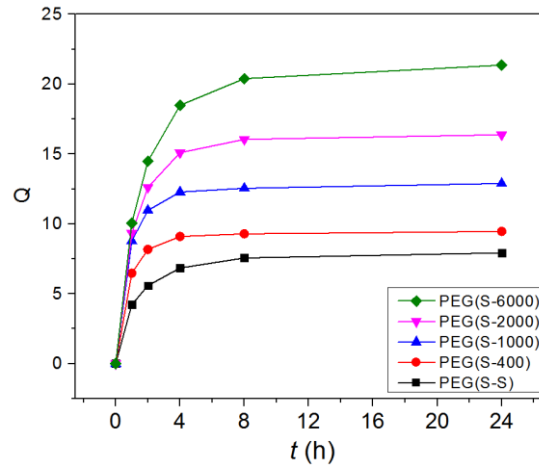


Figure 3.16: Degree of swelling Q of PEG(S-S), PEG(S-400), PEG(S-1000), PEG(S-2000) and PEG(S-6000) in water at 25°C.

The degree of swelling Q is defined as

$$Q = \frac{m_s - m_d}{m_d} \quad (3.15)$$

where, m_s is the mass of swollen network and m_d represents the mass of dry network.

As PEG is a hydrophilic and water soluble polymer it is expected that its networks would behave like a hydrogel and are able to absorb a large amount of water until the equilibrium swelling point is reached (see Figure 3.16). For instance, PEG(S-400) can absorb water about 8 times of its dry mass while for PEG(S-6000) the capacity of holding water within its structure goes up to about 20 times than its initial dry mass.

The swelling phenomenon of polymer networks is often described by the Flory-Rehner theory.¹⁸⁶ Their hypothesis states that thermodynamics of swelling of polymer networks is governed by two independent but opposite contributions. The first contribution comes from the osmotic pressure Π_{mix} which results from the polymer/solvent interaction while

the other contribution comes from the elastic pressure Π_{elas} , caused due to the stretching of polymer chains in between two cross-links. Hence, in the absence of any other contributions (e.g. presence of ionizable functional groups or pH-value variations) the elastic forces balance out the osmotic pressure after a certain degree of swelling and from this maximum allowed swelling values, one can get some basic understandings regarding the internal structure of networks (Eq. 3.16).

$$\Pi_{ext} = \Pi_{mix} + \Pi_{elas} \quad (3.16)$$

where, Π_{ext} represents any external pressure apart from osmotic and elastic forces and it should be zero at equilibrium. The number average molar mass \overline{M}_c between two cross-links can be calculated from a modified version of Flory-Rehner theory, presented by Bray-Merrill^{135,8} for the systems where the gelation process conducted in solution.

$$\frac{1}{\overline{M}_c} = \frac{2}{\overline{M}_n} - \frac{\frac{v_1}{V_1} [\ln(1 - v_2) + v_2 + \chi_{12}v_2^2]}{v_2^{1/3} - \left(\frac{2}{\phi}\right)v_2} \quad (3.17)$$

Here, χ_{12} represents the polymer-solvent interaction parameter which has the value of 0.426 for PEG^{187,188} in water, V_1 is the molar volume of water, v_1 is the specific volume of polymer, and ϕ represents the functionality of the cross-linker (i.e. $\phi = 3$). \overline{M}_n represents the average molar mass of linear chains between the two cross-links and this also includes the two adjacent arms of the cross-linker unit (molar mass of one PEG arm of the cross-linker unit is about 300 g/mol). Thus, for the PEG(S-1000) network \overline{M}_n is (300+1000+300) = 1600 g/mol. \overline{M}_n values of other networks are given in Table 3.6. The equilibrium polymer volume fraction, v_2 , which is the ratio of the dry gel and swollen gel volume, can be calculated as

$$v_2 = \frac{\rho_s}{Q\rho_p + \rho_s} \quad (3.18)$$

where ρ_s represents the density of solvent (water) and ρ_p is the density of the dry gel. For the density of networks, volume of the PEG networks was calculated by immersing a small piece of dry PEG network, of known mass, in a volumetric flask containig hexane.

As hexane and PEG are immiscible, probability of increase in volume of PEG networks due to swelling will be negligible. The increase in the volume of hexane due to the addition of PEG network was calculated and used later for the density calculations of PEG networks (density = mass / volume). Table 3.6 shows the values of \overline{M}_c calculated with Eq. 3.17 and the degree of swelling Q using Eq. 3.15 for PEG(S-400), PEG(S-1000), PEG(S-2000) and PEG(S-6000) networks.

Table 3.6: Precursor length \overline{M}_n , Degree of swelling Q , density ρ_p and molar mass between the cross-links \overline{M}_c of PEG(S-S), PEG(S-400), PEG(S-1000), PEG(S-2000) and PEG(S-6000) networks.

PEG Networks	Precursor length \overline{M}_n g/mol	Density ρ_p g/mL	Degree of swelling Q	Molar mass between the cross-links \overline{M}_c g/mol	$\frac{\overline{M}_c}{\overline{M}_n} \times 100$ %
PEG(S-S)	600	0.7	8	267	≈44
PEG(S-400)	1000	0.73	9	443	≈ 44
PEG(S-1000)	1600	0.76	13	731	≈ 46
PEG(S-2000)	2600	0.79	16	1200	≈46
PEG(S-6000)	6600	0.72	21	2838	≈43

In an ideal end-linked polymer network, the molar mass between the cross-links \overline{M}_c calculated by the swelling experiments should be either equal to the theoretically expected values \overline{M}_n or larger due to the presence of elastically inactive loops (discussed before). However, in our PEG networks, the \overline{M}_c values are almost 45% of the initial precursor \overline{M}_n , indicating a crosslink density much higher than expected for our system. These results are rather unexpected but in agreement with the finding of Truong *et al.*¹⁴⁶ for their PEG networks. They also worked on similar PEG networks except they used a four-arm cross-linker unit instead of three-arm unit, as used in this study. The \overline{M}_c values of their PEG cross-linked networks was also around 50 % of the theoretical value and

they found the reason for this unexpected high cross-linking density by performing cryo-SEM measurements on their networks in the swollen state. They saw macroporous structures, where the pores become wider with the increase in precursor molar mass, as shown in Figure 3.17. They concluded that the main reason for this macroporous structure formation is due to the inherent heterogeneous network structure, formed as a result of phase separation during gelation process.

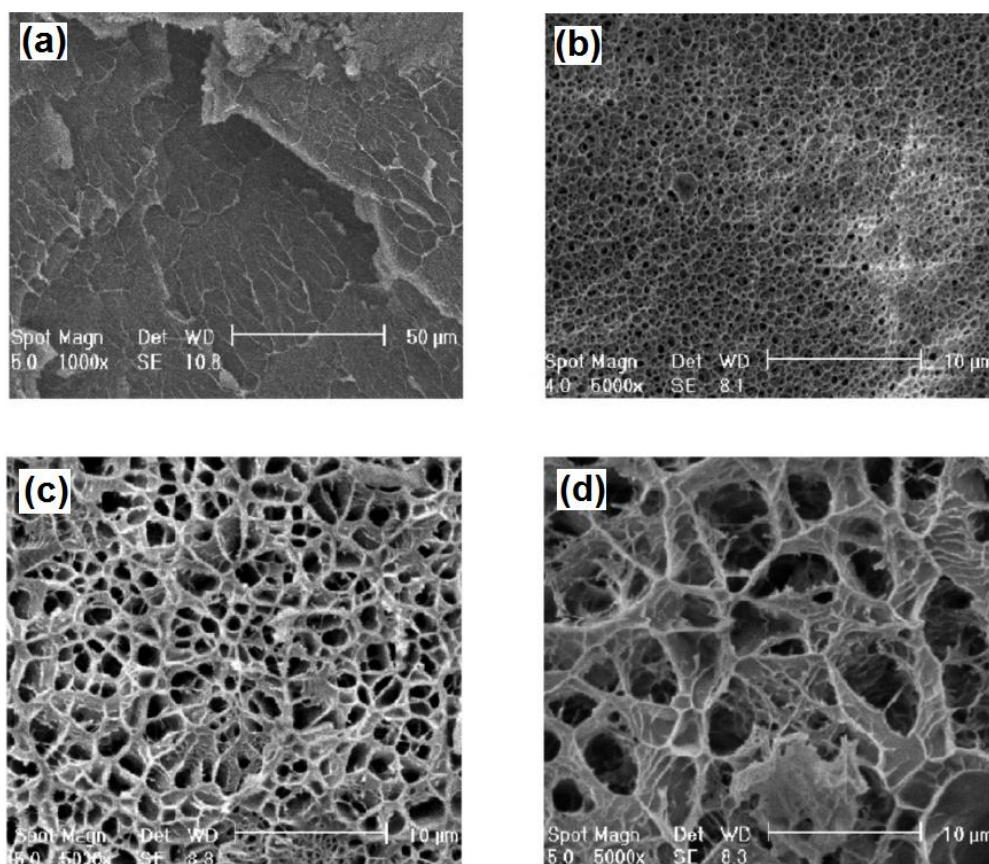


Figure 3.17: Cryo-SEM measurements performed by Truong *et al*¹⁴⁶ to determine the macroporous structure of PEG hydrogels having variable chain lengths i.e. (a) PEG1k, (b) PEG2k, (c) PEG4k and (d) PEG6k, after swelling in phosphate buffered saline (PBS) solution of pH 7.4 for 24 h at 23 °C.

Water is a relatively poor solvent for poly(ethylene glycol) as compared to alcohols and other chlorinated solvents and shows both upper and lower critical solution temperature (UCST and LCST) in water.¹⁸⁹ Moreover, it has been known that a critical concentration of PEG in water exists and after this concentration limit, cluster formation occurs which remain stable and in equilibrium with free polymer chains in water.¹⁹⁰ In our case, as the

network formation begins and the molar mass of PEG precursors start to increase, phase separation also begins. With time, the probability of an individually growing network structure to react with other growing structures decrease, and the chances of intramolecular reactions within the same growing structure increases. This phenomenon introduces an inter-woven organization of chains and entrapped physical cross-links in the network, which ultimately reduce the swelling and degree of freedom of polymer chains. Thus, the introduction of these additional physical cross-links (entrapped entanglements) in the network structure is the primary reason for the observed lower \overline{M}_c values.

3.1.6 Temperature Dependent Wide Angle X-ray Scattering (WAXS)

Temperature dependent WAXS diffraction patterns of PEG(S-1000), PEG(S-2000) and PEG(S-6000) are shown in Figure 3.18. All diffractograms show the characteristic pair of scattering peaks at $2\theta = 19.35^\circ$ and 23.54° which are associated with the (120) and (032)* Miller planes of the PEG monoclinic unit cell. It is comprised of four PEG chains with seven repeating units organized in a 7_2 helical structure.⁴⁸ The diffraction peak at $2\theta = 23.54^\circ$ results not only from the (032) plane but also from the $(\bar{1}32)$, (112), $(\bar{2}12)$, $(\bar{1}24)$, $(\bar{2}04)$, and (004) planes as well.¹⁹¹

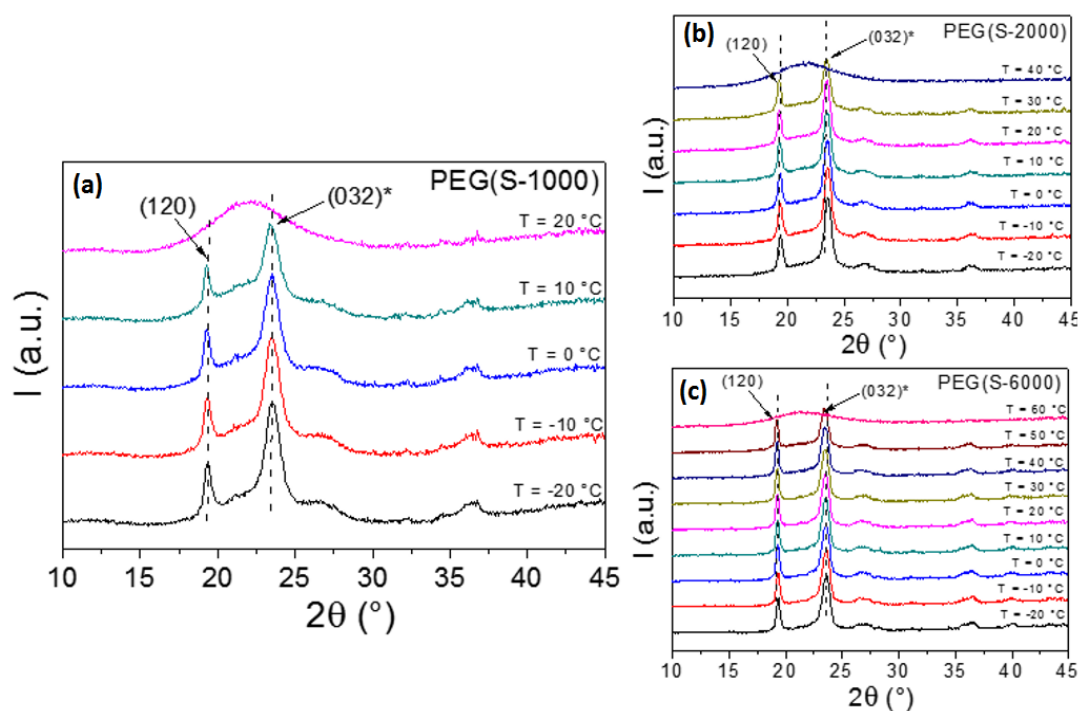


Figure 3.18: Temperature-resolved WAXS diffraction patterns of (a) PEG(S-1000), (b) PEG(S-2000) and (c) PEG(S-6000)

The crystallinity of PEG networks is determined from WAXS diffraction patterns by comparing the area of diffraction peaks (after subtracting the amorphous halo) with the area of the entire diffractogram. X'Pert HighScore software program is used to calculate the amorphous halo from the spectra. Values of the degree of crystallinity from the WAXS diffraction patterns are compared with the DSC method and are presented in Table 3.7.

Table 3.7: Degree of crystallinity values obtained from DSC and WAXS methods.

Sample	X_c (DSC) %	X_c (WAXS) %
PEG(S-1000)	29	26
PEG(S-2000)	35	36
PEG(S-6000)	50	51

The degree of crystallinity values from both DSC and WAXS methods show a good agreement with each other. The degree of crystallinity values increase with increasing chain length between the two cross-links of the respective PEG network. Figure 3.19(a) shows the degree of crystallinity values as a function of temperature for PEG(S-1000), PEG(S-2000), and PEG(S-6000). It can be observed that during heating, the degree of crystallinity of PEG(S-6000) remains almost constant until its final melting, whereas, the crystallinity values of the PEG(S-1000) and PEG(S-2000) networks decrease continuously until their final melting temperatures. This behavior describes that both PEG(S-1000) and PEG(S-2000) networks possess a relatively larger distribution of crystal sizes, where the smaller size crystals melt at comparatively lower temperatures. This results in the continuous decrease of crystallinity during the entire heating process. However, In the case of PEG(S-6000), the crystal size distribution is comparatively narrow, which results in the constant crystallinity values until the final melting.

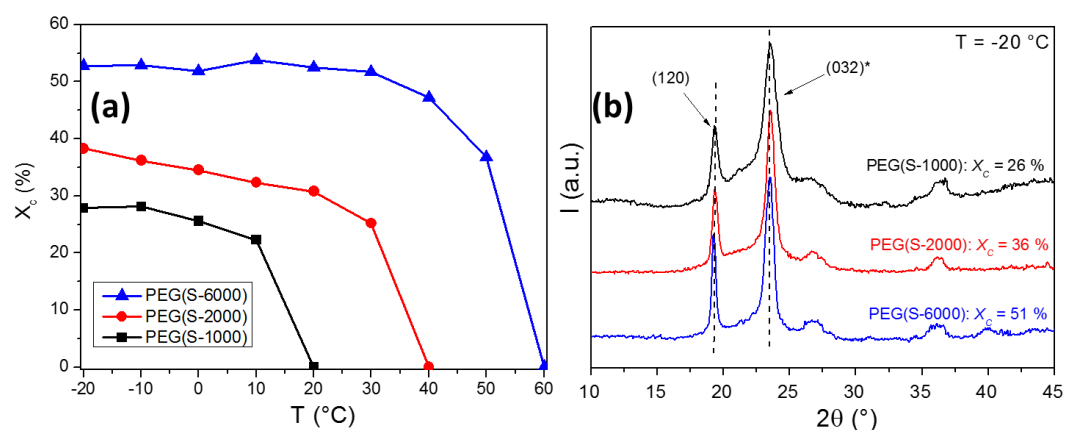


Figure 3.19: (a) Change of the degree of crystallinity of PEG networks with temperature from the WAXS data. (b) WAXS diffraction patterns of PEG(S-1000), PEG(S-2000) and PEG(S-6000) at -20°C .

Figure 3.19(b) shows WAXS diffraction patterns of all three PEG networks recorded at $T = -20^{\circ}\text{C}$ and it can be noticed that the diffraction peaks of PEG(S-1000) are broader as compared to PEG(S-2000), and PEG(S-6000). This broadening of the Bragg reflections in a WAXS spectrum comes usually from both, the instrumental imperfections and the sample's crystal structure itself. An imperfectly monochromatized X-ray beam, variations in the configuration of slits used in the diffractometer or any other misalignment in the

diffractometer are some of the many instrumental factors which cause the broadening of the diffracted beam. A typical way to measure the instrumental broadening contribution is to measure first a near-perfect sample, whose broadening contribution is negligible in comparison. LaB₆, BaF₂ and KCl are some of the suitable materials for this purpose. Furthermore, the variations in the width of Bragg peaks comes also from the crystallite size of the sample as the peaks get broader with the decrease in crystallite size of the sample. In 1918, Scherrer presented an expression¹⁹² (Eq. 3.19, also known as Scherrer equation) to obtain the crystallite size of the sample using the width of the WAXS reflections.

$$L_{(hkl)} = \frac{K_s \lambda}{\beta_{(hkl)} \cos \theta} \quad (3.19)$$

here, $L_{(hkl)}$ is the crystallite size obtained by using any particular reflection (hkl), K_s represents the Scherrer shape factor and its value is usually near unity ($K_s = 0.9$ for PEG),^{193,194} λ is the wavelength of the X-ray, θ is the Bragg diffraction angle, and $\beta_{(hkl)}$ is the measured full-width-half-maximum (FWHM) value. Although, for the determination of the more precise values, it is suggested^{195,196} that several reflections should be used for these calculations. However, in the WAXS spectra of all PEG networks only two prominent reflections are observed i.e. $2\theta = 19.2^\circ$ (120) and $2\theta = 23.5^\circ$ (032)*. Among them, only the (120) reflection can be selected for further calculations as the (032)* reflection is an overlap of various reflections,¹⁹¹ with different Miller indices and it will not be helpful for obtaining any realistic values. Figure 3.20 shows the $L_{(120)}$ values for all PEG networks and their linear PEG precursors at different temperatures.

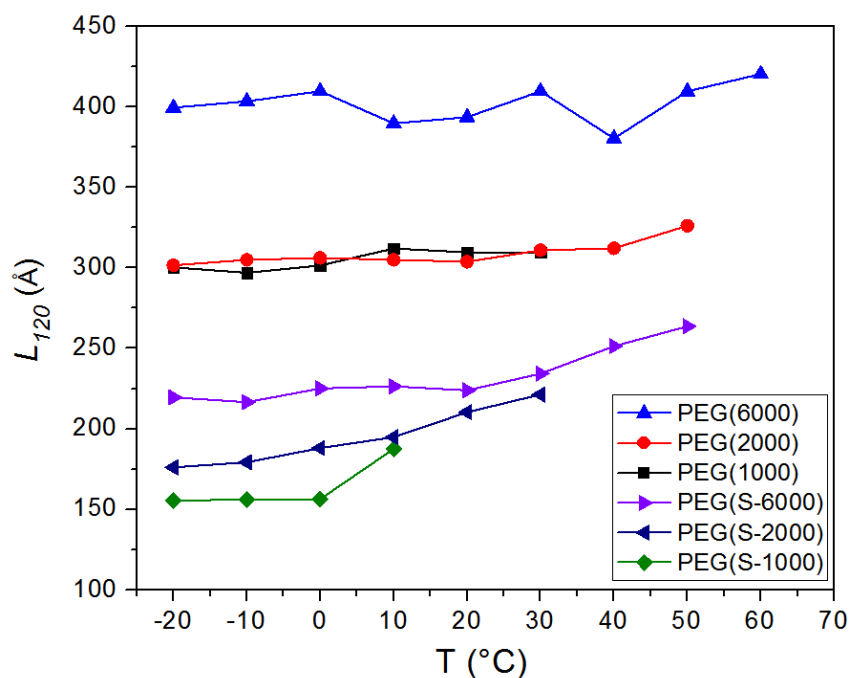


Figure 3.20: Crystallite size $L_{(120)}$ of PEG networks and of linear PEG chains at different temperatures.

It is important to mention here that as the same diffractometer and temperature program is used for all the samples, peak broadening due to the instrumental imperfection is assumed to be constant for all samples. From Figure 3.20, it can be seen that the average crystallite size $L_{(120)}$ for all PEG networks is smaller than the linear PEG chains having comparable lengths. For instance at $T = -20$ °C, $L_{(120)} \approx 150$ Å for PEG(S-1000) whereas for linear PEG(1000) $L_{(120)} \approx 300$ Å. These lower crystallite sizes of PEG networks are mainly due to their cross-linked nature where the cross-links act as a geometrical constraint which hinder the crystallization process of the PEG chains in the network. Furthermore, among the PEG networks the $L_{(120)}$ values of PEG(S-6000) are also larger than the PEG(S-1000) values which can be explained by the fact that the PEG(S-1000) has a higher cross-linking density than the PEG(S-6000), which allows only the smaller crystallites to form in the PEG(S-1000) network. Lastly, with an increase in the measurement temperature, an increase in the $L_{(120)}$ values is also observed for both, PEG networks and linear PEG chains. This is mainly due to the melting of smaller crystallites during heating, which results in an increase in the average value of crystallite sizes in both types of PEG systems.

3.1.7 Temperature Dependent Small Angle X-ray Scattering (SAXS)

In order to study in more detail the nanoscale structural arrangement of PEG chains in the PEG networks, temperature dependent small angle X-ray scattering measurements (SAXS) are performed for PEG(S-1000), PEG(S-2000) and PEG(S-6000) networks (see Figure 3.21). SAXS traces of PEG(S-1000) and PEG(S-2000) show only a first order maximum $1q^*$ at $q = 0.83 \text{ \AA}^{-1}$ and $q = 0.079 \text{ \AA}^{-1}$, respectively, whereas in the case of PEG(S-6000), a small second order peak $2q^*$ at $q = 0.097 \text{ \AA}^{-1}$ is also observed along with the first order peak $1q^*$ at $q = 0.047 \text{ \AA}^{-1}$. Furthermore, the $2q^*$ value of the second order peak was also found to be an integer multiple of first order peak at $1q^*$, which indicate that in PEG(S-6000) stacks of lamella are formed. Another important observation from the SAXS traces is the shift of $1q^*$ towards lower q -values with increasing measurement temperature, for all the three samples.

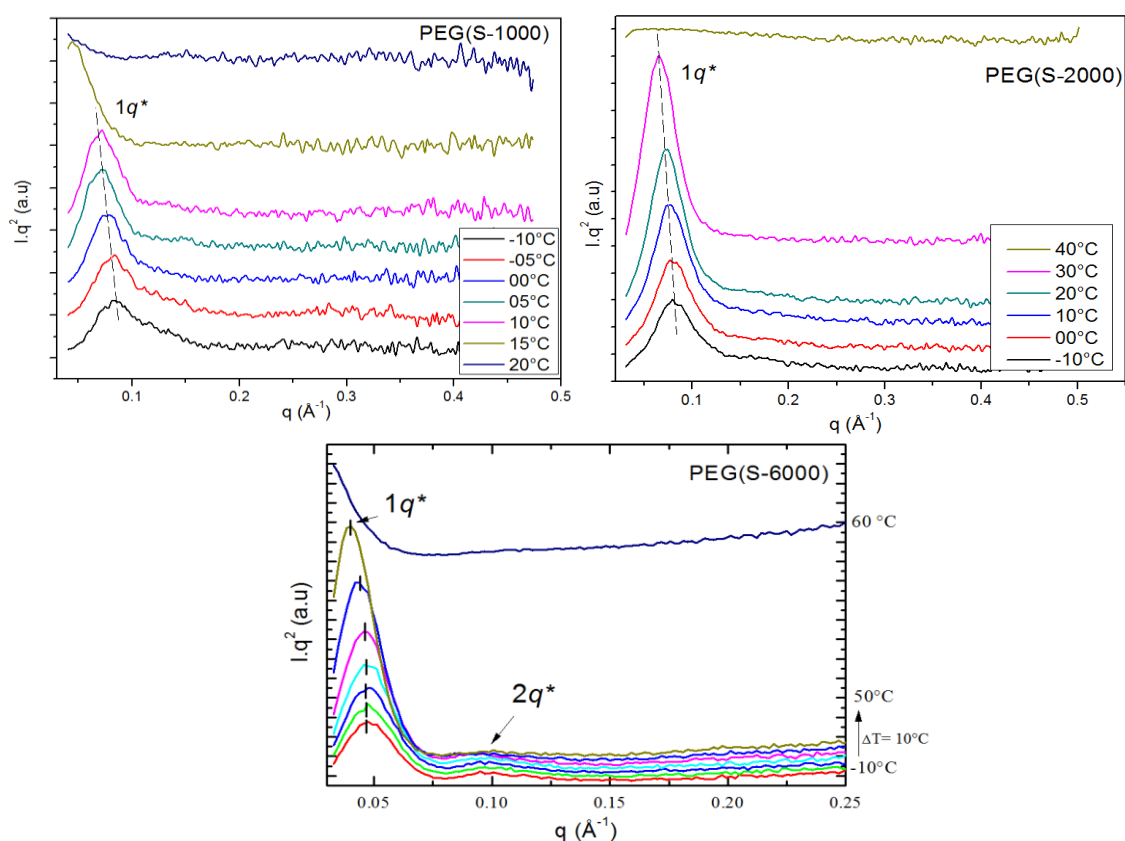


Figure 3.21: Temperature-resolved small angle X-ray scattering measurements (TR-SAXS) of PEG(S-1000), PEG(S-2000), and PEG(S-6000).

From the first order maximum $1q^*$, crystal-crystal distance d can be calculated using Eq. 3.20. Although, in a regularly arranged lamellar system, crystal-crystal distance d can then be further used to calculate the lamella thickness values l_c , however, the absence of higher order peaks indicates that the crystalline arrangement of PEG chains in the network is not a regular lamellar arrangement. Therefore, from these SAXS measurements, one can only find the values of average distances between the crystalline domains in the PEG networks, along with some qualitative assumptions. Values of $1q^*$ and d from the SAXS diffractograms of PEG(S-1000), PEG(S-2000) and PEG(S-6000) networks at different temperatures are presented in Table 3.8.

$$d = \frac{2\pi}{q^*} \quad (3.20)$$

Table.3.8: Values of the first order maximum $1q^*$ and crystal-crystal distance d of PEG(S-1000), PEG(S-2000) and PEG(S-6000) networks.

T °C	$1q^*$ Å ⁻¹	d Å
PEG(S-1000)		
-10	0.083	75.7
0	0.076	82.6
10	0.071	88.4
20	--	--
PEG(S-2000)		
-10	0.079	79.5
0	0.079	79.5
10	0.075	83.7
20	0.072	87.2
30	0.065	96.6
40	--	--
PEG(S-6000)		
-10	0.047	133.6
0	0.047	133.6
10	0.047	133.6
20	0.047	133.6
30	0.046	136.5
40	0.043	146.0
50	0.04	157.0
60	--	--

At $T = -10\text{ }^{\circ}\text{C}$, PEG(S-1000) and PEG(S-2000) have very similar $1q^*$ values i.e. $q = 0.083\text{ }\text{\AA}^{-1}$ and $q = 0.08\text{ }\text{\AA}^{-1}$, which corresponds to the crystal-crystal distance of $d = 75.7\text{ }\text{\AA}$ and $d = 79.5\text{ }\text{\AA}$, respectively. Although, the average crystal-crystal distance d in both networks are similar, however, the difference in the melting temperature and degree of crystallinity values of both networks indicates that the actual lamella thickness values cannot be the same. As the melting temperature T_m of a polymer crystal is a function of its lamella thickness, relatively higher values of T_m for PEG(S-2000) ($T_m = 41\text{ }^{\circ}\text{C}$), as compared to PEG(S-1000) ($T_m = 19\text{ }^{\circ}\text{C}$), indicate that it possesses crystals of a relatively larger lamellar thicknesses. Additionally, higher degree of crystallinity values for PEG(S-2000) ($X_c = 35\%$) compared to PEG(S-1000) ($X_c = 29\%$) indicate that it contains a larger number of crystallites per unit volume which consequently also results in a lower overall crystal-crystal distance d . In the case of PEG(S-6000), all values of d , T_m and X_c are higher from the other two PEG networks. This suggests that it possesses the PEG crystals with the largest lamella thicknesses however they also separated from each other by relatively long distances.

It is also observed from the SAXS diffraction patterns that the first order peak $1q^*$ is shifted to smaller q -values during heating. This observation can be interpreted in two ways i.e. either it is due to increase in crystal-crystal distance d (Eq. 3.20) or increase in the lamella thicknesses during heating. It was observed previously in WAXS measurements that the degree of crystallinity X_c of PEG networks decrease continuously during heating, due to an early melting of relatively smaller sized PEG crystals (see Figure 3.19(a)). The presence of this large distribution of crystal sizes in PEG networks is also evident from the DSC measurements (discussed previously in section 3.1.2.), where the melting endotherms of PEG networks are broader and at lower temperatures when compared to the linear PEG chains of comparative molar masses (*c.f.* Figure 3.5 (b)). Hence, an early melting of smaller PEG crystals during heating, results in the increase in amorphous region l_a which is later translated in SAXS measurements as a shift of $1q^*$ to lower q -values. A schematic representation of an increase in the crystal-crystal distance d during heating is shown in Figure 3.22 (a).

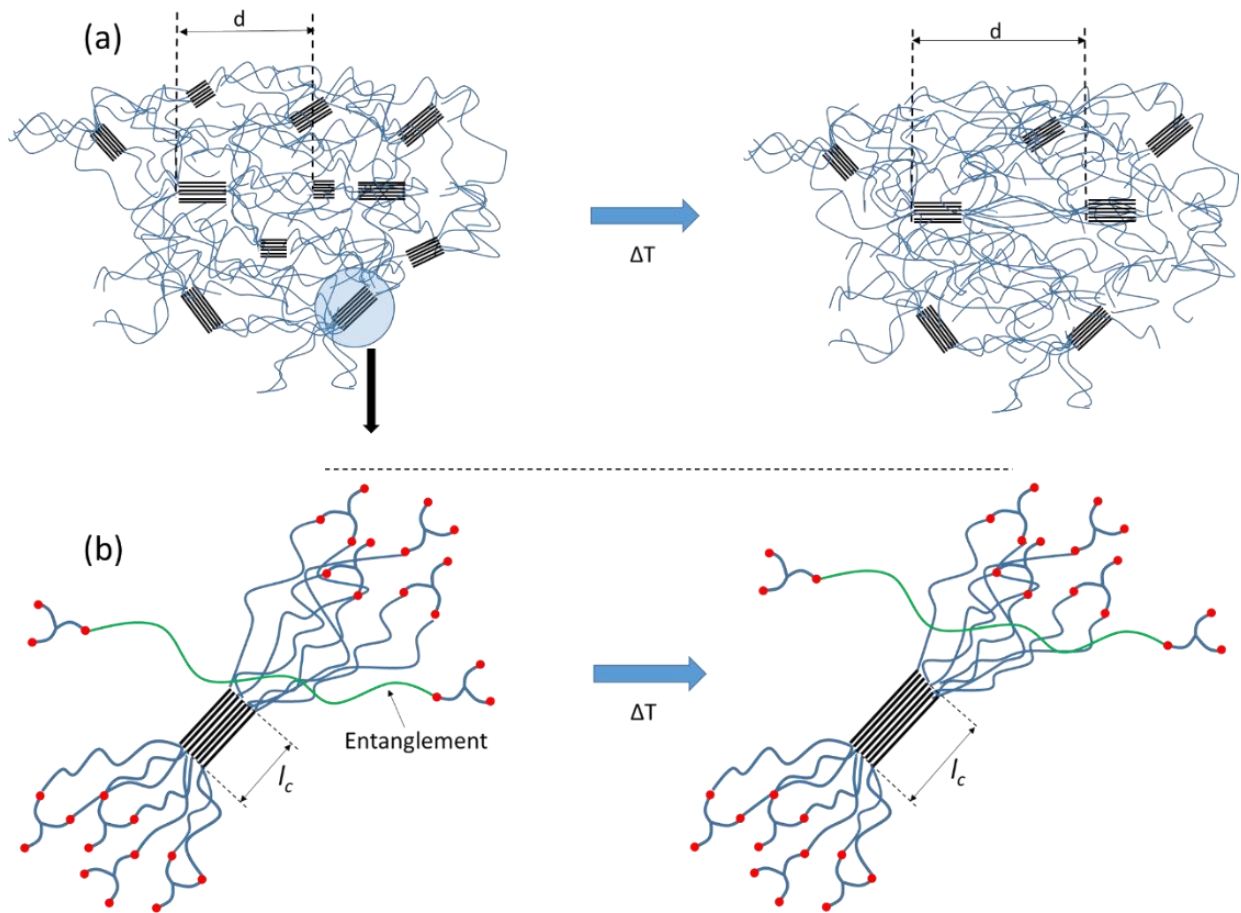


Figure 3.22: Schematic representation of (a) Melting of smaller crystallites during heating process with the increase in crystal-crystal distance d (b) lamella thickening of PEG crystal during heating

On the other hand, the shift of $1q^*$ to lower q -values can also be a result of lamella thickening process of PEG crystals in the network. Entanglements in a network structure are one of the constraints which hinders the crystallization process. However, during heating, they get more mobile allowing the lamella thickening process in PEG crystals to happen. A schematic representation of a lamella thickening process of PEG crystal during heating is shown in Figure 3.22 (b). Hence, from these observations, it can be hypothesized that the shift of $1q^*$ to lower q -values might be due to the simultaneous occurrence of both these affects.

3.2. Crystallization and Structural Studies of Linear Poly(ethylene glycol) Chains with a Well-Defined Point Defect in the Middle of the Polymer Chain

PEG₁₁-TR-PEG₁₁ is successfully synthesized by coupling PEG₁₁-Alkyne and PEG₁₁-Azide using Cu(I) catalyzed azide-alkyne cycloaddition (CuAAC) *click* reaction. The product obtained and purified is a white waxy solid with a melting temperature of $T_m = 22.8$ °C. For a detailed investigation of its crystallization process and a phase transition at higher temperatures, differential scanning calorimetry (DSC) measurements, temperature dependent small angle and wide angle X-ray scattering (SAXS and WAXS) measurements and polarized optical light microscopy (POM) measurements are performed and the results are discussed below.

3.2.1 Crystallization of PEG₁₁-TR-PEG₁₁

In order to study the effect of 1,4-disubstituted 1,2,3-triazole *TR* unit as a point defect in the middle of the PEG chain, PEG₁₁-TR-PEG₁₁ is investigated by the background corrected SAXS measurements as shown in Figure 3.23. After crystallizing PEG₁₁-TR-PEG₁₁ at $T = 0$ °C, a first order peak $1q^*$ at $q = 0.0875 \text{ \AA}^{-1}$ is observed along with its second ($2q^*$) and third ($3q^*$) orders. Using the scattering function (Eq. 2.1; section 2.2.4) and the long period d ($d = 2\pi/1q^* = 71.8 \text{ \AA}$), a lamella thickness value of $l_c = 32.6 \text{ \AA}$ is obtained. As this l_c value is almost half of the long period d , it also supports the observation that the almost missing second-order peak in the SAXS trace (at $T = 0$ °C) suggests a similar length for both amorphous and crystalline regions ($l_a \approx l_c$). Furthermore, this l_c value also agrees with the theoretical length of a PEG chain having 11–12 monomer units in a 7_2 helix.¹⁹⁷ This indicates that at $T = 0$ °C, one of the PEG₁₁ chains of PEG₁₁-TR-PEG₁₁ crystallizes in an extended chain fashion, as it was previously reported for PEGs with molar masses below $M_n \leq 3000 \text{ g/mol}$.^{55,58}

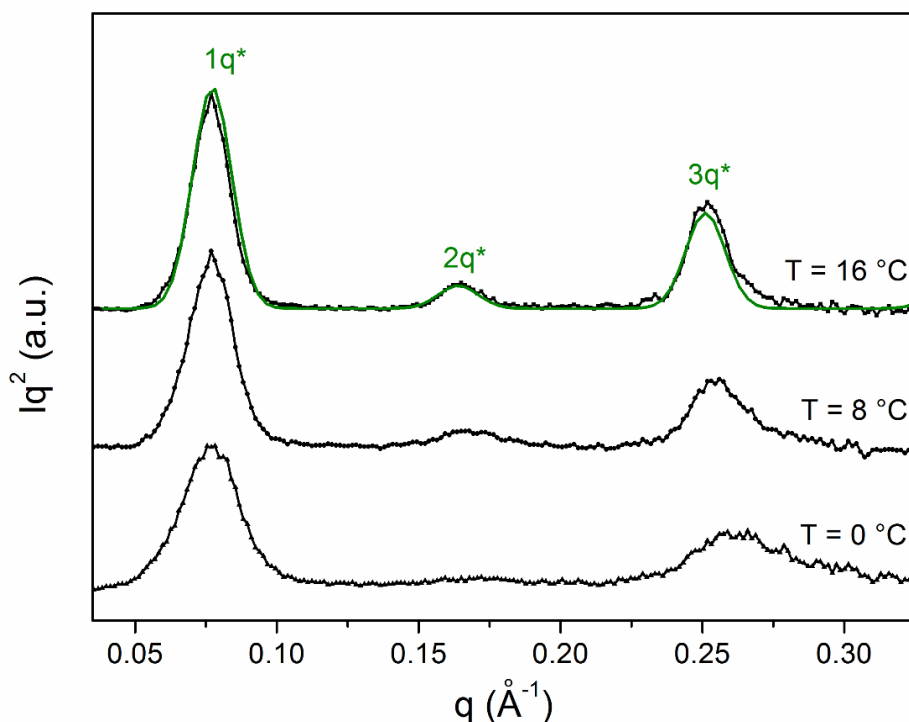


Figure 3.23: Temperature dependent and background corrected SAXS traces of PEG₁₁-TR-PEG₁₁ after crystallization at $T = 0\text{ }^\circ\text{C}$, the green line is the best fit of the data at $T = 16\text{ }^\circ\text{C}$ with the scattering function (Eq. 2.1; section 2.2.4).⁸⁸

During the course of heating, the long period d of PEG₁₁-TR-PEG₁₁ does not change significantly however, an increase in the intensities of peaks at $2q^*$ and $3q^*$ is observed, which indicates a change in the crystallinity of the overall system. By fitting the SAXS trace at $T = 16\text{ }^\circ\text{C}$ with the scattering function (Eq. 2.1; section 2.2.4), an increase in the degree of crystallinity is confirmed due to the thickening of the crystalline layer i.e. $l_c = 40.4\text{ }\text{\AA}$ which is found to be significantly larger than the theoretical length of one arm of PEG₁₁-TR-PEG₁₁ ($l_{c,th} = 30.9\text{ }\text{\AA}$).¹⁹⁷ From this observation, it might be assumed that upon heating, the 1,2,3-triazole unit TR also becomes incorporated into the PEG lamellae. Theoretically, it is possible as the size of a triazole ring ($2.12\text{ }\text{\AA}$;¹⁹⁸ without substituents) is small as compared to the helix-helix distance ($4.6\text{ }\text{\AA}$) in the monoclinic unit cell of PEG. These observations are completely different from the previous studies where the point defects, like the derivatives of phthalic acid, only manage to arrange themselves perpendicular to the lamellar basal surface of a folded PEG chain crystal.¹⁹⁹ Lastly, the SAXS trace of PEG₁₁-TR-PEG₁₁ after the complete melting (at $T = 30\text{ }^\circ\text{C}$) shows no remaining peak which indicates the absence of any phase separation between the

triazole rings and PEG chains. This observation is also in agreement with the fact that the liquid 1,2,3-triazole is a good solvent for PEG and this is additionally verified experimentally using PEG₂₂ and liquid 1,2,3-triazole. The mixture is homogeneous in the melt however, upon cooling shows an eutectic behavior (*cf.* Figure A23, Appendix).

3.2.2 Structural Changes of PEG₁₁-TR-PEG₁₁

Temperature dependent WAXS measurements (Figure 3.24 (a)) are carried out in order to obtain a more detailed understanding of the influence of the 1,2,3-triazole TR unit on the PEG crystallization in the PEG₁₁-TR-PEG₁₁ sample.

After crystallization at $T = -4$ °C, the WAXS diffraction patterns of PEG₁₁-TR-PEG₁₁ (Figure 3.24 (a)) shows the characteristic Bragg reflections of PEG (*cf.* Figure 3.24b), however, it is found that the (120) reflection of PEG₁₁-TR-PEG₁₁ appears at $2\theta = 19.37^\circ$ (at $T = -4$ °C) which is slightly higher than the value for PEG₂₂ at $2\theta = 19.15^\circ$ (at $T = -5$ °C). This indicates that the 7_2 helices in the PEG unit cells of PEG₁₁-TR-PEG₁₁ are slightly closer to each other than in the PEG₂₂ unit cell.⁴⁸ The same shift is also observed for the (032)* reflection at $2\theta = 23.52^\circ$ which is overlapped by the ($\bar{1}$ 32), (112), ($\bar{2}$ 12), ($\bar{1}$ 24), ($\bar{2}$ 04) and (004) reflections.¹⁹¹

The degree of crystallinity X_C at $T = -4$ °C is also calculated ($X_C = 41\%$) by comparing the area of WAXS diffractogram without an amorphous halo to the area including the amorphous halo. The X_C value obtained by WAXS is slightly lower as compared to the X_C value calculated from SAXS previously ($X_C \approx 50\%$) and this might be due to the effect of diffuse and incoherent scattering on the total scattering intensity which was not adjusted in these calculations.^{200,201} It is important to mention here that an attempt to measure the degree of crystallinity from the DSC technique will not give any reliable values as the total melting enthalpy also contains the contributions from the newly formed $C-H \cdots \pi$ interactions²⁰² which cannot be calculated separately.

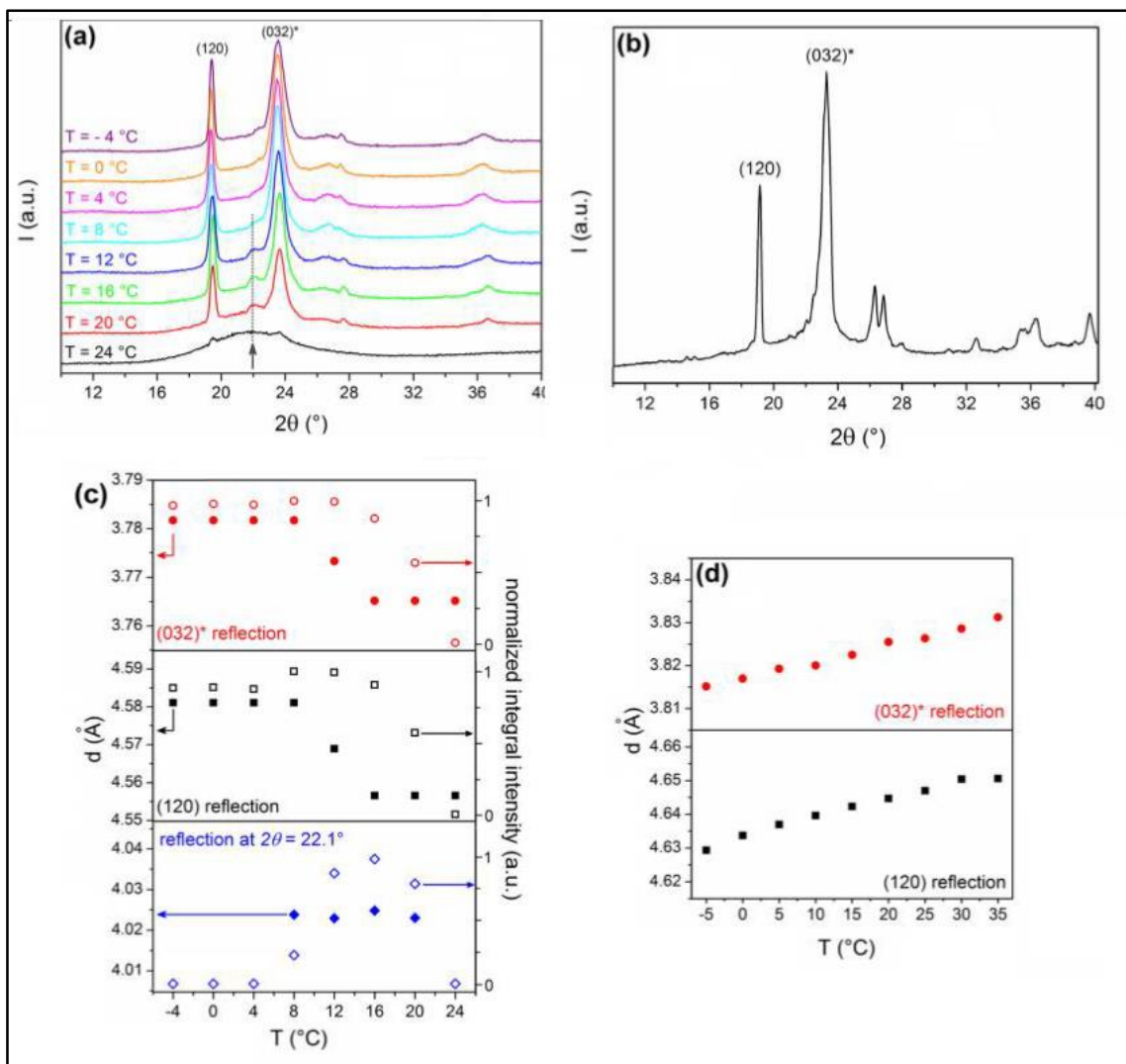


Figure 3.24. (a) Temperature dependent WAXS diffractograms of PEG₁₁-TR-PEG₁₁ from $T = -4\text{ °C}$ to $T = 24\text{ °C}$ in steps of $\Delta T = 4\text{ °C}$. The arrow indicates an appearance of a new reflection during the heating process. (b) WAXS diffractogram of PEG₂₂ at $T = 25\text{ °C}$. (c) Changes in the distances with temperature, calculated from the diffraction angle of the (120) and (032)* reflections as well as the reflection at $2\theta = 22.1^\circ$ (full symbols) and their normalized integral intensities (open symbols) as function of the temperature of PEG₁₁-TR-PEG₁₁. (d) Changes in the distances with temperature, calculated from the diffraction angle of (120) and (032)* reflections of PEG₂₂.⁸⁸

From the WAXS diffraction patterns of PEG₁₁-TR-PEG₁₁ two different changes can be observed during heating. First, both the (120) and (032)* reflections are shifted to higher diffraction angles, indicating a decrease in the distances of the respective Miller planes i.e. $\Delta d \approx 0.5\%$ (cf. Figure 3.24 (c)), during heating. However, no decrease in the distances

of the Miller planes of similar reflections is observed in the WAXS diffraction patterns of PEG₂₂ during heating (see Figure 3.24 (d)). Secondly, above $T \geq 8 \text{ }^\circ\text{C}$, an additional reflection in the WAXS diffraction patterns of PEG₁₁-TR-PEG₁₁ appears at $2\theta = 22.1^\circ$ (marked by an arrow in Figure 3.24 (a)) and its intensity increases until the final melting at $T = 24 \text{ }^\circ\text{C}$ (cf. open symbols in Figure 3.24 (c)). This additional reflection cannot be described either by the 7_2 helix based monoclinic unit cell of PEG or by the planar zigzag modification of PEG in a triclinic unit cell.⁵¹ To investigate these structural changes further, DSC and POM measurements are also performed and shown in Figure 3.25.

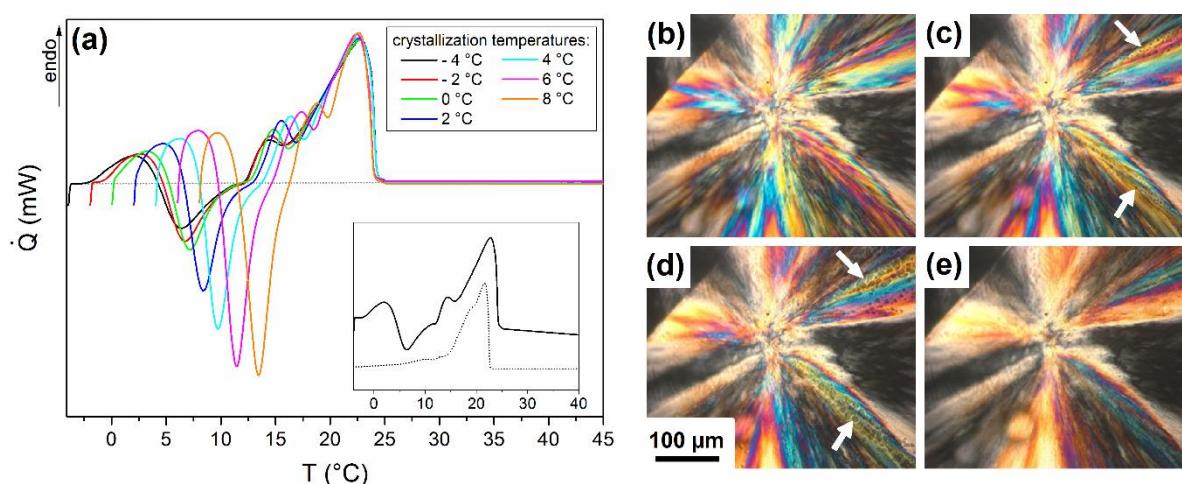


Figure 3.25. (a) DSC heating traces of PEG₁₁-TR-PEG₁₁ after isothermal crystallization at temperatures between $-4 \text{ }^\circ\text{C} \leq T \leq 8 \text{ }^\circ\text{C}$, recorded with a heating rate of $1 \text{ }^\circ\text{C}/\text{min}$. The inset shows the heating traces after crystallization at $T_c = -4 \text{ }^\circ\text{C}$ (full line) and the reheating curve after isothermal annealing at $T = 15 \text{ }^\circ\text{C}$ and cooling to $T = -20 \text{ }^\circ\text{C}$ (dotted line). (b-e) Spherulite morphology of PEG₁₁-TR-PEG₁₁ when crystallizes at (b) $T = -4 \text{ }^\circ\text{C}$ and during reheating at (c) $T = 6 \text{ }^\circ\text{C}$, (d) $T = 12 \text{ }^\circ\text{C}$ and (e) $T = 16 \text{ }^\circ\text{C}$, attained by POM technique. The white arrows in (c) and (d) show the emerging black regions (liquid/amorphous phase).⁸⁸

After isothermally crystallizing PEG₁₁-TR-PEG₁₁ at $T_c = -4 \text{ }^\circ\text{C}$, the DSC heating trace (Figure 3.25 (a)) shows an endothermal peak upon heating at $T = 2 \text{ }^\circ\text{C}$, indicating the incipient melting of the crystalline PEG chains of PEG₁₁-TR-PEG₁₁. It was mentioned before that the lamella thickness at $T = 0 \text{ }^\circ\text{C}$ is equal to the length of one PEG₁₁ arm whereas the TR rings are arranged on the surface of the PEG lamellae. Due of these facts, rearrangement processes become easily possible to stabilize the lamellae by attractive π - π interactions

of the TR rings combined with a larger lamella thickness. Furthermore, the exothermal peak with a minimum at $T = 6.4$ °C is also associated with these structural changes and is in perfect agreement with the WAXS measurements where the shift of the Bragg reflections was observed along with an appearance of a new reflection at $2\theta = 22.1^\circ$ upon heating. This type of DSC trace is typical for structural changes in polymers. For instance in the case of poly(1-butene), a 4_1 helix (orthorhombic crystals system) transforms into a 11_3 helix in a tetragonal unit cell²⁰³ or for paraffins where a chain defolding is observed during heating.²⁰⁴ Although, the latter can be excluded since the PEG₁₁-TR-PEG₁₁ crystallizes in extended chain crystals ECCs. Moreover, additional isothermal crystallization experiments are performed to get a deeper understanding of the structural changes during heating (Figure 3.25 (a)). It is observed that the first endothermal peak during heating does not shift to higher temperatures when the crystallization temperature is varied below $-4 \leq T_c \leq 8$ °C. However, it shifts to higher temperatures for $T_c \geq -4$ °C. In addition to this, the exothermal peak is also shifted with increasing T_c , demonstrating that both processes are interrelated. Therefore, it can be stated that the incipient melting of one PEG₁₁ arm of PEG₁₁-TR-PEG₁₁ is a prerequisite for the observed structural changes. These structural changes are also found to be irreversible in nature, since only the final melting endotherm is observed in the DSC reheating trace when the sample is heated and annealed at temperatures between 13 °C $\leq T \leq 17$ °C and afterward cooled down to $T = -20$ °C prior to measurement (see the inset of Figure 3.25 (a)).

These structural changes are also observable by the polarized optical microscopy (POM). After isothermally crystallizing PEG₁₁-TR-PEG₁₁ at $T_c = -4$ °C, spherulites can be observed (*cf.* Figure 3.25 (b)). Similar to the temperature in the DSC measurements, black areas are observed within the spherulites at $T = 6$ °C (Figure 3.25 (c)) indicating an amorphous/liquid isotropic intermediate phase. The POM images change further during heating when the formerly black areas grow and become colored (Figure 3.25 (d)), indicating the recrystallization after the rearrangement processes. After the complete recrystallization process, the spherulites have the same appearance as prior to the structural changes but with slightly different color (see Figure 3.25 (e)).

Solid-state ^{13}C MAS cross-polarization(CP) and single-pulse (SP) NMR measurements are also performed for PEG₁₁-TR-PEG₁₁ and a structural model is proposed where the reduced PEG helix-helix distances is explained by the attractive $C-H\cdots\pi$ interaction of the triazole rings within the lamella. However, the details of these studies are available elsewhere.⁸⁸

3.3. Solid-State Phase Transitions and Odd-Even Effect in Poly(ethylene glycol) Crystals Induced by Chain Defects of Variable Lengths

In this work, two PEG₁₁ chains are coupled with the homologous series of α,ω -diyne units *via* CuAAC *click* reaction in order to have two 1,4-disubstituted 1,2,3 triazole rings (TR), separated from each other by a different number of methylene units, in the middle of a PEG chain. The final product is abbreviated as PEG₁₁-TR-(CH₂)_{*n*}-TR-PEG₁₁, with $n = 2-8$. Their thermal behavior is investigated by differential scanning calorimetry (DSC) measurements where an interesting odd-even effect is observed in their melting temperatures. Besides, a solid-state phase transition during the crystallization of PEG₁₁-TR-(CH₂)_{*n*}-TR-PEG₁₁ is also observed by temperature dependent wide angle X-ray scattering (WAXS) and solid state ^{13}C MAS cross-polarization (CP) and single-pulse (SP) NMR spectroscopy measurements. Polarized light microscopy (POM) studies are also carried out to further investigate their morphological behavior.

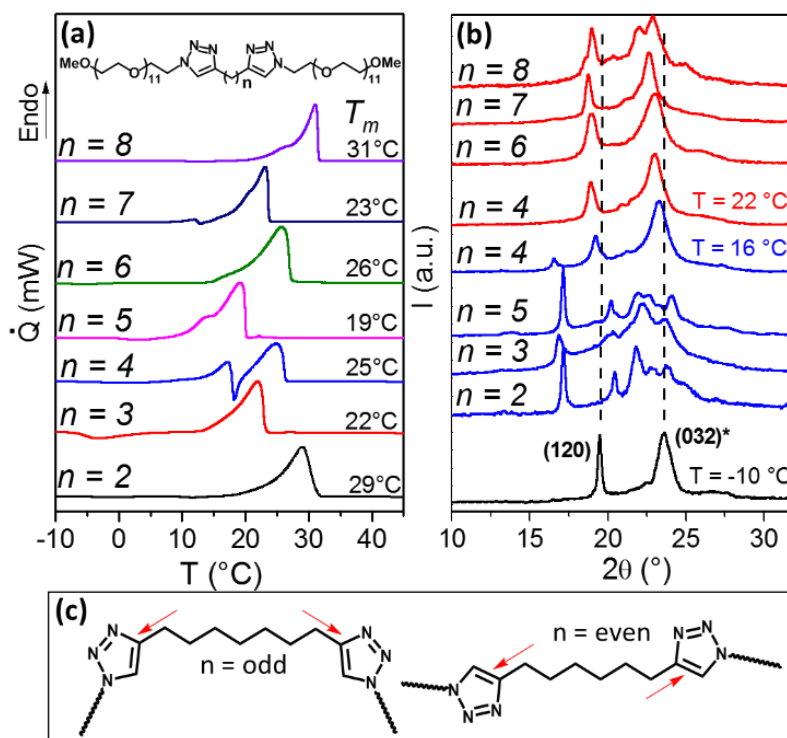


Figure 3.26: (a) DSC heating traces of PEG₁₁-TR-(CH₂)_n-TR-PEG₁₁ in the temperature range of $-10\text{ }^{\circ}\text{C} \leq T \leq 45\text{ }^{\circ}\text{C}$. (b) WAXS diffraction patterns of PEG₁₁-TR-(CH₂)_n-TR-PEG₁₁ ($n = 2-8$) before their final melting. As all diffraction patterns of PEG₁₁-TR-(CH₂)_n-TR-PEG₁₁ are similar after their crystallization from the melt, only the WAXS trace of PEG₁₁-TR-(CH₂)₂-TR-PEG₁₁ at $T = -10\text{ }^{\circ}\text{C}$ is shown. For PEG₁₁-TR-(CH₂)₄-TR-PEG₁₁, two WAXS diffraction patterns are displayed i.e. at $16\text{ }^{\circ}\text{C}$ and $22\text{ }^{\circ}\text{C}$ due to the two different types of phase transitions observed during heating (see text for details) (c) Schematic model of the difference in the vectors of the terminal bonds for odd (left) and even (right) n -alkyl spacers between the TR rings.

Figure 3.26 (a) shows the DSC traces of PEG₁₁-TR-(CH₂)_n-TR-PEG₁₁ samples with $2 \leq n \leq 8$ in the range of $-10\text{ }^{\circ}\text{C} \leq T \leq 45\text{ }^{\circ}\text{C}$, after cooling the samples to $T_C = -40\text{ }^{\circ}\text{C}$ with $1\text{ }^{\circ}\text{C}/\text{min}$. The samples with $n = \text{even}$ display a higher melting temperature relative to its neighbors in the homologous series with $n = \text{odd}$. The melting behavior of the polymer with $n = 4$ is more complicated because of the two melting endotherms separated by an exothermal peak. Additionally, the melting enthalpies also show this alternating behavior (see Appendix, Figure A24). Thus, at first glance, it might look as the n -alkyl moiety of the TR-(CH₂)_n-TR chain defect induces an odd-even effect into the melting temperatures of the

polymeric system under investigation. The vectors of the terminal bonds of the even n -alkanes are generally located parallel with respect to each other while for the respective odd n -alkanes they cross each other,²⁰⁵ as schematically shown for disubstituted TR-(CH₂) _{n} -TR in Figure 3.26(c). This simple geometrical effect causes a reduction of the crystal density due to the packing impairment of the odd n -alkanes and thus, they have a lower melting temperature than the corresponding even n -alkanes.⁹⁹ However, temperature dependent WAXS measurements challenge this simple assumption for the system under investigation. At low temperatures ($T = -10$ °C), the WAXS diffraction pattern for all samples show solely the Bragg reflections of a monoclinic unit cell of neat PEG, as shown in the lower trace of Figure 3.26 (b) where the WAXS diffractogram of PEG₁₁-TR-(CH₂)₂-TR-PEG₁₁ at $T = -10$ °C is shown as an example. However, during heating, all the PEG₁₁-TR-(CH₂) _{n} -TR-PEG₁₁ samples exhibit solid-state phase transitions at higher temperatures before their final melting. These phase transitions can be observed in WAXS diffractogram either by the appearance of a new set of Bragg reflections during heating or by the shifting of existing low-temperature PEG reflections to smaller angles. The respective WAXS traces of PEG₁₁-TR-(CH₂) _{n} -TR-PEG₁₁ ($n = 2-8$) after their phase transition and prior to their final melting are shown in Figure 3.26 (b).

According to the appearance of their solid-state phase transitions in the WAXS traces, PEG₁₁-TR-(CH₂) _{n} -TR-PEG₁₁ samples can be categorized into two main groups, except for $n = 4$. For the samples with $n = 2,3,5$, completely new Bragg reflections appeared during heating, while for $n = 6,7,8$ the Bragg reflections are similar to that of neat PEG but they are shifted to smaller angles. The sample with $n = 4$ seems to be a mixture of both groups, i.e. in the range of the first melting endotherm at $T \approx 17$ °C the pattern is similar to that of the samples with $n = 2,3,5$ and in the range of the second melting endotherm at $T = 22$ °C the trace is similar to that of $n = 6,7,8$. In order to understand the odd-even effect in the melting temperatures of the PEG₁₁-TR-(CH₂) _{n} -TR-PEG₁₁ samples, it is necessary to understand the crystallographic transformations of PEG as a function of temperature which must be influenced by the chain defects. Hence, at first, the phase transition in PEG₁₁-TR-(CH₂) _{n} -TR-PEG₁₁ with $n = 2,3,5$ will be discussed while afterward the phase transition in polymers with $n = 6,7,8$ will be described. At the end, the phase transitions in PEG₁₁-TR-(CH₂)₄-TR-PEG₁₁ will be discussed separately.

3.3.1 Phase Transitions in PEG₁₁-TR-(CH₂)_n-TR-PEG₁₁ with $n = 2, 3, 5$

Temperature dependent WAXS diffraction patterns of PEG₁₁-TR-(CH₂)_n-TR-PEG₁₁ with $n = 2, 3, 5$ are shown in Figure 3.27 (a-c). For all three samples, the WAXS diffraction pattern at $T = -10$ °C clearly reveals the presence of two prominent reflections corresponding to the (120) and (032)* Miller planes (indexed as (032)* means an overlap of (032), ($\bar{1}32$), (112), ($\bar{2}12$), ($\bar{1}24$), ($\bar{2}04$), and (004)) of the monoclinic unit cell with four 7₂ helices known from PEG homopolymer.⁴⁸ However, during heating, a new crystal system evolves for all the three samples with the disappearance of their initial low-temperature PEG reflections. In order to further investigate this type of phase transition, PEG₁₁-TR-(CH₂)₂-TR-PEG₁₁ is selected as a characteristic example from this group.

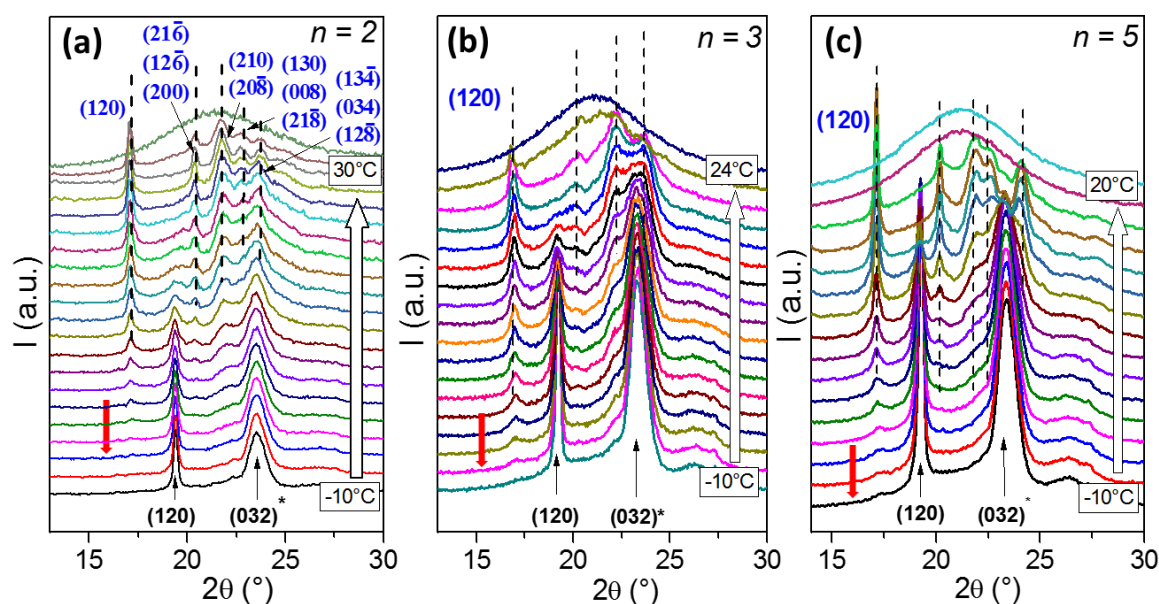


Figure 3.27: Temperature dependent WAXS diffraction patterns of PEG₁₁-TR-(CH₂)_n-TR-PEG₁₁ with (a) $n = 2$ (b) $n = 3$ and (c) $n = 5$, with temperature steps of $\Delta T = 2$ °C. During heating, solid-state phase transition occurs at a particular temperature for individual samples (indicated by red arrow) resulting in an entirely new crystal system.

The WAXS diffraction pattern of PEG₁₁-TR-(CH₂)₂-TR-PEG₁₁ at $T = -10$ °C clearly reveals the presence of two prominent reflections at $2\theta = 19.4^\circ$ and $2\theta = 23.5^\circ$, corresponding to the (120) and (032)* reflections. The calculated degree of crystallinity from the WAXS traces at $T = -10$ °C is $X_c \approx 44$ % (see Table A1 in the Appendix). Thus, one may assume

that at $T = -10\text{ }^{\circ}\text{C}$, one PEG₁₁ chain belongs to the crystal structure while the other PEG₁₁ chain of the polymer remains in the amorphous state. During heating, the Bragg reflections of the monoclinic unit cell of PEG gradually disappear and new reflections of a different crystal system at $2\theta = 17.1^{\circ}$, 20.4° , 21.7° , 22.7° , and 23.8° are observed (marked by black dashed vertical lines) until the final melting of PEG₁₁-TR-(CH₂)₂-TR-PEG₁₁ at $T_m \approx 29\text{ }^{\circ}\text{C}$. Since PEG homopolymers do not show this kind of phase transition during heating, it will be reasonable to assume that only the chain defect is responsible for the change of the WAXS diffraction pattern of PEG₁₁-TR-(CH₂)₂-TR-PEG₁₁ as a function of temperature.

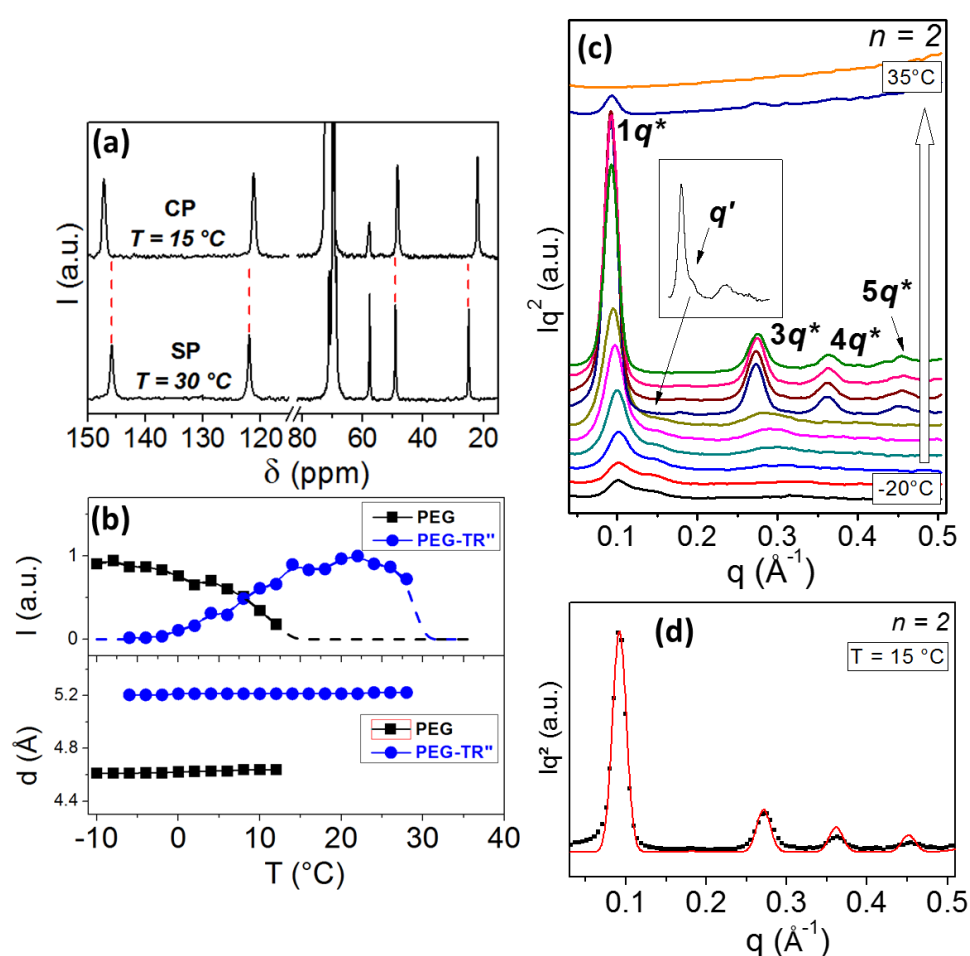


Figure 3.28. (a) Comparison of CP ($T = 15\text{ }^{\circ}\text{C}$) and SP ($T = 30\text{ }^{\circ}\text{C}$) ^{13}C MAS NMR spectrum of PEG₁₁-TR-(CH₂)₂-TR-PEG₁₁. The red dotted lines indicate the observed shift of the signals. (b) Normalized integral intensities (top) of the reflections at $2\theta = 17.1^{\circ}$ (PEG-TR'' phase) and $2\theta = 19.4^{\circ}$ (PEG phase) and their respective lattice spacing (bottom) as

function of the temperature. (c) Temperature dependent background corrected SAXS traces during heating $-20\text{ }^{\circ}\text{C} \leq T \leq 35\text{ }^{\circ}\text{C}$ with temperature steps of $\Delta T = 5\text{ }^{\circ}\text{C}$. The insets show the appearance of a shoulder at $q' = 0.152\text{ \AA}^{-1}$ which disappears later after the completion of the phase transition. (d) SAXS trace of $\text{PEG}_{11}\text{-TR-(CH}_2\text{)}_2\text{-TR-PEG}_{11}$ at $T = 15\text{ }^{\circ}\text{C}$; the red line represents the fitting of SAXS trace with the one-dimensional scattering function (Eq. 2.1).

Solid state ^{13}C magic angle spinning (MAS) cross-polarized (CP) and single-pulse (SP) NMR experiments are carried out to characterize the solid-state phase transition in more detail (Figure 3.28 (a)). The ^{13}C MAS CP NMR spectrum, which detects relatively less mobile nuclei in the system of $\text{PEG}_{11}\text{-TR-(CH}_2\text{)}_2\text{-TR-PEG}_{11}$ shows two sharp resonances at $\delta = 70.4\text{ ppm}$ and $\delta = 56.9\text{ ppm}$ indicating that PEG_{11} chains with their endgroups at $T = 15\text{ }^{\circ}\text{C}$ belong to the crystal system. Additionally, two sharp signals at $\delta = 120\text{ ppm}$ and $\delta = 146\text{ ppm}$ corresponding to the resonances of the TR rings and the signals from CH_2 groups of the spacer unit at $\delta = 21\text{ ppm}$ also appear in ^{13}C MAS CP NMR spectrum. Hence, it can be assumed that the complete $\text{TR-(CH}_2\text{)}_2\text{-TR}$ group probably be located in the crystalline phase, termed as $\text{PEG-TR}''$. Furthermore, by comparing the chemical shifts of the ^{13}C MAS SP NMR signals of molten $\text{PEG}_{11}\text{-TR-(CH}_2\text{)}_2\text{-TR-PEG}_{11}$ ($T = 30\text{ }^{\circ}\text{C}$) and the ^{13}C MAS CP NMR signals at $T = 15\text{ }^{\circ}\text{C}$, a shift of the resonances of the TR rings and the CH_2 groups between them is observed. This indicates the π - π interactions between the TR rings in the crystal of the $\text{PEG-TR}''$ phase. Such behavior is also discussed for thiophene rings in poly(3-hexylthiophene) by Russell and coworkers.²⁰⁶ The assumption of incorporation of the complete $\text{TR-(CH}_2\text{)}_2\text{-TR}$ defect upon heating is also supported when observing the temperature dependent intensity of the (120) reflection of the monoclinic PEG crystal and the reflection at $2\theta = 17.1^{\circ}$ of the $\text{PEG-TR}''$ crystal (Figure 3.28 (b)). The intensity of the (120) reflection of the PEG phase (black) starts to decrease at $T \approx -8\text{ }^{\circ}\text{C}$ indicating the incipient melting of the PEG phase whereas, at slightly higher temperatures, the intensities of the Bragg reflections of the $\text{PEG-TR}''$ modification (blue) start to increase $T \approx -6\text{ }^{\circ}\text{C}$.

SAXS measurements as shown in Figure 3.28 (c) also indicate the incorporation of the $\text{TR-(CH}_2\text{)}_2\text{-TR}$ defect into the crystal of $\text{PEG}_{11}\text{-TR-(CH}_2\text{)}_2\text{-TR-PEG}_{11}$ upon heating. After

crystallization at $T = -20\text{ }^{\circ}\text{C}$, the first order peak appears at $1q^* = 0.101\text{ }\text{\AA}^{-1}$ corresponding to a long period $d = 62.2\text{ }\text{\AA}$. Due to the absence of higher order peaks at nq^* , no proper lamellar ordering is established, rather a small peak at $q' = 0.152\text{ }\text{\AA}^{-1}$ ($d' = 41.3\text{ }\text{\AA}$) indicates a more complicated structure. During heating of the sample, the formation of the new crystallographic structure also induces significant changes in the SAXS trace ($10\text{ }^{\circ}\text{C} \leq T \leq 30\text{ }^{\circ}\text{C}$). First, the first order peak ($1q^*$) is shifted to the smaller q -values indicating an increase of the long period during the phase transition ($d = 69.6\text{ }\text{\AA}$; $T = 15\text{ }^{\circ}\text{C}$), along with the vanishing of q' peak. Secondly, several higher order scattering maxima appear up to the fifth order at $5q^*$. This confirms that a lamellar structure for the high-temperature modification is formed. As a simple rectangular two-phase model is not sufficient to describe the data, a slightly modified electron density profile was assumed (see Appendix, Figure A26). A layer of crystalline material (high electron density) is covered by an amorphous region (lower electron density) with additional slightly decreasing density towards its center (Figure 3.29). With this model, the thickness of the crystalline layer was determined by fitting the SAXS trace at $T = 15\text{ }^{\circ}\text{C}$ with the one-dimensional scattering function (Eq. 2.1), i.e. $l_c = 30.7\text{ }\text{\AA}$ (see Figure 3.28 (d)). This corresponds to the 44% volume fraction or approximately 46% crystallinity, which is similar to the value 48% obtained by WAXS (at $T = 16\text{ }^{\circ}\text{C}$). Along with the results obtained by ^{13}C MAS CP and SP NMR spectroscopy, it can be concluded that the TR-(CH₂)₂-TR unit is embedded in the PEG crystal after the phase transition. It should be noted that a quite similar effect was also observed in PEG₁₁-TR-PEG₁₁ (discussed in previous sections) where a highly oriented sample was obtained due to π - π interactions.⁸⁸ The SAXS trace of the molten PEG₁₁-TR-(CH₂)₂-TR-PEG₁₁ shows no remaining correlation peak indicating the miscibility of PEG and TR-(CH₂)₂-TR which is also reported for PEG and 4,4-bis(1,2,3-triazole).²⁰⁷ Furthermore, as the WAXS diffraction patterns of the PEG phase and the PEG-TR'' phase of PEG₁₁-TR-(CH₂)₂-TR-PEG₁₁ are completely different (*cf.* Figure 3.27 (a)), a change of the 7_2 helical conformations upon heating cannot be excluded *per se*. However, the ATR-FTIR spectra of the PEG-TR'' phase show the characteristic bands of the 7_2 helix conformation.²⁰⁸ (*cf.* Appendix, Figure A28).

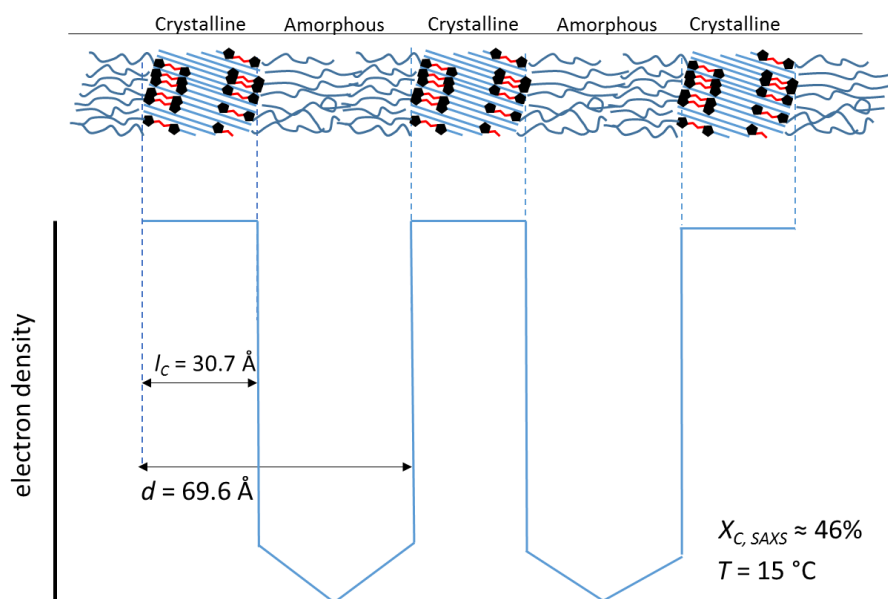


Figure 3.29: Schematic representation of a two-phase model of PEG₁₁-TR-(CH₂)₂-TR-PEG₁₁ with amorphous PEG regions and crystalline PEG regions. The lengths are estimated from the simulation (see Appendix, Figure A26).

Moreover, a structural model is proposed based on the 2D WAXS diffraction pattern of an oriented PEG₁₁-TR-(CH₂)₂-TR-PEG₁₁ sample as shown in Figure 3.30 (a). To get qualitative information, the azimuthal angle profiles are extracted from this pattern and shown in the Appendix, Figure A30 (c). The SAXS reflections center on the meridian of the pattern (*cf.* Figure 3.30 (a)) which indicates that the *c*-direction of the lamellae aligns nearly parallel to the meridian. The PEG-TR'' phase has also a monoclinic symmetry since every reflection appears four times with similar intensity on a reflection ring (except for those in shear direction (*hk0*) which are observed twice). Thus, the space group *P2₁/a* of PEG is also not changed during the phase transition upon heating, since a chiral sorting of right and left handed PEG helices during the incorporation of the TR-(CH₂)₂-TR group into the crystal is highly unlikely. Comparing both, the angle of the reflections with respect to the meridian and their intensities, the typical PEG reflections (see the assignment in Appendix, Figure A30(a)) appear too in the PEG-TR'' phase. Such strongly deformed PEG lattice is in agreement with FT-IR and NMR spectroscopy results, as discussed above. However, there are also some additional reflections (especially on the equator (*hk0*)) which do not belong to the PEG crystal system. The additional electron density in the PEG-TR'' phase is then the result of the crystallized TR-(CH₂)₂-TR group.

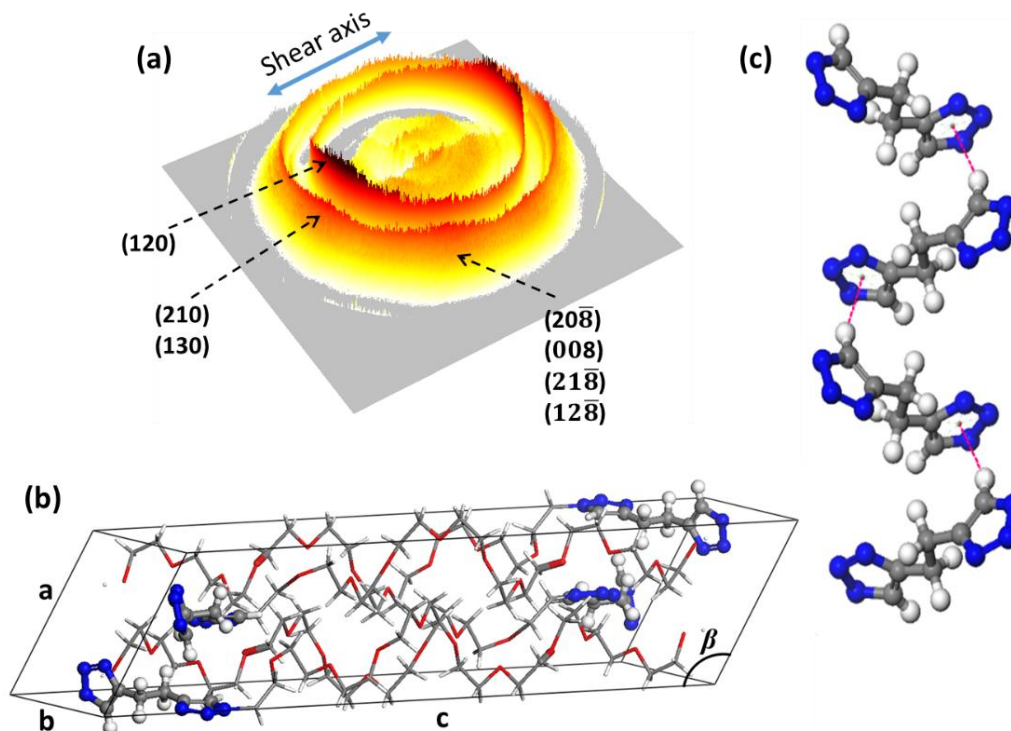


Figure 3.30. (a) The 2D WAXS diffraction pattern of the PEG-TR'' phase in the oriented PEG₁₁-TR-(CH₂)₂-TR-PEG₁₁ sample at $T = 20\text{ }^{\circ}\text{C}$. The Miller indices are included for the observed reflections (for details see Appendix, Figure A30 (a)) (b) Structure model of the PEG-TR'' phase of PEG₁₁-TR-(CH₂)₂-TR-PEG₁₁. (c) $C-H\cdots\pi$ interactions between the TR-(CH₂)₂-TR groups (magenta dotted lines).

Using these reflections, we can assign a unit cell for the PEG-TR'' phase. The lattice parameter c is calculated according to the method described by de Rosa and Auriemma²⁰⁹ and it is in good agreement with the approximated value of the lamella thickness from SAXS data (see discussion of Figure 3.28 (c)). The other unit cell parameters are refined using BIOVIA Materials Studio Reflex software. The parameters obtained are $a = 10.11\text{ \AA}$, $b = 13.02\text{ \AA}$, $c = 36.34\text{ \AA}$, and $\beta = 119.8^{\circ}$. The additional reflections at $2\theta = 21.7^{\circ}$ and $2\theta = 22.8^{\circ}$ belong to the (210) and (130) Miller planes, respectively. These reflections appear in a similar diffraction angle range as compared to the observed reflection in PEG₁₁-TR-PEG₁₁, which is caused by intermolecular $C-H\cdots\pi$ interactions of the TR rings. Thus, this can also be assumed for PEG₁₁-TR-(CH₂)₂-TR-PEG₁₁ since such interactions of the aromatic TR rings are also confirmed by ¹³C MAS CP NMR spectroscopy (see discussion above). The Bragg reflection at $2\theta \approx 20.4^{\circ}$ is assigned to the

(200) Miller plane (at the equator) as well as from the $(21\bar{6})$ or $(12\bar{6})$ Miller planes (at approximately 55° with respect to the equator). Thus, the position of the TR-(CH₂)₂-TR group is refined to the intensities of these reflections using the same software. Figure 3.30 (b) shows the received structure. As assumed above, the (210) and (200) reflections result from the intermolecular distances of the TR-(CH₂)₂-TR groups. In contrast, the (130), $(21\bar{6})$, and $(12\bar{6})$ reflections are caused by intramolecular distances of the TR-(CH₂)₂-TR group, as shown in Figure A31 in the Appendix. However, intermolecular *C-H*... π interactions, one of the three known subtypes of π - π interactions,^{202,210} are also observed for the PEG-TR'' phase of PEG₁₁-TR-(CH₂)₂-TR-PEG₁₁ as shown in Figure 3.30 (c) which explains the strong deformation of the initial PEG lattice. These attractive interactions are the driving force for the observed phase transition as there are many difficulties to overcome during recrystallization. The monoclinic angle of $\beta = 125.4^\circ$ in the initial PEG lattice needs to be reduced so that the TR rings can interact optimally. This causes the large deformation of the PEG lattice and it is obviously a slow process as discussed above.

3.3.2 Phase Transitions in PEG₁₁-TR-(CH₂)_{*n*}-TR-PEG₁₁ with *n* = 6,7,8

Temperature dependent WAXS diffraction patterns of PEG₁₁-TR-(CH₂)_{*n*}-TR-PEG₁₁ with *n* = 6,7,8 are presented in Figure 3.31 (a-c). In order to visualize the phase transition properly, zoomed sections ($18^\circ \leq 2\theta \leq 20^\circ$) of WAXS diffraction patterns of *n* = 7, 8, showing only the (120) reflections across a phase transition are shown in Figure 3.31 (b-c) (for complete WAXS diffraction patterns see Appendix, Figure A32). The WAXS diffraction pattern at *T* = -10 °C of all three samples, clearly reveals the presence of two prominent reflections corresponding to the (120) and (032)* of the monoclinic unit cell with four 7₂ helices known from PEG homopolymer.⁴⁸ However, during heating, a shift of both (120) and (032)* reflections to smaller diffraction angles is observed for all three samples. In order to further investigate this type of phase transition, PEG₁₁-TR-(CH₂)₆-TR-PEG₁₁ is selected as a characteristic example of this group for any additional characterization.

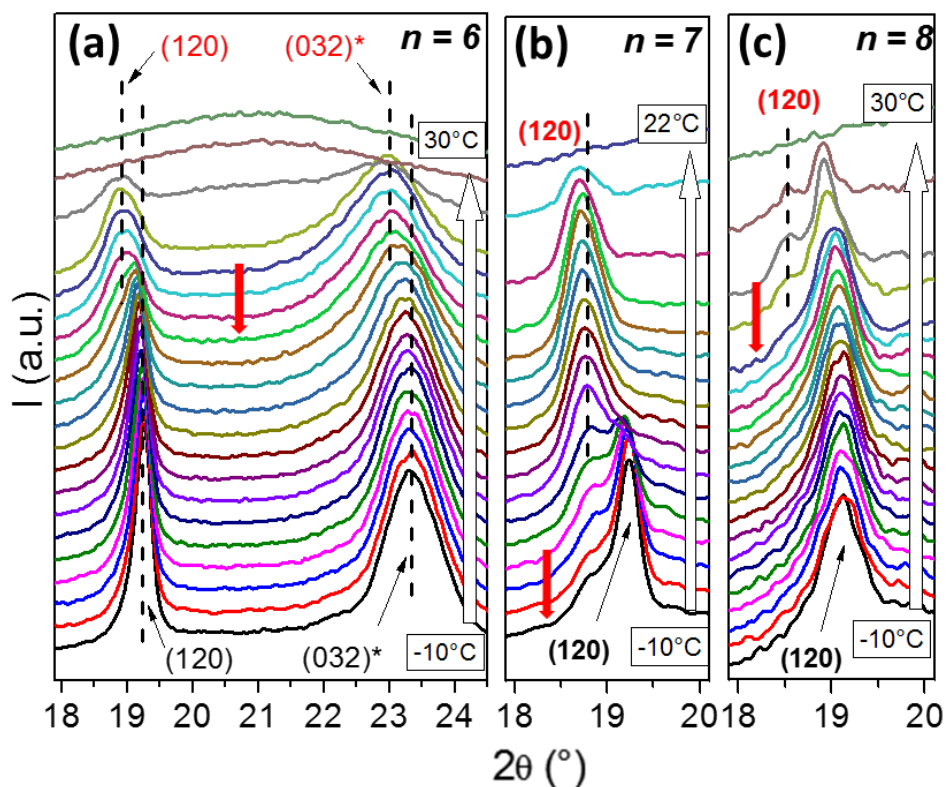


Figure 3.31: Temperature dependent WAXS diffraction patterns of PEG₁₁-TR-(CH₂)_{*n*}-TR-PEG₁₁ with (a) $n = 6$. Zoomed sections of WAXS diffraction patterns (showing only the (120) reflection of both phases) for (b) $n = 7$ and (c) $n = 8$, with temperature step of $\Delta T = 2^\circ\text{C}$. The red arrow indicates the WAXS diffraction pattern where the phase transition is first observed.

The WAXS spectrum of PEG₁₁-TR-(CH₂)₆-TR-PEG₁₁ at $T = -10^\circ\text{C}$ (Figure 3.31 (a)) shows the (120) and (032)* reflections of the PEG phase at $2\theta = 19.2^\circ$ and $2\theta = 23.3^\circ$, respectively. This is identical to the WAXS image of PEG₁₁-TR-(CH₂)₂-TR-PEG₁₁ at $T = -10^\circ\text{C}$. However, during heating a phase transition is noticed at around $T \approx 16^\circ\text{C}$ (indicated by the red arrow in Figure 3.31 (a)) where the new Bragg reflections of PEG₁₁-TR-(CH₂)₆-TR-PEG₁₁ appear at $2\theta = 18.9^\circ$ and $2\theta = 22.9^\circ$. This is slightly different to the PEG structure at lower temperatures and therefore, the calculated distances are also slightly different (see Figure 3.32 (a)). This might indicate that instead of the complete TR-(CH₂)₆-TR group, on TR ring and few adjacent CH₂ groups of TR-(CH₂)₆-TR unit might be incorporated into the crystal during this phase transition. This phase transition is much more comparable to the structural changes of PEG₁₁-TR-PEG₁₁, where one TR ring and

some adjacent CH₂ groups were incorporated into the crystal and also a small deformation of the distances of the (120) reflection was detected.⁸⁸ Such process is much more probable for the phase transition in PEG₁₁-TR-(CH₂)₆-TR-PEG₁₁, as a smaller crystal defect will deform the lattice less than a larger one. This will also be concluded by solid-state ¹³C MAS SP and CP NMR spectroscopy and SAXS measurements; discussed in the sections below. Thus, later in the discussion, we will name this phase formed by the PEG phase upon heating as *PEG-TR'* phase. A further characteristic observed for this phase transition is the coexistence temperature range of the PEG and PEG-TR' phase. It can also be observed in Figure 3.32 (a) that both phases only coexist over a relatively small temperature range ($\Delta T_{coex} \approx 4$ °C). This observation also supports the proposed model for *PEG-TR'* phase, since the incorporation of the one TR ring is less hindered as compared to a whole group containing two TR rings, as it was observed for the phase transition in PEG₁₁-TR-(CH₂)₂-TR-PEG₁₁.

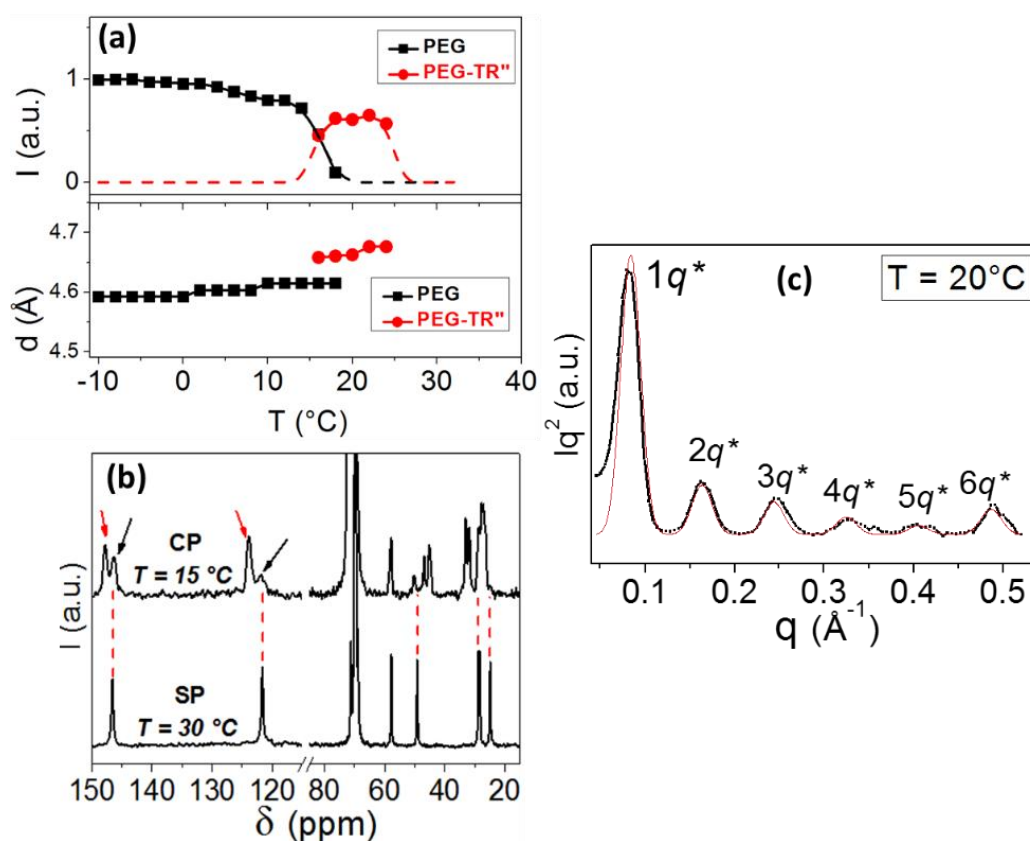


Figure 3.32. (a) Combined plot of the normalized integrated intensity of the (120) reflections for the PEG and PEG-TR' phases (top) and the distance calculated from the diffraction angle of the (120) reflections as the function of the temperature of PEG₁₁-TR-

(CH₂)₆-TR-PEG₁₁ (bottom). (b) ¹³C MAS CP NMR spectrum at $T = 15$ °C and ¹³C MAS SP spectrum at $T = 30$ °C of PEG₁₁-TR-(CH₂)₆-TR-PEG₁₁. Black and red arrows represent the corresponding PEG and PEG-TR' phases, respectively (see text for details) (c) Background corrected SAXS trace of PEG₁₁-TR-(CH₂)₆-TR-PEG₁₁ at $T = 20$ °C.

To get a deeper understanding of the PEG-TR' phase of PEG₁₁-TR-(CH₂)₆-TR-PEG₁₁, it is also investigated by ¹³C MAS SP and CP NMR spectroscopy and a comparison of the CP spectrum at $T = 15$ °C (PEG-TR' phase) and the corresponding SP spectrum at $T = 30$ °C (molten sample) is shown in Figure 3.32 (b). In analogy to the PEG-TR'' phase of PEG₁₁-TR-(CH₂)₂-TR-PEG₁₁, the CP spectrum of the PEG-TR' phase of PEG₁₁-TR-(CH₂)₆-TR-PEG₁₁ shows also pairs of resonances for the TR rings at $\delta = 121.6 - 123.6$ ppm and $\delta = 146 - 147.4$ ppm. However, each pair consists of a sharp signal (marked by a red arrow) and a relatively broad signal (marked by a black arrow). The appearance of these pair of signals for both TR rings at different chemical shifts indicates that both TR rings are in a different chemical environment. This observation supports the proposed model for the PEG-TR' phase of PEG₁₁-TR-(CH₂)₆-TR-PEG₁₁ where it is supposed that only one TR ring is incorporated into the crystal and the other one remains in the amorphous, but in a relatively ordered state, during the phase transition. This is also qualitatively supported by the comparison of the chemical shifts in the SP and the CP spectra. The broad peaks in the CP spectrum have the same chemical shifts as the corresponding SP signals confirming that these TR rings are in the same chemical environment i.e. in the amorphous(molten) state. In contrast, the sharp signals of the TR rings in the CP spectra have different chemical shifts, i.e. they are in a different chemical environment after incorporation into the crystal. Thus one can assume that they are stabilized by π - π interactions as reported by Russell *et al.* for poly(3-hexylthiophene).²⁰⁶ It should be noted that the line shape of signals in the CP spectrum of PEG₁₁-TR-(CH₂)₆-TR-PEG₁₁ also resembles that of PEG₁₁-TR-PEG₁₁ in the temperature range where the TR ring is incorporated into the crystal (during the incorporation process where some TR rings are amorphous and the other are in the crystalline part of the system⁸⁸) which also supports the above-mentioned hypothesis. In general, ¹³C MAS CP NMR spectroscopy is not a quantitative method, i.e. there is no accurate information on the ratio of the integral areas of the two (sharp and broad) resonances. Furthermore, the resonances of the six

CH₂ groups between the two TR rings show also a relatively complex line shape with sharp resonances and also broad components (20 ppm < δ < 35 ppm) indicating that only a certain amount of CH₂ groups are additionally incorporated into the crystal during the observed phase transition. This observation is also analogous to the structural changes observed previously in PEG₁₁-TR-PEG₁₁ where the TR ring and some adjacent CH₂ groups are incorporated into its crystal structure.⁸⁸

Additionally, SAXS measurements of PEG₁₁-TR-(CH₂)₆-TR-PEG₁₁ are carried out and the corresponding SAXS trace of the PEG-TR' phase at $T = 20$ °C is shown in Figure 3.32 (c). The first order maximum appears at $1q^* = 0.081\text{\AA}^{-1}$ and the corresponding long period is $d = 77.5$ Å. This value is slightly larger as compared to PEG₁₁-TR-(CH₂)₂-TR-PEG₁₁ which is not surprising since the number of the CH₂ groups between the TR rings is increased and thus, also the total length of the molecule. The higher order maxima are also observed in the SAXS trace of PEG₁₁-TR-(CH₂)₆-TR-PEG₁₁ at integer multiples of $1q^*$ confirming the lamellar structure of this PEG-TR' phase. The observation of up to the sixth order maximum at $6q^*$ (despite low crystallinity) also indicates perfectly arranged PEG chains in the lamella, which supports the postulated π - π interactions between the TR rings by means of ¹³C MAS CP NMR spectroscopy (see discussion above). The fitting with a lamellar electron density profile (see Appendix, Figure A27) lead to a crystalline volume fraction of 33% (i.e. $\approx 35\%$ crystallinity, similar to 33% obtained from WAXS at $T = 20$ °C: *c.f.* Table A1 Appendix), which is covered by an additional thin layer with intermediate electron density followed by the amorphous region (Figure 3.33). The intermediate layer is necessary to fit the SAXS profile and is assumed to contain some non-embedded TR groups. Temperature dependent SAXS traces of PEG₁₁-TR-(CH₂)_{*n*}-TR-PEG₁₁ with $n = 2$ -8 are shown in the Appendix, Figure A29.

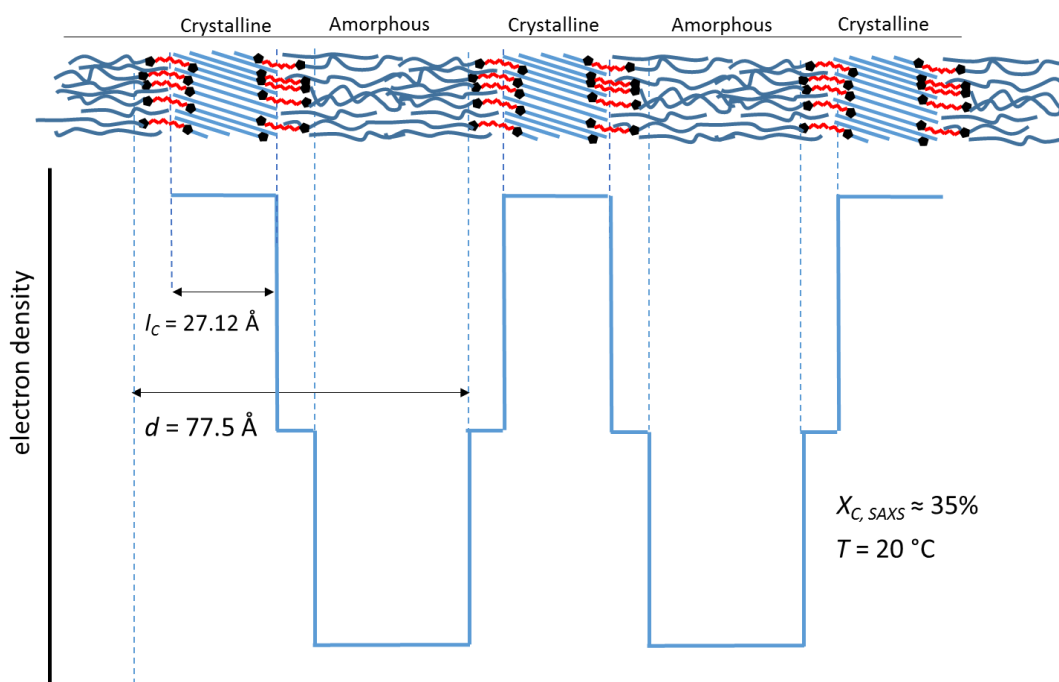


Figure 3.33: Schematic representation of a three-phase model of PEG₁₁-TR-(CH₂)₆-TR-PEG₁₁ with amorphous PEG region (low electron density), amorphous spacer region (intermediate electron density) and crystalline PEG + spacer region (high electron density). The lengths are estimated from the simulation (see Appendix; Figure A27).

3.3.3 Phase Transitions in PEG₁₁-TR-(CH₂)₄-TR-PEG₁₁

Figure 3.34(a) depicts the temperature dependent WAXS diffraction patterns of PEG₁₁-TR-(CH₂)₄-TR-PEG₁₁. In agreement with the other PEG₁₁-TR-(CH₂)_{*n*}-TR-PEG₁₁, the known PEG modification is observed in the WAXS diffractogram after crystallization at $T = -10$ °C. During heating, two phase transitions are observed. The first transition occurs at $T = 0$ °C where PEG₁₁-TR-(CH₂)₄-TR-PEG₁₁ begins to convert into the PEG-TR'' modification (*cf.* Figure 3.34 (b)) as known for the other PEG₁₁-TR-(CH₂)_{*n*}-TR-PEG₁₁ with $n \leq 5$. This is confirmed by both, the position of the appearing Bragg reflections (see Figure 3.34 (a) and (b)) and the ¹³C MAS CP NMR spectra (*cf.* Figure 3.34 (c) and (d)). However, this transition is not complete. At $T = 16$ °C, the integral intensity of the (120) reflection of the low-temperature PEG modification is not further decreasing with increasing temperature and simultaneously, the intensity of the reflection at $2\theta = 16.7^\circ$

of the PEG-TR'' phase is approaches a constant value. This is also in agreement with the ^{13}C MAS CP NMR data since the broad signal of the amorphous TR rings ($\delta = 121$ ppm and $\delta = 147$ ppm, marked by black arrows) also remains together with sharp resonances.

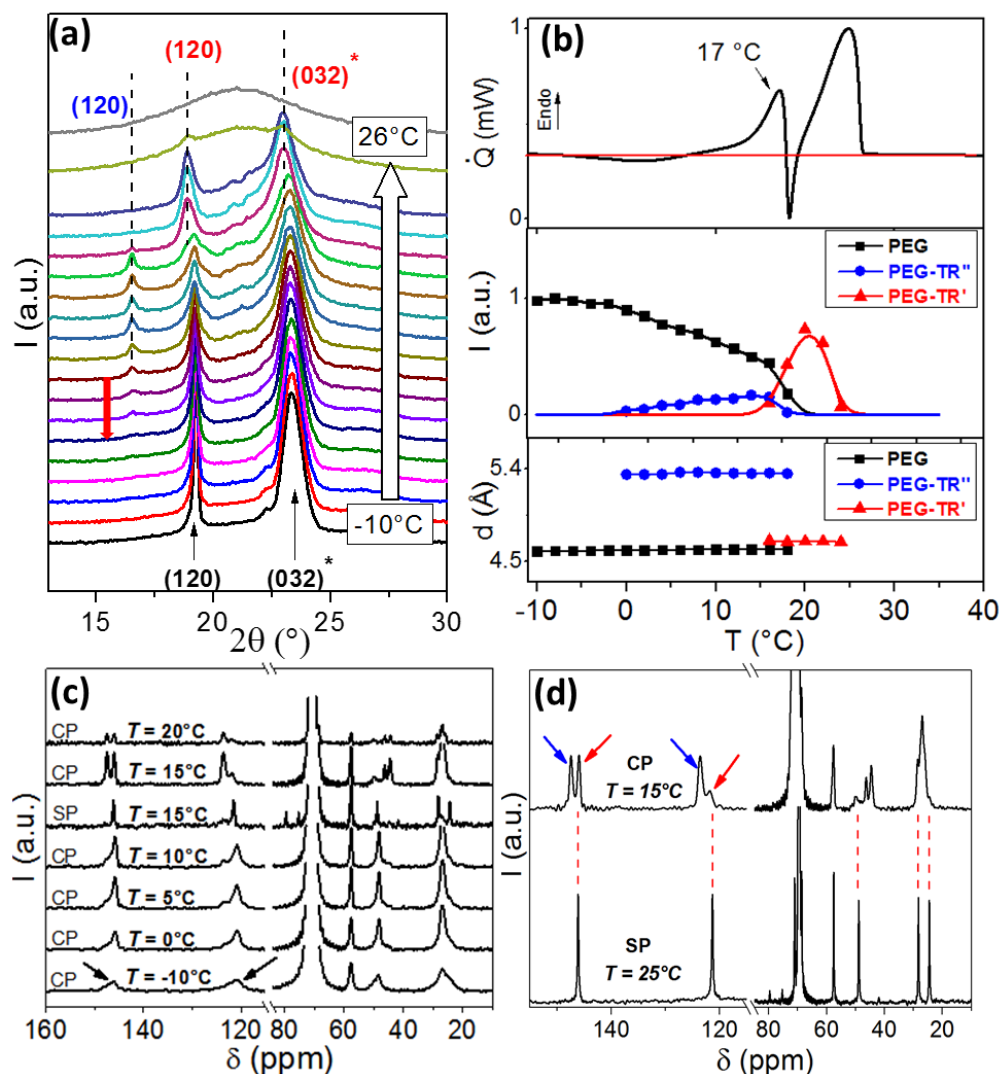


Figure 3.34. (a) Temperature dependent WAXS diffractograms of PEG₁₁-TR-(CH₂)₄-TR-PEG₁₁ during heating $-10\text{ }^{\circ}\text{C} \leq T \leq 26\text{ }^{\circ}\text{C}$ with the temperature steps of $\Delta T = 2\text{ }^{\circ}\text{C}$. Red arrow indicates the spectrum where the PEG-TR'' transition is start to observe (b) Combined plot of the DSC trace(top), normalized integrated intensity of the (120) reflections of the PEG and PEG-TR' phases (middle) and the distance calculated from the diffraction angle of the (120) reflections as the function of temperature of PEG₁₁-TR-(CH₂)₄-TR-PEG₁₁ (bottom). (c) Temperature dependent ^{13}C MAS CP NMR spectrum in the temperature range of $-10\text{ }^{\circ}\text{C} \leq T \leq 20\text{ }^{\circ}\text{C}$ in steps of $\Delta T = 5\text{ }^{\circ}\text{C}$. Additionally, the ^{13}C MAS

SP NMR spectrum at $T = 15\text{ }^{\circ}\text{C}$ is shown among the CP spectra. (d) Comparison of the ^{13}C MAS SP spectrum with the ^{13}C MAS CP NMR spectrum at $T = 15\text{ }^{\circ}\text{C}$ (top) and $T = 25\text{ }^{\circ}\text{C}$ (bottom), respectively. Blue and red arrows represent the corresponding PEG-TR'' and PEG-TR' phases, respectively (see text for details). The dotted lines highlight the observed shift of the NMR signals.

The reason for this observed phenomenon might be found in the PEG-TR'' phase of PEG₁₁-TR-(CH₂)₄-TR-PEG₁₁, since the distance of the Miller plane of the reflection at $2\theta = 16.7^{\circ}$ is significantly larger as compared to the other PEG₁₁-TR-(CH₂)_{*n*}-TR-PEG₁₁ with $n \leq 5$ (*cf.* Figures 3.34 (b) and 3.28 (b) as well as Figures A33 (a-b) in the Appendix). This means, that the largest deformation of the initial PEG lattice is measured for PEG₁₁-TR-(CH₂)₄-TR-PEG₁₁, indicating large problems during packing of the TR-(CH₂)₄-TR group. Thus, this might be an explanation for the incomplete first phase transition. The second phase transition is observed at $T \approx 18\text{ }^{\circ}\text{C}$. The Bragg reflections of both, the remained PEG modification and the formed PEG-TR'' phase disappear and new reflections of the PEG-TR' phase gradually appear in the diffractogram (see Figure 3.34 (a)). This is in good agreement with the DSC trace, where an endotherm at $T \approx 17\text{ }^{\circ}\text{C}$ followed by an exothermal peak is noticed (*cf.* Figure 3.34 (b)). Also, the ^{13}C MAS CP NMR spectrum at $T = 15\text{ }^{\circ}\text{C}$ (see Figure 3.34 (d)) shows the characteristic resonances of the PEG-TR' modification as observed for PEG₁₁-TR-(CH₂)₆-TR-PEG₁₁ (except the signals of the two missing CH₂ groups, obviously). It should be noted that not all of the PEG₁₁-TR-(CH₂)₄-TR-PEG₁₁ molecules are converted into the PEG-TR' phase since the ^{13}C MAS SP NMR spectrum of the PEG-TR' phase (*cf.* dotted curve in Figure 3.34 (c)) shows also the signals of some molten molecules. This is a clear indication that only one of the two observed coexisting modifications (PEG or PEG-TR'') is undergoing the second transition at $T \approx 17\text{ }^{\circ}\text{C}$. Thus, the question arises if the incomplete first phase transition is the reason for the observation of a second phase transition in PEG₁₁-TR-(CH₂)₄-TR-PEG₁₁, which is discussed below.

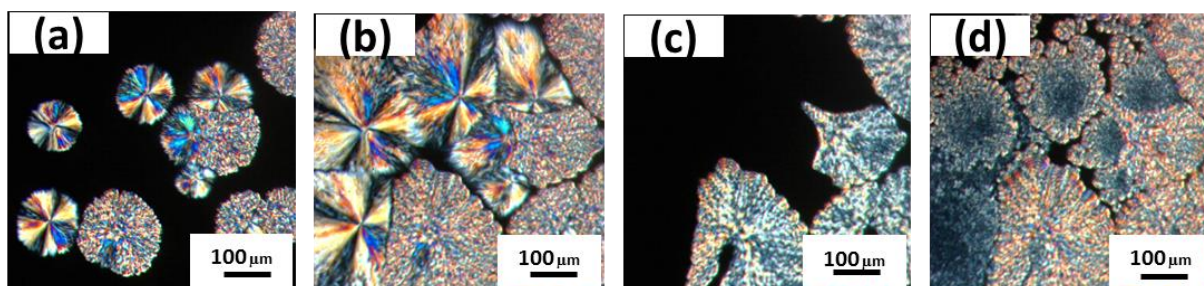


Figure 3.35. Polarized optical microscopy (POM) images of PEG₁₁-TR-(CH₂)₄-TR-PEG₁₁ during (a) isothermal crystallization at $T = 5\text{ }^{\circ}\text{C}$. (b) Spherulitic morphologies after complete crystallization. (c) Melting of one type of spherulites at $T = 18\text{ }^{\circ}\text{C}$ and (d) small crystallites are formed upon re-cooling to $T = 5\text{ }^{\circ}\text{C}$.

In order to characterize the phase transition in more detail, additional polarized optical microscopy (POM) studies of PEG₁₁-TR-(CH₂)₄-TR-PEG₁₁ were carried out (POM images of the other samples at $T_c = 5\text{ }^{\circ}\text{C}$ are shown in Appendix; Figure A34). After crystallization at $T_c = 5\text{ }^{\circ}\text{C}$ (the coexistence temperature of the PEG and PEG-TR'' phases, *cf.* Figure 3.34 (b)), the growth of two types of spherulites (see Figure 3.35 (a)) having a completely different morphology is observed. During heating, the melting of one spherulite type is observed and dark areas could be seen in the POM image at $T \approx 18\text{ }^{\circ}\text{C}$ as shown in Figure 3.35 (c) which is in perfect agreement with the melting temperature of the PEG-TR'' phase. Spherulites of the other type remain at this temperature. However, after cooling back the sample to $T = 5\text{ }^{\circ}\text{C}$, the dark areas become again colorful (see Figure 3.35 (d)) indicating the crystallization of PEG₁₁-TR-(CH₂)₄-TR-PEG₁₁ in the PEG-TR' modification which is also in agreement with the additional WAXS measurements performed to study the irreversibility of these phase transition (for details see the Appendix, Figure A35 and A36). Hence, these quite simple experiments demonstrate that only a solid-state phase transition from the low-temperature PEG modification is possible into the PEG-TR' or PEG-TR'' phases but not from the PEG-TR'' into the PEG-TR' modification. Furthermore, one of the important characteristics of the solid-state phase transition is an amorphous interphase during the transition process which is in the order of magnitude of about 10^{-6} to $10^{-11}\%$ for the low molar mass molecules^{211,212} and up to a few percent for polymers.^{88,203,204} The assumption of solid-state transition from the PEG-TR'' into the PEG-TR' phase (during re-cooling to $T = 5\text{ }^{\circ}\text{C}$, *cf.* Figure 3.35 (d)) needed the complete

melting of the whole PEG-TR'' modification (100 %) before PEG₁₁-TR-(CH₂)₄-TR-PEG₁₁ can recrystallize into the PEG-TR' modification, which cannot be assigned to a solid-state phase transition but it is more in agreement with the definition of a cold crystallization.²¹³ Moreover, the assumption of the transition from PEG-TR'' to PEG-TR' phase is also not a thermodynamically favorable process as the removal of one TR ring from the crystal will also reduce the stability of the crystals by decreasing the π - π interactions. Hence, it is suggested that the melting of the PEG-TR'' modification is the trigger for the transition of the remaining low-temperature PEG modification into the PEG-TR' phase.

3.3.4 The Odd-Even Effect

As it was mentioned before that the DSC traces of PEG₁₁-TR-(CH₂)_{*n*}-TR-PEG₁₁ samples with *n* = 2-8 (Figure 3.26 (a)) show an odd-even effect in their final melting temperature. The samples with *n* = even display a higher melting temperature and melting enthalpy as compared to its neighbors with *n* = odd. However, this odd-even effect cannot be simply assumed due to the crystallization of the TR-(CH₂)_{*n*}-TR chain defect because (i) the defect provides only 14.7 to 22.0 vol. % of the samples based on the van der Waals radii²¹⁴ which makes it unlikely that the new crystal structure for the samples with *n* = 2,3,5 is formed without contributions of the PEG₁₁ chains, (ii) the enthalpies of melting (see Appendix, Figure A24) are also too large in order to originate from the spacer alone without PEG₁₁ contributions, and (iii) the diffraction patterns for the samples with *n* = 6,7,8 are very similar to that of neat PEG. Additional WAXS and solid state NMR spectroscopy measurements revealed solid-state phase transitions in all samples under investigation prior to the final melting, as summarized Figure 3.36. The designation of the phases was done in agreement with both, WAXS and ¹³C MAS CP NMR spectroscopy, where the black bars represent the PEG phase while the blue and red bars represent the PEG-TR'' and PEG-TR' phases, respectively.

Apart from the odd-even effect in the final melting temperatures of PEG₁₁-TR-(CH₂)_{*n*}-TR-PEG₁₁ (black dashed line in Figure 3.36), the temperature where the incorporation of the

spacer in PEG crystal begins also follows an odd-even pattern (blue dashed line in Figure 3.36). The polymers having spacers with an odd number of CH₂ units incorporate at lower temperatures as compared to their neighboring analogs. The odd-samples have the lowest incorporation temperatures since they get easily mobile upon heating whereas the even samples need more energy for this process, resulting in a relatively higher incorporation temperature. Likewise, the melting temperature of the initial low-temperature PEG phase (black bars) also shows a zig-zag pattern (orange dotted line), where the PEG phase in the odd-samples melts at lower temperatures compared to their next member in the series, except between $n = 2$ and 3.

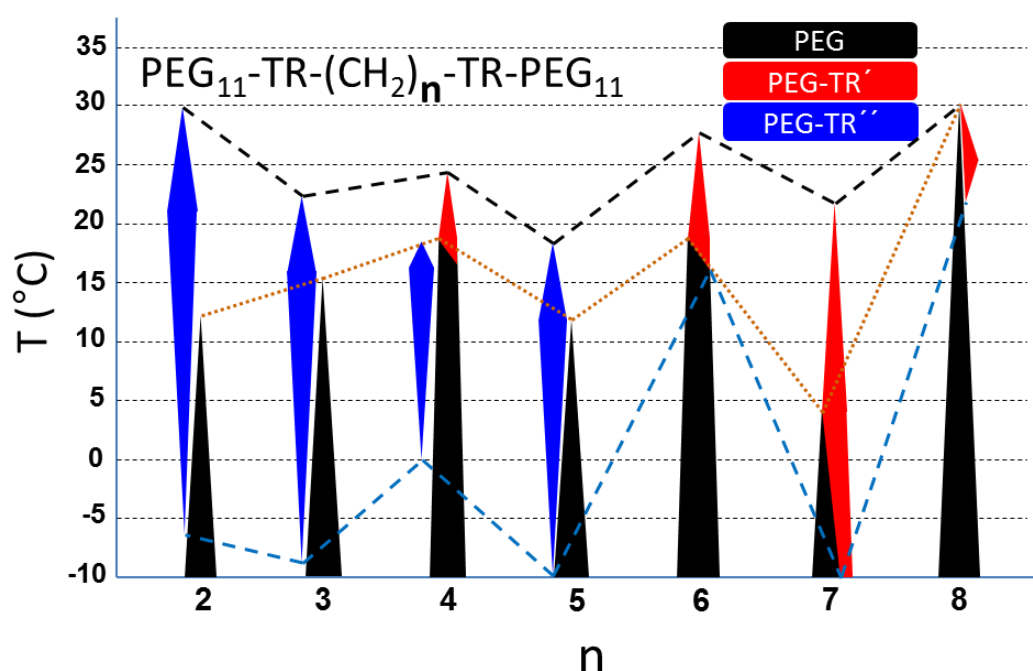


Figure 3.36. Bar scheme of the observed phases in the homologous series of PEG₁₁-TR-(CH₂)_n-TR-PEG₁₁ obtained from WAXS and ¹³C MAS CP NMR data (see text for details).

Proposing any single factor responsible for these odd-even effects and the solid-state transitions in PEG₁₁-TR-(CH₂)_n-TR-PEG₁₁ will not be correct, as there are several influencing factors affecting the system in different ways. For instance, the melting of the PEG-TR'' phases (blue bars in Figure 3.36) in PEG₁₁-TR-(CH₂)_n-TR-PEG₁₁ with $n \leq 5$, did not show this expected alternation of the melting points. In contrast, they only show a steady decreasing tendency of T_m with the increasing number of CH₂ groups. This is a clear indication that the melting temperature of the PEG-TR'' phase was dominantly

influenced by π - π interactions as revealed by ^{13}C MAS CP and SP NMR spectroscopy. With increasing number of CH_2 groups, the length of the $\text{TR}-(\text{CH}_2)_n\text{-TR}$ group was extended and thus, the crystal stabilizing π - π interactions are reduced, resulting in a lower melting temperature. This phenomenon was also observed for the melting points of the PEG-free $\text{Me-TR}-(\text{CH}_2)_x\text{-TR-Me}$ model compounds (see Appendix, Figure A37). This can also be the reason why the PEG-TR'' phase is not formed for $n > 5$.

PEG-TR' phase (red bars in Figure 3.36) is the high-temperature phase for samples $n = 4, 6-8$, and for this phase a structural model was proposed where one PEG_{11} chain, one TR ring and some adjacent CH_2 groups were crystalline while the remaining CH_2 groups and the TR ring of the $\text{TR}-(\text{CH}_2)_n\text{-TR}$ defect are amorphous but in a relatively ordered state. Although, the melting of PEG-TR' phase is influenced by π - π interactions, but one can also hypothesize that the exact number of CH_2 units incorporated in the PEG crystal might also has an affect. The incorporation of either even or an odd number of CH_2 unit in a PEG crystal structure will affect the crystal density of the new crystal system in a different way, resulting in an alternating behavior of melting temperature for $\text{PEG}_{11}\text{-TR}-(\text{CH}_2)_n\text{-TR-PEG}_{11}$, $n = 6-8$. Unfortunately, from the present experimental data, it is not possible to find the exact number of CH_2 units incorporated in the PEG crystal structure. However, additional measurements are now being performed to further investigate this matter. Hence, at this moment, it can be concluded that for $\text{PEG}_{11}\text{-TR}-(\text{CH}_2)_n\text{-TR-PEG}_{11}$, the odd-even pattern in the temperature of final melting, temperature of incorporation of spacer in PEG crystal, and in the temperature of melting of PEG phase is observed due to the mutual influences of π - π interactions, spacer length and by the odd or even number of CH_2 units incorporated in the PEG crystal (PEG-TR' phase).

4. Conclusions

In the first part of this thesis, well-defined poly(ethylene glycol) (PEG) networks were synthesized using copper(I)-catalyzed azide-alkyne cycloaddition (CuAAC) *click* reaction. Two types of PEG end-linked networks were prepared (i) *type A*: by connecting three-arm PEG star units with another three-arm PEG star and (ii) *type B*: by connecting three-arm PEG star units with bifunctional linear PEG oligomers of different molar masses. End-group functionalization of PEG oligomers with azide and alkyne moieties was successfully performed using sodium azide and propargyl bromide, respectively. For the CuAAC reaction, the catalytic system of CuSO₄ and sodium ascorbate in an aqueous environment was used. The successful conversion of the precursors and the formation of the networks were confirmed by ¹³C-MAS NMR and FT-IR spectroscopy. DSC studies show the decrease in the melting temperature and the degree of crystallinity values for the PEG networks compared to their linear analogs. Isothermal crystallization kinetic studies of the PEG network were also performed and the activation energy of isothermal crystallization of PEG networks was evaluated using the Arrhenius relationship. WAXS measurements at different temperatures show only the PEG reflections (monoclinic lattice) and the degree of crystallinity values obtained from these measurements were found to be in good agreement with the values obtained from the DSC measurements. From the temperature dependent SAXS measurements on the PEG networks, a random arrangement of PEG crystals was found as the SAXS traces either show no or very weak higher order peaks. A

shift of the first order peak to smaller q -values during the course of heating shows the increase in the average crystal-crystal distances because of the melting of smaller crystallites along with the possibility of lamella thickening process during heating. Swelling and ^1H double quantum NMR spectroscopy measurements reveal the presence of inhomogeneities and network defects like multiple links and dangling chain ends in all types of polymer networks.

In the second section, the synthesis of a linear $\text{PEG}_{11}\text{-TR-PEG}_{11}$ chain was performed where a 1,4 disubstituted 1,2,3 triazole ring was placed in the middle of the chain as a point defect. Temperature dependent SAXS measurements reveal that initially, at lower temperatures, one arm of $\text{PEG}_{11}\text{-TR-PEG}_{11}$ was crystallized and that the lamella thickness increased with the measurement temperature. Temperature dependent WAXS measurements revealed not only a reduction in the PEG helix-helix distance but a new Bragg peak appeared as the sample was heated. Additionally, in the DSC trace, an exothermal transition was observed during heating which coincides with the temperature range of the structural changes observed in the WAXS diffraction pattern. Moreover, before the exothermic transition in the DSC trace, a small endotherm is also observed indicating a liquid/amorphous phase, which was later also confirmed by POM where black regions are observed within the spherulites at these temperatures.

In the last part, a series of $\text{PEG}_{11}\text{-TR-(CH}_2)_n\text{-TR-PEG}_{11}$ ($n = 2\text{-}8$) samples having two TR rings, separated by n -alkyl spacers of different length in the center of the chain were synthesized and investigated for their crystallization and structural behavior. The DSC measurements showed an alternating pattern for the melting temperatures and molar enthalpies of $\text{PEG}_{11}\text{-TR-(CH}_2)_n\text{-TR-PEG}_{11}$, reminiscent of the classical odd-even effect of n -alkanes. However, additional WAXS, SAXS and solid state ^{13}C MAS CP and SP NMR spectroscopy measurements revealed a solid-state phase transition in all samples, prior to their final melting. Based on the appearance of their solid-state phase transitions in the WAXS traces, $\text{PEG}_{11}\text{-TR-(CH}_2)_n\text{-TR-PEG}_{11}$ samples were divided into two main groups, with the exception of $n = 4$. Samples with $n = 2,3,5$, shows completely new Bragg reflections during heating, while for the samples with $n = 6,7,8$, the Bragg reflections are similar to pure PEG but slightly shifted to smaller angles at higher temperatures. The

sample with $n = 4$ seems to be a mixture of both groups. After crystallizing the samples from the melt, one PEG₁₁ chain of all PEG₁₁-TR-(CH₂) _{n} -TR-PEG₁₁ samples crystallized in the known monoclinic 7₂ helix structure, whereas the TR-(CH₂) _{n} -TR group and the second PEG₁₁ chain remain amorphous. Upon heating, PEG₁₁-TR-(CH₂) _{n} -TR-PEG₁₁ with $n = 2, 3$ or 5 shows a phase transition (*PEG-TR''*) which was attributed to the incorporation of the whole TR-(CH₂) _{n} -TR group into the crystal. However, PEG₁₁-TR-(CH₂) _{n} -TR-PEG₁₁ with $n \geq 6$ undergoes a different phase transition during heating where it is assumed that only one TR ring and some adjacent CH₂ groups of the corresponding alkyl spacer were incorporated into the crystal structure (*PEG-TR'* phase). PEG₁₁-TR-(CH₂)₄-TR-PEG₁₁ shows both types of solid-state phase transitions during heating. The first phase transition is similar to that of PEG₁₁-TR-(CH₂) _{n} -TR-PEG₁₁ with $n \leq 5$, i.e. the *PEG-TR''* phase. However, before the completion of the first phase transition, a second transition is noticed where the untransformed PEG phase was converted into the *PEG-TR'* phase. Polarized optical microscopy was also used to visualize this unique phase transition. Along with the odd-even effect in the final melting temperatures of PEG₁₁-TR-(CH₂) _{n} -TR-PEG₁₁, the temperature of incorporation of spacer groups in the PEG crystal and temperature of melting of the low-temperature PEG phase also follows an odd-even pattern.

5. References

- (1) Hirata, Y.; Kondo, H.; Ozawa, Y. In *Chemistry, Manufacture and Applications of Natural Rubber*; Elsevier, 2014; pp 325–352.
- (2) Dhandayuthapani, B.; Yoshida, Y.; Maekawa, T.; Kumar, D. S. *Int. J. Polym. Sci.* **2011**, *2011*, 1–19.
- (3) Rezwan, K.; Chen, Q. Z.; Blaker, J. J.; Boccaccini, A. R. *Biomaterials* **2006**, *27* (18), 3413–3431.
- (4) Gottlieb, M. *Swelling of Polymer Networks*; Springer, 1988.
- (5) Gent, A. N.; Tobias, R. H. *J. Polym. Sci. Polym. Phys. Ed.* **1982**, *20* (12), 2317–2327.
- (6) Flory, P. J.; Rehner Jr, J. J. *Chem. Phys.* **1943**, *11* (11), 512–520.
- (7) Kramer, O. *Biological and Synthetic Polymer Networks*; Kramer, O., Ed.; Springer Netherlands: Dordrecht, 1988.
- (8) Bray, J. C.; Merrill, E. W. *J. Appl. Polym. Sci.* **1973**, *17* (12), 3779–3794.
- (9) *IUPAC Compendium of Chemical Terminology*; Nič, M., Jirát, J., Košata, B., Jenkins, A., McNaught, A., Eds.; IUPAC: Research Triangle Park, NC, 2009.
- (10) Odian, G. *Principles of Polymerization*; John Wiley & Sons, Inc.: Hoboken, NJ, 2004.
- (11) Jin, F. L.; Li, X.; Park, S. J. *J. Ind. Eng. Chem.* **2015**, *29*, 1–11.
- (12) Booth, E. W.; Beaver, D. J. *Rubber Chem. Technol.* **1940**, *13* (4), 918–925.
- (13) Toki, S.; Sainumsai, W.; Suchiva, K.; Rong, L.; Hsiao, B. In *Constitutive Models for Rubbers IX*; CRC Press, 2015; pp 515–520.
- (14) Noro, A.; Hayashi, M.; Matsushita, Y. *Soft Matter* **2012**, *8* (24), 6416–6429.
- (15) te Nijenhuis, K. *Polym. Bull.* **2007**, *58* (1), 27–42.
- (16) Arndt, K. F.; Richter, A.; Ludwig, S.; Zimmermann, J.; Kressler, J.; Kuckling, D.; Adler, H. J. *Acta Polym.* **1999**, *50* (11–12), 383–390.
- (17) Jiang, Y.; Hussain, H.; Kressler, J. *Macromol. Mater. Eng.* **2015**, *300* (2), 181–190.
- (18) Yokoyama, F.; Masada, I.; Shimamura, K.; Ikawa, T.; Monobe, K. *Colloid Polym. Sci.* **1986**, *264* (7), 595–601.
- (19) Binder, W. H.; Zirbs, R. In *Advances in polymer science*; Springer, 2006; Vol. 207, pp 1–78.
- (20) Tuncaboylu, D. C.; Sari, M.; Oppermann, W.; Okay, O. *Macromolecules* **2011**, *44* (12), 4997–5005.
- (21) Schubert, U. S.; Eschbaumer, C. *Angew. Chemie Int. Ed.* **2002**, *41* (16), 2892–2926.

- (22) Aida, T.; Meijer, E. W.; Stupp, S. I. *Science* (80-.). **2012**, 335 (6070), 813–817.
- (23) Shao, H.; Parquette, J. R. *Chem. Commun.* **2010**, 46 (24), 4285–4287.
- (24) *Supramolecular Polymer Networks and Gels*; Seiffert, S., Ed.; Springer International Publishing: Cham, 2015.
- (25) Steed, J. W.; Gale, P. A. *Supramolecular Chemistry*; Gale, P. A., Steed, J. W., Eds.; John Wiley & Sons, Ltd: Chichester, UK, 2012.
- (26) Teymour, F.; Campbell, J. D. *Macromolecules* **1994**, 27 (9), 2460–2469.
- (27) Stauffer, D. *J. Chem. Soc. Faraday Trans. 2 Mol. Chem. Phys.* **1976**, 72, 1354–1364.
- (28) Mark, H.; Whitby, G. S. *Collected papers of W. H. Carothers on high polymeric substances*; Mark, H., Whitby, G. S., Eds.; Interscience Publishers: New York, 1940.
- (29) Constantin V. Uglea. *Liquid Chromatography of Oligomers*; Marcel Decker, Inc.: New York. Basel. Hong kong, 1996.
- (30) Flory, P. J. *J. Am. Chem. Soc.* **1941**, 63 (11), 3083–3090.
- (31) Flory, P. J. *J. Phys. Chem.* **1942**, 46 (1), 132–140.
- (32) Stockmayer, W. H. *J. Chem. Phys.* **1943**, 11 (2), 45–55.
- (33) Gordon, M. In *Proceedings of the Royal Society of London A: Mathematical, Physical and Engineering Sciences*; The Royal Society, 1962; Vol. 268, pp 240–256.
- (34) Gordon, M.; Scantlebury, G. R. *Trans. Faraday Soc.* **1964**, 60, 604–621.
- (35) Miller, D. R.; Macosko, C. W. *J. Polym. Sci. Part B Polym. Phys.* **1988**, 26 (1), 1–54.
- (36) Bruneau, C. M. In *Annales De Chimie France*; 1966; Vol. 1, p 271.
- (37) Dusek, K.; Kuchanov, S. *Polymer Networks' 91*; CRC Press: Utrecht, Netherlands, 1992.
- (38) Kuchanov, S. I.; Panyukov, S. V. *Polym. Networks* **1992**, 91, 39–62.
- (39) *Handbook of Thermoplastics*, Second Edi.; Olabisi, O., Adewale, K., Eds.; CRC Press: Boca Raton, London, New York, 2015.
- (40) Sauter, E. *Zeitschrift für Phys. Chemie* **1933**, 21 (1), 186–197.
- (41) Huggins, M. L. *Physical chemistry of high polymers*; John Wiley & Sons: New York, 1958.
- (42) Huggins, M. L. *J. Chem. Phys.* **1945**, 13 (1), 37–42.
- (43) Davison, W. H. T. *J. Chem. Soc.* **1955**, 3270–3274.
- (44) Miyazawa, T. *J. Polym. Sci. Part A Polym. Chem.* **1961**, 55 (161), 215–231.
- (45) Miyazawa, T. *J. Chem. Phys.* **1961**, 35 (2), 693–713.
- (46) Chatani, Y.; Tadokoro, H.; Yoshihara, T.; Murahashi, S. In *Symposium on Polymer Sci*; Tokyo, Japan, 1961; p 11B–5.

- (47) Tadokoro, H.; Chatani, Y.; Yoshihara, T.; Tahara, S.; Murahashi, S. *Makromol. Chemie* **1964**, *73*, 109–127.
- (48) Takahashi, Y.; Tadokoro, H. *Macromolecules* **1973**, *6* (5), 672–675.
- (49) Miyazawa, T.; Fukushima, K.; Ideguchi, Y. *J. Chem. Phys.* **1962**, *37* (12), 2764–2776.
- (50) Price, F. P.; Kilb, R. W. *J. Polym. Sci.* **1962**, *57* (165), 395–403.
- (51) Takahashi, Y.; Sumita, I.; Tadokoro, H. *J. Polym. Sci. Polym. Phys. Ed.* **1973**, *11* (11), 2113–2122.
- (52) Iwamoto, R.; Saito, Y.; Ishihara, H.; Tadokoro, H. *J. Polym. Sci. Part A-2 Polym. Phys.* **1968**, *6* (8), 1509–1525.
- (53) Tadokoro, H.; Yoshihara, T.; Chatani, Y.; Murahashi, S. *J. Polym. Sci. Part B Polym. Lett.* **1964**, *2* (4), 363–368.
- (54) Arlif, J. P.; Spegt, P. A.; Skoulios, A. E. *Macromol. Chem. Phys.* **1966**, *99* (1), 160–174.
- (55) Godovsky, Y. K.; Slonimsky, G. L.; Garbar, N. M. *J. Polym. Sci. Part C Polym. Symp.* **2007**, *38* (1), 1–21.
- (56) Cheng, S. Z. D.; Chen, J.; Barley, J. S.; Zhang, A.; Habenschuss, A.; Zschack, P. R. *Macromolecules* **1992**, *25* (5), 1453–1460.
- (57) Spegt, P. P. *Die Makromol. Chemie* **1970**, *140* (1), 167–177.
- (58) Arlie, P.; Spegt, P.; Skoulios, A. *Die Makromol. Chemie* **1967**, *104* (2373), 212–229.
- (59) Cheng, S. Z. D.; Zhang, a; Barley, J. S.; Chen, J.; Habenschuss, a; Zschack, P. R. *Macromolecules* **1991**, *24* (13), 3937–3944.
- (60) Cheng, S. Z. D.; Zhang, A.; Chen, J. *J. Polym. Sci. Part C Polym. Lett.* **1989**, *28* (7), 233–239.
- (61) Lee, S.-W.; Chen, E.; Zhang, A.; Yoon, Y.; Moon, B. S.; Lee, S.; Harris, F. W.; Cheng, S. Z. D.; von Meerwall, E. D.; Hsiao, B. S.; Verma, R.; Lando, J. B. *Macromolecules* **1996**, *29* (27), 8816–8823.
- (62) Kovacs, A. J.; Gonthier, A. *Kolloid-Zeitschrift und Zeitschrift für Polym.* **1972**, *250* (5), 530–552.
- (63) Song, K.; Krimm, S. *Macromolecules* **1990**, *23* (7), 1946–1957.
- (64) Kim, I.; Krimm, S. *J. Polym. Sci. Part B Polym. Phys.* **1997**, *35* (7), 1117–1126.
- (65) Matyjaszewski, K. *Science (80-.)*. **2011**, *333* (2011), 1104–1105.
- (66) Bent, J. *Science (80-.)*. **2003**, *301* (5640), 1691–1695.
- (67) Chen, Z. *Science (80-.)*. **1997**, *277* (5330), 1248–1253.
- (68) De Rosa, C.; Auriemma, F.; De Ballesteros, O. R.; Resconi, L.; Camurati, I. *Macromolecules* **2007**, *40* (18), 6600–6616.

- (69) Alamo, R. G.; VanderHart, D. L.; Nyden, M. R.; Mandelkern, L. *Macromolecules* **2000**, *33* (16), 6094–6105.
- (70) Fortney, A.; Fossum, E. *Polymer* . **2012**, *53* (12), 2327–2333.
- (71) Tong, Z. Z.; Huang, Y.; Xu, J. T.; Fu, Z. S.; Fan, Z. Q. *J. Phys. Chem. B* **2015**, *119* (19), 6050–6061.
- (72) Tong, Z. Z.; Zhou, B.; Huang, J.; Xu, J. T.; Fan, Z. Q. *Macromolecules* **2014**, *47* (1), 333–346.
- (73) Rojas, G.; Inci, B.; Wei, Y.; Wagener, K. B. *J. Am. Chem. Soc.* **2009**, *131* (47), 17376–17386.
- (74) Baltá-Calleja, F. J.; Hosemann, R. *J. Polym. Sci. Polym. Phys. Ed.* **1980**, *18* (5), 1159–1165.
- (75) Martuscelli, E.; Pracella, M. *Polymer* . **1974**, *15* (5), 306–314.
- (76) Calleja, F. J. B.; Ortega, J. C. G.; de Salazar, J. M. *Polymer* . **1978**, *19* (9), 1094–1099.
- (77) Berda, E. B.; Wagener, K. B. *Macromol. Chem. Phys.* **2008**, *209* (15), 1601–1611.
- (78) Song, S.; Miao, W.; Wang, Z.; Gong, D.; Chen, Z. R. *Polym. (United Kingdom)* **2015**, *64*, 76–83.
- (79) Ortmann, P.; Lemke, T. A.; Mecking, S. *Macromolecules* **2015**, *48* (5), 1463–1472.
- (80) Zheng, Y. R.; Tee, H. T.; Wei, Y.; Wu, X. L.; Mezger, M.; Yan, S.; Landfester, K.; Wagener, K.; Wurm, F. R.; Lieberwirth, I. *Macromolecules* **2016**, *49* (4), 1321–1330.
- (81) Lee, S. W. S.-W.; Chen, E. Q.; Zhang, A. Q.; Yoon, Y.; Moon, B. S.; Lee, S. W. S.-W.; Harris, F. W.; Cheng, S. Z. D.; VonMeerwall, E. D.; Hsiao, B. S.; Verma, R.; Lando, J. B.; von Meerwall, E. D.; Hsiao, B. S.; Verma, R.; Lando, J. B. *Macromolecules* **1996**, *29* (27), 8816–8823.
- (82) Chen, E.-Q.; Lee, S.-W.; Zhang, A.; Moon, B.-S.; Honigfort, P. S.; Mann, I.; Lin, H.-M.; Harris, F. W.; Cheng, S. Z. D.; Hsiao, B. S.; Yeh, F. *Polymer* . **1999**, *40* (16), 4543–4551.
- (83) Chen, E. Q.; Lee, S. W.; Zhang, A.; Moon, B. S.; Mann, I.; Harris, F. W.; Cheng, S. Z. D.; Hsiao, B. S.; Yeh, F.; Von Merrewell, E.; Grubb, D. T. *Macromolecules* **1999**, *32* (15), 4784–4793.
- (84) Cheng, S. Z. D.; Wu, S. S.; Chen, J.; Zhuo, Q.; Quirk, R. P.; von Meerwall, E. D.; Hsiao, B. S.; Habenschuss, A.; Zschack, P. R. *Macromolecules* **1993**, *26* (19), 5105–5117.
- (85) Obadia, M. M.; Mudraboyina, B. P.; Allaoua, I.; Haddane, A.; Montarnal, D.; Serghei, A.; Drockenmuller, E. *Macromol. Rapid Commun.* **2014**, *35* (8), 794–800.
- (86) Colliat-Dangus, G.; Obadia, M. M.; Vygodskii, Y. S.; Serghei, A.; Shaplov, A. S.; Drockenmuller, E. *Polym. Chem.* **2015**, *6*, 4299–4308.
- (87) Obadia, M. M.; Mudraboyina, B. P.; Allaoua, I.; Haddane, A.; Montarnal, D.; Erghei,

- A.; Drockenmuller, E. *Macromol. Rapid Commun.* **2014**, *35* (8), 794–800.
- (88) Pulst, M.; Samiullah, M. H.; Baumeister, U.; Prehm, M.; Balko, J.; Thurn-Albrecht, T.; Busse, K.; Golitsyn, Y.; Reichert, D.; Kressler, J. *Macromolecules* **2016**, *49* (17), 6609–6620.
- (89) Binder, W. H.; Sachsenhofer, R. *Macromol. Rapid Commun.* **2007**, *28*, 15–54.
- (90) Malkoch, M.; Vestberg, R.; Gupta, N.; Mespouille, L.; Dubois, P.; Mason, A. F.; Hedrick, J. L.; Liao, Q.; Frank, C. W.; Kingsbury, K.; Hawker, C. J. *Chem. Commun.* **2006**, No. 26, 2774.
- (91) Donahoe, C. D.; Cohen, T. L.; Li, W.; Nguyen, P. K.; Fortner, J. D.; Mitra, R. D.; Elbert, D. L. *Langmuir* **2013**, *29*, 4128–4139.
- (92) Boese, R.; Weiss, H. C.; Blaser, D. *Angew. Chemie - Int. Ed.* **1999**, *38* (7), 988–992.
- (93) Torres, M. B.; Fernández, E. M.; Balbás, L. C. *Phys. Rev. B* **2005**, *71* (15), 155412.
- (94) Näher, U.; Bjørnholm, S.; Frauendorf, S.; Garcias, F.; Guet, C. *Phys. Rep.* **1997**, *285* (6), 245–320.
- (95) Harkins, W. D. *J. Am. Chem. Soc.* **1917**, *39* (5), 856–879.
- (96) Oddo, G. *Zeitschrift für Anorg. und Allg. Chemie* **1914**, *87* (1), 253–268.
- (97) Baeyer, A. *Berichte der Dtsch. Chem. Gesellschaft* **1877**, *10* (2), 1286–1288.
- (98) Caspari, W. A. *J. Chem. Soc.* **1928**, 3235–3241.
- (99) Boese, R.; Weiss, H.-C.; Bläser, D. *Angew. Chemie Int. Ed.* **1999**, *38* (7), 988–992.
- (100) Thalladi, V. R.; Boese, R.; Weiss, H.-C. *J. Am. Chem. Soc.* **2000**, *122* (6), 1186–1190.
- (101) Thalladi, V. R.; Boese, R.; Weiss, H.-C. *Angew. Chemie Int. Ed.* **2000**, *39* (5), 918–922.
- (102) White, N. A. S.; Ellis, H. A.; Nelson, P. N.; Maragh, P. T. *J. Chem. Thermodyn.* **2011**, *43* (4), 584–590.
- (103) Badea, E.; Nowicka, B. B.; Della Gatta, G. *J. Chem. Thermodyn.* **2014**, *68*, 90–97.
- (104) Badea, E.; Gatta, G. Della; D'Angelo, D.; Brunetti, B.; Rečková, Z. *J. Chem. Thermodyn.* **2006**, *38* (12), 1546–1552.
- (105) Badea, E.; Blanco, I.; Della Gatta, G. *J. Chem. Thermodyn.* **2007**, *39* (10), 1392–1398.
- (106) Dall'Acqua, L.; Della Gatta, G.; Nowicka, B.; Ferloni, P. *J. Chem. Thermodyn.* **2002**, *34* (1), 1–12.
- (107) Zhang, H.; Xie, C.; Liu, Z.; Gong, J. *Ind. Eng. Chem. Res.* **2013**, *52* (51), 18458–18465.
- (108) Zhang, H.; Yin, Q.; Liu, Z.; Gong, J.; Bao, Y.; Zhang, M.; Hao, H.; Hou, B.; Xie, C. *J. Chem. Thermodyn.* **2014**, *77*, 91–97.

- (109) Yang, K.; Cai, Z.; Tyagi, M.; Feygenson, M.; Neufeind, J. C.; Moore, J. S.; Zhang, Y. *Chem. Mater.* **2016**, *28* (9), 3227–3233.
- (110) Mishra, M. K.; Varughese, S.; Ramamurty, U.; Desiraju, G. R. *J. Am. Chem. Soc.* **2013**, *135* (22), 8121–8124.
- (111) Marcelis, A. T. M.; Koudijs, A.; Sudhölter, E. J. R. *Liq. Cryst.* **1995**, *18* (6), 843–850.
- (112) Pines, A.; Ruben, D. J.; Allison, S. *Phys. Rev. Lett.* **1974**, *33* (17), 1002.
- (113) Marčelja, S. *J. Chem. Phys.* **1974**, *60* (9), 3599–3604.
- (114) Holbrey, J. D.; Seddon, K. R. *J. Chem. Soc. Dalton Trans.* **1999**, No. 13, 2133–2140.
- (115) Stoliar, P.; Kshirsagar, R.; Massi, M.; Annibale, P.; Albonetti, C.; de Leeuw, D. M.; Biscarini, F. *J. Am. Chem. Soc.* **2007**, *129* (20), 6477–6484.
- (116) Heister, K.; Rong, H.-T.; Buck, M.; Zharnikov, M.; Grunze, M.; Johansson, L. S. O. *J. Phys. Chem. B* **2001**, *105* (29), 6888–6894.
- (117) Tao, F.; Bernasek, S. L. *Chem. Rev.* **2007**, *107* (5), 1408–1453.
- (118) Li, Y.; Li, P.; Wang, J.; Wang, Y.; Yan, H.; Thomas, R. K. *Langmuir* **2005**, *21* (15), 6703–6706.
- (119) Mukerjee, P. *Kolloid-Zeitschrift und Zeitschrift für Polym.* **1970**, *236* (1), 76–79.
- (120) Roviello, A.; Sirigu, A. *Die Makromol. Chemie* **1982**, *183* (4), 895–904.
- (121) Blumstein, A.; Thomas, O. *Macromolecules* **1982**, *15* (5), 1264–1267.
- (122) Mizuno, M.; Hirai, A.; Matsuzawa, H.; Endo, K.; Suhara, M.; Kenmotsu, M.; Han, C. D. *Macromolecules* **2002**, *35* (7), 2595–2601.
- (123) Yu, H.; Park, K. H.; Song, I.; Kim, M.-J.; Kim, Y.-H.; Oh, J. H. *J. Mater. Chem. C* **2015**, *3* (44), 11697–11704.
- (124) Uchida, H.; Miyata, K.; Oba, M.; Ishii, T.; Suma, T.; Itaka, K.; Nishiyama, N.; Kataoka, K. *J. Am. Chem. Soc.* **2011**, *133* (39), 15524–15532.
- (125) Marty, R.; Nigon, R.; Leite, D.; Frauenrath, H. *J. Am. Chem. Soc.* **2014**, *136* (10), 3919–3927.
- (126) Wu, J.; Qu, T.; Gao, L.; Yang, X.; Li, X.; Tu, Y.; Zhu, X. *Chinese J. Polym. Sci.* **2015**, *33* (8), 1069–1073.
- (127) de Groot, J.; Oborn, R.; Potreck, J.; Nijmeijer, K.; de Vos, W. M. *J. Memb. Sci.* **2015**, *475*, 311–319.
- (128) Wang, R.; Johnson, J. A.; Olsen, B. D. *Macromolecules* **2017**, *50* (6), 2556–2564.
- (129) Yang, K.; Tyagi, M.; Moore, J. S.; Zhang, Y. *J. Am. Chem. Soc.* **2014**, *136* (4), 1268–1271.
- (130) Yang, K.; Cai, Z.; Jaiswal, A.; Tyagi, M.; Moore, J. S.; Zhang, Y. *Angew. Chemie Int. Ed.* **2016**, 1–7.

- (131) Wu, J.; Wei, W.; Wang, L.-Y.; Su, Z.-G.; Ma, G.-H. *Biomaterials* **2007**, *28* (13), 2220–2232.
- (132) Burdick, J. A.; Anseth, K. S. *Biomaterials* **2002**, *23* (22), 4315–4323.
- (133) Klingshirn, M. A.; Spear, S. K.; Subramanian, R.; Holbrey, J. D.; Huddleston, J. G.; Rogers, R. D. *Chem. Mater.* **2004**, *16* (16), 3091–3097.
- (134) Sirkar, K.; Pishko, M. V. *Anal. Chem.* **1998**, *70* (14), 2888–2894.
- (135) Keys, K. B.; Andreopoulos, F. M.; Peppas, N. A. *Macromolecules* **1998**, *31* (23), 8149–8156.
- (136) Katashima, T.; Asai, M.; Urayama, K.; Chung, U.; Sakai, T. *J. Chem. Phys.* **2014**, *140* (7), 74902.
- (137) Saikia, A. K.; Mandal, U. K.; Aggarwal, S. *J. Polym. Res.* **2012**, *19* (5), 9871.
- (138) Shibayama, M.; Nishi, K.; Hiroi, T. *Macromol. Symp.* **2015**, *348* (1), 9–13.
- (139) Nomoto, Y.; Matsunaga, T.; Sakai, T.; Tosaka, M.; Shibayama, M. *Polymer* . **2011**, *52* (18), 4123–4128.
- (140) Peppas, N. A.; Keys, K. B.; Torres-Lugo, M.; Lowman, A. M. *J. Control. release* **1999**, *62* (1), 81–87.
- (141) Van Dijk, M.; Van Nostrum, C. F.; Hennink, W. E.; Rijkers, D. T. S.; Liskamp, R. M. J. *Biomacromolecules* **2010**, *11* (6), 1608–1614.
- (142) Hennink, W. E.; Van Nostrum, C. *Adv. Drug Deliv. Rev.* **2012**, *64*, 223–236.
- (143) Kolb, H. C.; Finn, M. G.; Sharpless, K. B. *Angew. Chemie - Int. Ed.* **2001**, *40*, 2004–2021.
- (144) Rostovtsev, V. V.; Green, L. G.; Fokin, V. V.; Sharpless, K. B. *Angew. Chemie Int. Ed.* **2002**, *41* (14), 2596–2599.
- (145) Crescenzi, V.; Cornelio, L.; Di Meo, C.; Nardecchia, S.; Lamanna, R. *Biomacromolecules* **2007**, *8* (6), 1844–1850.
- (146) Truong, V.; Blakey, I.; Whittaker, A. K. *Biomacromolecules* **2012**, *13* (12), 4012–4021.
- (147) Ossipov, D. A.; Hilborn, J. *Macromolecules* **2006**, *39* (5), 1709–1718.
- (148) Chen, E. Q.; Weng, X.; Zhang, A.; Mann, I.; Harris, F. W.; Cheng, S. Z. D.; Stein, R.; Hsiao, B. S.; Yeh, F. *Macromol. Rapid Commun.* **2001**, *22* (8), 611–615.
- (149) Saalwächter, K. *Prog. Nucl. Magn. Reson. Spectrosc.* **2007**, *51* (1), 1–35.
- (150) Ammann, C.; Meier, P.; Merbach, A. *J. Magn. Reson.* **1982**, *46* (2), 319–321.
- (151) Vonk, C. G. *Synthetic polymers in the solid state. Small Angle X-ray Scattering*; Glatter, O., Kratky, O., Eds.; Academic Press, 1982.
- (152) Samiullah, M. H.; Reichert, D.; Zinkevich, T.; Kressler, J. *Macromolecules* **2013**, *46*

- (17), 6922–6930.
- (153) Kulbokaite, R.; Ciuta, G.; Netopilik, M.; Makuska, R. *React. Funct. Polym.* **2009**, *69* (10), 771–778.
- (154) Chen, G. J.; Tao, L.; Mantovani, G.; Ladmiral, V.; Burt, D. P.; Macpherson, J. V.; Haddleton, D. M. *Soft Matter* **2007**, *3* (6), 732–739.
- (155) Hiki, S.; Kataoka, K. *Bioconjug. Chem.* **2007**, 2191–2196.
- (156) Chan, T. R.; Fokin, V. V. *QSAR Comb. Sci.* **2007**, *26*, 1274–1279.
- (157) Sigma Aldrich, Poly(ethylene glycol), BioUltra 1000 <http://www.sigmaaldrich.com/catalog/product/sigma/81188?lang=de®ion=DE> (accessed Jul 18, 2017).
- (158) Hellbach, B.; Gleiter, R.; Rominger, F. *Synthesis (Stuttg.)*. **2003**, *16*, 2535–2541.
- (159) Schirmacher, R.; Lakhrissi, Y.; Jolly, D.; Goodstein, J.; Lucas, P.; Schirmacher, E. *Tetrahedron Lett.* **2008**, *49* (33), 4824–4827.
- (160) Alemán, J. V.; Chadwick, A. V.; He, J.; Hess, M.; Horie, K.; Jones, R. G.; Kratochvíl, P.; Meisel, I.; Mita, I.; Moad, G.; Penczek, S.; Stepto, R. F. T. *Pure Appl. Chem.* **2007**, *79* (10), 1801–1829.
- (161) Buckley, C. P.; Kovacs, a. J. *Colloid Polym. Sci.* **1976**, *254* (8), 695–715.
- (162) Lorenzo, A. T.; Arnal, M. L.; Albuérne, J.; Müller, A. J. *Polym. Test.* **2007**, *26* (2), 222–231.
- (163) Kalkar, A. K.; Deshpande, A. A. *Polym. Eng. Sci.* **2001**, *41* (9), 1597–1615.
- (164) Avrami, M. *J. Chem. Phys.* **1939**, *7* (12), 1103.
- (165) Wang, Z. G.; Hsiao, B. S.; Sauer, B. B.; Kampert, W. G. *Polymer* . **1999**, *40* (16), 4615–4627.
- (166) Kolb, R.; Wutz, C.; Stribeck, N.; von Krosigk, G.; Riekkel, C. *Polymer* . **2001**, *42* (12), 5257–5266.
- (167) You, W.; Duan, B.; Wang, M.; Lam, W. In *Advances in Diverse Industrial Applications of Nanocomposites*; InTech, 2011; pp 953–978.
- (168) Li, J.; Zhou, C.; Wang, G.; Tao, Y.; Liu, Q.; Li, Y. *Polym. Test.* **2002**, *21* (5), 583–589.
- (169) Liu, M.; Zhao, Q.; Wang, Y.; Zhang, C.; Mo, Z.; Cao, S. *Polymer* . **2003**, *44* (8), 2537–2545.
- (170) Vyazovkin, S. *Phys. Chem. Chem. Phys.* **2016**, *18* (28), 18643–18656.
- (171) Imai, S.; Shimono, S.; Fukushima, Y.; Umezaki, K.; Okada, M.; Takahashi, M.; Matsuda, H. *Thermochim. Acta* **1995**, *267*, 259–268.
- (172) Fetters, L. J.; Lohse, D. J.; Richter, D.; Witten, T. A.; Zirkel, A. *Macromolecules* **1994**, *27* (17), 4639–4647.

- (173) Marand, H.; Xu, J.; Srinivas, S. *Macromolecules* **1998**, *31* (23), 8219–8229.
- (174) Hoffman, J. D.; Weeks, J. J. *J. Res. Natl. Bur. Stand. Sect. A Phys. Chem.* **1962**, *66A* (1), 13.
- (175) Strobl, G. *Prog. Polym. Sci.* **2006**, *31* (4), 398–442.
- (176) Heck, B.; Hugel, T.; Iijima, M.; Sadiku, E.; Strobl, G. *New J. Phys.* **1999**, *1* (1), 17.
- (177) Al-Husseini, M.; Strobl, G. *Macromolecules* **2002**, *35* (5), 1672–1676.
- (178) Hauser, G.; Schmidtke, J.; Strobl, G. *Macromolecules* **1998**, *31* (18), 6250–6258.
- (179) Sperling, L. H. *Introduction to Physical Polymer Science*; John Wiley & Sons, Inc.: Hoboken, NJ, USA, 2005.
- (180) Ozawa, T. *Polymer* . **1971**, *12* (3), 150–158.
- (181) Sattari, M.; Mirsalehi, S. A.; Khavandi, A.; Alizadeh, O.; Naimi-Jamal, M. R. *J. Therm. Anal. Calorim.* **2015**, *122* (3), 1319–1330.
- (182) Hu, D.; Chen, J.; Zhao, L.; Liu, T. *Thermochim. Acta* **2015**, *617*, 65–75.
- (183) LIU, J.; MO, Z.; QI, Y.; ZHANG, H.; CHEN, D. *Acta Polym. Sin.* **1993**, *1*, 0.
- (184) Myoung, S. H.; Im, S. S.; Kim, S. H. *Polym. Int.* **2016**, *65* (1), 115–124.
- (185) Liu, J.; Mo, Z.; Qi, Y.; Zhang, H.; Chen, D. *Acta Polym. Sin.* **1993**, No. 1, 1–6.
- (186) Flory, P. J.; Rehner, J. *J. Chem. Phys.* **1943**, *11* (11), 521.
- (187) Akalp, U.; Chu, S.; Skaalure, S. C.; Bryant, S. J.; Doostan, A.; Vernerey, F. J. *Polymer* . **2015**, *66*, 135–147.
- (188) Merrill, E. W.; Dennison, K. A.; Sung, C. *Biomaterials* **1993**, *14* (15), 1117–1126.
- (189) Özdemir, C.; Güner, A. *Eur. Polym. J.* **2007**, *43* (7), 3068–3093.
- (190) Polverari, M.; van de Ven, T. G. M. *J. Phys. Chem.* **1996**, *100* (32), 13687–13695.
- (191) Lai, C.-Y.; Hiltner, A.; Baer, E.; Korley, L. T. J. *ACS Appl. Mater. Interfaces* **2012**, *4*, 2218–2227.
- (192) Scherrer, P. Zsigmondy, R., Ed.; Springer Berlin Heidelberg: Berlin, Heidelberg, 1912; pp 387–409.
- (193) Jiang, S.; Qiao, C.; Tian, S.; Ji, X.; An, L.; Jiang, B. *Polymer* . **2001**, *42* (13), 5755–5761.
- (194) Yang, Y.; Huo, H. *J. Polym. Sci. Part B Polym. Phys.* **2013**, *51*, 1162–1174.
- (195) Monshi, A.; Foroughi, M. R.; Monshi, M. R. *World J. Nano Sci. Eng.* **2012**, *2* (3), 154–160.
- (196) Langford, J. I.; Wilson, A. J. C. *J. Appl. Crystallogr.* **1978**, *11* (2), 102–113.
- (197) Pfefferkorn, D.; Kyeremateng, S. O.; Busse, K.; Kammer, H.-W.; Thurn-Albrecht, T.; Kressler, J. *Macromolecules* **2011**, *44* (8), 2953–2963.

- (198) Goddard, R.; Heinemann, O.; Krüger, C. *Acta Crystallogr. Sect. C Cryst. Struct. Commun.* **1997**, *53* (12), 1846–1850.
- (199) Chen, E.-Q.; Xue, G.; Jin, S.; Lee, S.-W.; Mann, I.; Moon, B.-S.; Harris, F. W.; Cheng, S. Z. D. *Macromol. Rapid Commun.* **1999**, *20* (8), 431–434.
- (200) Ruland, W. *Acta Crystallogr.* **1961**, *14* (11), 1180–1185.
- (201) Balko, J.; Lohwasser, R. H.; Sommer, M.; Thelakkat, M.; Thurn-Albrecht, T. *Macromolecules* **2013**, *46* (24), 9642–9651.
- (202) Hunter, C. A.; Sanders, J. K. M. *J. Am. Chem. Soc.* **1990**, *112* (14), 5525–5534.
- (203) Lee, K.-H.; Snively, C. M.; Givens, S.; Chase, D. B.; Rabolt, J. F. *Macromolecules* **2007**, *40* (7), 2590–2595.
- (204) Ungar, G.; Stejny, J.; Keller, A.; Bidd, I.; Whiting, M. C. *Science* **1985**, *229* (4711), 386–389.
- (205) Florio, G. M.; Werblowsky, T. L.; Ilan, B.; Müller, T.; Berne, B. J.; Flynn, G. W. *J. Phys. Chem. C* **2008**, *112*, 18067–18075.
- (206) Shen, X.; Hu, W.; Russell, T. P. *Macromolecules* **2016**, *49* (12), 4501–4509.
- (207) Alabi, C. A.; Chen, Z.; Yan, Y. S.; Davis, M. E. *Chem. Mater.* **2009**, *21* (19), 4645–4652.
- (208) Brubach, J. B.; Ollivon, M.; Jannin, V.; Mahler, B.; Bourgaux, C.; Lesieur, P.; Roy, P. *J. Phys. Chem. B* **2004**, *108* (46), 17721–17729.
- (209) Rosa, C. De; Auriemma, F. *Crystals and Crystallinity in Polymers: Diffraction Analysis of Ordered and Disordered Crystals*; Wiley: Hoboken, NJ, 2014.
- (210) Janiak, C. *J. Chem. Soc., Dalt. Trans.* **2000**, 3885–3896.
- (211) Bradley, R. S. *J. Phys. Chem.* **1956**, *60* (2), 1347–1354.
- (212) Cagle Jr., F. W.; Eyring, H. *J. Phys. Chem.* **1953**, *57*, 942–946.
- (213) Wunderlich, B. *J. Chem. Phys.* **1958**, *29* (6), 1395–1404.
- (214) Bondi, A. *J. Phys. Chem.* **1964**, *68* (3), 441–451.
- (215) Simon, F. T.; Rutherford, J. M. *J. Appl. Phys.* **1964**, *35* (1), 82–86.

6. Appendix

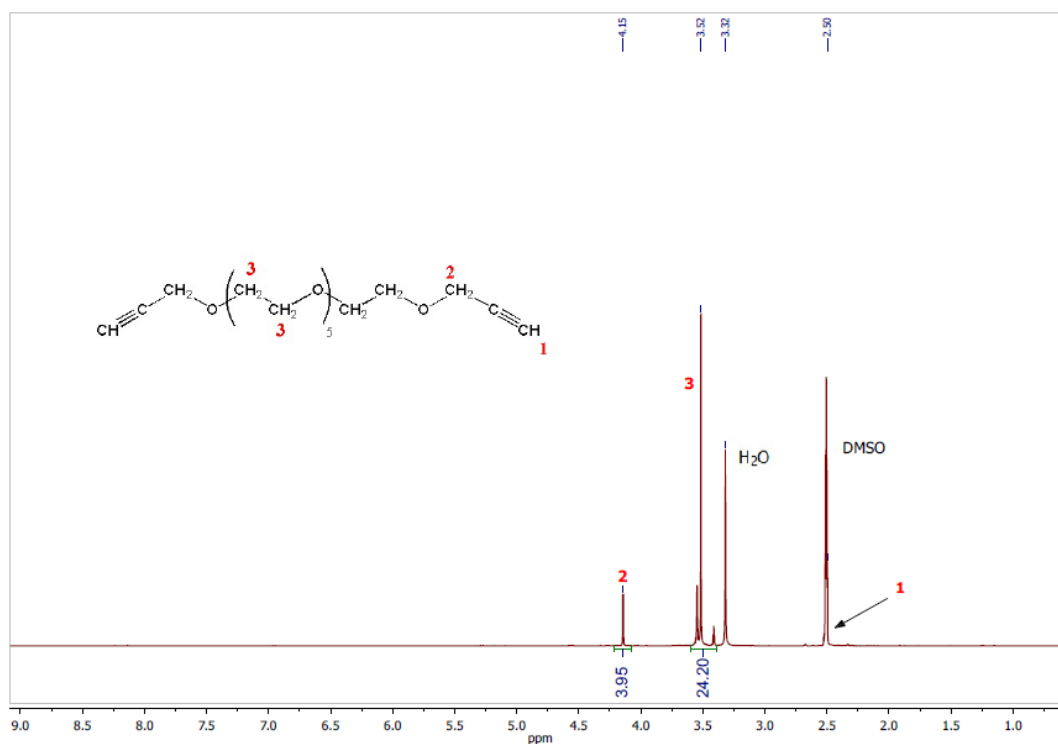


Figure A1: ¹H NMR spectrum of PEG(300)-Alkyne in DMSO-d₆ (400 MHz, 27 °C).¹⁵²

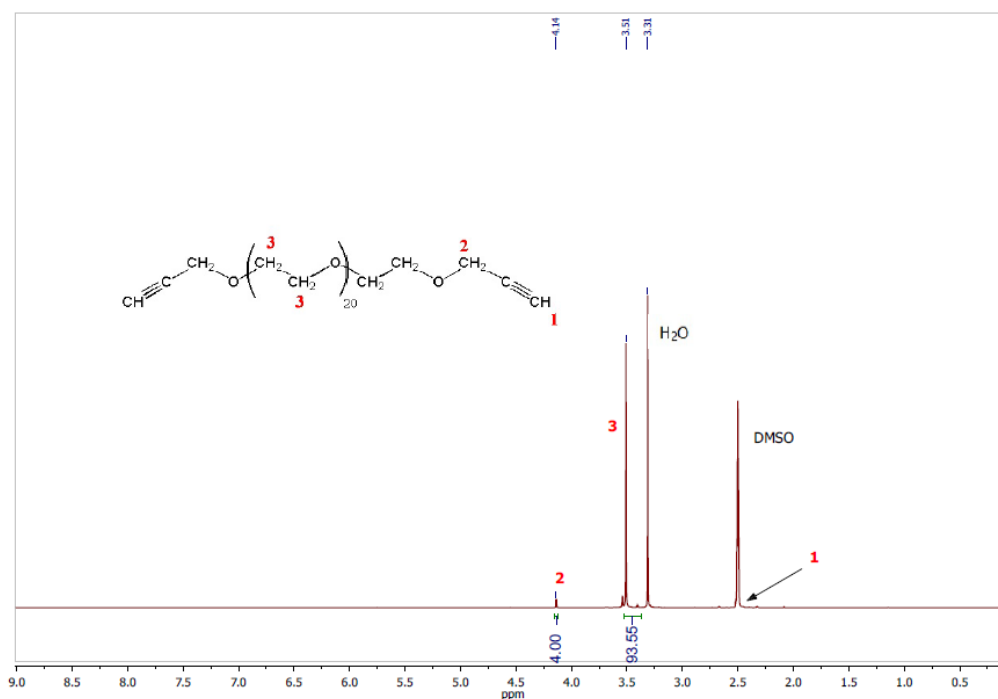


Figure A2: ¹H NMR spectrum of PEG(1000)-Alkyne in DMSO-d₆ (400 MHz, 27 °C).¹⁵²

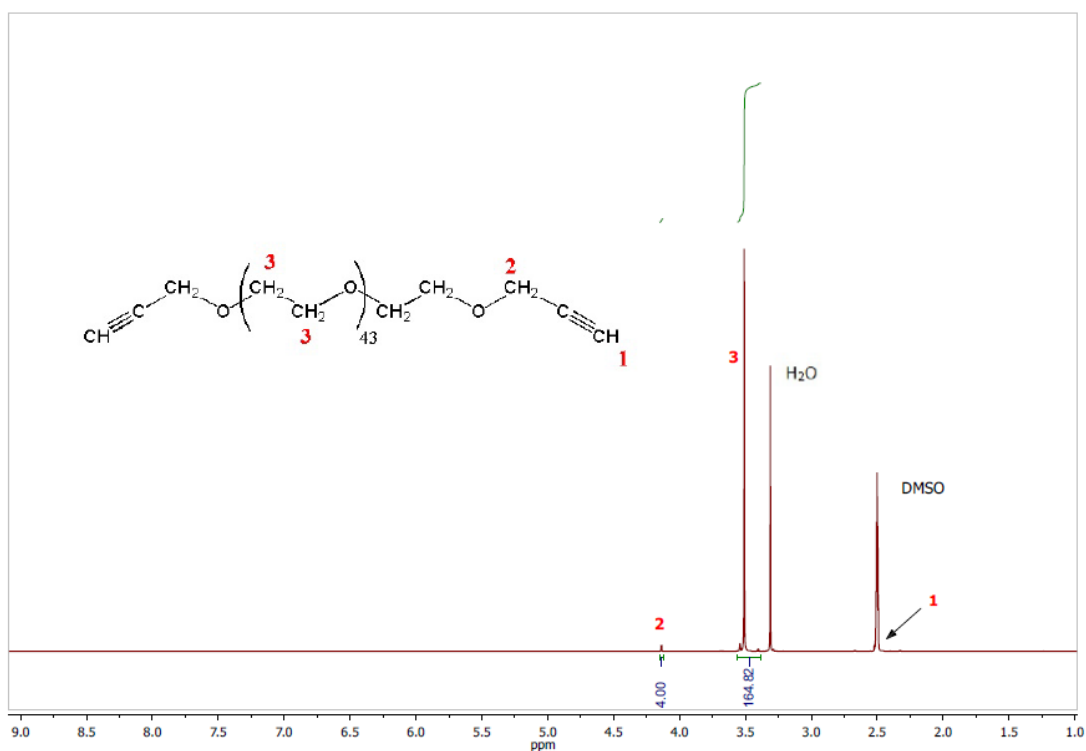


Figure A3: ¹H NMR spectrum of PEG(2000)-Alkyne in DMSO-*d*₆ (400 MHz, 27 °C).¹⁵²

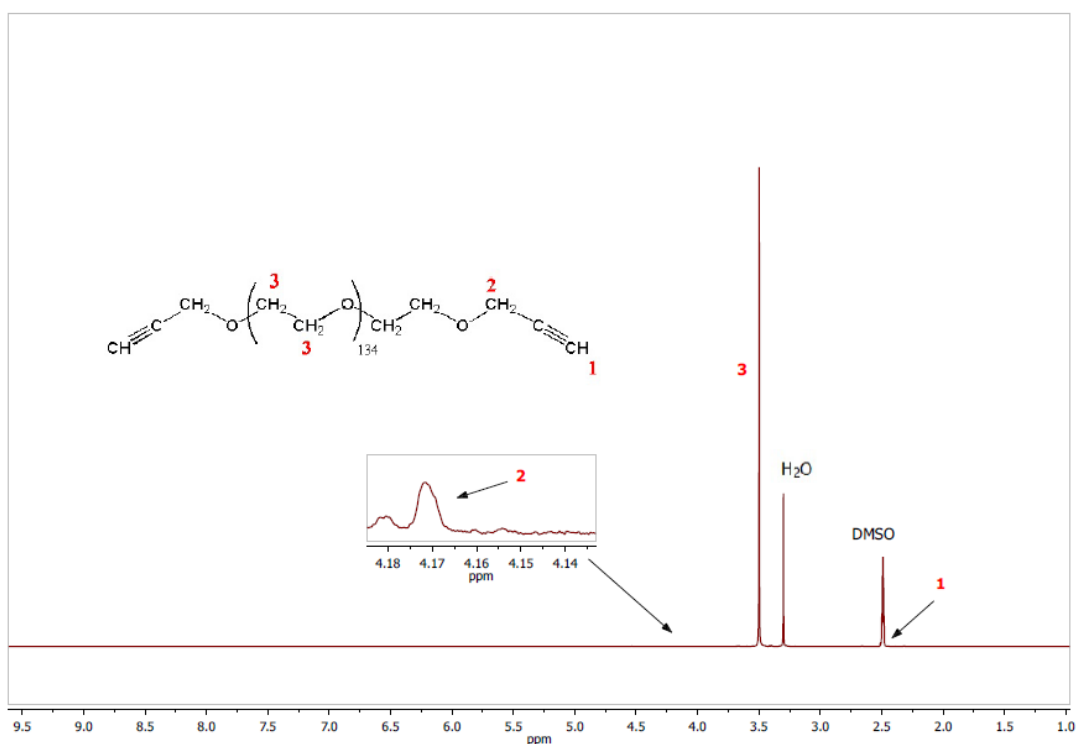


Figure A4: ¹H NMR spectrum of PEG(6000)-Alkyne in DMSO-*d*₆ (400 MHz, 27 °C).¹⁵²

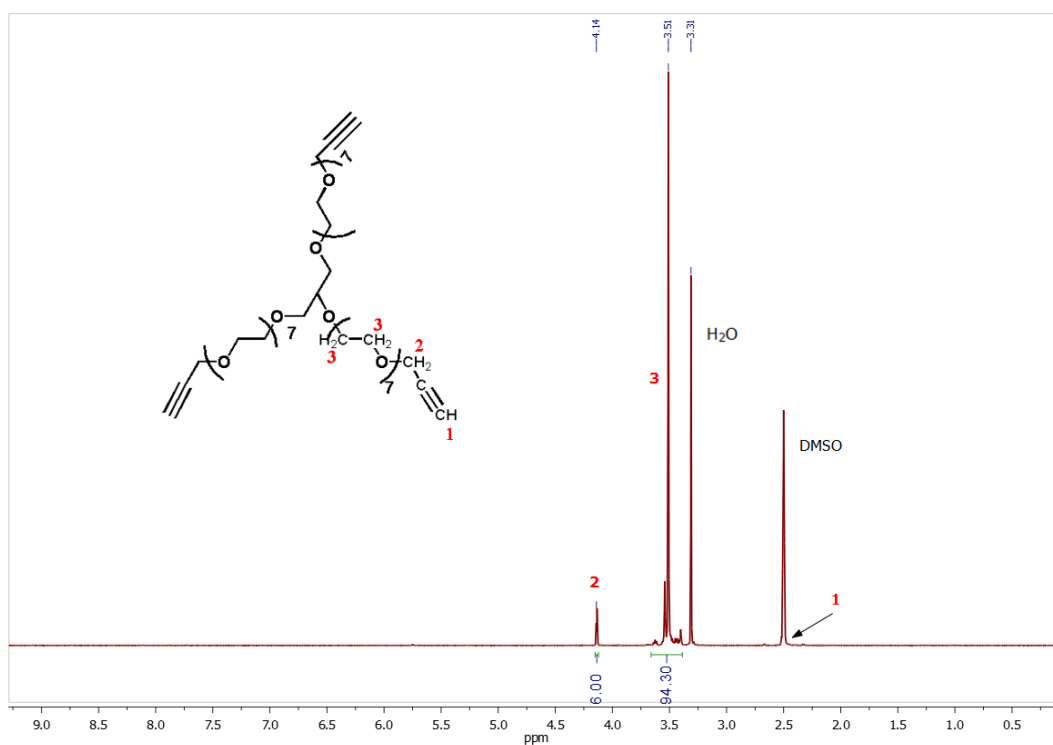


Figure A5: ^1H NMR spectrum of PEG(S)-Alkyne in $\text{DMSO-}d_6$ (400 MHz, 27 °C).¹⁵²

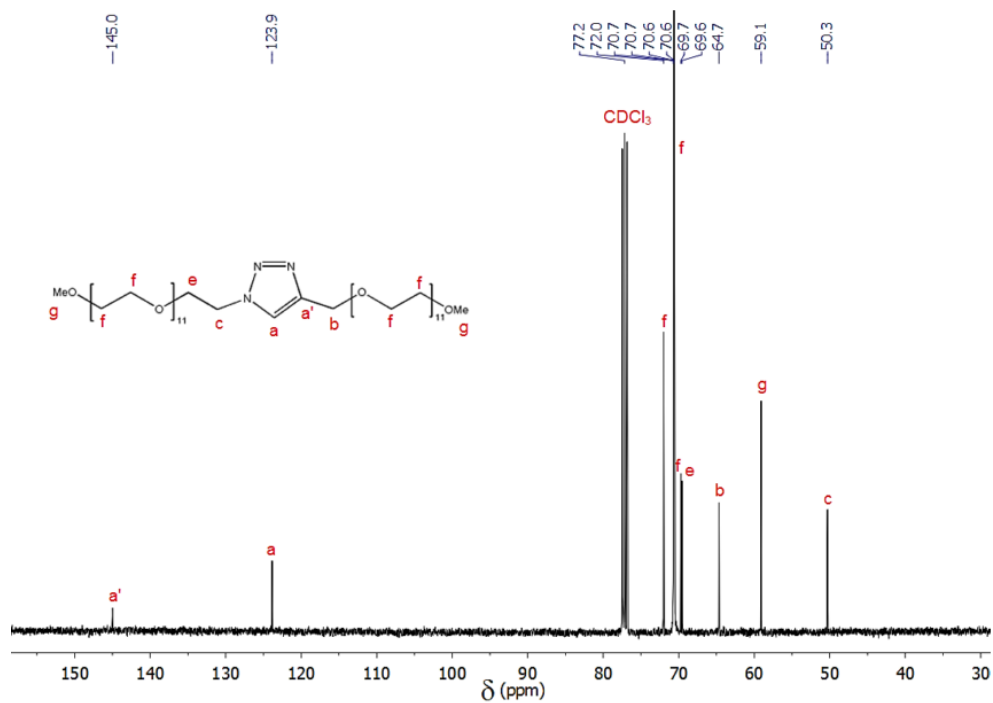


Figure A6: ^{13}C NMR spectrum of PEG₁₁-TR-PEG₁₁ in CDCl_3 (100 MHz, 27 °C).⁸⁸

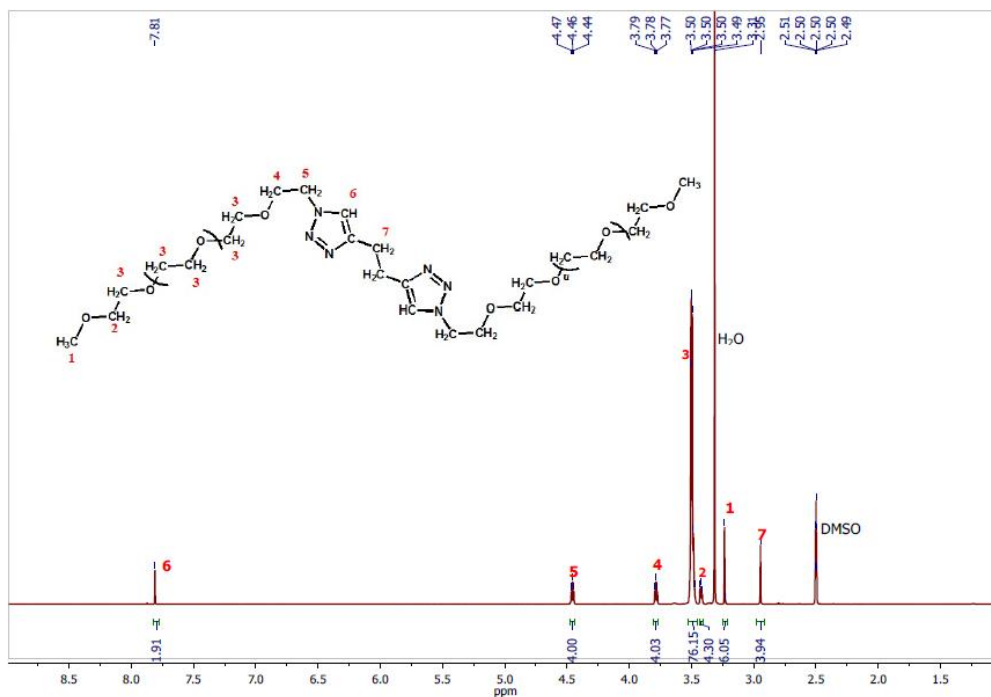


Figure A7: ^1H NMR spectrum of $\text{PEG}_{11}\text{-TR}(\text{CH}_2)_2\text{-TR-PEG}_{11}$ in $\text{DMSO-}d_6$ (500 MHz, 27 °C).

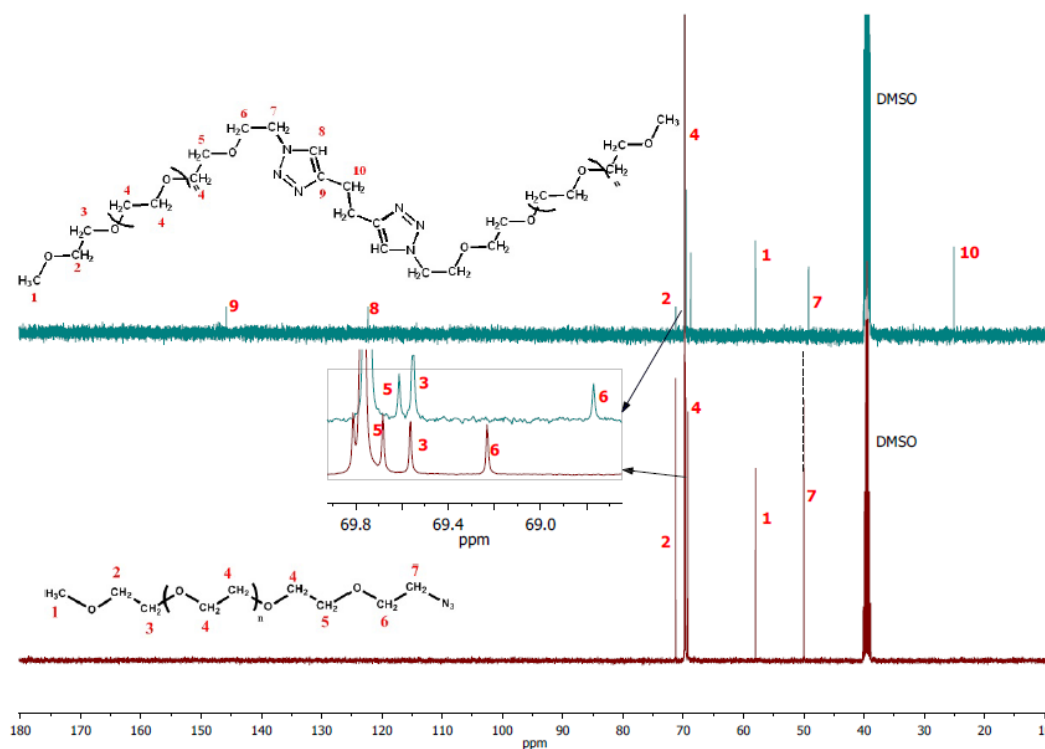


Figure A8: Comparative ^{13}C NMR spectra of $\text{PEG}_{11}\text{-TR}(\text{CH}_2)_2\text{-TR-PEG}_{11}$ (top) and $\text{PEG}_{11}\text{-Azide}$ (bottom) in $\text{DMSO-}d_6$ (125 MHz, 27 °C).

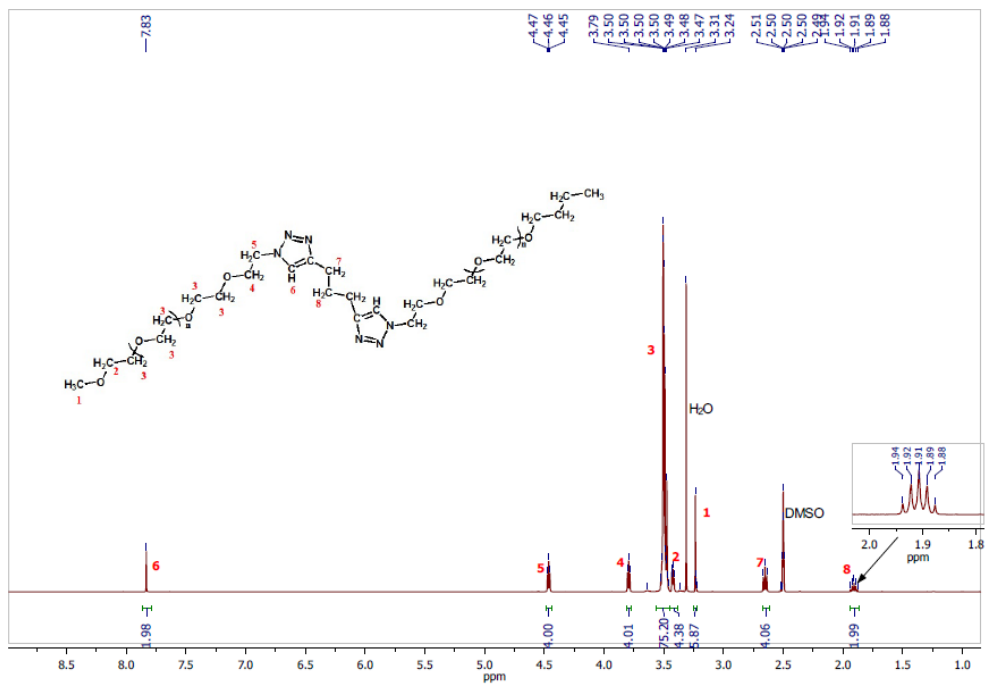


Figure A9: ¹H NMR spectrum of PEG₁₁-TR-(CH₂)₃-TR-PEG₁₁ in DMSO-*d*₆ (500 MHz, 27 °C).

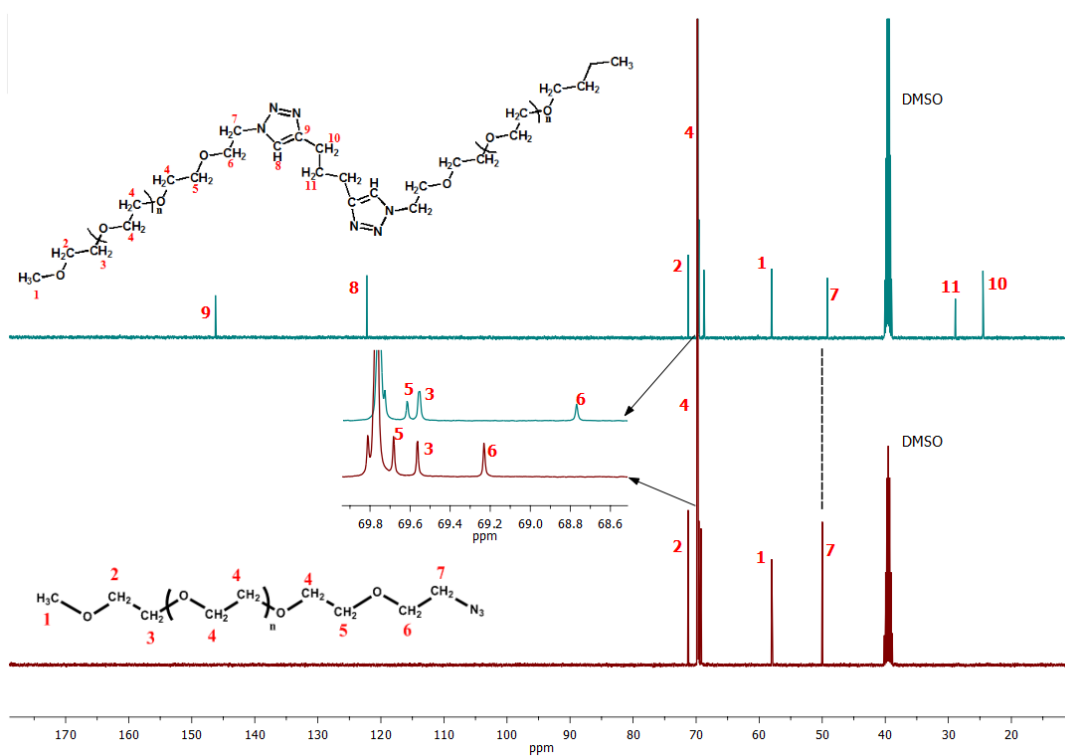


Figure A10: Comparative ¹³C NMR spectra of PEG₁₁-TR-(CH₂)₃-TR-PEG₁₁ (top) and PEG₁₁-Azide (bottom) in DMSO-*d*₆ (125 MHz, 27 °C).

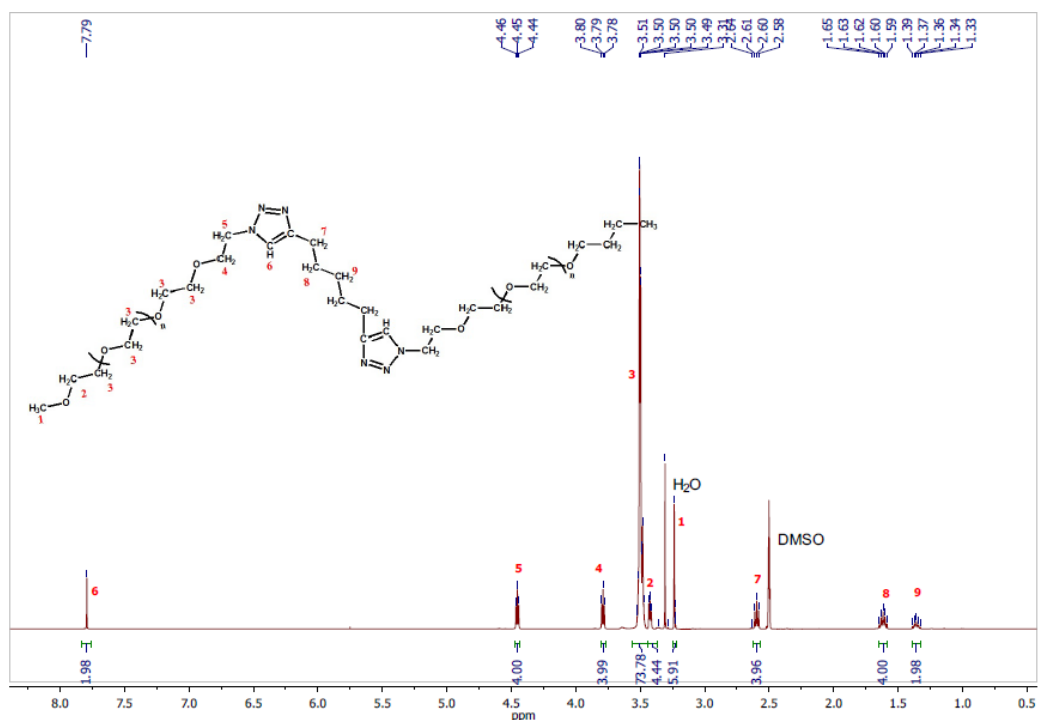


Figure A11: ¹H NMR spectrum of PEG₁₁-TR-(CH₂)₅-TR-PEG₁₁ in DMSO-*d*₆ (500 MHz, 27 °C).

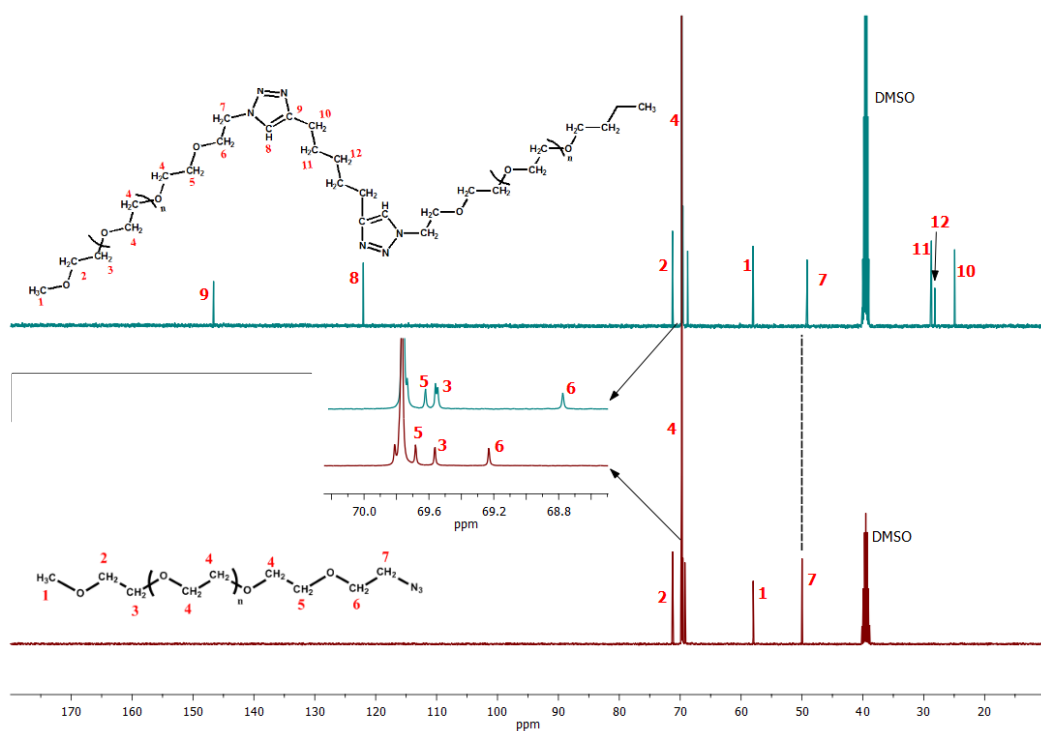


Figure A12: Comparative ¹³C NMR spectra of PEG₁₁-TR-(CH₂)₅-TR-PEG₁₁ (top) and PEG₁₁-Azide (bottom) in DMSO-*d*₆ (125 MHz, 27 °C).

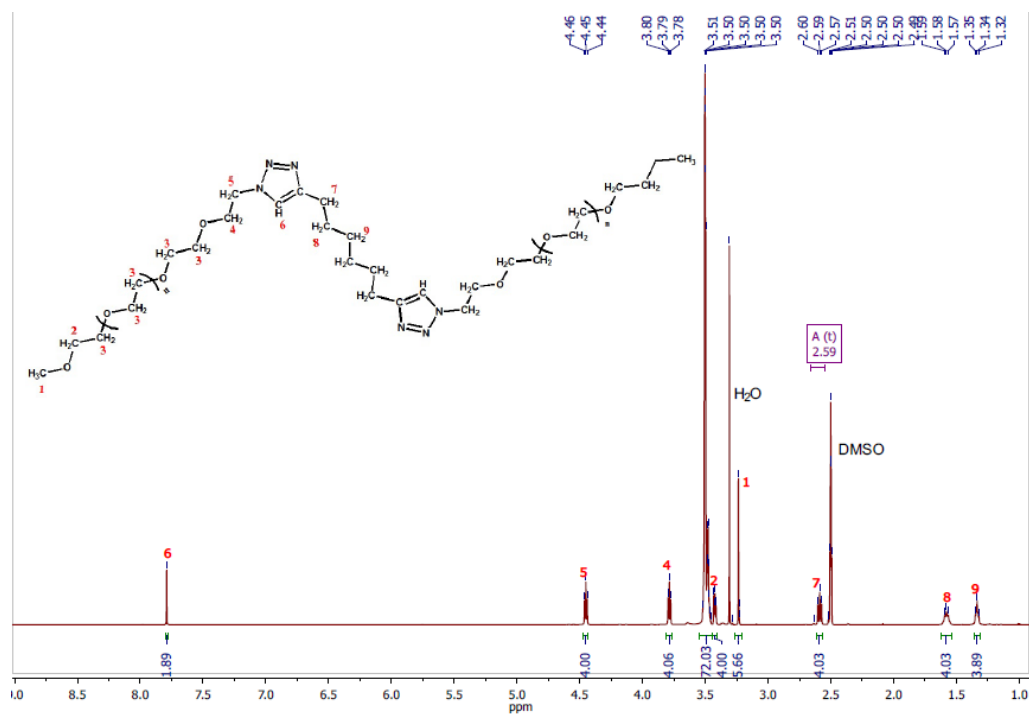


Figure A13: ¹H NMR spectrum of PEG₁₁-TR-(CH₂)₆-TR-PEG₁₁ in DMSO-*d*₆ (500 MHz, 27 °C).

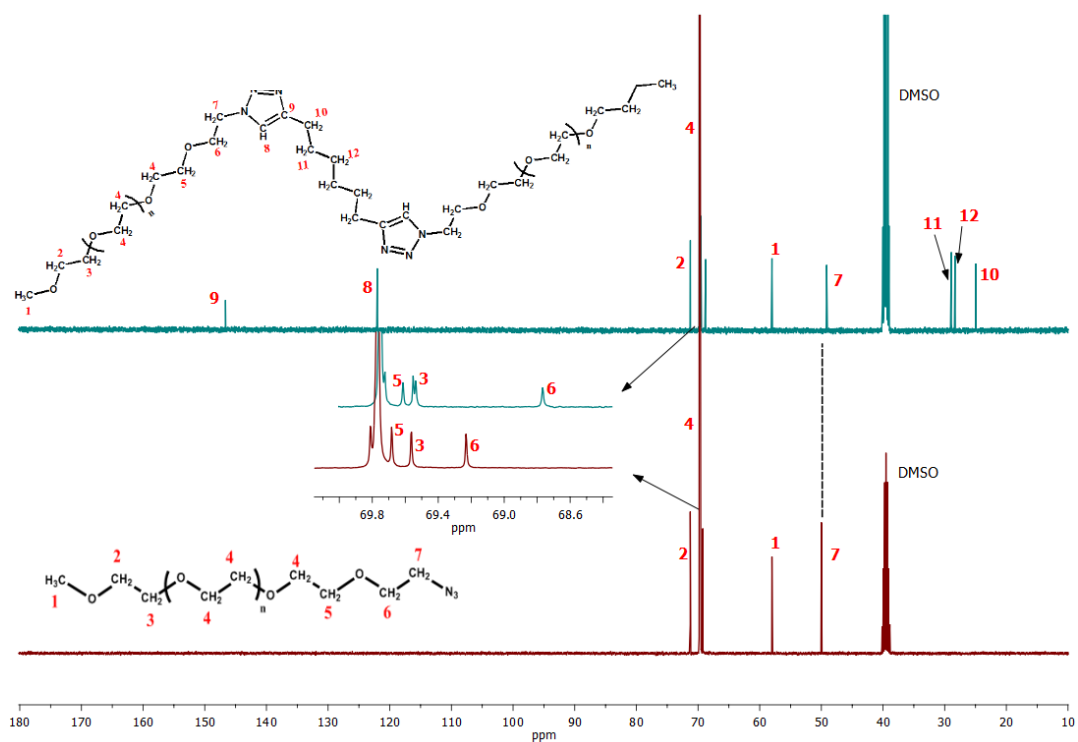


Figure A14: Comparative ¹³C NMR spectra of PEG₁₁-TR-(CH₂)₆-TR-PEG₁₁ (top) and PEG₁₁-Azide (bottom) in DMSO-*d*₆ (125 MHz, 27 °C).

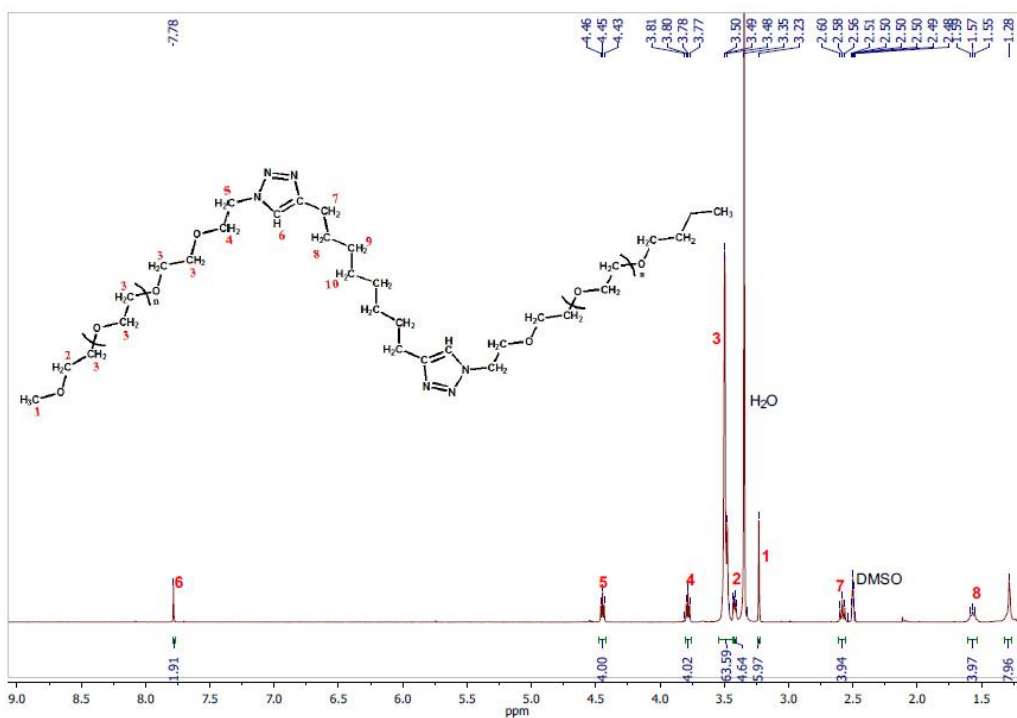


Figure A15: ¹H NMR spectrum of PEG₁₁-TR-(CH₂)₈-TR-PEG₁₁ in DMSO-*d*₆ (500 MHz, 27 °C).

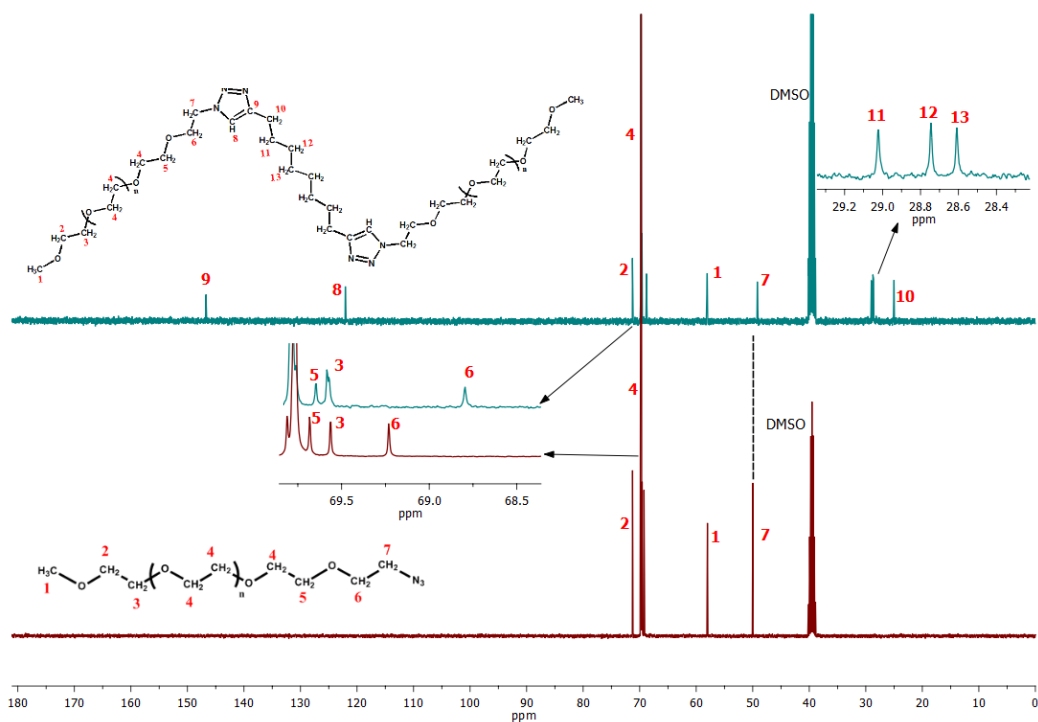


Figure A16: Comparative ¹³C NMR spectra of PEG₁₁-TR-(CH₂)₈-TR-PEG₁₁ (top) and PEG₁₁-Azide (bottom) in DMSO-*d*₆ (100 MHz, 27 °C).

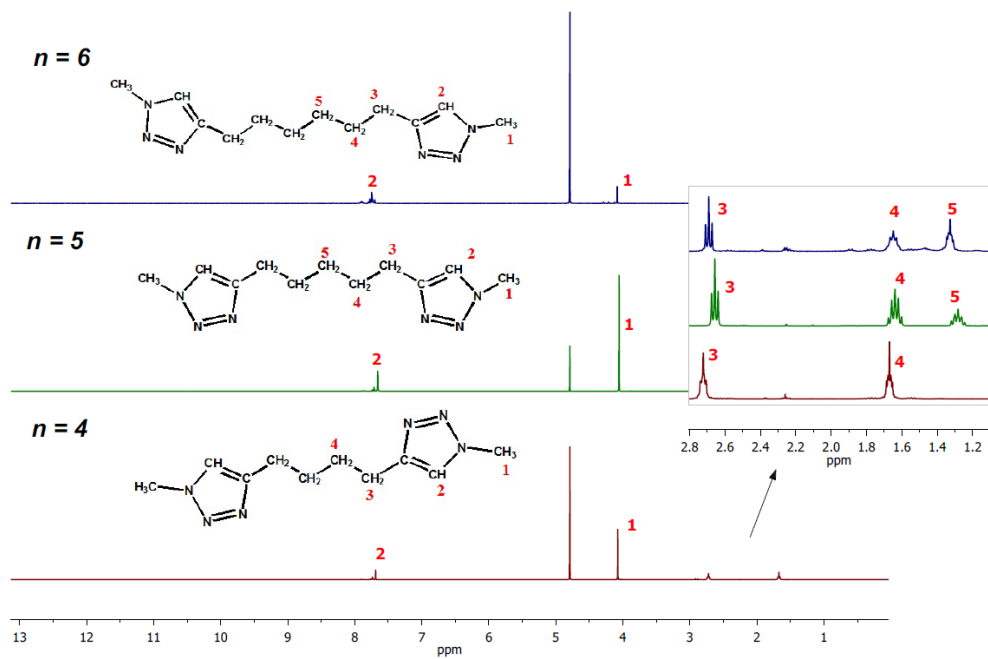


Figure A17: ^1H NMR spectra of Me-TR-(CH₂)_n-TR-Me ($n = 4-6$) in D₂O (400 MHz, 27 °C).

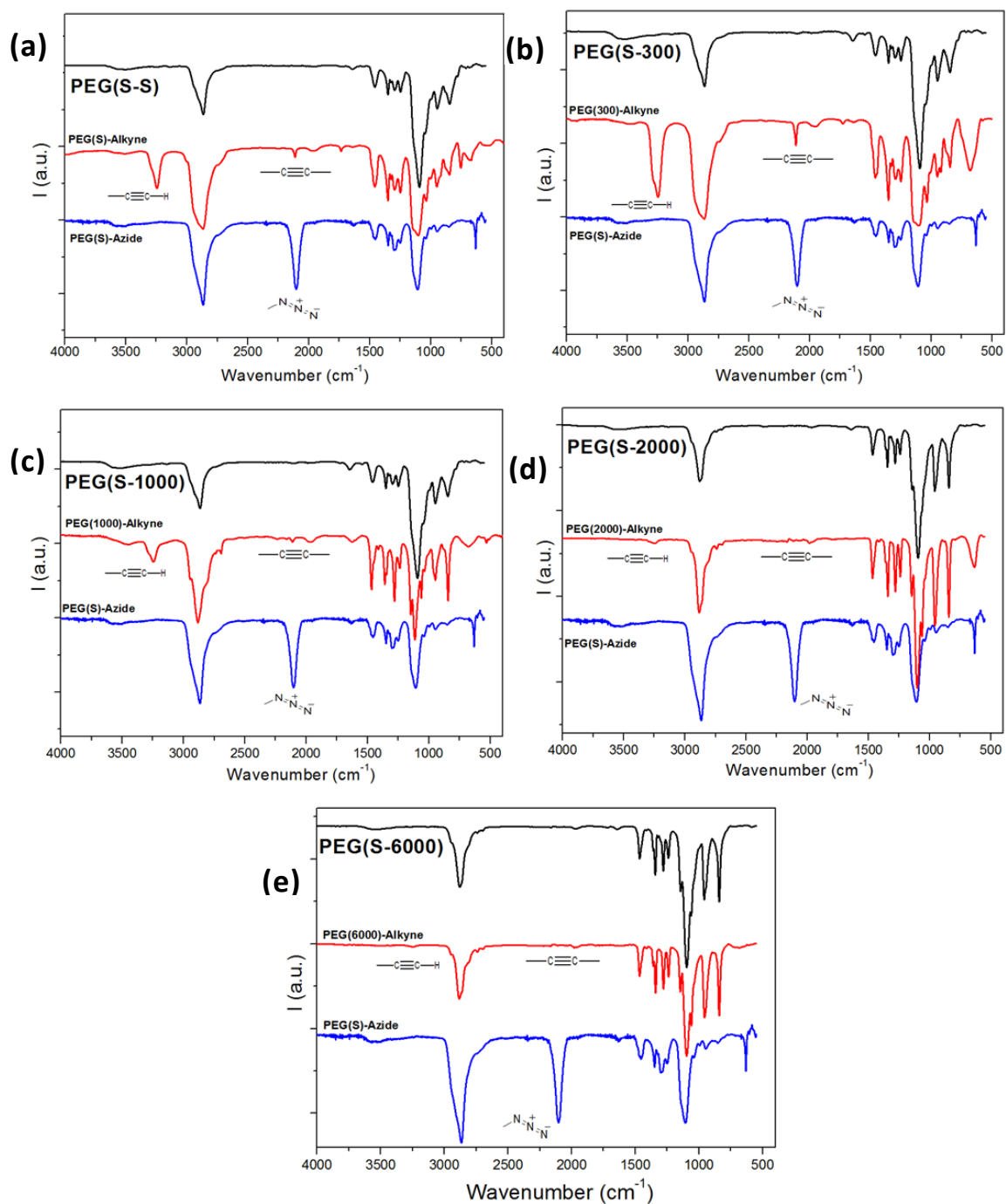


Figure A18: FT-IR spectra of (a) PEG(S-S), (b) PEG(S-300), (c) PEG(S-1000), (d) PEG(S-2000) and (e) PEG(S-6000).¹⁵²

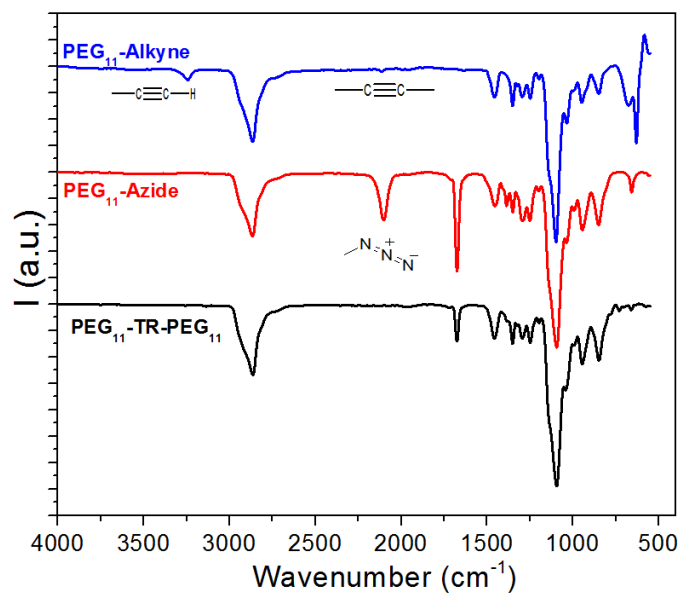


Figure A19: FT-IR spectra of PEG₁₁-TR-PEG₁₁, PEG₁₁-Alkyne and PEG₁₁-Azide.¹⁵²

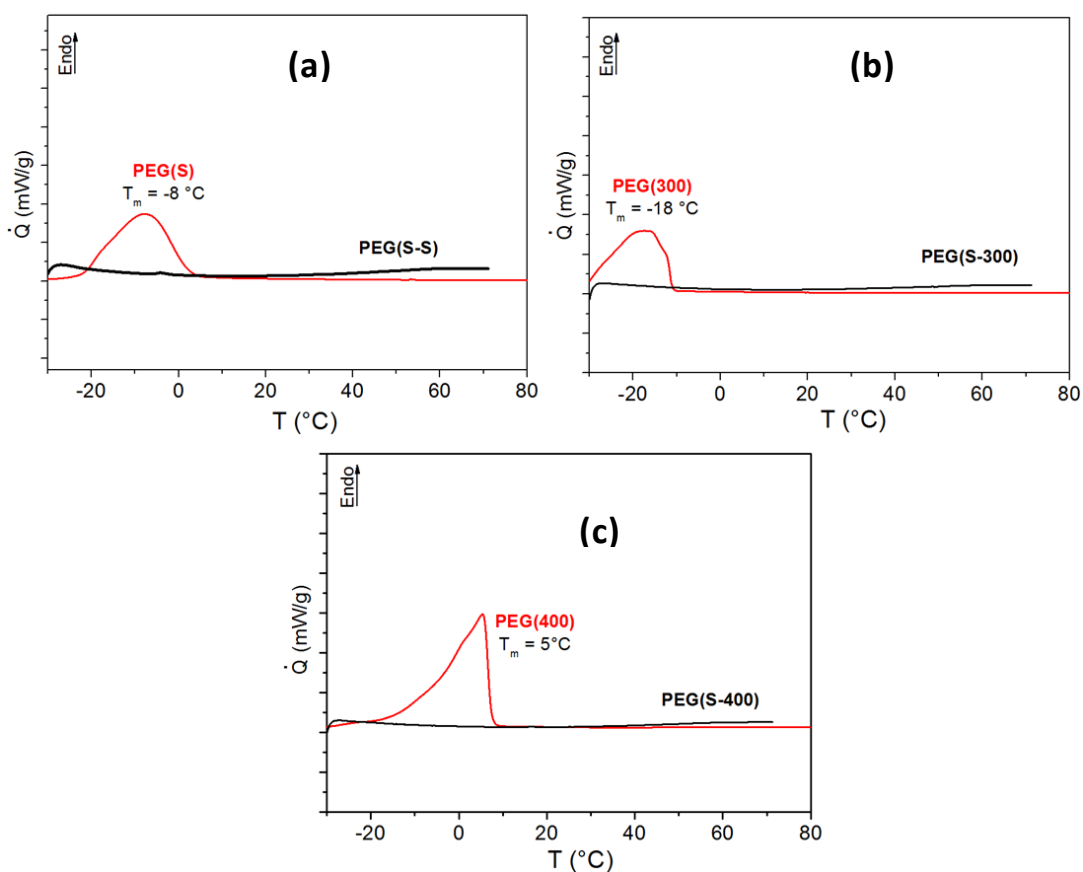


Figure A20: DSC traces of (a) PEG(S-S), (b) PEG(S-300) and (c) PEG(S-400)

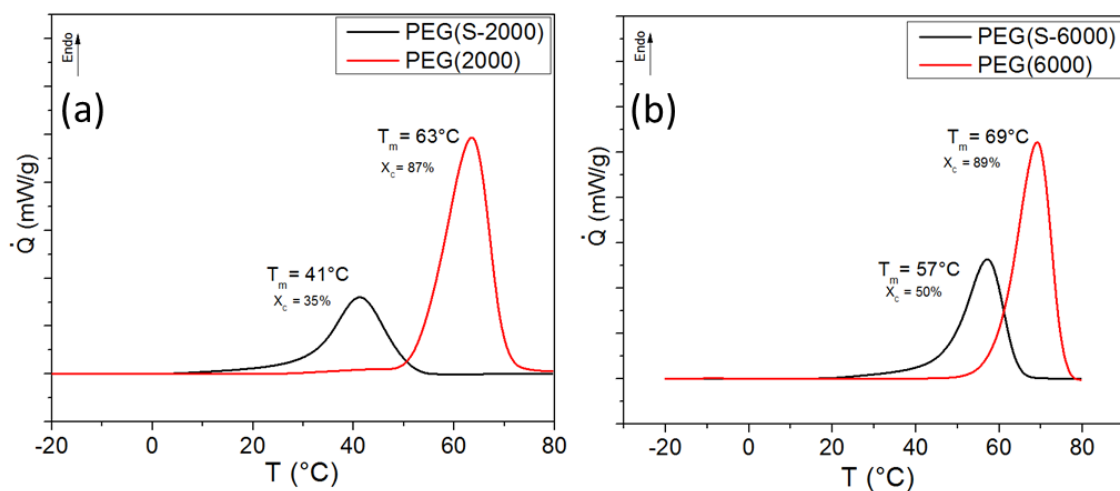


Figure A21: A combined DSC plot of (a) PEG(S-2000) and PEG(2000) and (b) PEG(S-6000) and PEG(6000).

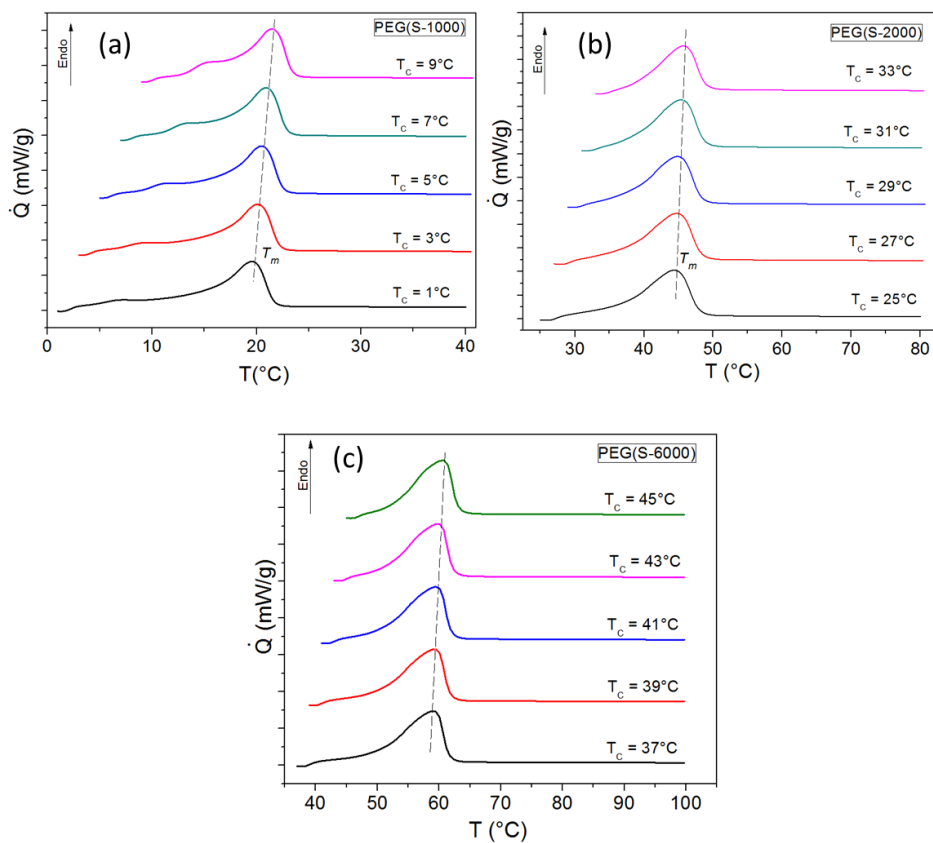


Figure A22: (a-c) DSC melting endotherms of PEG(S-1000), PEG(S-2000) and PEG(S-6000) after crystallization at different isothermal crystallization temperatures T_c

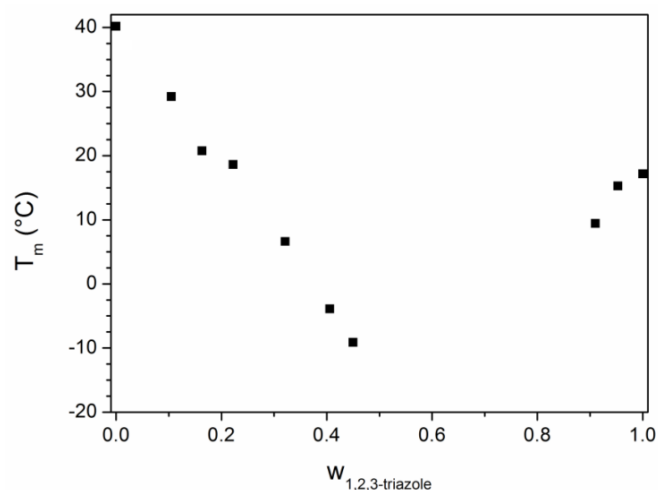


Figure A23. Phase diagram of mixtures of PEG₂₂ and 1,2,3-triazole where w is the mass fraction of 1,2,3- triazole. The melting temperatures of the mixtures were obtained by DSC. It should be noted that the mixtures with intermediate concentrations ($0.45 \leq w \leq 0.90$) showed no crystallization during cooling to $T = -40$ °C but also a homogeneous phase in the optical micrographs.⁸⁸

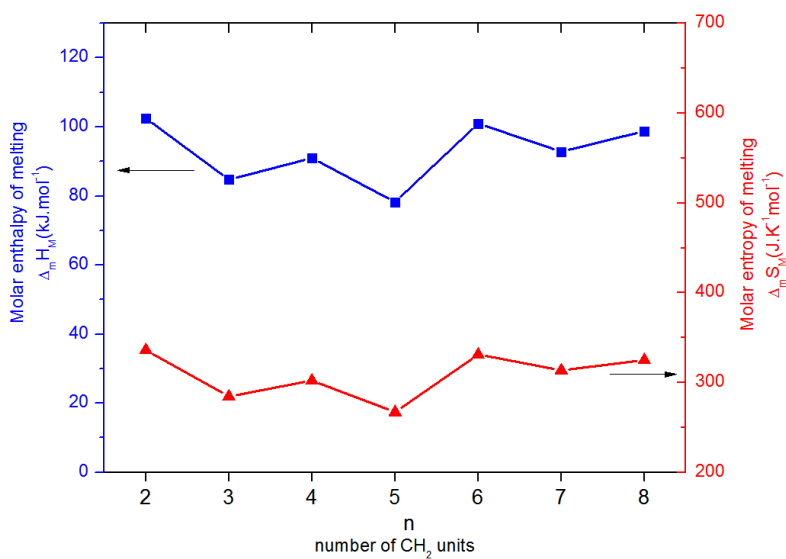


Figure A24: Molar enthalpy of melting $\Delta_m H_M$ and molar entropy of melting $\Delta_m S_M$ of PEG₁₁-TR-(CH₂)_n-TR-PEG₁₁ where $n = 2-8$.

Table A1: X_C values of PEG₁₁-TR-(CH₂)_n-TR-PEG₁₁, where $n = 2-8$,

n	T	X_C
	°C	%
2	-10	44
	16	47
3	-10	39
	16	32
4	-10	41
	14	35
	20	35
5	-10	41
	14	30
6	-10	43
	20	33
7	-10	39
	6	38
8	-10	39
	26	33

Small Angle X-ray Scattering (SAXS)

1. PEG₁₁-TR-(CH₂)₂-TR-PEG₁₁

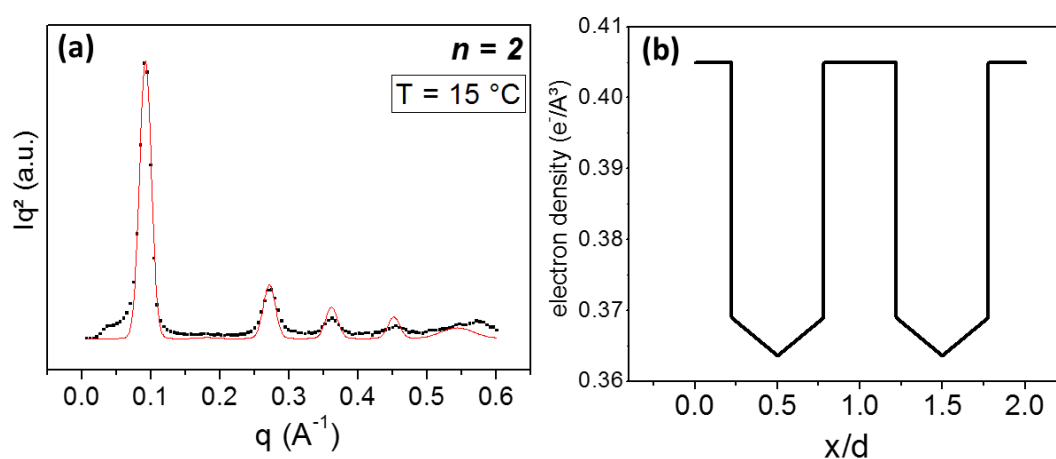


Figure A26: (a) SAXS trace of PEG₁₁-TR-(CH₂)₂-TR-PEG₁₁ at $T = 15$ °C; the red line represents the fitting of SAXS trace with the scattering function (Eq. 2.1, see main text)

for details). (b) Electron density profile of a two-phase model, consisting of a crystalline layer, and amorphous part with decreasing electron density to its center.

A constant electron density in the amorphous part was not sufficient to describe the data. Absolute values of electron density of crystalline ($\rho_c = 0.405 \text{ e}^-/\text{\AA}^3$) and amorphous part ($\rho_a = 0.369 \text{ e}^-/\text{\AA}^3$) are values of neat PEG²¹⁵ and not varied during fitting. Fitting results with crystallinities above 50% were neglected. The form factor of this model is:

$$F(n) = \left((\rho_c - \rho_a) \sin(n \cdot \pi \cdot \Phi_a) + 2\varepsilon \frac{1 - \cos(n \cdot \pi \cdot \Phi_a)}{n} \right)^2 / n^2$$

with the density decrease height ε within the amorphous phase. Free fit factors are Φ_a (volume fraction of amorphous phase), ε and from the structure factor q^* , width w , amplitude a and Debye-Waller-factor u^2 .

2. PEG₁₁-TR-(CH₂)₆-TR-PEG₁₁

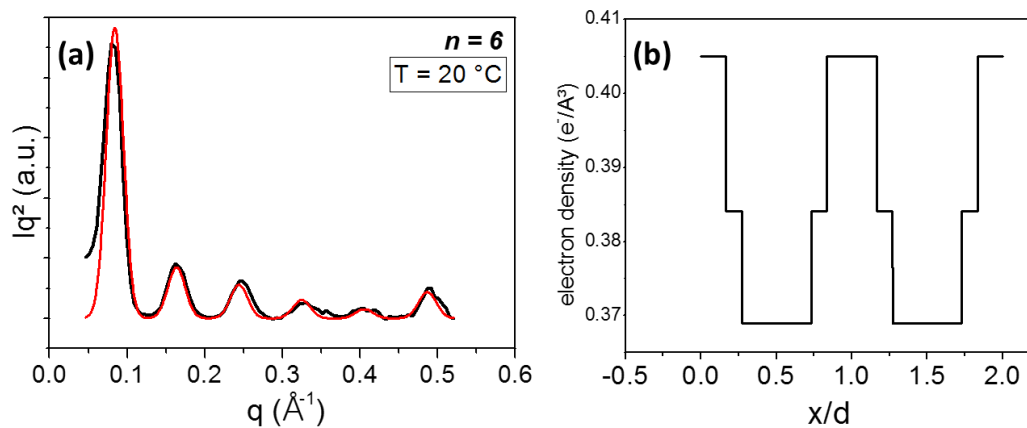


Figure A27: (a) SAXS trace of PEG₁₁-TR-(CH₂)₆-TR-PEG₁₁ at $T = 20 \text{ }^\circ\text{C}$; the red line represents the fitting of SAXS trace with the scattering function (eq. 2.1, see main text for details) using (b) electron density profile of a three-phase model, consisting of a crystalline layer, transition region and amorphous part.

A decrease of the electron density in the amorphous part was not necessary to fit the data, but a density profile without the additional transition region was not sufficient to

describe the data. Absolute values of electron density of crystalline ($\rho_c = 0.405 \text{ e}^-/\text{\AA}^3$) and amorphous part ($\rho_a = 0.369 \text{ e}^-/\text{\AA}^3$) are values of neat PEG²¹⁵ and not varied during fitting. Fitting results with crystallinities above 50% were neglected. The form factor of this model is:

$$F(n) = \frac{\left((\rho_c - \rho_t) \sin(n \cdot \pi \cdot (\Phi_t + \Phi_a)) + (\rho_t - \rho_a) \sin(n \cdot \pi \cdot \Phi_a) \right)^2}{n^2}$$

with volume fraction Φ_t and electron density ρ_t of the transition phase. Free fit factors are Φ_a , Φ_t and ρ_t and from the structure factor q^* , width w , amplitude a and Debye-Waller-factor u^2 .

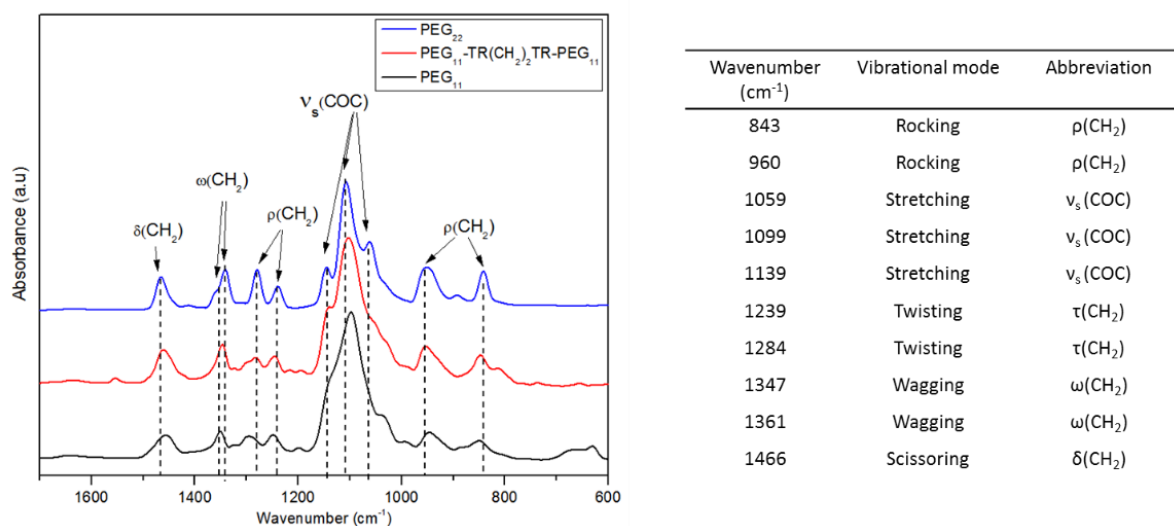


Figure A28: IR spectrum of the PEG-TR'' phase of PEG₁₁-TR-(CH₂)₂-TR-PEG₁₁ at $T = 20 \text{ }^\circ\text{C}$. The spectra of crystalline PEG₂₂ and molten PEG₁₁ are also shown for comparison. The arrows show the respective vibration modes at different wave number.

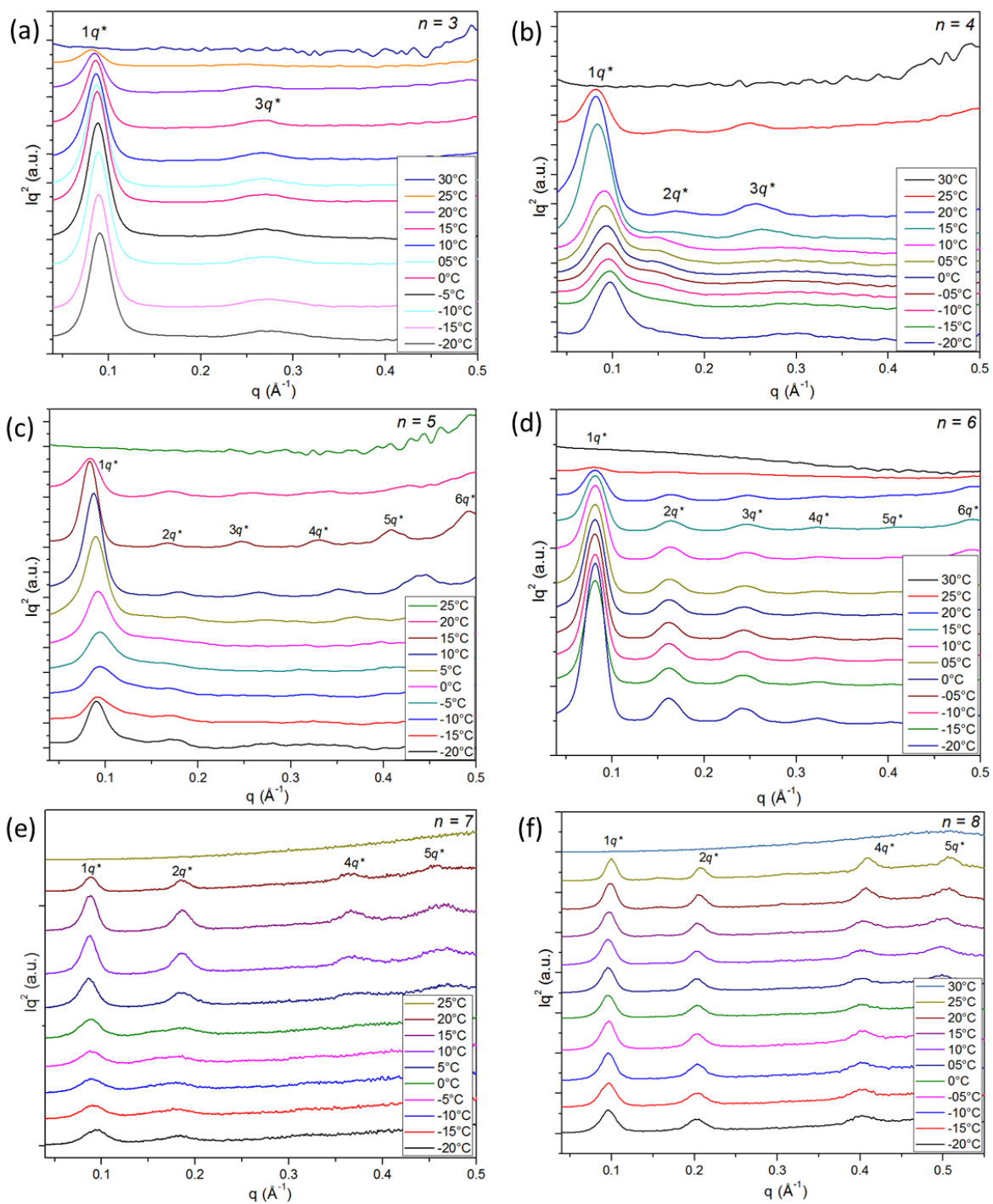


Figure A29: Temperature dependent SAXS traces of PEG₁₁-TR-(CH₂)_n-TR-PEG₁₁ for $n = 3-8$

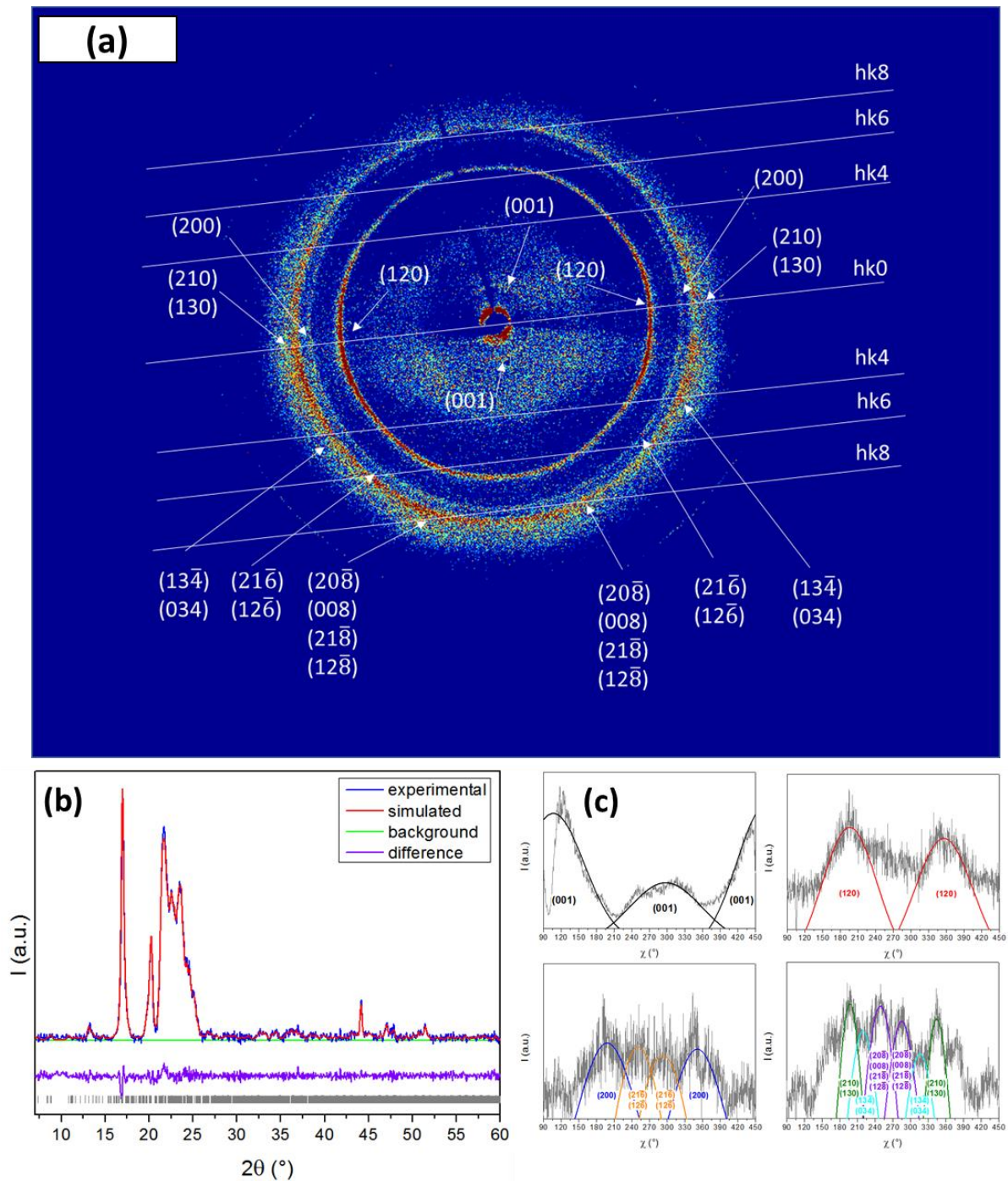


Figure A30: (a) The 2D-diffraction pattern of PEG₁₁-TR-(CH₂)₂-TR-PEG₁₁. **(b)** Refinement of the WAXS diffractogram of PEG₁₁-TR-(CH₂)₂-TR-PEG₁₁ at 18 °C with the 7₂ helix structure containing additionally the TR-(CH₂)₂-TR defect in the monoclinic unit cell (see main text for details) **(c)** Azimuthal intensity profiles of different reflections obtained from the oriented 2D WAXS pattern of PEG₁₁-TR-(CH₂)₂-TR-PEG₁₁ at $T = 18$ °C.

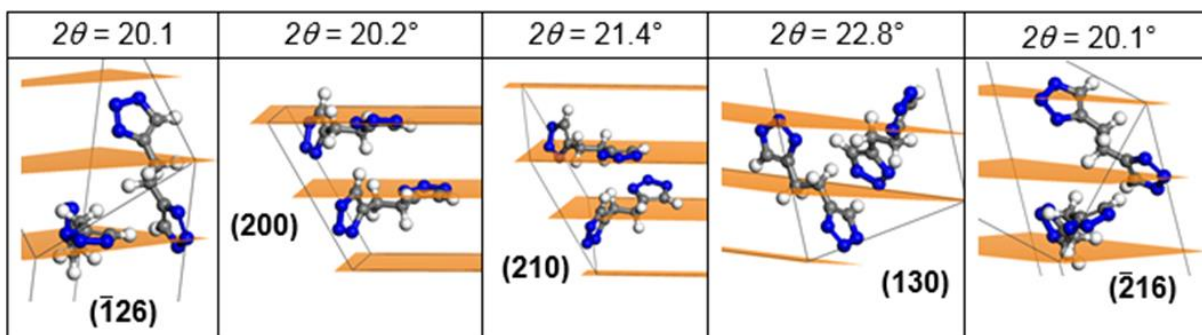


Figure A31: Intramolecular distances of the TR-(CH₂)₂-TR group

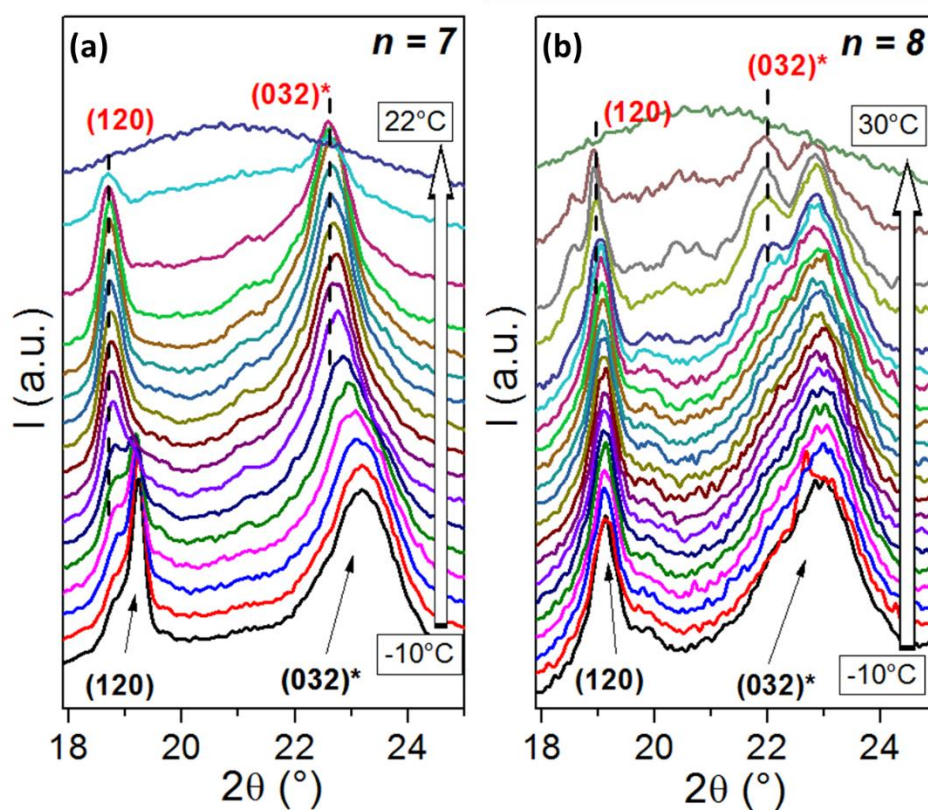


Figure A32: Temperature dependent WAXS diffraction pattern of PEG₁₁-TR-(CH₂)_n-TR-PEG₁₁ where (a) $n = 7$ and (b) $n = 8$ with the temperature step of $\Delta T = 4^\circ\text{C}$.

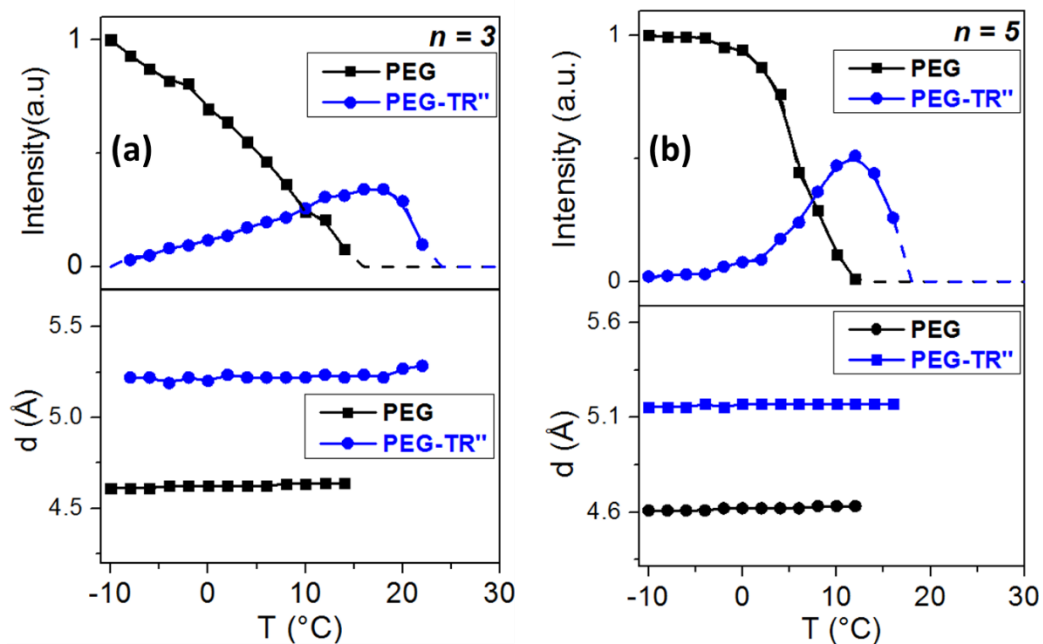


Figure A33: Normalized integral intensities (top) of the (120) reflection of low-temperature PEG phase and PEG-TR'' phase along with their respective interplanar distances (bottom) for PEG₁₁-TR-(CH₂)_n-TR-PEG₁₁ where, **(a)** $n = 3$, **(b)** $n = 5$.

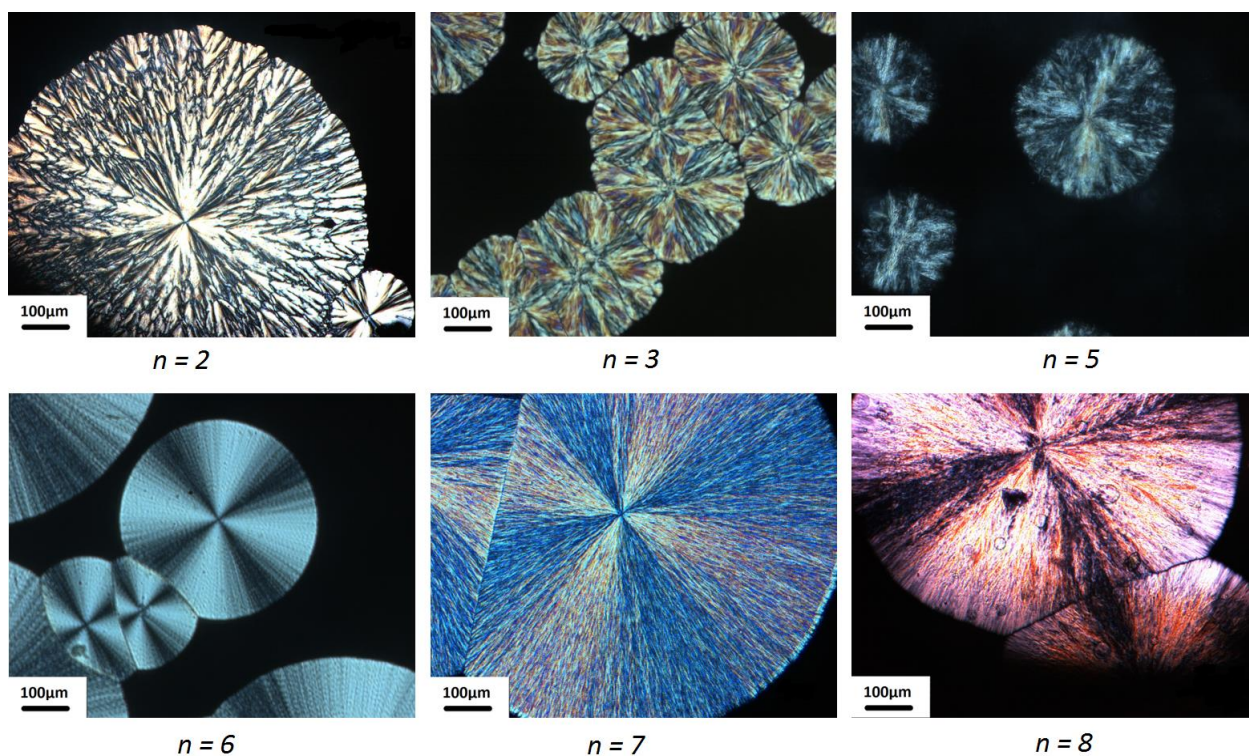


Figure A34: POM images of PEG₁₁-TR-(CH₂)_n-TR-PEG₁₁ where, $n = 2, 3, 5, 6, 7, 8$, isothermally crystallizes at $T = 5\text{ }^{\circ}\text{C}$

Irreversible phase transition in PEG₁₁-TR-(CH₂)_n-TR-PEG₁₁ ($n = 2, 4$)

1. PEG₁₁-TR-(CH₂)₂-TR-PEG₁₁

Temperature dependent wide angle X-ray scattering measurements were performed to observe an irreversible phase transition in PEG₁₁-TR-(CH₂)₂-TR-PEG₁₁ sample (see Figure A35). It can be observed that initially at $-10\text{ }^{\circ}\text{C}$, only two characteristic diffraction peaks of PEG monoclinic system was observed i.e. at $2\theta = 19.4^{\circ}$ (120) and $2\theta = 23.5^{\circ}$ (032)*. However upon heating, (120) reflection at $2\theta = 19.4^{\circ}$ of low-temperature PEG phase starts to diminish and disappeared completely at around $T = 16\text{ }^{\circ}\text{C}$. In the meanwhile, a new reflection at $2\theta = 17.1^{\circ}$, belongs to the (120) reflection of modified monoclinic system (see main text for detailed description) starts to appear at $T \approx -4\text{ }^{\circ}\text{C}$ and continuously grow in intensity until the final temperature. The second PEG diffraction peak (032)* at $2\theta = 23.5^{\circ}$ was also split upon heating into four new reflections which belong to the PEG-TR'' phase i.e. $2\theta = 21.7^{\circ}$ $2\theta = 22.7^{\circ}$ and $2\theta = 23.8^{\circ}$ along with a new reflection at $2\theta = 20.4^{\circ}$ belongs to TR-(CH₂)₂-TR unit. (see main text for details). This final PEG-TR'' phase remains intact upon cooling back the sample to $-10\text{ }^{\circ}\text{C}$ and later reheating it to the complete melting of the sample. This simple experiment shows that the phase transition from initial low-temperature PEG monoclinic system to the modified PEG-TR'' monoclinic system is an irreversible phase transition process. The irreversibility of the phase transition could be attributed to the kinetic effect as PEG-TR'' phase requires more time to form as compared to PEG phase when the sample was initially crystallized from its molten state. One can also hypothesize that the formation of initial PEG phase might be a requirement or an assistance to the formation of final PEG-TR'' phase.

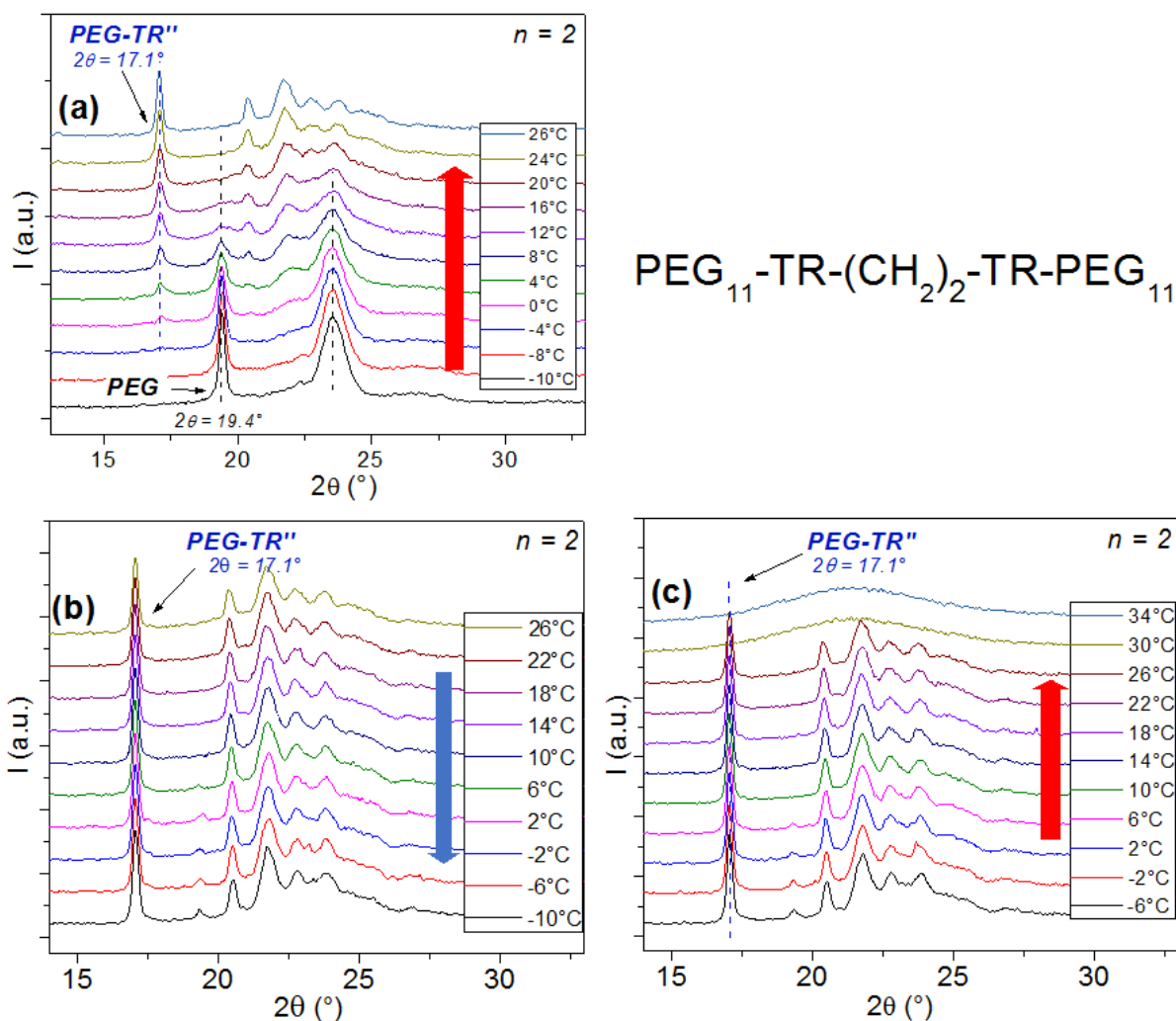


Figure A35: Temperature dependent wide angle X-ray scattering measurements were performed to observe an irreversible phase transition in $\text{PEG}_{11}\text{-TR-(CH}_2\text{)}_2\text{-TR-PEG}_{11}$ sample. After crystallization at -10°C , (a) the sample was first heated to $T = 26^\circ\text{C}$ where the initial PEG phase is completely transformed into the new PEG-TR'' phase, while the sample is still not melted then, (b) the sample was cooled again to -10°C and (c) reheated until its complete melting.

1. $\text{PEG}_{11}\text{-TR-(CH}_2\text{)}_4\text{-TR-PEG}_{11}$

Temperature dependent wide angle X-ray scattering measurements were performed to observe an irreversible phase transition in $\text{PEG}_{11}\text{-TR-(CH}_2\text{)}_4\text{-TR-PEG}_{11}$ sample (see Figure A36). It can be observed that initially at -10°C , only two characteristic

diffraction peaks of PEG monoclinic system was observed i.e. at $2\theta = 19.5^\circ$ (120) and $2\theta = 23.6^\circ$ (032)*. However, upon heating, both (120) and (032)* reflections of low-temperature PEG phase start to shift to lower 2θ values (i.e. $2\theta = 19.1^\circ$ and $2\theta = 23.3^\circ$) which belong to the (120) and (032)* reflections of the high-temperature PEG-TR' phase. During this phase transformation process, at $T = 2^\circ\text{C}$ an additional reflection at $2\theta = 16.7^\circ$ also starts to appear however, it disappears at $T = 16^\circ\text{C}$ before the low-temperature PEG phase completely transform into PEG-TR' phase (see main text for the detailed description of this phenomenon). On cooling the system to $T = -10^\circ\text{C}$ again, the final PEG-TR' crystal system remains stable and it stays intact until the complete melting of the sample. This simple experiment shows that the phase transition from initial low-temperature PEG monoclinic system to the modified PEG-TR' monoclinic system is an irreversible solid-solid phase transition process. The irreversibility of the phase transition could be attributed to the kinetic effect as the formation of PEG-TR' phase, during the initial crystallization of sample from the molten state, is comparatively slower as compared to the formation of simple PEG phase. One can also have hypothesized that the formation of initial PEG phase might be an essential or act as an assistance to the formation of final PEG-TR' phase.

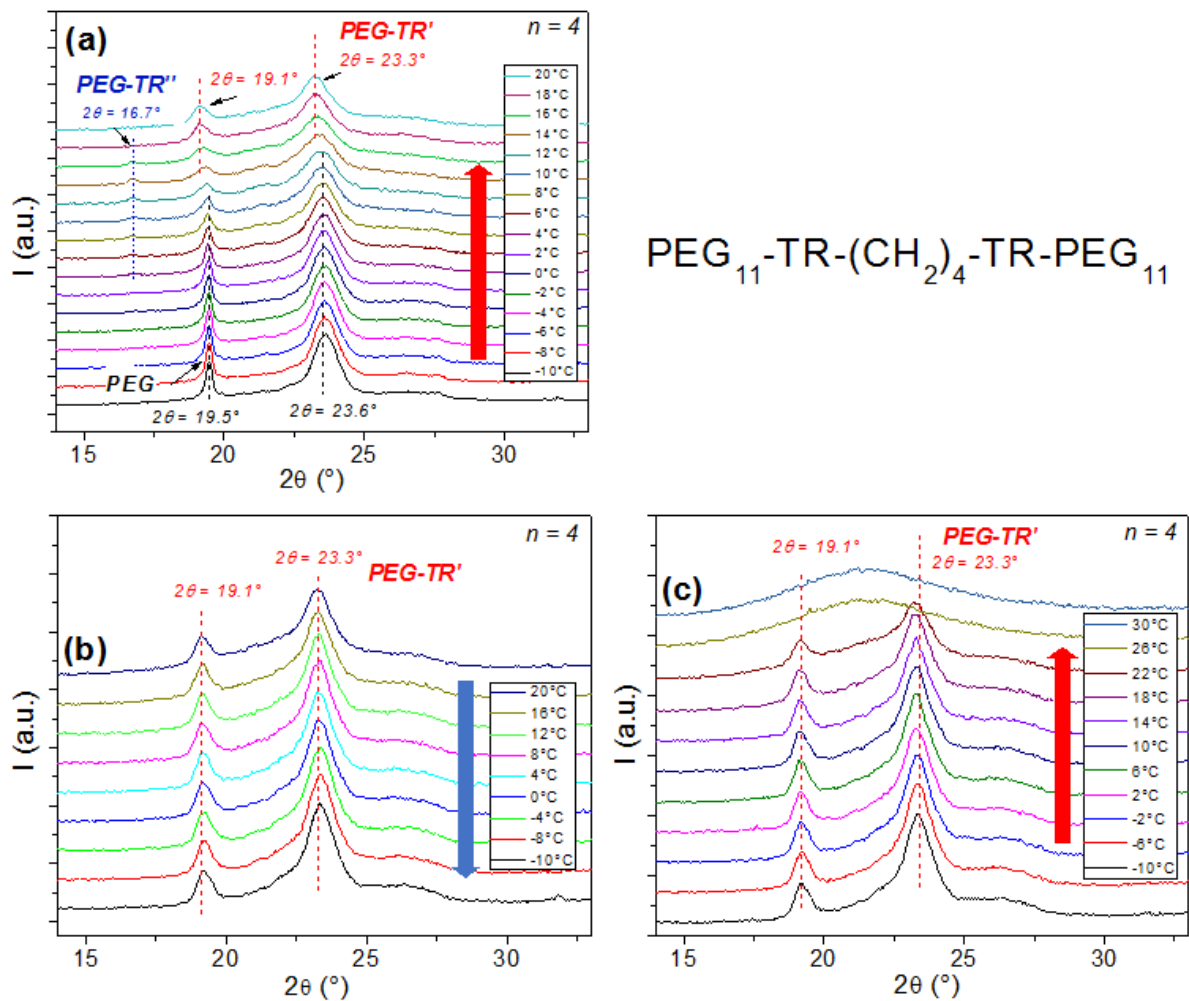


Figure A36: Temperature dependent wide angle X-ray scattering measurements were performed to observe an irreversible phase transition in $\text{PEG}_{11}\text{-TR-(CH}_2\text{)}_4\text{-TR-PEG}_{11}$ sample. After crystallization at -10°C (a) the sample was first heated to the temperature where the initial PEG phase was completely transformed into the new PEG-TR' phase while the sample was still not melted i.e. $T = 20^\circ\text{C}$. (b) The sample was then cooled again to -10°C and later(c) reheated until its complete melting.

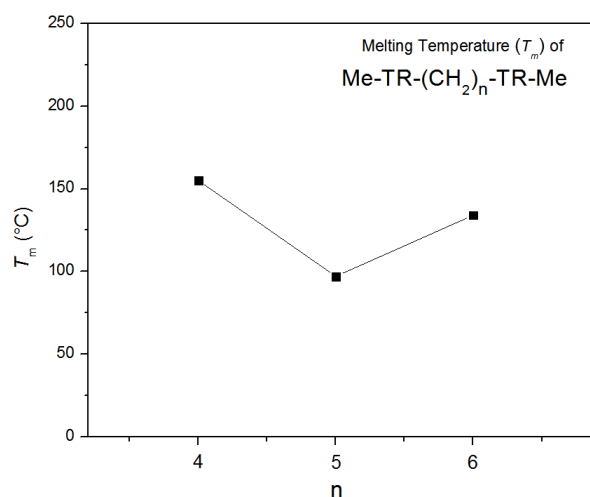


Figure A37: Melting temperatures (T_m) of Me-TR-(CH₂)_n-TR-Me ($n = 4-6$) units.

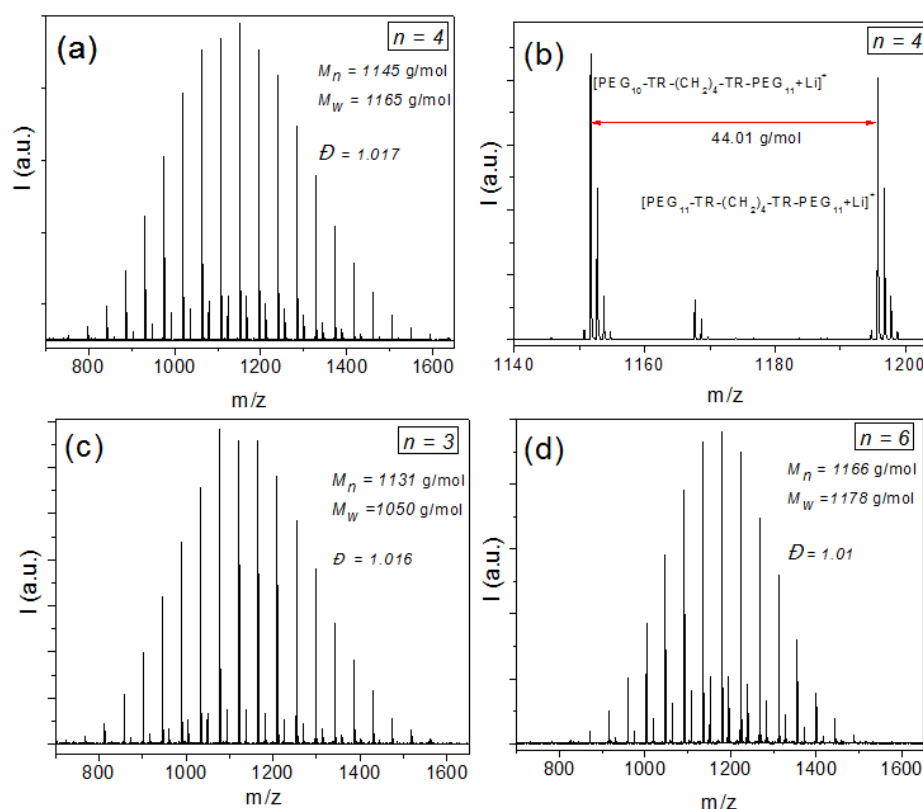


Figure A38: (a) MALDI-ToF mass spectrum and polydispersity index \mathcal{D} of PEG₁₁-TR-(CH₂)₄-TR-PEG₁₁, (b) A zoomed version of MALDI-ToF mass spectrum of PEG₁₁-TR-(CH₂)₄-TR-PEG₁₁ for two chain lengths differing by one monomer unit. (c) MALDI-ToF mass spectrum and polydispersity index \mathcal{D} of PEG₁₁-TR-(CH₂)₃-TR-PEG₁₁ and (d) PEG₁₁-TR-(CH₂)₆-TR-PEG₁₁.

The polydispersity index \mathcal{D} is calculated as

$$\mathcal{D} = \frac{M_w}{M_n}$$

with

$$M_n = \frac{\sum n_i \cdot M_i}{\sum n_i}$$

$$M_w = \frac{\sum n_i \cdot M_i^2}{\sum n_i \cdot M_i}$$

where, M_n is the number average molar mass, M_w is the weight average molar mass, M_i represents the mass of polymer chain with i units while n_i represents the number of chains of i units.

7. List of Publications

- (1) Kirsch, C.; Pulst, M.; **Samiullah, M. H.**; Ruda, P.; Hasan, N.; Kressler, J. 1,2,3-Triazole Mediated Li⁺-Ion Conductivity in Poly(ethylene Oxide) Based Electrolytes. *Solid State Ionics* **2017**, *309*, 163–169.
- (2) Bilal, M.; Prehm, M.; Njau, A.; **Samiullah, M.H.**; Meister, A.; Kressler, J. Enzymatic Synthesis and Characterization of Hydrophilic Sugar Based Polyesters and Their Modification with Stearic Acid. *Polymers (Basel)*. 2016, *8* (3), 80.
- (3) Pulst, M.; **Samiullah, M. H.**; Baumeister, U.; Prehm, M.; Balko, J.; Thurn-Albrecht, T.; Busse, K.; Golitsyn, Y.; Reichert, D.; Kressler, J. Crystallization of Poly(ethylene Oxide) with a Well-Defined Point Defect in the Middle of the Polymer Chain. *Macromolecules* 2016, *49* (17), 6609–6620.
- (4) **Samiullah, M. H.**; Reichert, D.; Zinkevich, T.; Kressler, J. NMR Characterization of PEG Networks Synthesized by CuAAC Using Reactive Oligomers. *Macromolecules* 2013, *46* (17), 6922–6930.

Meeting Abstracts

- (1) Bilal, M.; **Samiullah, M.H.**; Kressler, J. Preparation and characterization of nanoparticles from fatty acid modified polyesters. 248th ACS National Meeting, San Francisco, CA. August 2014
- (2) **Samiullah, M.H.**; Reichert, D.; Zinkevich, T.; Kressler, J. Synthesis and characterization of Well-defined PEG-Networks. International Symposium on Amphiphilic Polymers, Networks, Gels and Membranes (APNGM 15). Budapest, Hungary. August, 2015

Curriculum Vitae

Personal Details

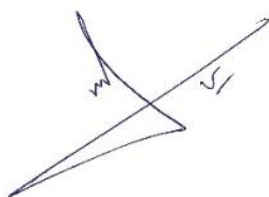
Name	Muhammad Haris Smaiullah
Date/Place of Birth	05-11-1984, Karachi (Pakistan)
Marital Status	Single

Educational Details

09/2011-till today	Ph.D. student at the Institute of Chemistry Martin Luther Universität Halle Wittenberg, Halle (Saale), in the group of Prof. Dr. Jörg Kreßler
10/2008-06/2011	Master of Science (MSc) in Applied Polymer Science at Martin Luther Universität Halle-Wittenberg
10/2002-08/2006	Bachelors of Engineering in Polymer Engineering at Hamdard University, Karachi(Pakistan)

Work Experience

10/2006-09/2008	Shift Engineer at Dadex Eternit Ltd. Karachi, Pakistan
-----------------	--



Halle (Saale), 20-09-2017
Muhammad Haris Samiullah

Erklärung

Hiermit erkläre in an Eides statt, dass ich die vorliegende Arbeit selbständig und ohne fremde Hilfe verfasst habe. Ich habe keine anderen Quellen und Hilfsmittel als die angegebenen verwendet und anderen Werken wörtlich oder inhaltlich entnommene Stellen als solche gekennzeichnet. Diese Arbeit habe ich an keiner anderen Hochschule vorgelegt und mich zu keinem früheren Zeitpunkt um den Doktorgrad beworben.

Muhammad Haris Samiullah

Halle (Saale), 20-09-2017